

Flatland Photonics: Circumventing Diffraction with Planar Plasmonic Architectures

Thesis by
Jennifer Anne Dionne

In Partial Fulfillment of the Requirements
for the Degree of
Doctor of Philosophy



California Institute of Technology
Pasadena, California
2009

(Defended October 10, 2008)

In honor of my parents, George and Sandra Dionne;
in joyful memory of my grandmother,
Barbara G. Draper;
& with deepest gratitude to Nhat and Jenn.

Acknowledgements

Just over five years ago, I received an out-of-area phone call in my St. Louis apartment. The caller asked if a ‘Miss Deon’ was available, mispronouncing my last name in the same way many telemarketers do. For some reason, telemarketers loved my telephone number, and I had grown accustomed to giving a fairly standard reply: “Yes, she is, but I don’t believe she’s interested in what you’re offering.” Thankfully, that evening I refrained from a terse response. On the line was Professor Rob Phillips, calling to offer me admission to the Applied Physics graduate program at Caltech. It is hard to overstate the feelings of joy, honor, and excitement I experienced as a result of that phone call. I hardly expected admission to any graduate program, let alone at a premier research institute like Caltech. In the following weeks, other attractive admission offers did arrive. However, the opportunity to study at a school where scientists like Millikan, Pauling and Feynman once roamed the halls could not be refused.

It is hard to believe that Rob’s phone call was so long ago. Five years have passed by in a heartbeat, with many experiences gained and many perspectives changed along the way. To this day, however, I still feel an enormous sense of honor and pride about being a part of the Caltech community. It is my pleasure to acknowledge those individuals who have made this experience so memorable.

First and foremost, I would like to thank my advisor, Professor Harry Atwater. Harry combines a passion for research with unparalleled intelligence and a genuine concern for the well-being of his students. Within the past five years, I have developed a deep respect for Harry that reflects both his intellectual abilities and his character. On a scientific level, Harry has been one of the best mentors and colleagues I could ask for - he provides valuable feedback, asks probing questions, and is not afraid to offer constructive criticism. As a graduate student, however, I have been most inspired by Harry’s character. Harry is among the most compassionate and selfless individuals I know. Harry is a real “people person”, and always seems to put the needs and desires of others ahead of his own. All things considered, Harry exemplifies what it means to be a “renaissance man” - he combines scientific success with entrepreneurial accomplishments and a deep concern for his personal relationships. It has been a true privilege to work for him, and I will always be grateful for all that he has taught me in the past five years.

Alongside Harry, a huge ‘thank-you’ goes to Professor Albert Polman of the FOM-Institute, AMOLF. In my first year, I was fortuitously assigned to share an office with Albert, who was on a year-long sabbatical in Harry’s group. Our initial interactions involved discussions of food, culture, geography, and family. It was not long, however, before Albert was sharing with me his passion for photonics and the rare-earth elements. Those discussions ultimately led to our first calculations of plasmons on planar interfaces - calculations that have laid the foundation for this thesis. Albert exhibits uncanny physical insight and an ability to explain complex and convoluted optical phenomena with a few basic overarching concepts. In many ways, Albert has been like a second advisor to me, and without his support, this thesis would not be possible.

My first interest in optics was sparked just before my arrival at Caltech,

when I read a report in *Science* by Dr. Henri Lezec. In this article, Henri demonstrated that nanostructured metallic films could overcome the weak and diffuse transmission associated with diffraction-limited optics. Needless to say, I was very excited to learn everything I could from Henri when he joined Harry's group in 2005. In the two years that I worked with Henri, I learned more about science and about being a scientist than most prior experiences combined. Henri exhibits an enthusiasm for work that is highly contagious, and I regard him as one of the finest scientists that I have had the opportunity to work with. Our collaborations led to the MIM waveguide experiments described in the first half of Chapter 4 and the negative refraction experiments of Chapter 5.

Throughout graduate school, I have had the good fortune of working with many gifted colleagues. In particular, I would like to thank those graduate students who have joined me as co-authors on various papers: Ken Diest, Luke Sweatlock, and Ewold Verhagen. Ken joined Caltech from a position at HP Labs, and contributed an incredible knowledgebase to our group regarding device fabrication. Ken and I worked side-by-side for months on the optical MOS modulator described in Chapter 6, and also collaborated on a plasmon-based full-color display. Many of my fondest optics-lab memories involve working with Ken, who could always add the right touch of wit, sarcasm, and Ag paint to a less-than-ideal measurement. Luke Sweatlock taught me everything I know about numerical methods for plasmonics. Since my first day at Caltech (which was Hawaiian shirt day for Luke), he has served as a great student-mentor and a fountain of information about plasmonics. Luke provided valuable feedback on the calculations of Chapter 2, and helped implement the plasMOSTor circuit simulations of Chapter 6. I first had the opportunity to work with Ewold Verhagen during my 7-week 'mini-sabbatical' at FOM-AMOLF. Ewold is a brilliant physicist who combines keen scientific insight with healthy skepticism. He has been a wonderful collaborator as we worked together on the negative index calculations of Chapter 5 and the near-field measurements of Chapter 4. I am looking forward to working with him on the future negative-index projects described in Chapter 5 and Chapter 7.

In addition to graduate student collaborators, I have also been fortunate to work with an extraordinary Caltech undergraduate, Philip Munoz. Phil joined me as a SURF in the summer of 2007, and has continued working with me this summer. He and I worked together on the the photoactive polymer work described in Chapter 3 and also on the local density of states simulations in Chapter 7.

Harry's group is both large and diverse, and my graduate experience has greatly benefitted from interactions with students whose interests range from photovoltaics to ferroelectrics to Si-based photonics. In particular, I would like to acknowledge Melissa Archer, Matthew Dicken, and Katsu Tanabe, who joined Harry's group concurrently with me. Melissa generously provided assistance for any high-vacuum-related project and could always cook up a delicious meal. Matt also provided me with much-needed feedback in my attempts to resurrect the sputterer. Katsu combined a passion for photovoltaics with an interest in plasmonics, and I enjoyed opportunities to discuss both topics with him. Among other group members, I would like to thank (in alphabetical order):

Natali Alster, Julie Biteen, Julie Brewer, Ryan Briggs (my AB effect buddy, and one of the brightest third years I know), Stan Burgos, Claudine Chen (a superb WMW mentor), Matt Czubakowski, Davis Darvish, Mike Deceglie, Vivian Ferry (a quantum dot and yoga virtuoso), Micha Fireman, Anna Hiszpanski (a very fun conference roomie), Seokmin Jeon, Mike Kelzenberg, Greg Kimball, Beth Lachut, Andrew Leenheer, Maribeth Mason, Morgan Putnam, Imogen Pryce (my Santa Barbara buddy), Christine Richardson, Jen Ruglovsky, Dan Turner-Evans, Robb Walters (who taught me everything I know about IR-based optical excitation and detection), and Emily Warmann.

With such a large group, I think many students would be lost without the assistance of some very talented postdoctoral researchers. In particular, I would like to acknowledge: Domenico Pacifici, Pieter Kik, Koray Aydin, Mike Filler, Anna Fontcuberta i Morral, Sungjee Kim, Keisuke Nakayama, Jeremy Munday, Deirdre O’Carroll, and Young-Bae Park. Thanks also to Prof. Stefan Maier and Prof. Mark Brongersma, former Atwater-group members, who have graciously shared their immense knowledge of plasmonics with me.

Outside of Harry’s group, I have also benefitted from discussions with other students in Applied Physics, including Matt Eichenfeld, Mike Shearn, Tom Johnson, Chris Michael, Dave Henry, Andrea Armani, and Auna Moser. The staff of the micro-nano lab and the KNI lab have also provided invaluable scientific support. In particular, I would like to thank Ali Ghaffari, Guy deRose, Melissa Melendes, and Bophan Chhim. The Applied Physics and KNI administration has been a continual source of support. I would like to thank those assistants who made the department run smoothly, including: Cierina Marks, Eleonora Vorobieff, Irene Loera, Connie Rodriguez, Rosalie Rowe, and Mary Sikora. April Neidholdt has served as Harry’s assistant since my third year of graduate school. If Harry is a renaissance man, April is certainly a renaissance woman. She balances everything from grants to travel to p-card reports to techmart. Our group would be lost without her - she has been an amazing assistant, and also one of my closest friends. I am grateful for all that she has offered me during my graduate career.

In the past five years, Watson 248 has been a second home for me. My officemates always made work a pleasant and fun environment, whether chilling on a Friday afternoon or surviving ‘a case of the Mondays’. A resounding thanks to Brendan Kayes, Krista Langeland, Gerald Miller, Jimmy Zahler, and Darci Taylor.

While many nights of my graduate career were spent in Watson, I was fortunate to have friendly roommates to welcome me back home: Claire Levallant was a brilliant mathematician who taught me both number theory and a bit of French. Eve Stenson combined her enthusiasm for science with an always-cheerful greeting. Heidi Privett knew how to cook a wholesome southern meal, and didn’t seem to mind my late-night thesis-writing sessions; she has been a pleasant companion during my last year of graduate school. Dawn Schaffer roomed with me in Amsterdam; together we braved countless journeys to Damrak though wind, fire, and rain. Emily McD always brought spirit to a girl’s-night out. I would like to particularly thank Carrie Hofmann, who has been one of the best roommates I could ask for...One might think that working

and living together would be difficult, but being around Carrie was a pleasure. I am grateful to have had her company throughout my years as a graduate student.

While traveling for research, a number of individuals have made me feel like I was at home, scientifically. In particular, I would like to thank the past and present members of the FOM-Institute who welcomed me as a group member, and with whom I've shared many stimulating scientific discussions: Femius Koenderink, Rob van Loon, Ernst Jan Vasseur, Martin Kuttge, Sabastian Bidault, Kylie Catchpole, Rene de Waele, Anna Tchebotareva, Joan Peninkhof, and Jeroen Kalkman. Thanks also to Chris deRuiter of TU/E and Phillips Research.

I have been fortunate to interact and collaborate with many skilled scientists who directly contributed to this thesis. However, my experience of graduate school will be recalled with deep fondness because of the friendships I have formed. I am happy to say that the classmates who shared APh coursework with me my first year are among my closest friends: Vikram Deshpande, Raviv Perahia, Waheb Bishara, Tristan Ursell, and Deepak Kumar. Words cannot describe how grateful I am to these friends for making my experience at Caltech so enjoyable - from braving blizzard conditions in the Sierra's to weekend windsurfing. Saying goodbye to these friends will not be easy, but I anticipate many fun years of scientific and social collaboration to come.

I also have enjoyed many memorable on and off-campus adventures with Dave Ebner, Tris Smith, Jenny Roizen, Hernan Garcia, Anna Kilroi, Erin Koos, Sam Daly, Erik Peterson, Rizal Hariadi, Glenn Garrett, Andy Downard, Evan Neidholdt, Jan Streuff, Kakani Young, Steph Johnson, and Geoff Lovely. Thank you for the gift of your friendship.

Of course, this thesis would not be possible without the unconditional support of my family. Words cannot express how grateful I am to my mom and dad, who sacrificed so much so that I could pursue my personal dreams. I also thank Jenn Stockdill - not formally a member of my family, but in many ways a sister to me. Jenn is the most thoughtful individual I have ever met, and the best friend I could ask for. A part of me will be missing when she moves to NY. Nhat Vu has given my life meaning since freshman year of college. His love and support have meant the world to me in the past nine years. This thesis is dedicated to these immediate and extended family members.

Lastly, I would like to thank the faculty and funding agencies who have provided me with the opportunity to pursue a PhD. I gratefully acknowledge fellowship support from Caltech, the National Science Foundation, and the National Defense Science and Engineering Graduate Fellowship Program. Many thanks to the members of my candidacy committee, including Professors Axel Scherer, Kerry Vahala, and Rob Phillips - your feedback steered my research in the right direction. Thanks also to Professor Julia Greer, who is a tremendous female-faculty role model. I hope we will have to opportunity to collaborate in the future. My thesis committee members include Professors Oskar Painter, Kerry Vahala, Erik Antonsson, and John Preskill. Oskar and Kerry have provided much valuable feedback in the past year, both regarding research and career opportunities. Erik has been a pleasure to interact with, since he bridges

the domain between academia and industry. John was an engaging lecturer for first-year classical mechanics, one whose teaching style I hope to emulate.

I have consistently been humbled and amazed by the quality of Caltech's faculty and students. I am grateful to the entire Caltech community for providing me with a most memorable graduate experience.

*Jennifer A. Dionne
October 2008
Pasadena, CA*

Abstract

On subwavelength scales, photon-matter interactions are limited by diffraction. The diffraction limit restricts the size of optical devices and the resolution of conventional microscopes to wavelength-scale dimensions, severely hampering our ability to control and probe subwavelength-scale optical phenomena. Circumventing diffraction is now a principle focus of integrated nanophotonics. Surface plasmons provide a particularly promising approach to sub-diffraction-limited photonics. Surface plasmons are hybrid electron-photon modes confined to the interface between conductors and transparent materials. Combining the high localization of electronic waves with the propagation properties of optical waves, plasmons can achieve extremely small mode wavelengths and large local electromagnetic field intensities. Through their unique dispersion, surface plasmons provide access to an enormous phase space of refractive indices and propagation constants that can be readily tuned with material or geometry.

In this thesis, we explore both the theory and applications of dispersion in planar plasmonic architectures. Particular attention is given to the modes of metallic core and plasmon slot waveguides, which can span positive, near-zero, and even negative indices. We demonstrate how such basic plasmonic geometries can be used to develop a suite of passive and active plasmonic components, including subwavelength waveguides, color filters, negative index metamaterials, and optical MOS field effect modulators. Positive index modes are probed by near- and far-field techniques, revealing plasmon wavelengths as small as one-tenth of the excitation wavelength. Negative index modes are characterized through direct visualization of negative refraction. By fabricating prisms comprised of gold, silicon nitride, and silver multilayers, we achieve the first experimental demonstration of a negative index material at visible frequencies, with potential applications for sub-diffraction-limited microscopy and electromagnetic cloaking. We exploit this tunability of complex plasmon mode indices to create a compact metal-oxide-Si (MOS) field effect plasmonic modulator (or plasMOStor). By transforming the MOS gate oxide into an optical channel, amplitude modulation depths of 11.2 dB are achieved in device volumes as small as one one-fifth of a cubic wavelength. Our results indicate the accessibility of tunable refractive indices over a wide frequency band, facilitating design of a new materials class with extraordinary optical properties and applications.

Contents

| | |
|--|------------|
| List of Figures | xv |
| List of Publications | xix |
| 1 Introduction | 1 |
| 1.1 Light-matter interactions on subwavelength scales | 1 |
| 1.1.1 The <i>hole</i> story | 2 |
| 1.1.2 What are surface plasmons? | 3 |
| 1.2 Scope of this thesis | 5 |
| 2 Electromagnetic Modes of Multilayer Waveguides | 9 |
| 2.1 Maxwell in multilayers: old equations, new applications | 9 |
| 2.2 Optical characterization of metallic films | 10 |
| 2.3 Bound modes of planar metal plasmon waveguides | 12 |
| 2.3.1 Single interface surface plasmons | 12 |
| 2.3.2 Coupled surface plasmons: The insulator-metal-insulator waveguide | 19 |
| 2.3.3 Outlook for insulator-metal-insulator waveguides | 26 |
| 2.4 The Metal-Insulator-Metal Waveguide: Balancing localization and loss | 28 |
| 2.4.1 Slot waveguide dispersion: Plasmonic and photonic modes | 29 |
| 2.4.2 Mode propagation and penetration | 33 |
| 2.4.3 Electromagnetic energy density | 36 |
| 2.5 Chapter Summary | 40 |
| 3 Experimental Imaging of Surface Plasmons, Part I: Metallic Surfaces | 41 |
| 3.1 Far-field excitation and detection | 41 |
| 3.2 Near-field imaging with photoactive polymers | 45 |
| 3.3 Chapter Summary | 51 |
| 4 Experimental Imaging of Surface Plasmons, Part II: The Metal- Insulator-Metal Waveguide | 53 |
| 4.1 Plasmonic waveguides for optoelectronic networking | 53 |
| 4.2 Far-field excitation and detection | 54 |
| 4.2.1 Slab waveguides | 56 |
| 4.2.2 Finite width waveguides (i.e., MIM ‘wires’) | 59 |
| 4.3 Near-field imaging with scanning optical microscopy | 63 |
| 4.4 Chapter Summary | 69 |

| | |
|--|------------|
| 5 Plasmon-based Negative Index Materials | 71 |
| 5.1 Reversing Newton's prism: The physics of negative index materials | 71 |
| 5.1.1 Negative indices and negative refraction | 71 |
| 5.1.2 Metamaterials | 73 |
| 5.2 Plasmonic metamaterials: Theory | 74 |
| 5.2.1 Waveguides as Materials: Theoretical foundations | 74 |
| 5.2.2 Lossy dispersion and the necessary condition for negative indices | 77 |
| 5.2.3 Mapping indices and figures of merit: A guide to the experimentalist | 82 |
| 5.2.4 Section summary: Theoretical negative index materials | 86 |
| 5.3 Negative refraction at visible wavelengths | 88 |
| 5.3.1 Snell's law and surface plasmons | 89 |
| 5.3.2 MIM-metamaterial prisms for negative refraction | 91 |
| 5.3.3 Section summary: Experimental negative index materials | 96 |
| 5.4 Ongoing research in plasmonic metamaterials | 96 |
| 5.4.1 NIM Electrodynamics: Toward direct observation of negative phase | 97 |
| 5.4.2 Toward a three-dimensional negative index material | 99 |
| 5.5 Chapter Summary | 101 |
| 6 Active Plasmonic Devices Based on Dispersion Engineering | 103 |
| 6.1 Plasmonic dispersion has a silver lining | 103 |
| 6.2 The PlasMOSTor: A metal-oxide-Si field effect plasmonic modulator | 104 |
| 6.3 Photonic and plasmonic color displays | 114 |
| 6.4 Chapter Summary | 121 |
| 7 Summary and Outlook | 123 |
| A Ag and SiO₂ Optical Constants | 133 |
| B Plasmon Dispersion and Minimization Routines | 135 |
| B.1 Derivation of the thin film dispersion relations for 3-layer, symmetric geometries | 135 |
| B.2 Derivation of the thin film dispersion relations for 5-layer, arbitrary materials geometries | 140 |
| B.3 Numerical Methods | 143 |
| C Plasmotor Sample Preparation and Experimental Techniques | 147 |
| D Scattering from an Abruptly Terminated Plasmon Waveguide | 151 |
| Bibliography | 155 |

List of Figures

| | | |
|------|---|----|
| 1.1 | Beaming light from a subwavelength aperture. | 2 |
| 1.2 | Particle and planar plasmon geometries. | 3 |
| 1.3 | The Lycergus Cup, 4 th century A.D.: optical dichroism based on metallic nanoparticles. | 4 |
| 1.4 | Pictorial overview of this thesis. | 8 |
| 2.1 | Real and imaginary components of the permittivity for Ag and SiO ₂ | 12 |
| 2.2 | Surface plasmon dispersion for a single metal-dielectric interface. | 14 |
| 2.3 | Phase, group, and energy velocities for single-interface surface plasmons. | 15 |
| 2.4 | Surface plasmon propagation lengths for a single metal-dielectric interface. | 16 |
| 2.5 | Surface plasmon field penetration into the metal and dielectric for a single-interface geometry. | 17 |
| 2.6 | Surface plasmon electric energy density and field profiles for single-interface geometries. | 18 |
| 2.7 | Characteristic magnetic field profiles in multilayer plasmonic waveguides. | 21 |
| 2.8 | Thin film plasmon dispersion, computed using a lossless Drude model. | 22 |
| 2.9 | Thin film plasmon dispersion, computed using empirically-determined optical constants. | 23 |
| 2.10 | Plasmon propagation lengths along thin metallic films embedded in a symmetric dielectric environment. | 24 |
| 2.11 | Plasmon propagation lengths along thin metallic films as a function of plasmon wavelength. | 26 |
| 2.12 | Modal skin depth for surface plasmons propagating along thin metallic films. | 27 |
| 2.13 | Transverse magnetic dispersion relations and tangential electric field profiles for metal-insulator-metal planar waveguides. | 30 |
| 2.14 | Transverse magnetic dispersion relations and tangential electric field profiles for thin core metal-insulator-metal waveguides. | 32 |
| 2.15 | TM-polarized propagation and skin depth for thick-core metal-insulator-metal waveguides. | 33 |
| 2.16 | TM-polarized propagation lengths and field penetration for the H _y field symmetric mode of thin core MIM waveguides. | 34 |
| 2.17 | TM-polarized propagation lengths and field penetration for the H _y field antisymmetric mode of thin core metal-insulator-metal waveguides. | 36 |

| | | |
|------|---|----|
| 2.18 | TE-polarized propagation for thin-core metal-insulator-metal waveguides as a function of wavelength. | 37 |
| 2.19 | Electromagnetic energy density for the modes of a metal-insulator-metal waveguide with a 250-nm-thick dielectric core. | 38 |
| 2.20 | Electromagnetic energy density for the modes of a metal-insulator-metal waveguide with a 100-nm-thick dielectric core. | 39 |
| 3.1 | Grating coupling photons to plasmons. | 42 |
| 3.2 | Spectral response of decoupled plasmons on a thick metallic film | 44 |
| 3.3 | Experimental surface wave decay and plasmon propagation lengths along an Ag/air interface. | 46 |
| 3.4 | Chemical structure of the photoactive polymer, poly Disperse Red 1 Methacrylate | 47 |
| 3.5 | Single groove scatterers and corrals for plasmon photolithography. | 48 |
| 3.6 | Non-contact atomic force microscopy images of plasmonic waveguides and resonators, generated through plasmon printing with a photoactive polymer. | 49 |
| 3.7 | Experimental atomic force microscope image and finite-difference time-domain simulation of a circular corral. | 50 |
| 3.8 | Experimental atomic force microscope image and finite-difference time-domain simulation of an elliptical resonator. | 51 |
| 4.1 | Metal-insulator-metal waveguide fabrication sequence and experimental schematic. | 55 |
| 4.2 | Experimental spectra for two-dimensional slab waveguides with nitride core thicknesses of $t = 50$ nm and 100 nm. | 57 |
| 4.3 | Experimental metal-insulator-metal slab waveguide transmission and propagation with slit inputs and outputs. | 59 |
| 4.4 | Experimental metal-insulator-metal slab waveguide transmission and propagation with grating inputs and outputs. | 60 |
| 4.5 | Experimental intensities and propagation lengths of metal-insulator-metal wires with a rectangular cross-section. | 62 |
| 4.6 | Experimental schematic and scanning electron micrographs of the near-field interferometric metal-insulator-metal geometry. | 64 |
| 4.7 | Near and far-field aperture emission maps. | 65 |
| 4.8 | Near-field scan of a metal-insulator-metal waveguide with a single-slit output, and simulated electric field intensities. | 67 |
| 4.9 | Near-field scans of metal-insulator-metal waveguide-cavities. | 69 |
| 4.10 | Experimentally-determined metal-insulator-metal dispersion, based on near-field interferometry. | 70 |
| 5.1 | Photorealistic image of a negative refractive index material. | 72 |
| 5.2 | Split-ring resonator metamaterial designed for microwave frequencies. | 73 |
| 5.3 | Lossless dispersion for metal-insulator-metal, insulator-insulator-metal, and metal-insulator-metal positive and negative index waveguides. | 76 |

| | | |
|------|---|-----|
| 5.4 | Lossy dispersion for metal-insulator-metal waveguides, including both positive and negative index modes. | 79 |
| 5.5 | Lossy dispersion for insulator-insulator-metal waveguides, including positive and negative index branches. | 80 |
| 5.6 | Lossy dispersion for insulator-metal-insulator waveguides, including positive and negative index branches. | 81 |
| 5.7 | Metal-insulator-metal negative index and figure of merit maps for Ag/GaP geometries. | 83 |
| 5.8 | Finite-difference time domain simulation of negative refraction into a metal-insulator-metal waveguide. | 84 |
| 5.9 | Metal-insulator-metal negative index and figure of merit maps for Ag/Si ₃ N ₄ geometries. | 85 |
| 5.10 | Insulator-insulator-metal mode index and figure of merit maps for Ag/GaP-based geometries. | 86 |
| 5.11 | Insulator-insulator-metal mode index and figure of merit maps for Ag/Si ₃ N ₄ -based geometries. | 87 |
| 5.12 | Insulator-metal-insulator mode index and figure of merit maps for Ag/GaP-based geometries. | 88 |
| 5.13 | Insulator-metal-insulator index and figure of merit maps for Ag/Si ₃ N ₄ -based geometries. | 89 |
| 5.14 | Implementation of positive- and negative-index metal-insulator-metal waveguides. | 90 |
| 5.15 | Cross-section and plan-view of negative refraction experiment. . . | 92 |
| 5.16 | Three-dimensional schematic of negative refraction experiment. . | 93 |
| 5.17 | Direct visualization of negative refraction. | 94 |
| 5.18 | Wavelength-dependent refraction through a negative index prism. | 95 |
| 5.19 | Waveguide indices as determined from interferometry. | 95 |
| 5.20 | Tabulated experimental negative indices. | 97 |
| 5.21 | Direct probe of electrodynamics in negative index materials. . . | 98 |
| 5.22 | Simulation and fabrication of a negative index near-field interferometer. | 99 |
| 5.23 | Indices for three-dimensional negative index geometries. | 100 |
| 5.24 | Negative refraction into metal-insulator-metal multilayers. . . . | 101 |
| 6.1 | Schematic and band diagram of a conventional n-MOSFET. . . . | 105 |
| 6.2 | Schematic of a plasmonic MOSFET (plasmistor) for modulation of optical signals. | 106 |
| 6.3 | Geometry of the fabricated plasmistor | 107 |
| 6.4 | Dispersion relations and tabulated mode properties of the plasmistor. | 108 |
| 6.5 | Finite difference time domain simulations of the plasmistor, operating at a free-space wavelength of 1.55 μm | 109 |
| 6.6 | Finite difference time domain simulations of the plasmistor, operating at a free-space wavelength of 685 nm. | 110 |
| 6.7 | Experimental electrical and optical characterization of the plasmistor. | 112 |
| 6.8 | An all-optical, SOI-based plasmistor. | 113 |

| | | |
|------|--|-----|
| 6.9 | Schematic metal-insulator-metal ‘flat-panel’ display and associated dispersion relations. | 116 |
| 6.10 | Display colors as a function of voltage and input-output separation. | 117 |
| 6.11 | Display colors as a function of voltage and output slit depth. | 118 |
| 6.12 | Experimental color filtering in passive metal-insulator-metal waveguides. | 119 |
| 6.13 | Experimental spectra of passive metal-insulator-metal waveguides. | 120 |
| 6.14 | Perspective view of a metal-insulator-metal-based pixel element and full-color display. | 121 |
| | | |
| 7.1 | Calculations of the effective permittivity and permeability in plasmonic waveguides, for both positive and negative index modes. | 125 |
| 7.2 | Calculations of the mode wavevector, permittivity and permeability in negative-index plasmonic waveguides. | 126 |
| 7.3 | Dispersion relationships and simulated fields for a plasmonic cloak. | 127 |
| 7.4 | Experimental schematic and prototype fabrication of a ‘perfect lens’. | 129 |
| 7.5 | Finite difference time domain simulations of the local density of optical states in a homogeneous media. | 130 |
| 7.6 | Simulations in search of a plasmon mirage. | 131 |
| | | |
| B.1 | Geometry of a three-layer, symmetric waveguide. | 135 |
| B.2 | Geometry of a five-layer waveguide. | 141 |
| B.3 | Complex k -space landscape of mono-modal and multi-modal systems. | 143 |
| B.4 | Graphical versus analytic minimization routines. | 144 |
| | | |
| C.1 | Scanning electron micrographs of the fabricated plasmistor membrane and devices, from the centimeter-scale to the nanometer-scale. | 147 |
| C.2 | Raman spectra and x-ray diffraction reciprocal space maps of the plasmistor membrane. | 148 |
| | | |
| D.1 | Scattering from a three-layer symmetric plasmon waveguide. | 152 |

List of Publications

Portions of this thesis have been drawn from the following publications:

Are negative index materials achievable with surface plasmon waveguides? A case study of three plasmonic geometries. J. A. Dionne, E. Verhagen, A. Polman, and H. A. Atwater, *Optics Express*, **16**, 19001 (2008).

PlasMOSTor: a metal-oxide-Si field effect plasmonic modulator. J. A. Dionne*, K. Diest*, L. Sweatlock, and H. A. Atwater. Submitted, 2008.

Near field visualization of strongly confined surface plasmon polaritons in metal-insulator-metal waveguides. E. Verhagen, J. A. Dionne, L. Kobas Kuipers, H. A. Atwater, and A. Polman, *Nano Letters*, **8**, 2925 (2008).

Negative Refraction at Visible Wavelengths. H. J. Lezec*, J. A. Dionne*, and H. A. Atwater, *Science*, **316**, 430 (2007)

Highly confined photon transport in subwavelength metallic slot waveguides. J. A. Dionne, H. J. Lezec, and H. A. Atwater, *Nano Letters*, **6**, 1928 (2006)

Silver diffusion bonding and layer transfer of lithium niobate to silicon. K. Diest, M. Archer, J. A. Dionne, M. Czubakowski, and H. A. Atwater, *Applied Physics Letters*, **93**, 092906 (2008).

Plasmon slot waveguides: Towards chip-scale propagation with subwavelength-scale localization. J. A. Dionne, L. Sweatlock, A. Polman, and H. A. Atwater, *Phys. Rev. B*, **73**, 035407 (2006)

Planar metal plasmon waveguides: frequency-dependent dispersion, propagation, localization, and loss beyond the free electron model. J. A. Dionne, L. Sweatlock, A. Polman, and H. A. Atwater, *Phys. Rev. B*, **72**, 075405 (2005)

The new 'PN junction': Plasmonics enables photonic access to the nanoworld. H. A. Atwater, S. Maier, A. Polman, J. A. Dionne, and L. Sweatlock, *MRS Bulletin*, 30 (2005)

Subwavelength-scale plasmon waveguides. H. A. Atwater, J. A. Dionne, and L. Sweatlock, In M. L. Brongersma and P. G. Kik (ed.), *Surface Plasmon Photonics*, pp. 87-104. Springer Series in Optical Sciences (2007)

1 Introduction

‘No new fundamental particles, no new cosmology - but surprises, adventure, the quest to understand - yes, [plasmonics] has all of those, and more.’

-Bill Barnes

1.1 Light-matter interactions on subwavelength scales

The interaction of light with matter is among the most important physical processes on the planet - governing phenomena from atomic transitions to photosynthesis. Precise control of this interaction has enabled technologies ranging from transoceanic telecommunication to single-molecule detection. On subwavelength scales, however, light-matter interactions are limited by diffraction. The weak and diffuse transmission of light through isolated subwavelength apertures provides unequivocal evidence of this phenomenon. As calculated by Bethe [19] and Roberts [124], wave transmission through a small hole in a perfectly conducting screen scales inversely with the fourth power of the wavelength, λ . If the hole diameter is reduced to about half the wavelength, transmission through the hole becomes evanescent.

The diffraction limit severely hampers our ability to control and probe subwavelength scale optical phenomena. Diffraction assigns a lower bound on the dimensions with which light can be confined. Assuming light propagates through a media with refractive index n , the diffraction limit is given by $d = \lambda/2n$. For example, light cannot be guided by an optical fiber with dimensions less than d ; rather, incident radiation will diffract and decay evanescently. Additionally, the diffraction limit restricts the resolution of conventional light microscopes. In fact, Ernst Abbe, a German physicist and employee of Carl Zeiss, formulated the diffraction limit in 1873 when attempting to improve the resolution of light microscopes. Abbe determined that light microscopes could not resolve two features spaced closer than $\lambda/2n$, regardless of technical precision used in lens manufacturing.

For centuries, this diffraction limit has restricted many optics applications to wavelength-scale dimensions. Highly integrated, on-chip optical interconnects, for example, have suffered from a large size-mismatch with their counterpart electronic components. In addition, subwavelength-scale imaging has been limited to electron microscopy, near-field microscopy, or fluorescence microscopy - techniques that rely on precise environmental conditions and sample or wavelength scans to fully reconstruct an image. Moreover, optical components for routing, switching, and focusing light on subwavelength dimensions have remained out-of-reach with conventional dielectric materials.

While dielectric components are diffraction-limited, it is only natural that optical systems would utilize dielectric media for signal transfer. After all, dielectrics are generally transparent, facilitating low loss propagation of light.

Metals, in contrast, are poor transmitters of optical signals due to their high reflectivity and generally high absorption. Ironically, the same year transatlantic optical-fiber telephone cables became operational, metals would become front-runner materials for subwavelength-scale photonics.

1.1.1 The *hole* story

In 1988, a physical chemist at NEC Research Laboratories in Japan sought to perform Raman spectroscopy on single molecules.¹ The researcher, Thomas Ebbesen, asked a colleague to fabricate an array of holes in an opaque metal film; the holes would serve as capsules for each molecule, while the metal would ensure that each molecule was isolated from the next. Ebbesen requested that his molecular ‘muffin tin’ contain several thousand holes, each with a diameter of approximately 150 nm, spaced by about 1 μm from its nearest neighbor. When the hole array fabrication was complete, the sample incited more research than the molecules: by eye, the perforated metallic film appeared transparent. Moreover, the transmission spectra revealed several peaks, some showing a sevenfold enhancement in signal compared with Bethe’s theory. Despite the subwavelength nature of the holes, more light was being transmitted through the holes than was directly incident on them [45]!

These intriguing observations were followed by equally surprising results on single subwavelength apertures. In a set of experiments led by Henri Lezec, concentric ring-shaped grooves were patterned around a single hole in an optically-opaque metal film [82]. While the film was several hundred nanometers thick, the circular grooves were patterned to a depth of only several tens of nanometers. This ‘bullseye’ structure channeled normally-incident light on the film towards

¹Adapted from my recollection of Ebbesen’s 2004 EMRS Plenary talk in Strasbourg, and T. Thio’s article ‘A Bright Future for Subwavelength Light Sources’, *American Scientist*, January 2006

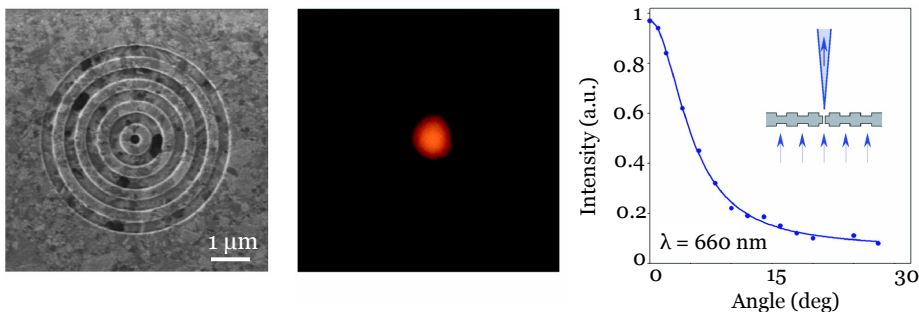


Figure 1.1. Beaming light from a subwavelength aperture, adapted from H. J. Lezec *et al.*, Reference [82]. A subwavelength aperture with a diameter of 250 nm is flanked by shallow concentric grooves in an optically-opaque Ag film. The bullseye structure both enhances light transmission through the hole and shapes the output beam with a very narrow angular divergence, as seen in the intensity plots.

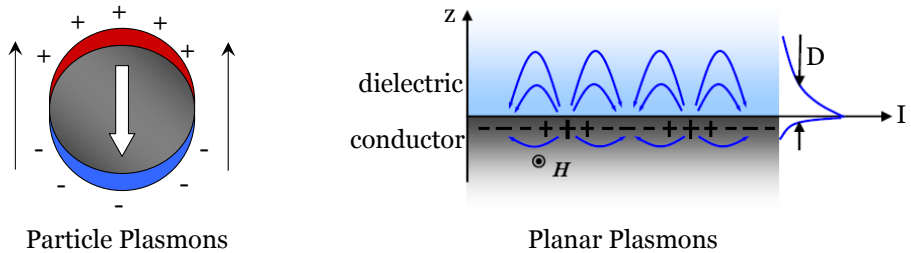


Figure 1.2. Examples of basic particle (left) and planar (right) surface plasmon geometries. For particle geometries, an incident electromagnetic field induces charge localization at the particle poles. A dipole-like excitation is then sustained at the plasma frequency. For planar plasmonic geometries, an incident field excites a charge compression wave that propagates along the metal/dielectric interface. In both geometries, surface plasmons are characterized by small wavelengths and high field intensities I compared with free-space values.

the hole, so that more light was transmitted through the hole. In addition, by patterning the exit side of the hole with a similar bullseye, the output emission could be sculpted with a very narrow divergence of $\pm 3^\circ$ (see Figure 1.1). This ‘beaming’ light from a subwavelength aperture appeared to overcome two key challenges facing subwavelength photonics: namely, diffraction and weak transmission.

Thus began a slurry of papers, communications, presentations, and debates on the extraordinary light transmission through subwavelength holes (see, for instance [53] and references therein). The results of both experiments were attributed to surface waves propagating along the metal and interfering at the aperture. Among these diffracted surface waves, surface plasmons received particular attention. Though the basic properties of surface plasmons had been well understood for decades, these two studies prompted a renaissance of plasmonics for nanophotonics.

1.1.2 What are surface plasmons?

In the broadest of terms, surface plasmons (SPs) are hybrid electron-photon oscillations that occur at the interface between a conductor and a dielectric [121]. As longitudinal electron density oscillations, plasmons resemble light waves confined to the surface of a metal. However, SPs are non-radiative in nature, implying that they cannot directly couple to photons. Instead, a prism, grating, or scattering center must be used to resolve the momentum-mismatch between plasmons and photons. Surface plasmon electric fields are evanescent in the dielectric, but can be extremely high at the metal-dielectric interface. Moreover, SP wavelengths can be extremely short compared to free-space photon wavelengths: as we will see in later chapters, even x-ray wavelengths can be attained at optical frequencies.

While SPs can occur at any metal-dielectric interface, particle and planar plasmon geometries have received particular attention. Figure 1.2 depicts two

examples of these geometries with just one metal-dielectric interface. As seen, particle plasmons resemble dipoles, with clouds of charge localized at the poles. At their resonant frequency, these *localized* surface plasmons will be categorized by a large scattering coefficient and a large extinction cross-section. Accordingly, particle-based geometries can act as optical nano-antennas, concentrating incident radiation to a subwavelength physical region. Such properties have been exploited in applications ranging from surface-enhanced Raman spectroscopy [54, 51, 179] to photothermal tumor ablation [104, 59]. In contrast, planar plasmonic geometries are characterized by *propagating* charge-compression waves localized to the metal-dielectric interface. Depending on the excitation wavelength and the specific materials used, the field penetration into the dielectric can be subwavelength. Additionally, plasmon propagation lengths in planar geometries can approach centimeter scales.

Though surface plasmons have only recently been considered for optoelectronic applications, the properties of metallic nanostructures have been exploited for centuries. For example, dating as far back as the 4th century AD, Roman artisans exploited small metal particles to create dichroic glass sculptures. By annealing metallic salts in transparent glass, the artisans could create suspensions of sub-100-nm-diameter nanoparticles. The Lycergus cup is the only surviving artwork from this era, shown in Figure 1.3. Due to the optical dichroism of the nanoparticles, this vase appears jade green in reflected light but a brilliant red in transmission.

Quantitative studies of metallic nanostructures began in the early twentieth century. In 1902, Robert Wood observed an unusual dip in transmission around the lattice constant of metallic gratings [173]; his observation, known as the ‘Wood’s anomaly,’ is still invoked in contemporary theories of extraordinary transmission through subwavelength apertures. Shortly thereafter, Maxwell Garnett described an electromagnetic framework for the colors observed in metal-doped glasses such as the Lycergus Cup [94]. Building on this



Figure 1.3. The Lycergus Cup, a Roman vase dating from the 4th century A.D. Due to small metallic nanoparticles in the glass, the vase appears jade green when viewed in reflection and red when viewed in transmission. Photo from Reference [9]

work, Gustav Mie developed a fully quantitative model for light scattering from small, spherical particles in 1908 [96]. His description included an analysis of gold colloidal particles ranging from wavelength to subwavelength-scale dimensions. In 1956, David Pines described the losses of fast electrons penetrating a metal film in terms of volume plasmons [119]. Rufus Ritchie extended this work to thin metallic films in 1957, demonstrating that metal surfaces can also support collective electronic modes, and providing the first theoretical description of surface plasmons [123].

Optical excitation of surface plasmons was pioneered by Andreas Otto, Erich Kretschmann, and Heinz Ritchie in 1968 [105]. In their work, Otto, *et al.* illustrated that the photon-plasmon momentum-mismatch could be overcome by prism-coupling, making plasmonics accessible to a number of researchers. Six years later, Martin Fleischman observed an enhanced Raman signal from molecules adsorbed onto roughened metallic surfaces [50]. David Jeanmarie and Richard van Duyne described the enhancement in terms of electrodynamic metal-molecule interactions [68], pioneering the field of surface-enhanced Raman spectroscopy.

Plasmonics has now expanded to applications ranging from nanoscale optical waveguides and devices to electromagnetic metamaterials that may enable ‘perfect lenses’ and invisibility. The explosive growth of the field is reflected in the scientific literature: since 1990, the number of papers related to surface plasmons has doubled every five years [25]. While the rate of progress and the number of contributors may seem daunting to new researchers in the field, Edwin Abbott’s *Flatland* provides perspective: “Be patient, for the world is broad and wide.” And so too are planar plasmonic waveguides, the topic of this thesis.

1.2 Scope of this thesis

This thesis describes both the theory and applications of planar surface plasmon waveguides. As seen in Figure 1.2, such geometries are composed of one or more metallo-dielectric interfaces that support propagating electromagnetic modes. By judicious design of the waveguide dimensions and materials, these structures can serve as subwavelength-scale optical waveguides, color filters, negative refractive index materials, or even metal-oxide-Si field effect optical modulators. Here, we present the theoretical framework and the experimental realization of all such applications.

Chapter 2 presents a numerical analysis of surface plasmon dispersion, propagation, and localization in two- and three-layer planar plasmonic waveguides. In the first half, attention is given to determining the wavelength-dependent behavior of thin metallic slab waveguides embedded in a symmetric dielectric environment. Rather than considering the metal as a damped free electron gas or Drude material, the metal is described by experimentally-determined optical constants. This chapter thus represents a first description of plasmonic waveguides based on realistic, wavelength-dependent materials parameters. Analytic dispersion calculations indicate a splitting of plasmon modes - corresponding to symmetric and antisymmetric magnetic field distributions - as film thickness is

decreased below 50 nm. However, unlike the results of prior theories based on Drude models, we find that the surface plasmon wavevector remains finite at resonance with one plasmon mode converging to a pure photon mode for very thin films. In addition, allowed modal solutions are found to exist between the bound and radiative branches of the dispersion curve. The propagation characteristics of all modes are determined, and for thin films, propagation distances range from microns to centimeters. While the energy density of most long-range surface plasmons exhibits a broad spatial extent with limited confinement in the waveguide, it is found that high field confinement does not necessarily limit propagation. In fact, enhanced propagation is observed for metal films at ultraviolet wavelengths despite strong field localization in the metal.

The second half of Chapter 2 describes a numerical analysis of plasmon slot, or metal-insulator-metal (MIM) waveguides. Composed of a dielectric core and conducting cladding, these waveguides are found to exhibit both long-range propagation and high spatial confinement of light, with lateral dimensions of less than 10 percent of the free-space wavelength. Attention is given to characterizing the dispersion relations, wavelength dependent propagation, and energy density decay in two-dimensional MIM structures with waveguide thicknesses ranging from 12 nm to 250 nm. As in conventional planar insulator/metal/insulator (IMI) surface plasmon waveguides, analytic dispersion results indicate a splitting of plasmon modes - corresponding to symmetric and antisymmetric magnetic field distributions - as core thicknesses are decreased below 100 nm. However, unlike IMI structures, surface plasmon momentum does not always exceed photon momentum, and mode indices can be negative for thinner dielectrics. From visible to near infrared wavelengths, plasmon propagation exceeds tens of microns with fields confined to within 20 nm of the structure. As the core thickness is increased, propagation distances also increase with localization remaining constant. Conventional waveguiding modes of the structure are not observed until the core thickness approaches 100 nm. At such thicknesses, both transverse magnetic and transverse electric modes can be observed. Interestingly, considerable field enhancement in the waveguide core can be observed, rivaling the intensities reported in resonantly-excited metallic nanoparticle waveguides. The surface plasmon characteristics described in this chapter provide a numerical springboard for engineering the plasmonic geometries described in the rest of the thesis.

In Chapter 3, we present experimental methods for coupling photons to plasmons along planar metallic core geometries. The first section probes the evolution of surface electromagnetic waves generated from free-space optical modes via grating coupling. Gratings of varying periodicity and order (i.e., number of grooves) are used to incouple and outcouple surface waves on a thick metal film. Input-output separation is varied from 5 through 60 μm , and far-field spectroscopy is used to monitor wave evolution. Results indicate surface plasmons are always present among surface waves generated by the incoupling structures; however, other diffracted orders may be present within several microns of the input grating. The second section of Chapter 3 probes the local electromagnetic field in plasmonic geometries. A novel photolithographic technique is used to investigate both linear plasmon waveguides and elliptical corrals with deep

subwavelength resolution. By using a unique photoactive polymer, the surface plasmon field is recorded as a topological deformation that can be probed with atomic force microscopy. The technique reveals plasmonic localization on scales as small as 50 nm (a tenth of the free-space wavelength used for excitation), and simulations of the local field confirm our results.

In Chapter 4, we report the first experimental realization of subwavelength-scale MIM waveguides, using both near- and far-field microscopy. Attention is given to both planar and rectangular waveguides with a Si_3N_4 core and Ag cladding; core thicknesses of 50 - 100 nm and widths of 250 nm - 10 μm are explored. Propagation lengths of approximately five times the excitation wavelength are achieved with light confined to lateral and transverse dimensions of $\lambda/5$ and $\lambda/2$, respectively. While far-field interferometry can be used to determine the plasmon wavevector, near-field microscopy can be used to probe SP propagation with subwavelength resolution. Using near- and far-field interferometry, we directly determine the SP MIM wave vector, showing that the wavelength is shortened to values as small as 156 nm for a free-space wavelength of 532 nm.

Chapter 5 is devoted to exploring the theory and applications of plasmonic geometries as negative index materials. In the first section, we present a theoretical analysis of planar plasmonic waveguides that support propagation of negative index modes. Particular attention is given to the modes of metal-insulator-metal (MIM), insulator-metal-insulator (IMI), and insulator-insulator-metal (IIM) geometries at visible and near-infrared frequencies. We find that all three plasmon geometries are characterized by negative indices over a finite range of visible frequencies, with figures of merit approaching 20. Moreover, using finite-difference time-domain simulations, we demonstrate that a visible-wavelength beam propagating from free space into these geometries can exhibit negative refraction. Refractive index and figure-of-merit calculations are presented for Ag/GaP- and Ag/ Si_3N_4 - based structures with waveguide core dimensions ranging from 5 to 50 nm and excitation wavelengths ranging from 350 nm to 850 nm. These results provide the design criteria for realization of broadband, visible-frequency negative index materials and transformation-based optical elements.

In the second half of Chapter 5, we report the first experimental realization of a two-dimensional negative-index material in the blue-green region of the visible, substantiated by direct geometric visualization of negative refraction. Negative indices are achieved using an ultrathin Au/ Si_3N_4 /Ag waveguide sustaining a surface-plasmon-polariton mode with antiparallel group and phase velocities. By shaping this bimetal waveguide into a prism, negative refraction is observed at the interface between this negative index material and a conventional Ag/ Si_3N_4 /Ag slot waveguide. The results may enable the development of practical negative-index optical designs in the visible regime, including sub-diffraction-limited superlenses and electromagnetic cloaks.

Chapter 6 is devoted to development of active plasmonic devices. In the first section, we demonstrate a subwavelength-scale optical Si modulator, based on field-effect modulation of plasmon modes in a MOS geometry. Near-infrared transmission between an optical source and drain is controlled by a gate voltage that drives the MOS into accumulation. Using the gate oxide as an optical

channel, amplitude modulation depths as large as 11.2 dB are observed. Electro-optic modulation is achieved in device volumes as small as one-fifth of a cubic wavelength with femtoJoule switching energies and nanosecond switching speeds. This “plasMOStor” may thus form the basis for a deeply subwavelength optoelectronic transistor technology. The second half of this chapter introduces a concept for a full-color, ‘flat-panel’ display based on MIM waveguide-resonators. By appropriate design of the resonator dimensions and end-facets, broadband light is filtered into individual colors that span the visible spectrum; the filtered colors can be switched by replacing the MIM core with an active transparent dielectric.

Chapter 7 provides an outlook for future work on surface-plasmon-based geometries. Particular attention is given to discussion of time-resolved probes for negative index metamaterials, plasmonic manipulation of the local density of states, plasmon mirages, two and three-dimensional ‘perfect lenses’, and plasmonic-based cloaking technologies. Note that throughout this thesis, emphasis is given to plasmonic concepts and results, rather than techniques and derivations. Information on specific theoretical derivations, numerical techniques, and experimental methods may be found in the appendices.

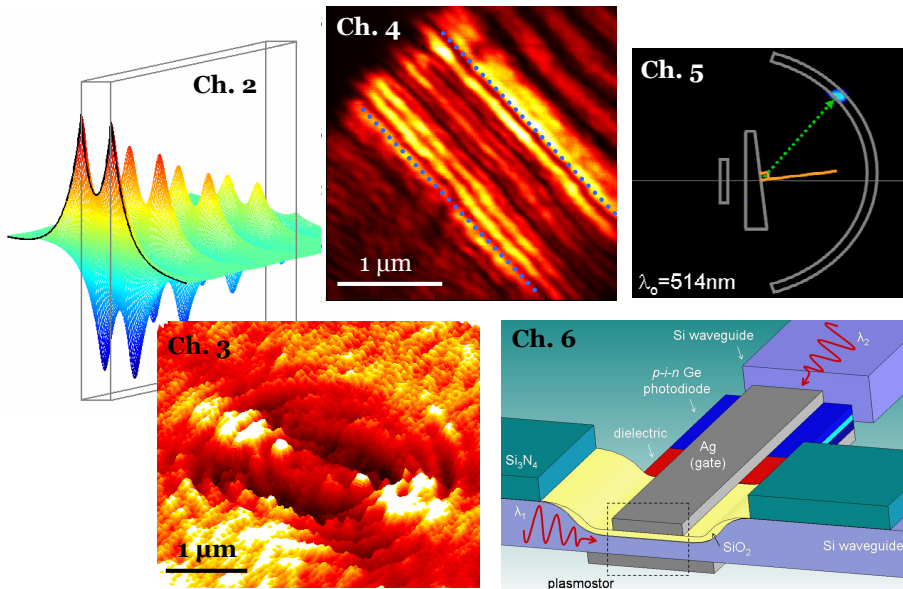


Figure 1.4. Pictorial overview of this thesis. Chapter 2 presents the theory for planar surface plasmon waveguides. Chapters 3 and 4 present experimental techniques for coupling to insulator-metal-insulator and metal-insulator-metal waveguides. Chapter 5 discusses plasmon geometries for negative index materials and presents the first experimental demonstration of visible-frequency negative refraction. Chapter 6 presents active device applications based on planar plasmon waveguides, including an optical MOSFET and a full-color, ‘flat-panel’ display.

2 Electromagnetic Modes of Multilayer Waveguides

‘In a few years, all great physical constants will have been approximately estimated, and the only occupation which will be left to men of science will be to carry these measurements to another place of decimals.’

-James C. Maxwell

2.1 Maxwell in multilayers: old equations, new applications

Photonics has experienced marked development with the emergence of nanoscale fabrication and characterization techniques. This progress has brought with it a renewed interest in surface plasmons (SPs) - electron oscillations that allow electromagnetic energy to be localized, confined, and guided on subwavelength scales. Waveguiding over distances of $0.5 \mu\text{m}$ has been demonstrated in linear chains of metal nanoparticles [90], and numerous theoretical and experimental studies [129, 27, 37, 101] indicate the possibility of multicentimeter plasmon propagation in thin metallic films. Moreover, as we saw in Chapter 1, the locally-enhanced field intensities observed in plasmonic structures promise potential for molecular biosensing [131, 61, 95, 57, 58], surface enhanced Raman spectroscopy [54, 51, 179], nonlinear optical devices [148, 22, 160, 137, 11], and transformation-based optical elements [114, 133].

The recent research and progress in plasmonics is by no means a reflection of the field’s youth. Indeed, collective electronic motion in planar metal films has received considerable attention since Ritchie [123] first described the plasma losses of electrons incident on a metal. In 1967, Kliever and Fuchs [72] determined the dispersion characteristics of thin-film surface plasmons (SPs), considering the conduction electrons as a free electron gas (FEG). Subsequently, Economou [46] extended the theory to multi-layer metallodielectric systems, using a FEG dielectric function but including retardation effects. In 1986, Burke and Stegeman [27] reported on damped surface plasma oscillations in a metal film, solving the thin-film dispersion relations at a given frequency (free space wavelength $\lambda=633\text{nm}$) and determining wavelength-dependent attenuation by modifying the FEG dielectric function with a Drude damping term. For thin films excited at $\lambda = 1 \mu\text{m}$, multicentimeter propagation was found, providing the first hint that surface plasmons might have profound applications for subwavelength-scale optical interconnects.

In planar metallodielectric geometries - the subject of this thesis - plasmon oscillations emerge from a straightforward application of the Helmholtz equation subject to appropriate boundary conditions. Had researchers accepted Maxwell’s assessment of science quoted above, theoretical plasmonics might have plateaued

in the 1980s. And yet, nearly twenty years after the work of Burke and Stegeman, original and significant contributions to the theory of planar surface plasmon oscillations are still possible. The reason lies not in new equations, but in new applications. Planar plasmonic geometries support a variety of electromagnetic modes, each with a unique propagation constant, field distribution, and energy density. Twenty years ago, modes with negative wavevectors, near-zero group velocities, or propagation lengths less than 100 nm would not have seemed relevant; today, they form the basis for a suite of novel nanoscale phenomena and devices.

In this chapter, we discuss the complete set of modes supported by planar, multilayer plasmonic geometries. Particular attention is given to determining the frequency-dependent behavior of surface plasmons arising from the experimentally-determined optical constants of plasmonic materials. Indeed, to date, many analytical models lack a quantitative consideration of surface plasmon (SP) properties that arise when the metal is described by experimentally-determined optical constants rather than a damped free electron gas. And, if models do employ empirical optical constants [27, 17, 15, 16, 14], attenuation characteristics are determined for a given frequency rather than throughout a broad spectral range. Moreover, few works have explicitly determined the spatial decay of the plasmon electric field and the energy density in the metal and dielectric as a function of film thickness. From both a fundamental and an applied perspective, quantitative knowledge of such wavelength-dependent SP characteristics seems essential.

Our analysis begins with a review of the optical characterization of metals. This materials framework provides the basis for all optical and electromagnetic modeling of metalodielectric multilayer structures. Section 2.3 discusses plasmon properties in metallic core geometries, including single interface surface plasmons and insulator-metal-insulator (IMI) waveguides. Section 2.4 discusses the bound modes of metal-insulator-metal (MIM) structures. For all multilayer waveguides, particular attention is given to mapping the dispersion relations, determining the wavelength-dependent propagation and electric field skin depth, and characterizing the energy density of bound modes in the relevant passive media. To solve the complex dispersion relations, we exploit numerical techniques grounded in physically relevant phenomena. A discussion of such techniques is included both in this chapter and in Appendix B.

2.2 Optical characterization of metallic films

General electron transport in metals is most often described by the free electron gas model developed by Drude. In this theory, the metallic permittivity takes the form:

$$\varepsilon(\omega) = 1 - \frac{\omega_p^2}{\omega(\omega + i\gamma)}, \quad (2.1)$$

where ω_p defines the bulk plasma frequency of the material and γ denotes the relaxation rate. Separating $\varepsilon(\omega)$ into real and imaginary components, and as-

suming $\omega \gg \gamma$, this expression simplifies to:

$$\varepsilon(\omega) = 1 - \left(\frac{\omega_p}{\omega}\right)^2, \quad (2.2)$$

While this form of the dielectric function is commonly quoted as an adequate optical characterization of metallic films (see, for instance, references [72, 46, 149, 113], which use this form to determine surface plasmon dispersion), its validity is limited only to near-infrared frequencies, where bound electron contributions are negligible. An improved description of materials properties can be achieved by modifying the Drude permittivity with Lorentz oscillator terms:

$$\varepsilon(\omega) = 1 - \frac{f_0\omega_{p,0}^2}{\omega(\omega + i\gamma_0)} + \sum_{j=1}^{j_{\max}} \frac{f_j\omega_{p,j}^2}{\omega_j^2 - \omega^2 - i\gamma_j\omega}. \quad (2.3)$$

Physically, this Drude-Lorentz model treats the free electrons in the metal as damped harmonic oscillators subject to electromagnetic driving fields. Accordingly, each oscillator is characterized by four free parameters, including the oscillator strength f_j , plasma frequency $\omega_{p,j}$, damping rate γ_j , and oscillator frequency ω_j . Provided all terms are properly fitted, this model can provide sound agreement to measured optical constants throughout visible and infrared frequencies. However, independent of any fit parameters, the most accurate description of metallic behavior throughout the electromagnetic spectrum requires use of empirically-determined optical constants.

Bulk metals are most often described by the refractive index ($n+i\cdot k$) data sets of Johnson and Christy [69] and from the Palik Handbook of Optical Constants[109]. Considering Ag - one of the most common plasmonic metals - as an example, the optical constants of Johnson and Christy were determined through measurements of reflection and transmission at normal incidence and transmission of p-polarized light at 60° . In contrast, the optical constants compiled by Palik (including the works of Leveque [81] from 200 to 360 nm, Winsemius [171] from 360 nm to 2000 nm and Dold and Mecke [40] from 1265 to 2000 nm) were obtained via reflectance measurements using synchrotron radiation [81] and polarimetric measurements [171, 40]. Note that the refractive index data can be readily converted to a complex permittivity via the relations:

$$\varepsilon' = n^2 - k^2, \quad (2.4a)$$

$$\varepsilon'' = 2nk. \quad (2.4b)$$

Figure 2.1 shows the dielectric function $\varepsilon_1(\omega) = \varepsilon'_1(\omega) + i\cdot\varepsilon''_1(\omega)$ of Ag as derived from the data of both Johnson and Christy (JC) and Palik. For reference, Figure 2.1 also includes the FEG dielectric function of equation (2.2), as well as the permittivity of SiO_2 (ε_2 , plotted as $-\varepsilon_2$). As seen, the metal exhibits a large, negative real component of the permittivity for most visible and infrared wavelengths. At shorter wavelengths, $\text{Real}(\varepsilon_1(\omega))$ passes through zero, corresponding to the bulk plasma frequency. Thereafter, the metal exhibits a regime of anomalous dispersion, where $\text{Real}(\varepsilon_1(\omega))$ decreases with increasing ω .

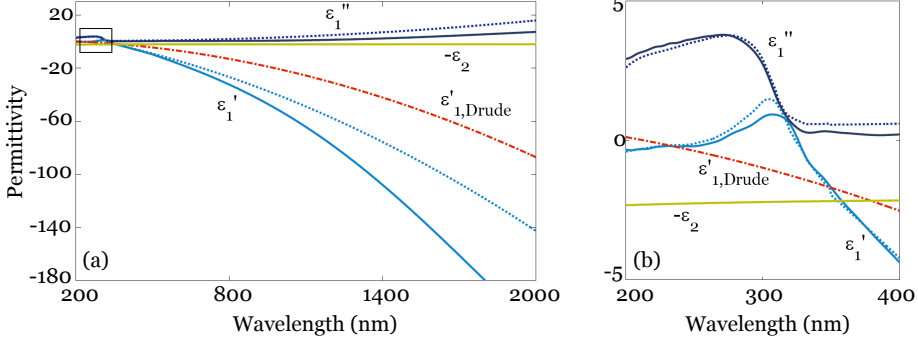


Figure 2.1. The real and imaginary components of Ag permittivity ($\epsilon_1 = \epsilon_1' + i \cdot \epsilon_1''$) using a lossless Drude model (red dash-dot), data from Johnson and Christy (blue solid), and the Palik Handbook (blue dotted). For reference, the polynomial fit through Palik's SiO₂ data is also included (yellow, plotted as $-\epsilon_2$). Panel (b) shows an enlarged view of the region of anomalous dispersion for all materials data sets.

Despite the transparency of metals within this regime, the imaginary component of the permittivity can be substantially higher than the real component for such frequencies.

To describe the Ag permittivity continuously between 200 nm and 2000 nm, the empirical data of JC and Palik was fit using a cubic spline within the region of anomalous dispersion and polynomial fits elsewhere. All fits were designed to be continuous, smooth, and Kramers-Kroenig consistent throughout the wavelength range $200 \text{ nm} \leq \lambda \leq 2000 \text{ nm}$ and agree with the experimental data within 5%. For wavelengths less than 400 nm, the agreement is within 0.01% - an agreement not readily achieved with conventional Drude or Drude-Lorentz fitting models. Note that the JC and Palik data sets exhibit fair agreement for wavelengths between 200 nm and 600 nm. However, significant differences are observed between 600 nm and 2000 nm, with ϵ_1' of Johnson and Christy falling off faster with wavelength and ϵ_1'' growing more slowly than the corresponding data of Palik. Given the general use of both data sets to describe bulk silver, surface plasmon properties in this chapter were separately calculated considering each data set, where illustrative.

2.3 Bound modes of planar metal plasmon waveguides

2.3.1 Single interface surface plasmons

As introduced in Chapter 1, surface plasmons are the quanta of collective plasma oscillations localized at the interface between a metal and a dielectric. Provided the thickness of the metal film exceeds the plasmon skin depth, oscillations at each metal-dielectric interface are decoupled, and independent surface plasmon modes at each metal-dielectric interface are sustained. A cross section of the geometry is shown as an inset in Figure 2.2; the metal is contained in the half-

space $z \geq 0$ with the metallodielectric interface located at $z=0$. Wave propagation is along the x -direction.

Assuming a perpendicularly polarized electric field incident on the structure, the surface plasmon electric field takes the form

$$E(x, z, t) \sim E_0 e^{i(k_x x - k_z |z| - \omega t)},$$

with components given by

$$E_x^{\text{metal}} = E_0 e^{i(k_x x - k_{z1} |z| - \omega t)}, \quad (2.5a)$$

$$E_x^{\text{dielectric}} = E_0 e^{i(k_x x - k_{z2} |z| - \omega t)}, \quad (2.5b)$$

$$E_y^{\text{metal}} = E_y^{\text{dielectric}} = 0, \quad (2.5c)$$

$$E_z^{\text{metal}} = E_0 \left(\frac{-k_x}{k_{z1}} \right) e^{i(k_x x - k_{z1} |z| - \omega t)}, \quad (2.5d)$$

$$E_z^{\text{dielectric}} = E_0 \left(\frac{-\varepsilon_1 k_x}{\varepsilon_2 k_{z1}} \right) e^{i(k_x x - k_{z2} |z| - \omega t)}. \quad (2.5e)$$

Demanding continuity of the tangential \mathbf{E} and normal \mathbf{D} fields at the interface yields the surface plasmon dispersion relations defined by [121]

$$k_x = \frac{\omega}{c} \sqrt{\frac{\varepsilon_1 \varepsilon_2}{\varepsilon_1 + \varepsilon_2}} \quad \text{and} \quad k_{z1,2}^2 = \varepsilon_{1,2} \left(\frac{\omega}{c} \right)^2 - k_x^2. \quad (2.6)$$

Provided $\varepsilon_1'' < |\varepsilon_1'|$ — a condition satisfied in Ag for $\lambda \geq 328$ nm using the optical constants of Johnson and Christy and $\lambda \geq 331$ using Palik — the in-plane wave vector can be written as $k_x = k_x' + i \cdot k_x''$, with

$$k_x' = \left(\frac{\omega}{c} \right) \sqrt{\frac{\varepsilon_1' \varepsilon_2}{\varepsilon_1' + \varepsilon_2}} \quad \text{and} \quad k_x'' = \left(\frac{\omega}{c} \right) \left(\frac{\varepsilon_1' \varepsilon_2}{\varepsilon_1' + \varepsilon_2} \right)^{3/2} \left(\frac{\varepsilon_1''}{2\varepsilon_1'} \right). \quad (2.7)$$

Figure 2.2 illustrates the dispersion characteristics for this mode, considering a thick Ag film coated with SiO₂. Figure 2.2a plots SP dispersion assuming the Ag is described as a lossless free electron gas (FEG) with $\omega_p = 8.85 \times 10^{15} \text{ s}^{-1}$. For energies below 3.3 eV, the bound surface plasmon-polariton (SPP) mode is observed, asymptoting at short wave vectors to the light line and at large wave vectors to the surface plasmon resonant frequency ω_{SP} (defined by the wavelength where $\varepsilon_1' = -\varepsilon_2$). Above 5.8 eV, the onset of the radiative plasmon-polariton (RPP) mode can be seen. For energies between the SPP and RPP modes, the plasmon wave vector is purely imaginary (represented as a dotted line in the figure), indicating that modes in this regime are forbidden. Historically, this region between ω_{SP} and ω_p is referred to as the plasmon bandgap.

In contrast to free-electron-like behavior, dispersion arising from use of Johnson and Christy optical constants is plotted in Figure 2.2b. Though not shown, dispersion is nearly identical using the optical constants of Palik. For reference, the dispersion curve for the SiO₂ light line ($k_x = \sqrt{\varepsilon_2} \cdot \omega/c$) is also included.

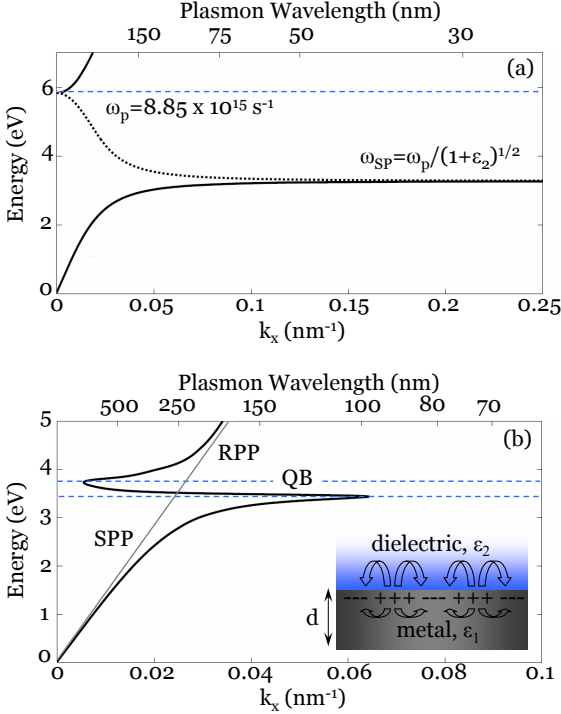


Figure 2.2. **(a)** Surface plasmon dispersion relation for a Ag/SiO₂ geometry computed using a lossless Drude model for Ag. Note the existence of allowed modes (solid) for frequencies below ω_{SP} and above ω_p , in contrast to the forbidden (i.e., purely imaginary) modes between these frequencies (dotted). **(b)** Bound (SPP), radiative (RPP) and quasi-bound (QB) surface plasmon dispersion relation for a Ag/SiO₂ geometry computed using the optical constants of Johnson and Christy. Unlike the free electron dispersion of panel **(a)**, modes are allowed throughout the entire frequency range. The SiO₂ light line (gray) is also included for reference.

Below 3.5 eV the SPP mode is observed, approaching the light line at short wave vectors but terminating at a *finite* wave vector on resonance ($k_x = 0.065 \text{ nm}^{-1}$ at ω_{SP}). As seen, the fairly large SPP wave vectors (and hence small SPP wavelengths) achieved near resonance compete with the largely reduced group velocity in this frequency range. Above 3.8 eV the RPP is observed, corresponding to wavelengths satisfying the relation $\epsilon_1'' > |\epsilon_1'|$ (i.e., $\lambda < 328 \text{ nm}$). For energies between the SPP and RPP modes, k_x is determined by Equation 2.6 and what we term ‘quasibound’ (QB) modes appear to exist. Unlike the imaginary modes of the FEG dispersion, the modes plotted here have mathematically real components and hence are not *a priori* forbidden.

Strikingly, quasibound modes appear to exhibit negative group velocities $v_g = d\omega/dk$ between the bulk and surface plasmon resonances and infinite group velocities directly on resonance. However, for absorbing media (such as metals

around resonances), this linearization of v_g does not apply, and the propagation velocity of the wavepacket must be modified to account for amplitude damping and wave profile deformation [154]. The most general definition for the wavepacket velocity is then given by the energy velocity, $v_E = \bar{S}/\bar{W}$, where \bar{S} is the average power flow in the waveguide and \bar{W} is the time-averaged energy density [126]. As shown in Figure 2.3, the phase velocity and energy velocity of modes in this QB regime are both positive and finite. Nevertheless, these modes may exhibit significant physical effects on the timescale of short-lifetime plasmon processes, including plasmon decoherence by electron-hole pair generation and electron-phonon coupling.

Figure 2.4 illustrates the propagation distance for an Ag/SiO₂ interface plasmon as a function of wavelength for both the Johnson and Christy and Palik dielectric data sets. The surface plasmon intensity decreases as $\exp(2\text{Real}\{ik_x x\})$ so that the propagation length is given by $L = |2\text{Real}\{ik_x\}|^{-1}$. As seen, at the important telecommunications wavelength of 1550 nm, propagation distance approaches $\sim 400 \mu\text{m}$ using the Johnson and Christy data set and $\sim 70 \mu\text{m}$ using Palik; at shorter wavelengths, both curves converge toward nanometer-scale propagation at the surface plasmon resonance. Thus, although large surface plasmon wave vectors can be achieved near resonance, these attributes are often at the expense of propagation length.

Still, Figure 2.4 does reveal the presence of a local maximum in propagation existing close to the plasmon resonant frequency. Indicating the transition between the QB and RPP modes, the neighborhood about this maximum corresponds to the region of anomalous dispersion in the silver dielectric constant. Accordingly, the relative magnitude of this maximum can be controlled by altering the refractive index of the surrounding dielectric.

To illustrate the effects of varying the dielectric optical constant, the inset of Figure 2.4 plots propagation lengths for Ag/Air, Ag/SiO₂, and Ag/Si interface plasmons over the spectral range of 200-500 nm.¹ By using materials of varying

¹Damping in Si was accounted for in the usual way, via inclusion of the imaginary component of the dielectric function.

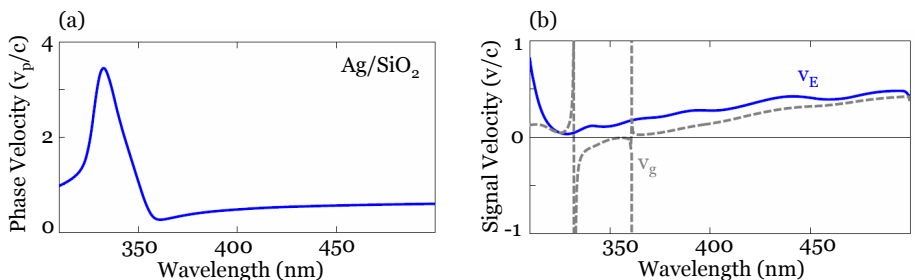


Figure 2.3. Phase, group, and energy velocities for surface plasmons propagating along a single Ag/SiO₂ interface. Note that the phase and energy velocity are exclusively positive, despite the existence of modes exhibiting negative slope ($d\omega/dk < 0$) on the dispersion diagram.

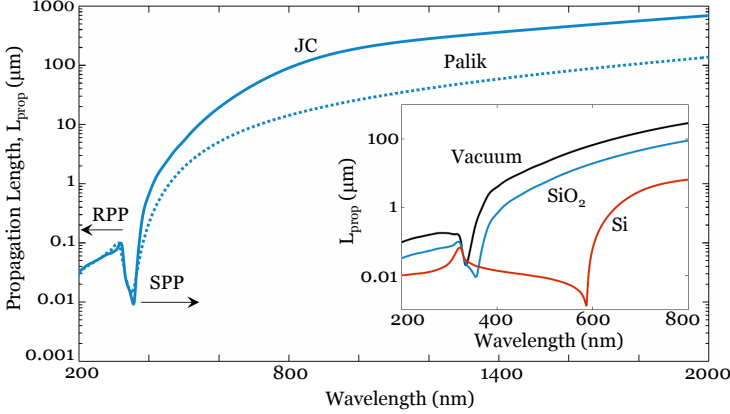


Figure 2.4. Surface plasmon propagation length for the Ag/SiO₂ geometry calculated using the optical constants of Johnson and Christy (solid) and Palik (dotted). A vanishing propagation length occurs at the surface plasmon resonance, located at $\lambda = 355$ nm (358 nm) for the Palik (JC) data sets, respectively. The local maximum at $\lambda \sim 320$ nm coincides with the transition between QB and RPP modes. Inset: Comparison of SP propagation for Ag/Air, Ag/SiO₂ and Ag/Si geometries plotted near the SP resonance frequency.

refractive indices, the surface plasmon resonant frequency can be tuned through a broad spectral range. As a result, the energetic location of the maxima and minima in the propagation distance plot can be controlled. Alternatively, at a given frequency, the surface plasmon wavelength (and hence damping) can be tuned by the dielectric constant. Such results suggest that by altering the optical properties of the embedding dielectric (i.e., with an electro-optic material), propagation might be dynamically switched under optical pumping. Note that significant shifts for single-interface surface plasmons require refractive index differentials of order $\Delta n = 0.1$: at a free-space wavelength of $\lambda = 1550$ nm, such index contrast can lead to a $6 \mu\text{m}$ change in propagation length.² However, as we will see later in this thesis (Chapter 6), even small shifts in Δn can lead to large modulation ratios in regions of flat modal dispersion.

The inset also reveals that for a given free-space wavelength, the longest propagation lengths are achieved for insulating materials with the smallest dielectric constant. However, combining data as in Figures 2.2b and 2.4 for various dielectrics (data not shown), we find that the optimal combination of small plasmon wavelength and low damping is observed for a dielectric with the largest refractive index. We will return to this observation in Chapter 5 during our discussion of negative index materials.

Figure 2.5 plots the surface plasmon electric field skin depth ($1/e$ decay length) in both Ag and SiO₂ as a function of wavelength. Note that in this

²While typical refractive index differentials in semiconductors do not exceed 1%, nonlinear index changes as high as $\Delta n = 0.14$ have been observed in multilayer quantum wells. See, for instance, Reference [26]

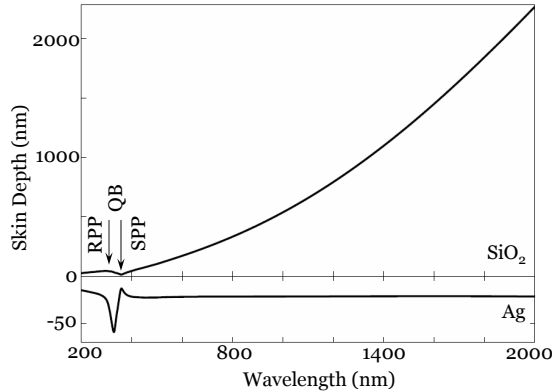


Figure 2.5. Surface plasmon electric field penetration (i.e., skin depth) into Ag and SiO₂, computed using the materials data of Johnson and Christy. The local penetration maximum at shorter wavelengths corresponds to the transition between the quasi-bound and radiative surface plasmon modes.

graph, decay into the metal is plotted below $z = 0$. For clarity, the figure only includes skin depth computed using the JC data set. As expected, the SPP skin depth into the dielectric increases with increasing wavelength, reaching values of $1.3 \mu\text{m}$ ($1.1 \mu\text{m}$) in SiO₂ at $\lambda = 1550 \text{ nm}$ for the JC (Palik) data sets, respectively. In contrast, the SPP skin depth into the metal remains roughly constant at $\sim 20 \text{ nm}$ (25 nm) for wavelengths beyond the plasmon resonance. At resonance, field penetration in the metal reaches a minimum in both the metal and dielectric (with $\sigma \sim 15 \text{ nm}$ for both Ag and SiO₂). For even shorter wavelengths, field penetration exhibits a maximum in the metal and a local maximum in SiO₂ (with $\sigma_{\text{Ag}} \sim 60 \text{ nm}$ and $\sigma_{\text{SiO}_2} \sim 40 \text{ nm}$). Not surprisingly, this maximum occurs around $\lambda = 330 \text{ nm}$ - a wavelength regime corresponding to anomalous Ag dispersion and marking the onset of the radiative plasmon polariton.

This observation raises an interesting distinction between the system resonances corresponding to the extrema in the plot of propagation length versus wavelength (i.e., the local maximum and the global minimum in Figure 2.4). At one system resonance, corresponding to anomalous dispersion, propagation is slightly enhanced despite high field confinement within the metal. However, at the surface plasmon resonance, propagation approaches single nanometer scales despite minimal energy density within the metal. The latter result is explained by the vanishing SPP excitation group velocity near the plasmon resonance. Still, the contradiction to the common localization versus loss heuristic is evident: field localization within the metal does not necessarily result in increased loss.

Figure 2.6 illustrates the tangential field (E_x) distribution and *electric* energy density decay into both the metal and the dielectric as a function of distance from the metallodielectric interface for wavelengths characteristic of the SPP and RPP modes. Only results obtained using the Johnson and Christy data sets are shown; the behavior is qualitatively similar considering dielectric function

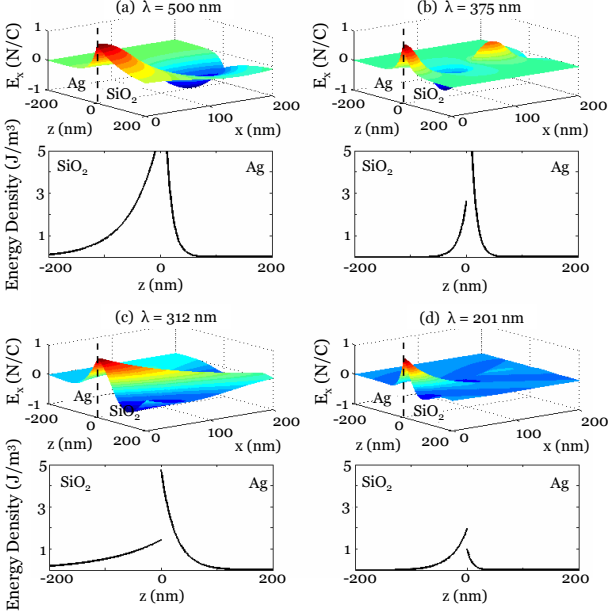


Figure 2.6. Spatial distribution of the surface plasmon tangential field and corresponding electric energy density in the metal ($z > 0$) and dielectric ($z < 0$) for wavelengths characteristic of the surface plasmon-polariton modes, **(a)**: $\lambda = 500$ nm, **(b)**: $\lambda = 375$ nm, and the radiative plasmon-polariton modes, **(c)**: $\lambda = 312$ nm, **(d)**: $\lambda = 201$ nm.

data from Palik. Outside the waveguide, the electric energy density is defined in the usual way, with:

$$u_{SiO_2} = \frac{1}{2} \vec{E} \cdot \vec{D}^* = \frac{1}{2} \epsilon_2 \vec{E} \cdot \vec{E}^* \quad (2.8)$$

while within the waveguide, the energy density is derived from Poynting's theorem in linear, lossy dispersive media [79]:

$$u_{Ag} = \frac{1}{2} \text{Re} \left[\frac{d(\omega \epsilon_1)}{d\omega} \right] \vec{E} \cdot \vec{E}^*. \quad (2.9)$$

Figure 2.6a and b shows the SPP mode and energy density at 2.48 eV ($\lambda = 500$ nm) and 3.31 eV ($\lambda = 375$ nm), respectively. Calculations are made for an incident field normalized to 1 N/C. As the free-space wavelength is decreased toward the surface plasmon resonance, the energy density becomes increasingly localized at the interface, with most of the field contained on the Ag side. Figure 2.6c illustrates the energy density of the RPP mode at 3.98 eV ($\lambda = 312$ nm), just beyond the onset of the RPP. This region of the RPP mode is marked by a damped oscillation into the dielectric and an evanescent wave into the metal. For increasing energy (Figure 2.6d, 6.17 eV, $\lambda = 201$ nm), the maximal amplitude of

each wave decreases and oscillations become increasingly damped. This behavior is in contrast to the radiative mode predicted by the FEG model, characterized by a pure photon mode in the dielectric with a constant energy density of $u \sim 1 \text{ J/m}^3$ in the metal and $u \sim 21 \text{ J/m}^3$ in SiO_2 (data not shown).

While study of decoupled plasmons provides a first-order approximation to SPP behavior in bulk metals, the results of Figure 2.6 suggest that this approximation breaks down for metal films no thicker than $\sim 70 \text{ nm}$. As the thickness of the film is decreased, one can no longer ignore the interaction between plasmons on each side of the metal film.

2.3.2 Coupled surface plasmons: The insulator-metal-insulator waveguide

The eigenmodes of planar multilayer structures may be solved via the vector wave equation under constraint of tangential \mathbf{E} and normal \mathbf{D} field continuity. Uniqueness of the results is guaranteed by the Helmholtz theorem. For unpolarized waves in a three layer symmetric structure, the electromagnetic fields take the form:³

$$E(x, z, t) = (E_x \hat{x} + E_y \hat{y} + E_z \hat{z}) \cdot e^{i(k_x x - \omega t)} \quad (2.10a)$$

$$B(x, z, t) = (B_x \hat{x} + B_y \hat{y} + B_z \hat{z}) \cdot e^{i(k_x x - \omega t)} \quad (2.10b)$$

with E_y , B_x , and B_z identically zero for the transverse magnetic (TM) polarization and E_x , E_z , and B_y identically zero for the transverse electric (TE) polarization.

Inside the waveguide, the field components for each polarization may be written as:

$$E_x^{in} = e^{-ik_{z1}z} \pm e^{ik_{z1}z} \quad (2.11a)$$

$$E_y^{in} = 0 \quad (2.11b)$$

$$E_z^{in} = \left(\frac{k_x}{k_{z1}}\right)(e^{-ik_{z1}z} \mp e^{ik_{z1}z}) \quad (2.11c)$$

$$B_x^{in} = 0 \quad (2.11d)$$

$$B_y^{in} = \left(\frac{-\omega \varepsilon_1}{ck_x}\right)(e^{-ik_{z1}z} \mp e^{ik_{z1}z}) \quad (2.11e)$$

$$B_z^{in} = 0 \quad (2.11f)$$

³In this chapter, we will focus our attention on three-layer symmetric structures. Chapter 5 will introduce the general dispersion formalism for arbitrary multilayer stacks. Further details on multilayer dispersion, including derivation of the dispersion relations and discussion of the minimization routines used for solving them, can be found in Appendix B.

for TM polarized waves and as:

$$E_x^{in} = 0 \quad (2.12a)$$

$$E_y^{in} = e^{ik_{z1}z} \pm e^{-ik_{z1}z} \quad (2.12b)$$

$$E_z^{in} = 0 \quad (2.12c)$$

$$B_x^{in} = \left(\frac{-k_{z1}c}{\omega}\right)(e^{ik_{z1}z} \mp e^{-ik_{z1}z}) \quad (2.12d)$$

$$B_y^{in} = 0 \quad (2.12e)$$

$$B_z^{in} = \left(\frac{ck_x}{\omega}\right)(e^{ik_{z1}z} \pm e^{-ik_{z1}z}) \quad (2.12f)$$

for TE polarized waves.

Outside the guide, the components are given by:

$$E_x^{out} = (e^{-ik_{z1}d/2} \pm e^{ik_{z1}d/2})e^{ik_{z2}(z-d/2)} \quad (2.13a)$$

$$E_y^{out} = 0 \quad (2.13b)$$

$$E_z^{out} = \left(\frac{\varepsilon_1 k_x}{\varepsilon_2 k_{z1}}\right)(e^{-ik_{z1}d/2} \mp e^{ik_{z1}d/2})e^{ik_{z2}(z-d/2)} \quad (2.13c)$$

$$B_x^{out} = 0 \quad (2.13d)$$

$$B_y^{out} = \left(\frac{-\omega\varepsilon_1}{ck_x}\right)(e^{-ik_{z1}d/2} \mp e^{ik_{z1}d/2})e^{ik_{z2}(z-d/2)} \quad (2.13e)$$

$$B_z^{out} = 0 \quad (2.13f)$$

for TM polarized waves and as:

$$E_x^{out} = 0 \quad (2.14a)$$

$$E_y^{out} = (e^{ik_{z1}d/2} \pm e^{-ik_{z1}d/2})e^{ik_{z2}(z-d/2)} \quad (2.14b)$$

$$E_z^{out} = 0 \quad (2.14c)$$

$$B_x^{out} = \left(\frac{-k_{z1}c}{\omega}\right)(e^{ik_{z1}d/2} \mp e^{-ik_{z1}d/2})e^{ik_{z2}(z-d/2)} \quad (2.14d)$$

$$B_y^{out} = 0 \quad (2.14e)$$

$$B_z^{out} = \left(\frac{k_x c}{\omega}\right)(e^{ik_{z1}d/2} \pm e^{-ik_{z1}d/2})e^{ik_{z2}(z-d/2)} \quad (2.14f)$$

for TE polarized waves.

The in-plane wavevector k_x is defined by the dispersion relations:

$$L^+ : \begin{cases} \varepsilon_1 k_{z2} + \varepsilon_2 k_{z1} \tanh\left(\frac{-ik_{z1}d}{2}\right) = 0 & \text{TM} \\ k_{z2} + k_{z1} \tanh\left(\frac{-ik_{z1}d}{2}\right) = 0 & \text{TE} \end{cases} \quad (2.15)$$

$$L^- : \begin{cases} \varepsilon_1 k_{z2} + \varepsilon_2 k_{z1} \coth\left(\frac{-ik_{z1}d}{2}\right) = 0 & \text{TM} \\ k_{z2} + k_{z1} \coth\left(\frac{-ik_{z1}d}{2}\right) = 0 & \text{TE} \end{cases} \quad (2.16)$$

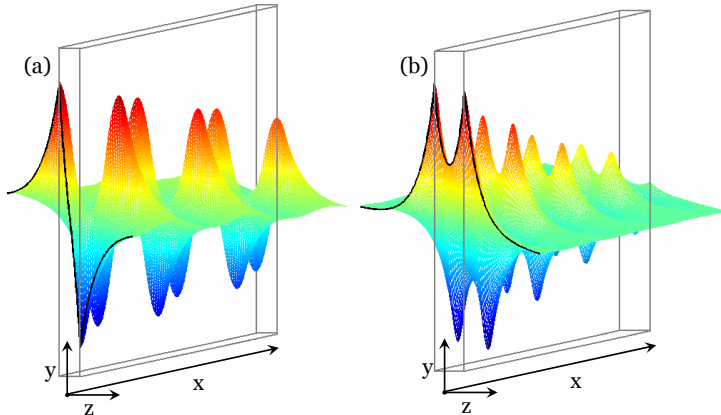


Figure 2.7. Characteristic magnetic field profile in the metal slab waveguide with thickness $z=d$. **(a)** the antisymmetric H_y field mode, corresponding to solution of L^- ; **(b)** the symmetric H_y field mode, corresponding to solution of L^+ . The propagation direction x is indicated by arrows.

with k_z defined by momentum conservation:

$$k_{z1,2}^2 = \varepsilon_{1,2} \left(\frac{\omega}{c} \right)^2 - k_x^2. \quad (2.17)$$

The analysis assumes the structure is centered at $z = 0$ with core thickness d and wave propagation occurring along the positive x -direction (see Figure 2.7). The core (cladding) is composed of material with complex dielectric constant ε_1 (ε_2); we assume all materials are nonmagnetic so that the magnetic permeability μ has been taken equal to 1. Since surface plasmons represent charge density oscillations, the dispersion relations of equations 2.15 and 2.16 define magnetic field (H_y) configurations that are either symmetric (L^+) or antisymmetric (L^-) with respect to the waveguide median. TE surface plasmon waves do not generally exist in planar metallodielectric structures, since continuity of E_y forbids charge accumulation at the interface.

While no exact solution exists for the dispersion relations 2.15 and 2.16 in the real frequency domain, $|L^+|$ and $|L^-|$ do appear in the denominator of the expression for the energy loss probability of electrons penetrating a thin metal film [115, 74]. It follows that minimization of $|L^+|$ and $|L^-|$ corresponds to a maximum in the energy loss probability and hence a maximum in the plasmon intensity distribution.

To obtain the complex wavevectors, numerical solution of $\min|L^+|$ and $\min|L^-|$ was accomplished through implementation of a two-dimensional unconstrained Nelder-Mead minimization algorithm. The routine relied on an adaptive simplex method [100] and guaranteed convergence through the strict convexity of $|L^+|$ and $|L^-|$.⁴ All returned wavevectors minimized the functions $|L^+|$ and $|L^-|$ with

⁴For general multilayer waveguides, the dispersion relation can only be formulated as a matrix equation $\det(L)=0$, where L is in general nondiagonal. In this case, a singular value

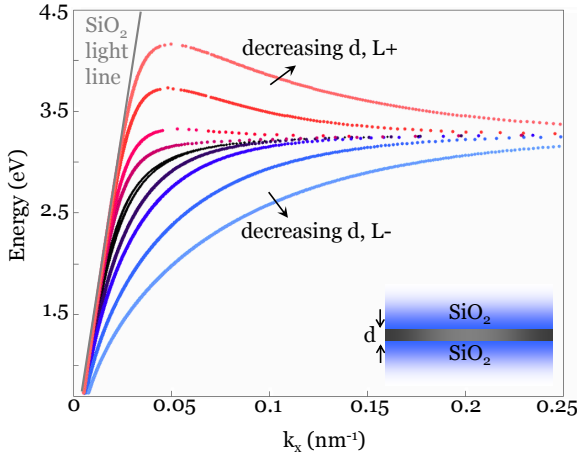


Figure 2.8. Dispersion for the $\text{SiO}_2/\text{Ag}/\text{SiO}_2$ geometry for five Ag thicknesses (100, 50, 35, 20, 12 nm), computed using a lossless Drude model for Ag.

a tolerance of 10^{-5} nm^{-1} .

Figure 2.8 plots the thin-film dispersion relations obtained via the adaptive simplex method, considering Ag as a free electron gas with bulk plasma frequency $\omega_p = 8.85 \times 10^{15} \text{ s}^{-1}$. The results are in good agreement with the theoretical dispersion characteristics predicted by Kliewer and Fuchs [72]. As film thickness is decreased from 100 nm to 12 nm, the degeneracy of the two interface plasmons is split, with each mode asymptoting at short wavevectors to the light line and at large wavevectors to the free electron gas SP resonant frequency, $\omega_{SP} = \omega_p / [1 + \epsilon_2]^{1/2}$. Note that both modes exhibit nearly-degenerate RPP branches above the bulk plasma frequency (data not shown).

The L- modes are plotted in hues of blue. As seen, these modes possess a larger wavevector at lower energies than the decoupled SPs of thick Ag films. Exploiting these modes in thin films, extremely short plasmon wavelengths can be achieved for frequencies well below the plasmon resonance. Figure 2.8 also plots the free electron gas L+ mode dispersion, shown in hues of red. Unlike the L- mode, this solution set exhibits wavevectors that approach the light line for reduced thicknesses. Moreover, enhanced maxima at energies above ω_{SP} can be seen for decreasing film thicknesses. Approaching the SP resonant frequency from above, a negative group velocity is observed for larger wavevectors. Since the FEG model assumes zero loss in the Ag, such modes are characterized by negative indices, and could form the basis for two-dimensional negative index materials at optical frequencies.

Figure 2.9 plots the dispersion curves generated using the Ag optical constants of Johnson and Christy. Nearly identical results were obtained using the

decomposition (SVD) is implemented prior to minimization. This SVD reduces the dispersion relationship to $\det(A)=0$, where A is a diagonal matrix composed of the squares of the eigenvalues of A. Then, each squared eigenvalue can be individually minimized. Though not essential for minimization, the SVD reduces the number of local minima in each minimization. Details can be found in Appendix B.

optical constants of Palik. As with the semi-infinite thick film geometry, the dispersion relations reveal the presence of SPP, RPP, and quasi-bound modes.

Considering the antisymmetric plasmon mode (L-, Figure 2.9a), the JC thin-film SPP exhibits behavior qualitatively similar to the FEG SPP for energies below the plasmon resonance. As seen, at a given frequency, the thin-film SPP is pushed toward higher wavevectors as film thickness is decreased. However, unlike FEG dispersion, thin-film SPPs exhibit a maximum wavevector at λ_{SP} rather than asymptoting to this frequency. For a 12 nm thick film, the SPP has a wavevector as large as $k_x \sim 0.2 \text{ nm}^{-1}$ at λ_{SP} , corresponding to a surface plasmon wavelength of $2\pi/k_x = 30 \text{ nm}$. Above λ_{SP} , the quasi-bound modes are observed up to 3.8 eV, marking the onset of the RPP. Note that the RPP of the symmetric mode is found at increasingly higher energies as film thickness is decreased. This behavior indicates that despite the existence of quasi-bound modes, the antisymmetric mode of thin Ag films still exhibits a bandgap between the SPP and RPP dispersion branches.

Considering the H_y symmetric plasmon mode (L+, Figure 2.9b), the thin-film SPP dispersion shifts toward smaller wavevectors at lower energies as film thickness decreases (just as in the free electron gas model). As energy is increased above the plasmon resonance, the antisymmetric SPP reaches a maximum wavevector before cycling back to smaller wavevectors through the quasi-bound modes and into the RPP. In fact, for energies up through the SP resonance, the L+ dispersion relation for the 12-nm-thick film is almost indistinguishable from the light line. The observed behavior is quite unlike that predicted by the free electron model, but seems to be in accord with dispersion curves from experimental electron loss spectra [168].

In addition to the positive wavevector modes plotted in Figure 2.9b, this

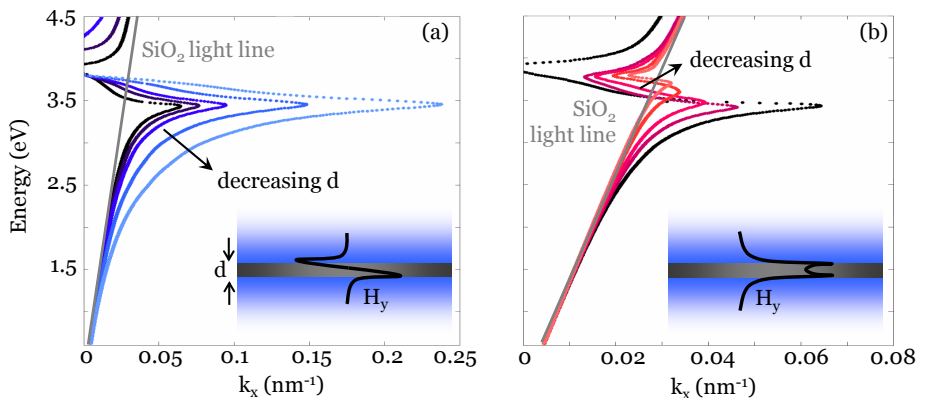


Figure 2.9. Dispersion for the $\text{SiO}_2/\text{Ag}/\text{SiO}_2$ geometry for five Ag thicknesses (100, 50, 35, 20, 12 nm), computed using the empirically-determined optical constants of Johnson and Christy. Note that dispersion for the 100-nm-thick film is plotted in black, and is nearly identical to the single-interface dispersion relation. Dispersion functions for the L- mode are shown in (a), while those for the L+ mode are shown in (b).

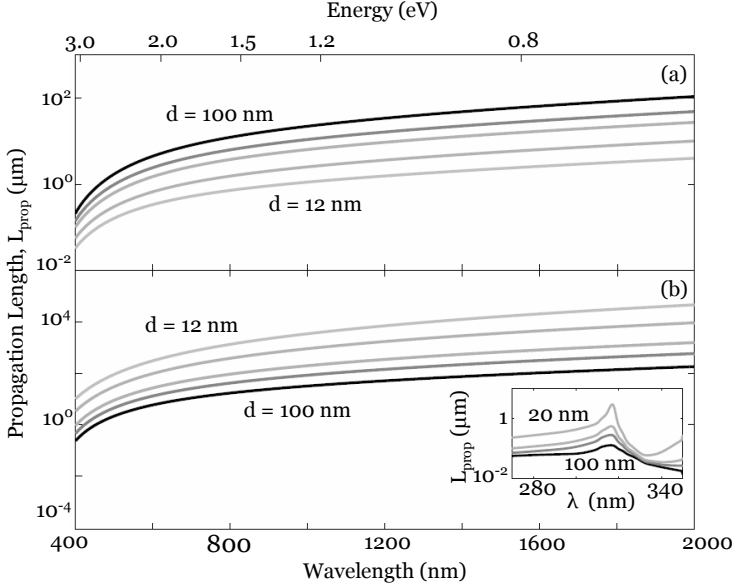


Figure 2.10. $\text{SiO}_2/\text{Ag}/\text{SiO}_2$ plasmon propagation lengths computed for five Ag thicknesses (12, 20, 35, 50, and 100 nm), using the optical constants from Palik's Handbook. **(a)** Lower energy, antisymmetric H_y field mode (L-), **(b)** Higher energy, symmetric H_y field mode (L+). The inset of **(b)** plots propagation distance for wavelengths characteristic of the regime of anomalous Ag dispersion.

symmetric mode also exhibits highly damped modes ($\text{Im}\{k_x\} \gg 0$) with negative $\text{Real}\{k_x\}$. These negative- k modes represent the negative-slope modes of the FEG dispersion, and could form the basis for visible-frequency negative index materials. Because the properties of these negative- k modes are a strong function of wavelength, waveguide composition, and thickness, we defer a detailed discussion until Chapter 5. The remainder of this chapter will exclusively focus on positive- k modes.

Figure 2.10 illustrates surface plasmon propagation lengths for both the symmetric and antisymmetric modes as a function of wavelength, using the optical constants from the Palik Handbook. (Propagation using the optical constants of Johnson and Christy is qualitatively similar.) As seen, decreasing film thickness reduces propagation to the micron scale for the antisymmetric mode (L-) and increases propagation to tens of centimeters for the symmetric mode (L+). While a discrepancy of about a factor of 10 is observed between predicted propagation lengths using the data of Johnson and Christy and Palik (with JC leading to longer propagation lengths), long-range propagation is still obtained in both cases. For a 12-nm-thick film, propagation distances for the antisymmetric mode approach $18 \mu\text{m}$ ($2 \mu\text{m}$) (JC/Palik data) at a free-space wavelength 1550 nm. At the same wavelength, propagation distances for the antisymmetric mode are calculated to be as large as 7 cm (1 cm).

As in the decoupled SP geometry, the propagation lengths of thin films ex-

hibit a minimum about the surface plasmon resonance and a local maximum about the region of anomalous dispersion. Note that for the L+ mode, the minimum in propagation shifts to shorter wavelengths as thickness is decreased, in agreement with the energy shift of the wavevector maximum observed in Figure 2.9b. For thicker films ($d \geq 50$ nm), this maximum does not much exceed the amplitude of the local maximum of the semi-infinite geometry observed in Figure 2.4. However, as film thickness is decreased below 50 nm, propagation appears to approach the micron scale. Such results are not a numerical artifact for the L+ mode and thus may be a promising avenue for future subwavelength waveguiding research, provided signal dispersion is not dominant. To the contrary, enhanced propagation at short wavelengths is not observed for the L-mode, since these wavelengths correspond to the surface plasmon stop-band regime (where $\text{Real}\{k_x\}=0$).

While experiments to measure propagation distances are typically performed by critical coupling of light at a particular free space frequency, waveguiding applications require the simultaneous optimization of surface plasmon wavelength and propagation distance. Figure 2.11 illustrates the dependence of propagation length on SP wavevector for bound surface plasmon polariton modes. As seen in Figure 2.11a, plasmon propagation distances for the antisymmetric mode (L-) are maximized for thick films with shorter SP wavevectors (larger SP wavelengths). However, for SP wavevectors exceeding $k_x=0.03 \text{ nm}^{-1}$ ($\lambda_{SP} \leq 210$ nm), longer propagation distances are observed for thinner films. A 12-nm-thick Ag film, for example, can sustain SP propagation over $1.03 \mu\text{m}$ with a mode wavelength of 200 nm.

In contrast, plasmon propagation for the symmetric mode (L+) is maximized for thin films with shorter SP wavevectors (larger SP wavelengths). However, as SP wavelengths are decreased beyond $\lambda_{SP} \sim 210$ nm, thicker films optimize the tradeoffs between plasmon localization and loss. While a 12 nm thick film can achieve propagation distances on the order of 2 cm at an SP wavevector of 0.01 nm^{-1} ($\lambda_{SP} = 630$ nm), propagation quickly falls to ≤ 350 nm at an SP wavevector of 0.03 nm^{-1} ($\lambda_{SP} \leq 210$ nm).

It is noteworthy that the intersection of all curves at $k_x = 0.03 \text{ nm}^{-1}$ does not occur at the transition between SPP and QB modes. Rather, this crossover occurs at energies well below the SP resonance, in regions where the group velocity is still non-negligible. Mathematically, this node represents the compromise between signal speed (as determined by the real component of the wavevector) and plasmon damping (as determined by the imaginary component). Just as observed in the semi-infinite geometry, then, large surface plasmon wavevectors are achieved at the expense of propagation length. However, maximum mode propagation for a given SP wavevector can be obtained by selecting films of an optimal thickness.

Figure 2.12 plots the $1/e$ decay length (skin depth) of the surface plasmon electric field into SiO_2 as a function of wavelength for both the symmetric and antisymmetric modes, calculated using Johnson and Christy optical constants. For oscillatory mode profiles, $1/e$ decay length was determined by considering decay of the exponential envelope. As can be seen, skin depth of the bound symmetric mode increases into the dielectric with decreasing film thickness. Conversely, for

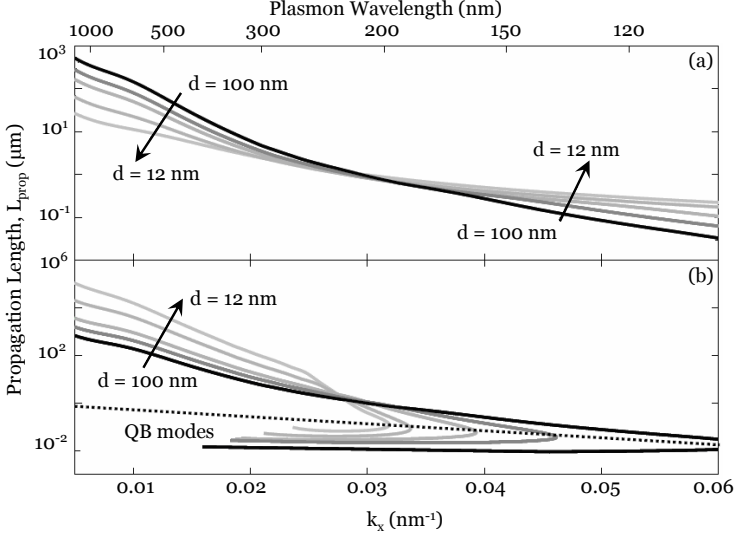


Figure 2.11. Propagation distance as a function of in-plane wavevector for five different Ag film thicknesses (12, 20, 35, 50, and 100 nm). Arrows indicate the trend of decreasing film thickness. For both the antisymmetric H_y field mode (L^- , **a**) and the symmetric H_y field mode (L^+ , **b**), the optimal combination of low damping and long wavevector is achieved at $\lambda_{SP} = 210$ nm.

the bound antisymmetric mode, field penetration into the dielectric decreases with decreasing film thickness. At near-infrared wavelengths (1550 nm), the charge-symmetric electric field profile for a 12-nm-thick Ag film is highly delocalized, extending to $5 \mu\text{m}$ in the SiO_2 . The antisymmetric charge configuration, in contrast, produces a field that extends only ~ 400 nm into the dielectric for the same film thickness at the same wavelength.

As with infinitely thick films, the skin depth of the H_y symmetric (L^+) mode exhibits a local maxima for energies above the plasmon resonance (see Figure 2.12, inset). The magnitude of this maxima increases with decreasing film thickness, more than doubling for each film thickness down to 12 nm. Related to the local maxima seen in the propagation length, this enhanced field penetration arises from the partial transparency of the metal above the bulk plasma frequency.

2.3.3 Outlook for insulator-metal-insulator waveguides

The preceding sections have outlined the properties of surface plasmons propagating along metallic slabs, considering the metal as described by empirically determined optical constants rather than a free electron gas model. Using the data sets of Johnson and Christy and from the Palik Handbook, surface plasmon dispersion, propagation, and skin depth was analyzed for both thick and thin films. Results were obtained over the wavelength range from 200 nm to 2000 nm and for all positive- k modes supported by the structure.

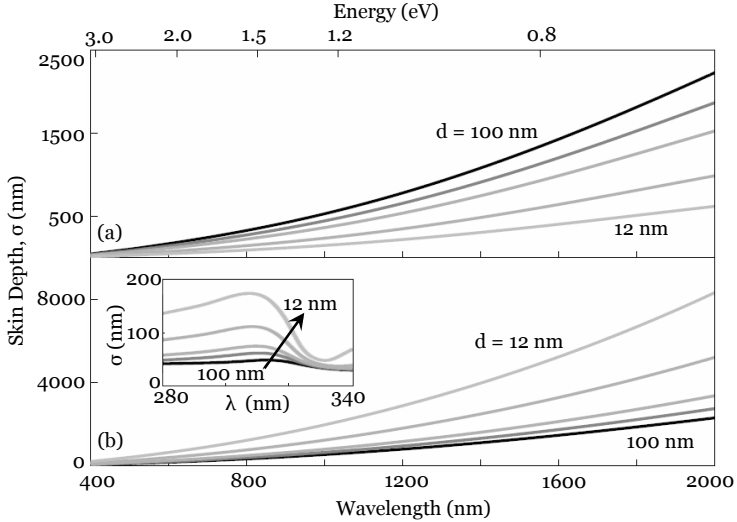


Figure 2.12. Skin depth for bound surface plasmon modes propagating along $\text{SiO}_2/\text{Ag}/\text{SiO}_2$ geometries, computed using the optical constants of Johnson and Christy. **(a)** Lower energy, antisymmetric mode (L-); **(b)** Higher energy, antisymmetric mode (L+) for five Ag film thicknesses (12, 20, 35, 50, and 100 nm). The inset shows field penetration depth into the dielectric for wavelengths below the surface plasmon resonance, with the arrow indicating the trend of decreasing waveguide thickness.

In thick films, the dispersion curve was found to exhibit three distinct branches corresponding to surface plasmon-polariton, radiative plasmon-polariton, and a feature not previously reported, which we term quasi-bound modes. Propagation distances of surface plasmons approached the micron scale in the near-infrared and sub-nanometer scales at the SPP resonant frequency. For higher frequencies, the propagation distance exhibited a local maximum, corresponding to the transition between the QB and RPP modes. Interestingly, at this wavelength, electric field penetration into the metal reached a maximum, while at the SPP resonance field penetration approached single nanometer scales. These results suggest that high field localization alone is not necessarily detrimental to plasmon propagation. Moreover, calculations using dielectrics other than SiO_2 indicated the potential for dynamic tuning of propagation length, particularly in regions of flat dispersion.

The properties of thin-film plasmons were obtained by implementing a numerical algorithm to determine the maxima of the electron energy loss spectra. Considering Ag as a free electron gas, results were in strong agreement with previous theoretical predictions. However, the dispersion characteristics obtained considering the empirical optical constants of Ag deviated significantly from the free electron gas data. Most notably, the dispersion curve terminated on resonance at a finite wavevector and exhibited quasi-bound modes.

The propagation characteristics of all positive wavevector thin-film modes

were determined, and results were justified by considering the field penetration into the metal and dielectric. Of the two modes (L+ and L-), it was found that the H_y antisymmetric (L-) surface plasmon mode exhibited decreasing propagation length and enhanced field confinement in the metal with decreasing film thickness. In contrast, the H_y symmetric (L+) plasmon mode exhibited increasing propagation length and decreasing plasmon wavevector with decreasing film thickness. Propagation distances generally decreased with increasing surface plasmon momentum for both the L- and L+ modes. Interestingly, identical antisymmetric (L-) and symmetric (L+) plasmon propagation lengths were observed for all film thicknesses at an SP wavevector of $k_x \sim 0.03 \text{ nm}^{-1}$. While long-range propagation in the infrared was accompanied by a broad electric field distribution in the dielectric, micron-scale propagation lengths were observed over a narrow bandwidth at ultraviolet wavelengths.

The above results suggest that thin film plasmons may find applications in micro- and nano-photonics interconnects. However, as we will see in the next section, more optimal trade-offs between mode propagation and mode localization can be achieved by turning IMI waveguides inside-out to form their conjugate: the MIM waveguide.

2.4 The Metal-Insulator-Metal Waveguide: Balancing localization and loss

The dispersion properties of long-ranging SPs on thin metallic slabs mimic those of a photon. However, as we saw in the last section, multi-micron propagation is often accompanied by significant field penetration into the surrounding dielectric. For thin Ag films ($d \sim 10 \text{ nm}$) excited at telecommunications frequencies, electric field skin depths can exceed $5 \mu\text{m}$ [27, 37]. In terms of designing highly integrated photonic and plasmonic structures, a more favorable balance between localization and loss is required.

While metals are characteristically lossy, the bound SP modes of a single metal/dielectric interface can propagate over several microns under optical illumination [37, 121]. In such a geometry, the field skin depth increases exponentially with wavelength in the dielectric but remains approximately constant ($\sim 25 \text{ nm}$) in the metal for visible and near-infrared excitation frequencies. This observation has inspired a new class of plasmon waveguides that consist of an insulating core and conducting cladding. Not unlike conventional waveguides (including dielectric slab waveguides at optical frequencies, metallic slot waveguides at microwave frequencies, and the recently proposed semiconductor slot waveguides of Reference [5]), these metal-insulator-metal (MIM) structures guide light via the refractive index differential between the core and cladding. However, unlike dielectric slot waveguides, both plasmonic and conventional TE and TM waveguiding modes can be accessed, depending on transverse core dimensions. MIM waveguides may thus allow optical mode volumes to be reduced to subwavelength scales - with minimal field decay out of the waveguide physical cross section - even for frequencies far from the plasmon resonance.

Several theoretical studies have already investigated surface plasmon prop-

agation and confinement in MIM structures [46, 178]. However few studies have investigated wavelength-dependent MIM properties arising from realistic models for the complex dielectric function of metals. The critical dependence of waveguiding experiments on excitation wavelength and surface plasmon frequency renders such an analysis essential. In this section, we discuss the surface plasmon and conventional waveguiding modes of MIM structures, characterizing the metal by the empirical optical constants of Johnson and Christy [69] and numerically determining the dispersion, propagation, and localization for both field symmetric and antisymmetric modes. As we will see, plasmon propagation in these waveguides can exceed tens of microns with fields confined to within 20 nm of the structure, even for waveguides with lateral dimensions of less than 10% of the free-space wavelength.

2.4.1 Slot waveguide dispersion: Plasmonic and photonic modes

When a plasma is excited at a metallodielectric interface, electrons in the metal create a surface polarization that gives rise to a localized electric field. In IMI structures, electrons of the metallic core screen the charge configuration at each interface and maintain a near-zero or minimal field within the waveguide. As a result, the surface polarizations on either side of the metal film remain in phase and a cutoff frequency is not observed for any transverse waveguide dimension. In contrast, screening does not occur within the dielectric core of MIM waveguides. At each metal/dielectric interface, surface polarizations may arise and evolve independently of the other interface, and plasma oscillations need not be energy or wavevector-matched to each other. Therefore, for certain MIM dielectric core thicknesses, interface SPs may not remain in phase but will exhibit a beating frequency; as transverse core dimensions are increased, “bands” of allowed energies/wavevectors and “gaps” of forbidden energies will be observed.

This behavior is illustrated in Figure 2.13, which plots the TM dispersion relations for an MIM waveguide with core thicknesses of 250 nm (Figure 2.13a) and 100 nm (Figure 2.13b). Since TE modes in MIM guides resemble those of a conventional dielectric core / conducting cladding waveguide, their dispersion is not explicitly considered here. The waveguide consists of a three-layer metallodielectric stack with a SiO₂ core and a Ag cladding. The metal is defined by the empirical optical constants of Johnson and Christy [69] and the dielectric constant for the oxide is adopted from Palik’s Handbook [108]. As before, solution of the dispersion relations (Equations 2.15 and 2.16) was achieved via application of a Nelder-Mead minimization routine in complex wavevector space. Note that we consider only propagating, positive- k modes, unless otherwise noted; Chapter 5 will discuss in detail negative- k modes that can also be found. For reference, Figure 2.13a and b includes the degenerate waveguide TM₀ and TM₁ dispersion curves in the limit of infinite core thickness, plotted in black. Allowed wavevectors are seen to exist for all free space wavelengths (energies) and exhibit exact agreement with the dispersion relation for a single Ag/SiO₂ interface SP.

Figure 2.13a plots the ‘bound’, propagating modes (here, modes occurring at frequencies below the SP resonance) of an Ag/SiO₂/Ag waveguide with core thickness $d = 250$ nm. MIM modes above the SP resonance will be considered

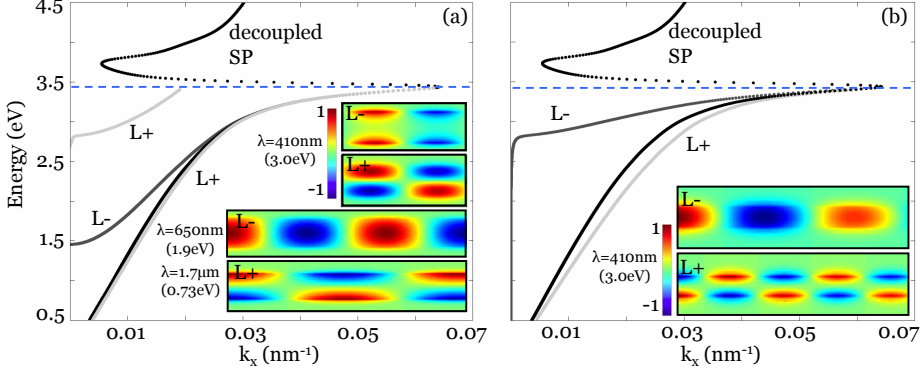


Figure 2.13. Transverse magnetic dispersion relations and tangential electric field (E_x) profiles for MIM planar waveguides with a SiO₂ core and an Ag cladding. Dispersion of an infinitely thick core is plotted in black and is in exact agreement with results for a single Ag/SiO₂ interface plasmon. **(a)** For oxide thicknesses of 250 nm, the structure supports conventional waveguiding modes with cutoff wavevectors observed for both the H_y field antisymmetric (L⁻, dark gray) and symmetric (L⁺, light gray) configurations. **(b)** As oxide thickness is reduced to 100 nm, both conventional and plasmon waveguiding modes are supported. Accordingly, tangential electric fields (E_x) are localized within the core for conventional modes but propagate along the metal/dielectric interface for plasmon modes, (inset, plotted in **(a)** at free-space wavelengths of $\lambda = 410$ nm (3 eV) (top two panels), $\lambda = 650$ nm (1.9 eV), and $\lambda = 1.7$ μ m (0.73 eV), and in **(b)** at $\lambda = 410$ nm (3 eV)).

in Chapter 5. The H_y symmetric bound modes correspond to solution of L⁺ and are plotted in light gray; the H_y antisymmetric bound modes correspond to solution of L⁻ and are plotted in dark gray. As seen, multiple bands of allowed and forbidden frequencies are observed. The allowed L⁺ modes follow the single-interface Ag/SiO₂ surface plasmon dispersion curve for all energies. An additional L⁺ modal solution can be found for energies above 2.8 eV, with dispersion there resembling a conventional dielectric core/ perfectly-conducting cladding waveguide. Tangential electric fields E_x in each regime are plotted in the inset and highlight the distinction in mode localization: At $\lambda = 410$ nm, the tangential electric is localized within the waveguide core and resembles a conventional TM waveguide profile. At $\lambda = 1.7$ μ m, dispersion is more plasmon-like and field maxima of the mode occur at each metal-dielectric interface.

In contrast to the L⁺ modes, the L⁻ modes are only observed for energies between 1.5 and 3.2 eV. Lower-energy dispersion for this mode is reminiscent of conventional dielectric core/ dielectric cladding waveguides, with an endpoint asymptote corresponding to a near-zero tangent line slope (effective group index) at 1.5 eV. For energies exceeding ~ 2.8 eV, wavevectors of the L⁻ mode are matched with those of the SP, and the tangential electric field transits from a core mode to an interface mode (see the first(~ 3 eV) and third (~ 1.9 eV) panels of the inset). This hybrid photonic-plasmonic mode may find applications in

two-dimensional transformation-based applications, where both the mode profile and refractive index of a material need to be continuously tuned. As the core layer thickness is increased through $1\ \mu\text{m}$ (data not shown), the number of L+ and L- bands increases with the L+ modes generally lying at higher energies. In analogy with conventional waveguides, larger (but bounded) core dimensions increase the number of modes supported by the structure.

Figure 2.13b plots the bound mode dispersion curves for an MIM waveguide with a SiO_2 core thickness of $d = 100\ \text{nm}$. Again, the allowed L+ modes are plotted in light gray while the allowed L- modes are dark gray. Here, the L+ mode is seen to exhibit plasmon-like behavior for all frequencies; the higher energy L+ mode seen in Figure 2.13a lies at energies above the surface plasmon resonance. The L- mode can still be found below the SP resonance, but its dispersion has been substantially flattened. As expected, conventional waveguiding modes are found only at higher energies (over a range of $\sim 1\ \text{eV}$), where photon wavelengths are small enough to be guided by the structure. The inset shows snapshots of the tangential electric field for both modes at a free-space wavelength $\lambda = 410\ \text{nm}$ ($3\ \text{eV}$). As seen, the L- field is concentrated in the waveguide core with minimal penetration into the conducting cladding. In contrast, the L+ field is highly localized at the surface, with field penetration approximately symmetric on each side of the metal/dielectric interface. The presence of both of conventional and SP waveguiding modes represents a transition to subwavelength-scale photonics. Provided momentum can be matched between the photon and the SP, energy will be guided in a polariton mode along the metal/dielectric interface. Otherwise, the structure will support a conventional waveguide mode, but propagation will only occur over a narrow frequency band.

As MIM core thickness is reduced below $100\ \text{nm}$, the structure can no longer serve as a conventional waveguide. Light impinging the structure will diffract and decay evanescently, unless it is coupled into a SP mode. Figure 2.14 illustrates the TM dispersion of such subwavelength structures as core thickness is varied from $50\ \text{nm}$ down to $12\ \text{nm}$. As in Figure 2.13, the dispersion curve in the limit of infinite core thickness is also included (black curve).

Figure 2.14a plots the TM dispersion relation for the L- bound modes with $d = 50, 35, 20,$ and $12\ \text{nm}$. Here, the magnitude of the wavevector is plotted, since this mode is characterized by exclusively negative wavevectors below the SP resonance. Insets plot the tangential electric field profiles for $d = 50\ \text{nm}$ and $d = 12\ \text{nm}$ at free-space wavelengths of $\lambda = 1.55\ \mu\text{m}$ ($0.8\ \text{eV}$) and $\lambda = 350\ \text{nm}$ ($3.5\ \text{eV}$), respectively. Functionally, the dispersion behaves like the thin-film L- modes of the metallic-core (IMI) guides, with larger wavevectors achieved at lower energies for thinner films. As free-space energies approach SP resonance, the wavevector reaches its maximum magnitude before cycling through the higher energy “quasi-bound” modes (not shown). A 12-nm -thick oxide can reach wavevectors as high as $|k_x| = 0.2\ \text{nm}^{-1}$ ($\lambda_{SP} = 31\ \text{nm}$), comparable to the resonant wavevectors observed in $12\ \text{nm}$ Ag IMI waveguides. However, unlike IMI structures, the wavevector magnitude does not always exceed the single-interface (thick film) limit. Over a finite energy bandwidth, SP momentum magnitude exceeds photon momentum both in SiO_2 and in vacuum. The $50\ \text{nm}$ thick oxide provides the most striking example of this behavior: dispersion lies

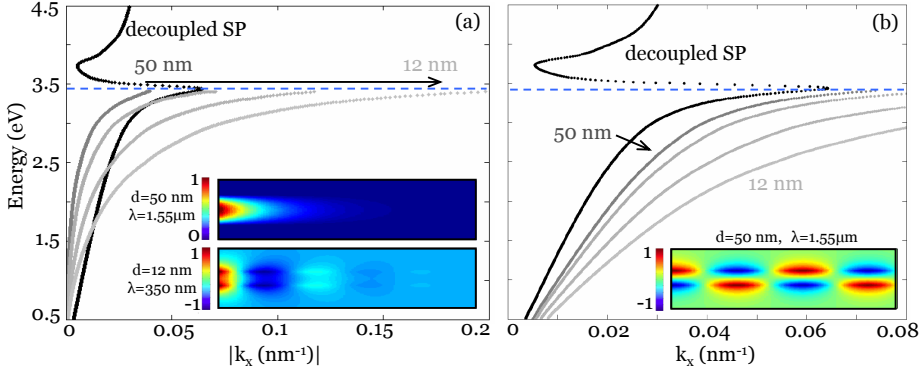


Figure 2.14. Transverse magnetic dispersion relations and tangential electric field (E_x) snapshots of MIM (Ag/SiO₂/Ag) structures as oxide thickness d is varied between 12 nm, 20 nm, 35 nm, and 50 nm. As in Figure 2.13, dispersion for an infinitely thick oxide core is plotted in black. While both the field antisymmetric (a) and symmetric (b) modes exhibit plasmon-like dispersion, the results do not parallel the behavior observed in IMI waveguides. In (a), plasmon wavevectors are actually negative, with the magnitude of SP momentum exceeding photon momentum both in SiO₂ and in vacuum for certain wavelengths. In (b), the symmetric mode is seen to exhibit dispersion similar to the antisymmetric mode of IMI guides.

completely to the left of the decoupled SP mode. In addition, the low-energy asymptotic behavior follows a light line corresponding to a refractive index of $n = 0.15$. This low effective index suggests that polariton modes of MIM structures more highly sample the imaginary component of the metal dielectric function than the core dielectric function. Indeed, these negative- k modes are characterized by considerable losses below the SP resonance. Nevertheless, these modes can form the basis for materials with positive energy velocities but negative phase velocities. A detailed discussion of such modes both below and above the resonance is deferred to Chapter 5.

Figure 2.14b plots the TM dispersion relation for the L+ bound modes, again with $d = 50, 35, 20,$ and 12 nm. The tangential electric field profile (see inset, plotted for $d = 50$ nm at $\lambda = 1.55 \mu\text{m}$) confirms the purely plasmonic nature of the mode. In contrast with IMI structures, where L+ dispersion approaches the light line for thinner films, wavevectors of the MIM structure achieve larger values at lower energies. For energies well below the SP resonance (ω_{SP}), the observed behavior is quite similar to the L- modes of IMI guides. However, unlike the L- modes of IMI guides, the field penetration remains constant in the region surrounding the core, without compromising propagation length. In the next section, we will see how this decay length and skin depth varies as a function of wavelength and core dimensions.

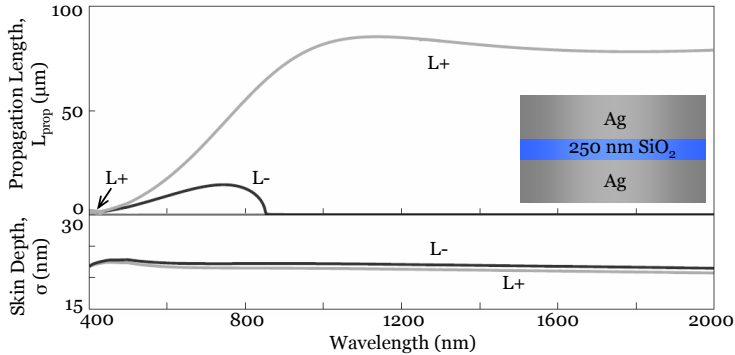


Figure 2.15. MIM (Ag/SiO₂/Ag) TM-polarized propagation and skin depth plotted as a function of wavelength for a core thicknesses of $d = 250$ nm. Both L+ and L- modes are observed and exhibit cutoff in accordance with the dispersion curve of Figure 2.13.

2.4.2 Mode propagation and penetration

Surface plasmon dispersion and propagation are governed by the real and imaginary components, respectively, of the in-plane wavevector. Generally, propagation is high in regimes of near-linear dispersion where high signal velocities overcome internal loss mechanisms. In IMI structures, multicentimeter propagation is observed for near-infrared wavelengths where dispersion follows the light line. However, this long-range propagation is achieved at the expense of confinement: transverse field penetration typically exceeds microns in the surrounding dielectric. In MIM structures, SP penetration into the cladding will be limited by the skin depth of optical fields in the metal. This restriction motivates the question of how skin depth affects propagation, particularly for thin films.

Propagation for the Transverse Magnetic Polarization

Figures 2.15, 2.16, and 2.17 illustrate the interdependence of skin depth and propagation in MIM structures for film thickness from 12 nm through 250 nm. The top panels plot propagation of the TM modes for the structure as a function of free space wavelength; the bottom panels plot the corresponding skin depth.

Figure 2.15 plots propagation and skin depth for a 250-nm-thick oxide layer. In accordance with the dispersion relations, wave propagation exhibits allowed and forbidden bands for the symmetric and antisymmetric modes. The L- mode is seen to propagate for wavelengths between 400 and 850 nm, with maximum propagation distances of approximately $15 \mu\text{m}$. The skin depth for this mode is approximately constant over all wavelengths, never exceeding 22 nm in the metal.⁵ In contrast, the L+ mode is seen to propagate for all wavelengths, much like SP modes on a single metal-dielectric interface. For visible to near-infrared wavelengths, propagation distances increase with increasing wavelength. How-

⁵While skin depth calculations for forbidden modes are of no physically relevant consequence, they do indicate field penetration depths of the diffracted wave. In particular, even though $k_x=0$ for forbidden modes, k_z can still assume a finite value.

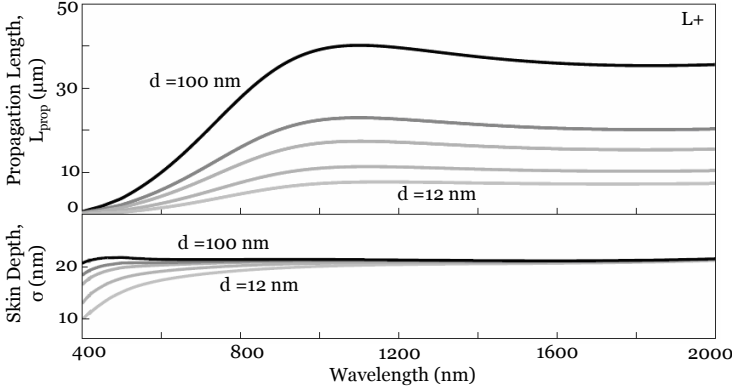


Figure 2.16. MIM (Ag/SiO₂/Ag) TM-polarized propagation and skin depth for the H_y symmetric mode, plotted as a function of wavelength for core thicknesses of $d = 12$ nm, 20 nm, 35 nm, 50 nm, and 100 nm. Here, the field symmetric modes of MIM guides are seen to propagate over $10 \mu\text{m}$ with skin depths never exceeding 20 nm.

ever, around a wavelength of 1000 nm, propagation lengths plateau at $80 \mu\text{m}$. Recall in IMI geometries, propagation lengths increased nearly exponentially with wavelength. Whereas the plasmon field could be increasingly guided in the dielectric for thin metallic films, MIM modes will remain confined to 20-30 nm of the core, regardless of wavelength. Thus, this plateau of propagation lengths represents a compromise between the energy density contained in the dielectric core and that in the metal. Note that in addition to this SP-like mode, L+ mode propagation is also sustained via a photonic mode for wavelengths below 450 nm. However, propagation distances for this branch do not exceed $2 \mu\text{m}$. For both L+ solutions, skin depth remain approximately constant at 20 nm. Interestingly, the figure indicates only a slight correlation between propagation and skin depth for both the L+ and L- modes. This relation suggests that absorption in the metal is not the limiting loss mechanism for wave propagation in MIM structures.⁶

Figure 2.16 illustrates the propagation distance and skin depth for the L+ bound mode for oxide thicknesses from 12 nm through 100 nm. The continuous plasmon-like dispersion relations of Figures 2.13b and 2.14b are well correlated with the observed propagation: decay lengths are generally longer for larger wavelengths, where dispersion follows the light line. As with the plasmon mode of Figure 2.15, propagation generally peaks and plateaus around $\lambda = 1000$ nm, indicating the wavelength of optimal metal-dielectric electromagnetic energy distribution. As expected, plasmon propagation generally increases with increasing film thickness, approaching $10 \mu\text{m}$ for a 12 nm oxide layer and $40 \mu\text{m}$ for a 100-nm-thick oxide. Nevertheless, field penetration remains approximately constant in the Ag cladding, never exceeding 20 nm. Thus, unlike IMI plas-

⁶This observation is further supported by data for thin waveguides ($d < 100$ nm), presented in Figures 2.16 and 2.17

mon waveguides, MIM waveguides can achieve micron-scale propagation with nanometer-scale confinement.

Figure 2.17 plots propagation and skin depth for the L- bound modes of thin films. As with the L+ modes, larger oxide thicknesses support increased propagation distances. However, the wave remains evanescent for thicknesses up through 50 nm, with propagation not exceeding 10 nm for longer wavelengths. As SiO₂ thicknesses approach 100 nm, a band of allowed propagation is observed at higher frequencies, reflecting the dispersion of Figure 2.13b: at $\lambda=400$ nm, propagation lengths are as high as 500 nm. In addition, thin films exhibit a local maximum in propagation for wavelengths (see inset), within the quasi-bound regime, analogous to IMI guides [37]. For films with $d \leq 35$ nm, only a single peak is observed; here, propagation lengths can be ‘as high as’ 60 nm.⁷ As film thickness is increased, the peak begins to split with the lower energy peak forming the first band of allowed propagation. The transition indicates a dissociation of the quasi-bound modes and marks the onset of conventional waveguiding. While this regime is characterized by a slight increase in skin depth, field penetration for a given d remains generally constant over the full wavelength range. Thus, whether MIM structures support propagating modes or purely evanescent fields, skin depth is limited by absorption in the metal and will not exceed 30 nm.

On the existence of transverse electric MIM modes

Surface plasmons are generally transverse magnetic in nature, with interface charges allowed by the discontinuity of E_z . In planar IMI waveguides, transverse electric SP modes are not supported since E_y is continuous. However, the existence of conventional and SP modes in MIM guides suggests that TE waves might propagate for certain oxide core thicknesses and excitation wavelengths. Figure 2.17 illustrates TE propagation for MIM waveguides with core thicknesses of 12 nm through 50 nm. Panel (a) plots propagation of the L+ mode, while panels (b) plots propagation of the L- mode.

Though not plotted, thicker oxide cores ($d \geq 100$ nm) can support notable TE wave propagation. Although both the L+ and L- modes exhibit cutoff, TE waves can propagate several microns; distances can even exceed decay lengths observed for TM-polarized waves. A 100 nm thick oxide core, for example, propagates L+ TE-polarized light over distances of 2 μm at an excitation wavelength of $\lambda = 400$ nm. In contrast, the L+ TM mode decays in about a quarter of the distance, propagating approximately 680 nm. For both the L- and L+ modes, bands of allowed propagation shift toward shorter wavelengths as oxide thickness is reduced. As wavelengths approach the regime of anomalous Ag dispersion, all modes become evanescent. Thin film propagation, plotted in Figure 2.18, does not exceed the nanometer scale for all wavelengths. However, like the L-

⁷This propagation length may not sound high, but keep in mind that these modes have extremely short wavelengths and negative real components of the wavevector (i.e., are characterized by negative indices). By increasing the core dielectric from that of SiO₂, to, e.g., that of GaP ($n \sim 3$), the quasi-bound modes can be brought to lower frequencies that farther away from the bulk plasma resonance - thereby minimizing Ag losses. As we will see in Chapter 5, we can use these modes to achieve negative index materials with fairly low loss - with propagation lengths of many plasmon wavelengths.

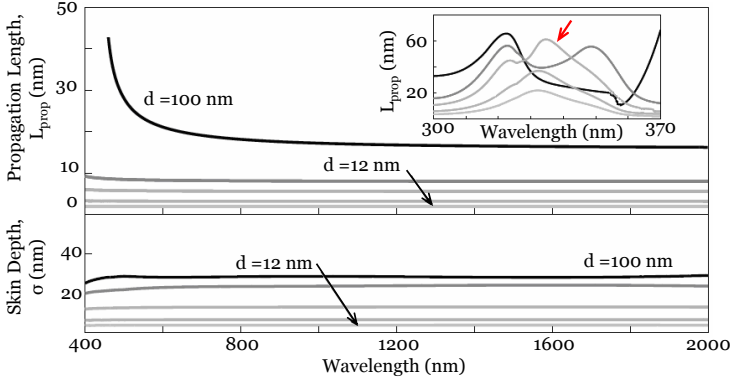


Figure 2.17. MIM (Ag/SiO₂/Ag) TM-polarized propagation and skin depth for the H_y antisymmetric mode, plotted as a function of wavelength for core thicknesses of $d = 12$ nm, 20 nm, 35 nm, 50 nm, and 100 nm. For wavelength below the surface plasmon resonance, this ‘mode’ remains evanescent for all wavelengths. However, as d approaches 100nm, conventional waveguiding modes can be accessed, and a region of enhanced propagation is observed for $\lambda = 400$ nm. Inset: Propagation lengths of this antisymmetric mode for wavelengths characteristic of the quasi-bound regime. Notice that thin films can exhibit a local maximum in propagation length, shown by the red arrow for $d = 35$ nm. The dissociation of the thin-film single peak to the thick-film double peak indicates the onset of conventional waveguiding.

TM-polarized modes of Figure 2.17, a local maximum in propagation is observed for shorter wavelengths. This maximum increases with film thickness until the onset of conventional waveguiding is observed.

The combined results of Figures 2.15, 2.16, and 2.17 suggest that MIM modes can propagate many microns throughout a wide spectral range as core thicknesses are reduced from wavelength to subwavelength scales. For thicker films, this propagation results from a hybrid-polarized wave. As oxide thickness is decreased, the TE polarization is filtered, and only TM waves can propagate in the guide. This mixed TM-TE mode characteristic may be an important consideration in design of MIM tapered waveguides.

2.4.3 Electromagnetic energy density

In an electrostatics limit, MIM waveguides locally serve as parallel-plate capacitors. At each metal/dielectric interface, localized charges will either interact with nearest neighbors in the conductor or across the dielectric. While the former situation is indicative of a surface charge wave, the latter suggests strong field concentration within the dielectric. Thus, unlike skin depth, the distribution of energy density in each media is a prime discriminator of wave propagation in MIM structures.

Figures 2.19 and 2.20 plot the electromagnetic energy density profiles of Ag / SiO₂ / Ag structures as a function of distance from the waveguide median.

Intensities have been normalized such that the power coupled into the guide is equivalent for each mode. Within the dielectric core, electromagnetic energy density is defined as:

$$u_{SiO_2} = \frac{1}{2}(\vec{E} \cdot \vec{D}^* + \vec{B} \cdot \vec{H}^*) = \frac{1}{2}(\varepsilon_{SiO_2} \vec{E} \cdot \vec{E}^* + \vec{B} \cdot \vec{B}^*), \quad (2.18)$$

while outside the waveguide, the energy density is derived from Poynting's theorem in lossy dispersive media [79]:

$$u_{Ag} = \frac{1}{2}(\text{Re}[\frac{d(\omega\varepsilon_{Ag})}{d\omega}])\vec{E} \cdot \vec{E}^* + \vec{B} \cdot \vec{B}^*). \quad (2.19)$$

Figures 2.19a and b consider energy density both in the core and cladding for a 250-nm-thick oxide layer. Panel (a) plots the total energy density (including TE and TM contributions) at a free-space wavelength of 410 nm (~ 3.2 eV). Panel (b) illustrates the separate contributions of each polarization. Note that energy density values in the cladding are indicated on the left scale of the plot; values inside the core are shown on the right.

As seen in Figures 2.19a, total energy density of the L+ mode is reminiscent of conventional waveguiding modes, with high density concentrations both in the waveguide and at the metal surface. In the waveguide center, the density profile is nearly parabolic, reaching a maximum value at $z=0$. Outside the guide, energy density decays exponentially from the interface with a decay length of 16 nm. In contrast, total energy density of the L- mode is reminiscent of a surface mode, with high electromagnetic densities concentrated at the interface. Inside the guide, intensity exhibits a minimum at $z = 0$ and attains maximal amplitude at the Ag/SiO₂ interface. Outside the core, energy densities decay within 11 nm of the interface. Such results suggest that the long-ranging modes

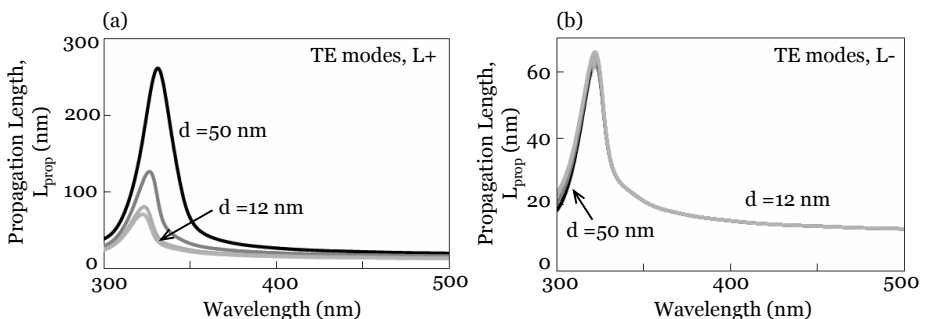


Figure 2.18. MIM (Ag/SiO₂/Ag) TE-polarized propagation plotted as a function of wavelength for core thicknesses of $d = 12$ nm, 20 nm, 35 nm, and 50 nm. Panel (a) plots propagation of the field symmetric modes while panel (b) plot propagation of the field antisymmetric modes. In both panels, propagation does not exceed the nanometer scale for all wavelengths. However, as d approaches 100 nm (data not shown), conventional waveguiding modes can be accessed, and propagation lengths can exceed several microns.

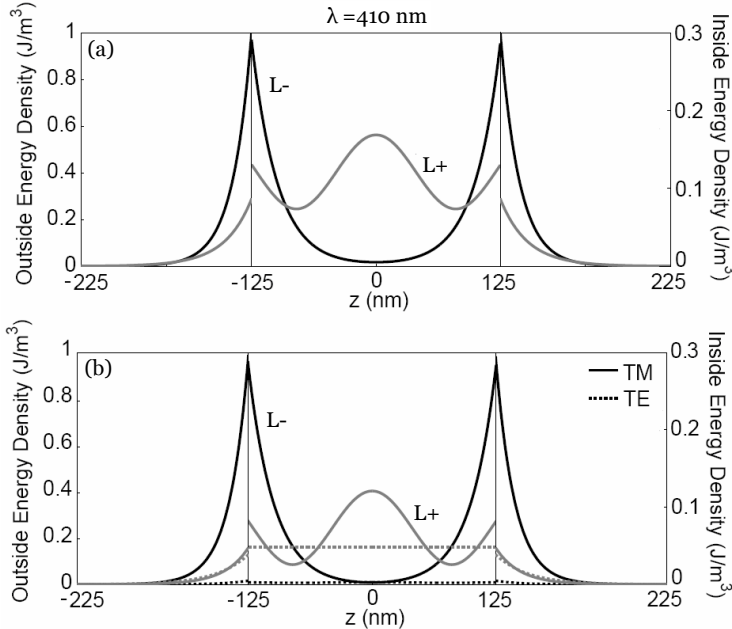


Figure 2.19. Normalized electromagnetic energy density profiles plotted as a function of distance from the waveguide median ($z = 0$) for MIM (Ag/SiO₂/Ag) structures with core thickness $d = 250$ nm. Note that energy density axes relevant for the metal are shown on the left while those relevant for the oxide are shown on the right. (a) Total energy density (TE + TM polarizations) for the symmetric (L+, gray) and antisymmetric (L-, black) dispersion solutions. (b) Separate TE (dotted) and TM (solid) energy density contributions for the L+ (gray) and L- (black) modes. In each panel, the excitation wavelength has been set to $\lambda = 410$ nm.

of MIM waveguides generally have high densities at the metal-dielectric interface, in analogy with surface electromagnetic waves.

Figure 2.19b plots the separate TM and TE contributions to energy density for a 250 nm SiO₂ core, holding wavelength fixed at $\lambda = 410$ nm. TM contributions are plotted using solid-line type; TE contributions are dotted. Additionally, L- modes are shown in black and L+ modes are plotted in gray. As the figure illustrates, TM energy densities mimic those observed in panel (a). Intensity of the TE L+ mode is constant throughout the waveguide core, while intensity of the TE L- mode is minimal throughout the waveguide and functionally behaves much like the TM L+ mode. Interestingly, the TE L+ wave represents the only polarization that does not propagate several microns in the waveguide. This observation is supported by decay lengths of energy density in the Ag: the TE L+ mode extends to 20 nm in the Ag, while decay lengths for the TE L- and TM L+ and L- modes are, respectively, 14 nm, 12.8 nm, and 14 nm.

Figures 2.20a and b plot energy densities in the core and cladding for a 100-nm-thick SiO₂ oxide layer. Again, wavelength is held fixed at 410 nm, and

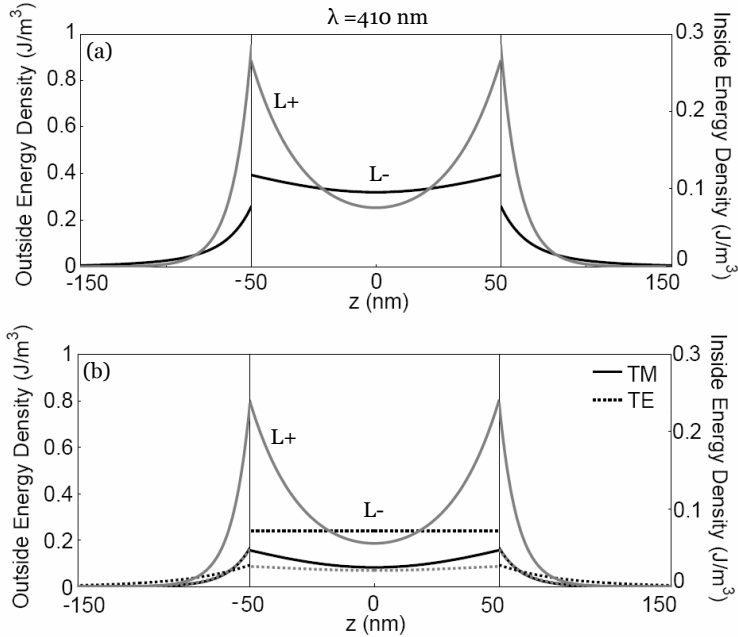


Figure 2.20. Normalized electromagnetic energy density profiles plotted as a function of distance from the waveguide median ($z = 0$) for MIM (Ag/SiO₂/Ag) structures with core thickness $d = 100$ nm. Again, energy density axes relevant for the metal are shown on the left while those relevant for the oxide are shown on the right. **(a)** Total energy density (TE + TM polarizations) for the symmetric (L+, gray) and antisymmetric (L-, black) dispersion solutions. **(b)** Separate TE (dotted) and TM (solid) energy density contributions for the L+ (gray) and L- (black) modes.

both total and contributed energy density profiles are considered. As seen in Figure 2.20a, both L+ and L- modes are characterized by energy densities that are concave-up, exhibit a minimum at $z = 0$, and reach a maximum at the Ag/SiO₂ interface. The L+ mode decays within 11 nm of the waveguide core (contrasted with a 20 nm decay length for the L- mode), explaining the enhanced propagation lengths observed for this mode. Recall that at $\lambda = 410$ nm, the L+ mode propagates $\sim 1 \mu\text{m}$ (TM) / $1.7 \mu\text{m}$ (TE) while the L- mode propagates $\sim 0.5 \mu\text{m}$ (TM) / 20 nm (TE).) Figure 2.20b reveals that TE and TM modes are of competing magnitudes inside the waveguide. The equivalence in form and magnitude of the TE and TM L+ modes reflects their comparable propagation lengths at this wavelength. The TE L- polarization is the only non-propagating field at $\lambda = 410$ nm, and exhibits constant intensity within the core. As with the 250-nm-thick oxide guide, near-constant core energy density is accompanied by large decay lengths in the metal. The TE L-polarization extends 42 nm into the Ag, while decay lengths for the TE L+ and TM L+ and L- modes are, respectively, 14.5 nm, 10.5 nm, and 13 nm.

Interestingly, the non-propagating TE L- polarization achieves higher energy

density values at the waveguide median than any other polarization. Here, energy densities in the oxide approach 80% of those observed in the metal (for the same mode). As film thickness is decreased through 12 nm, TE intensities in the core can equal and even exceed maximal Ag energy densities. Such results suggest that the propagating modes of subwavelength structures are generally surface modes, with field localization dominant within a narrow band about the metal/dielectric interface. However, the core energy densities of non-propagating TE modes can rival the intensities observed in resonantly excited metal nanoparticle arrays [152]. This interdependence of energy density, mode polarization, and oxide thickness suggests potential for both waveguiding and field-sensitive applications, including biological sensing.

2.5 Chapter Summary

Device architectures of present are reliant on index-contrasted media for signal storage and transmission. Accordingly, conventional optical waveguides and dielectric fibers are well understood and heavily utilized for light propagation on macroscopic scales. However, as device sizes are scaled to theoretical limits, light-matter interactions must be tuned to support electromagnetic modes within nanoscopic dimensions. Conversion of the photon mode into a surface plasmon mode is one such mechanism for subwavelength-scale signal transmission.

In thin metallic films, surface plasmons can propagate over tens of centimeters at infrared wavelengths. However, this long-range propagation is achieved at the expense of confinement: field penetration increases exponentially from the metal/dielectric interface, extending over several microns into the surrounding dielectric. In contrast, the skin depth of MIM structures is limited by optical decay lengths in the metal. As the waveguide core is reduced to nanometer sizes, the structure still supports propagation over 10 μm , with fields confined to within 20 nm of the structure.

Depending on transverse dimensions, MIM waveguides can support both conventional and plasmonic modes; cutoff wavevectors are not observed for any transverse core dimensions smaller than ~ 100 nm. This superposition of modes results in wide tunability of energy density throughout the electromagnetic spectrum. While energy densities are generally high at the metal interface, intensities within the waveguide can be comparable to values observed in the gaps of nanoparticle arrays.

Judicious arrangement of IMI and MIM plasmon waveguides promises potential for two-dimensional planar loss-localization balance. When combined with the recent remarkable progress in nanoscale fabrication, the aforementioned results might inspire a new class of waveguide architectures - ultimately, a class of subwavelength plasmonic interconnects, not altogether different from the silicon-on-insulator networks of today.

3 Experimental Imaging of Surface Plasmons, Part I: Metallic Surfaces

‘The truth is, the science of Nature has been already too long made only a work of the brain and the fancy: It is now high time that it should return to the plainness and soundness of observations on material and obvious things’

-Robert Hooke

Chapters 1 and 2 introduced surface plasmons as electron density fluctuations in metallodielectric geometries. As described, plasmonic structures support extremely large mode wavevectors and hence very small mode wavelengths compared with dielectric media. In theory, then, plasmonic structures enable subwavelength-scale confinement of photons and provide a powerful mechanism for nanophotonic manipulation. In practice, however, plasmonic geometries are merely mirrors; suppressing reflection to enable efficient coupling of photons to plasmons is therefore non-trivial.

In this chapter, we explore techniques for coupling photons to plasmons, giving particular attention to grating and groove coupling. Though rather rudimentary, efficient coupling and probing of surface plasmons is paramount to any plasmon-based application. Our analysis centers on the evolution and scattering of surface plasmons in-plane, yielding both the propagation length and local field of plasmonic modes. In the first section, we discuss the far-field spectra of modes bound to a metallic surface. Our results illustrate the presence of both propagating surface plasmons and evanescent diffracted waves generated by a square-wave grating. In the second section, we map the local field of plasmonic waveguides and resonators, using a photosensitive polymer to obtain field profiles with deep subwavelength-scale resolution. Emphasis is given to a *qualitative* understanding of the photon-plasmon interaction on metallic surfaces. This introduction to experimental techniques serves as a prelude to the more quantitative discussions to follow in Chapters 4 through 6.

3.1 Far-field excitation and detection

On planar metallodielectric interfaces, subwavelength-scale confinement of photons is enabled by the large momentum of surface plasmons. Compared to photons in free-space, surface plasmons are characterized by larger wavevectors β , larger local electromagnetic field intensities, and hence smaller wavelengths λ_{SP} . This feature renders plasmons non-radiative, implying that a prism, grating, or scattering center must be used to overcome the momentum mismatch between photons and plasmons. As mentioned in Chapter 1, the ability to prism-couple photons to plasmons opened the field of plasmonics to a number of researchers. Prior to this discovery, surface plasmons had only been excited by charged particle impact.

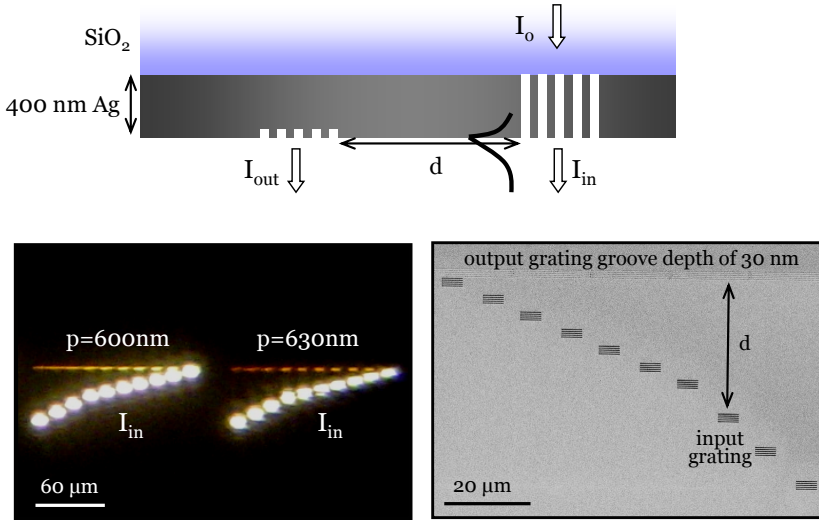


Figure 3.1. Schematic geometry, optical image, and SEM of sample used for grating coupling photons to plasmons. Normally-incident light from a lamp or laser transmits through subwavelength slits in a thick metal film. These slits convert free-space modes into non-radiative surface waves bound to the Ag/air interface. Such surface waves are later reconverted to photons by a shallow periodic corrugation a distance d away from the input.

Prisms allow for photon-plasmon coupling by shifting the linear dispersion of photons to larger wavevectors. For a prism of refractive index n , light of frequency ω will carry momentum $k_0 = n\omega/c$. These photons can then be momentum-matched to plasmons propagating along a metal-air interface, which have a maximum momentum of $k = \omega/c$. A similar principle applies to grating coupling. For a one-dimensional grating of period p , incident light will gain momentum in integral proportion to the grating vector, $k_g = 2\pi/p$:

$$k_{\text{surface}} = k_0 \sin(\theta) + mk_g, \quad (3.1)$$

where k_{surface} is the wavevector of the grating-coupled wave, θ is the angle of incidence, and m is an integer.

Figure 3.1 shows an example scheme for grating-coupling photons to plasmons. Here, slits and grooves are patterned onto an optically-opaque metallic film. Light illuminates the slits, exciting bound surface waves that propagate along the metal/air interface. These surface waves are decoupled back into photons by the grooves, spaced a distance d away from the input slits. Both the period and the order (number of grooves) can be varied to study surface wave evolution along the metal/dielectric interface. For example, Figure 3.1 includes optical transmission from a sample composed of 400 nm Ag evaporated on a 1-mm-thick fused silica substrate. Using a focussed ion beam, input slits were patterned with a period of $p_{in} = 600$ nm and 630 nm and spaced various dis-

tances away from a 30-nm-deep groove grating, with $p_{out}=p_{in}$. Gratings were designed with a 50% duty cycle, defining the slit width. The structure was illuminated with a normally-incident, unpolarized broadband source through the silica substrate. Upon interacting with the slits, free-space modes are converted into non-radiative surface waves bound to the Ag/air interface. Accordingly, the metal appears dark between the input slits and the output grooves. At the grooves, however, these surface waves are reconverted to photons. As evidenced by the red and orange hues of the output, the grating has filtered the incident light, selectively coupling to a narrow band of surface wavevectors.

To investigate surface wave evolution in detail, we varied the separation of slits from $d=5\ \mu\text{m}$ to $60\ \mu\text{m}$, the number of slits from $N=1$ to 9, and the grating period from $p=500\ \text{nm}$ to $700\ \text{nm}$ in $20\ \text{nm}$ increments. To eliminate cross-talk between various grating structures, individual input-output pairs were separated from their nearest neighbors by $500\ \mu\text{m}$. Input slits were patterned to a length of $10\ \mu\text{m}$, while output grooves were patterned to a length of $30\ \mu\text{m}$. The longer output-groove length ensured that all surface wave signal was acquired. Spatially localized detection was achieved using a 50x, 0.45 N.A. objective coupled to a dispersive grating monochromator and a cooled CCD. Imaging of any one particular structure (i.e., either the input slits or the output grooves) could be achieved with high spectral resolution between $400\ \text{nm}$ and $1000\ \text{nm}$.

As noted above, grating-coupling is generally thought to produce a well-defined in-plane momentum vector. According to standard theory, for normal incidence illumination, the surface wavevector will be given by $k_g = 2\pi/p$. Consequently, the output spectra should be dominated by a peak about the free-space wavelength corresponding to k_g , as determined by plasmon dispersion. For an Ag/air interface, dispersion indicates that an input grating with period $p=600\ \text{nm}$ should produce a spectral peak about $\lambda=620\ \text{nm}$.

Figure 3.2 illustrates the spectral response of the output grooves as the number of input slits is varied from $N_{in}=1$ to 9. The input period is set to $p_{in}=600\ \text{nm}$ and input-output separations of $d=5, 7, 10, 15, 20, 25, 30, 40, 50,$ and $60\ \mu\text{m}$ are considered. All spectra have been normalized with respect to the input lamp spectra. Figure 3.2a plots the spectra generated from a single groove - and hence spectrally-unbiased - output structure. As seen in the top panels (short d), spectral features are fairly broad, even as N_{in} is increased to 9. At a separation of $d=5\ \mu\text{m}$, no clear plasmon peak exists, and increasing N_{in} results only in an increase in overall spectral intensity. At $d=7\ \mu\text{m}$, wavelengths longer than p_{in} are suppressed, and a peak closely matched to the surface plasmon wavelength can be discerned. By $d=10\ \mu\text{m}$, the surface plasmon peak becomes the principal spectral feature. Suppression of longer wavelength components continues through $20\ \mu\text{m}$, where the surface plasmon peak dominates for all $N_{in} \geq 3$.

Of course, the broadband characteristics of the single groove output do not imply the absence of a surface plasmon for short d . Figure 3.2b plots the spectra generated using a grating output, with period $p_{out}=p_{in}=600\ \text{nm}$ and $N_{out}=5$. While spectral features are again broad at shorter separations, evidence of a surface plasmon peak is apparent even for $d=5\ \mu\text{m}$. By $d=10\ \mu\text{m}$, the surface plasmon-peak completely dominates the spectra for all $N_{in} \geq 3$. This

periodic output thus serves to select the surface plasmon-like wavevectors in the launched wavepacket, filtering all other components in half the distance required for the single groove output.

As the spectra Figure 3.2a and b imply, surface wave evolution is relatively agnostic to input grating order. Increasing N_{in} increases spectral intensity but does not decrease the distance required for pronounced spectral emission at the grating vector. However, grating order does affect the spectral spread of the propagating surface wave. For $d \geq 10 \mu\text{m}$, the spectral full-width half-maximum (FWHM) decreases linearly with the number of input slits (a fit to this parameter yields $\text{FWHM} = 142.5 - 7.5 \cdot N_{in}$). For $N_{in} = 9$, the FWHM about $\lambda = 620 \text{ nm}$ is as small as 75 nm .

By monitoring the output intensity as a function of wavelength and input-

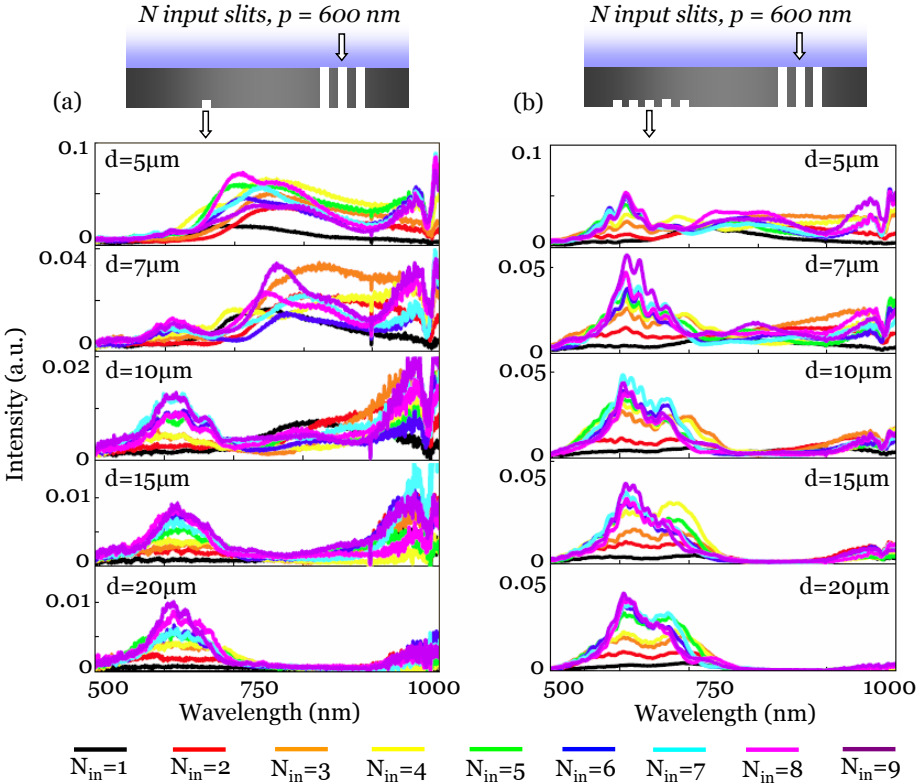


Figure 3.2. The spectral response of plasmons propagating on a thick metallic film, generated by a slit grating of pitch 600 nm , and decoupled by a single groove (a) or periodic corrugation (b). Spectra are plotted for various input-output separations d and grating orders (number of grooves) N . For single-groove outputs, the surface plasmon peak at 620 nm is only evident from other diffracted waves for $d \geq 10 \mu\text{m}$. However, outputs with grating vectors matched to the surface plasmon wavevector will selectively filter plasmon modes, even for $d \leq 10 \mu\text{m}$.

output separation, a decay length for surface waves can be determined. As seen in Chapter 2, surface plasmons decay exponentially with distance from the source. In contrast, the intensity of diffracted evanescent waves from a linear grating will decay as $1/x^2$ [84, 52]. Figure 3.3 illustrates the intensity decay of both surface plasmons and evanescent diffracted waves along metal-dielectric interface. Spectral intensity is plotted on a logarithmic scale as a function of d for all $N_{in} \geq 3$ and for $\lambda = 620$ nm (Figure 3.3a) and $\lambda = 750$ nm (Figure 3.3b). Results are shown for a periodic output grating, with $p_{out} = p_{in} = 600$ nm; however, qualitatively similar results were found using a single-groove output.

Not surprisingly, intensities at $\lambda = 620$ nm decay exponentially with distance from the source. For this input period, $1/e$ decay lengths are determined to be $40 \mu\text{m}$, in agreement with calculated plasmon propagation lengths. In contrast, decay at $\lambda = 750$ nm is highly non-linear, exhibiting a fitted decay of $I(x) = \frac{2.5}{x^2} e^{-0.25x}$. Accordingly, this 600-nm-period grating will most efficiently couple to surface plasmon wavevectors closely matched to the grating vector. By varying the input-output grating period from 500 nm to 700 nm, plasmon propagation lengths can be mapped as a function of wavelength. Figure 3.3 shows the observed propagation lengths, determined by using grating orders with the highest output intensity for a given d . For wavelengths between 500 nm and 750 nm, the experimentally-determined propagation length is in fair agreement with the calculated decay. While propagation lengths lie below calculated values, this discrepancy likely arises from surface roughness and oxidation that shift the Ag optical constants.

The results of Figures 3.2 and 3.3 suggest that gratings convert photons into both surface plasmons and diffracted waves with a large momentum spread. For distances close to the input ($d \leq 10 \mu\text{m}$), the diffracted wave can produce broadband spectral features that dominate those of the surface plasmon. However, use of a grating output can selectively filter the plasmon wave even at short input-output separations. By varying the grating pitch and order, plasmon propagation lengths may be determined; on a Ag/air interface, plasmon propagation lengths range from 20 to $60 \mu\text{m}$ at visible wavelengths. Normalized to the light incident on the slits, coupling efficiencies for the gratings studied here can be as high as 8%. Through appropriate design of the grating geometry, coupling efficiencies can be further increased to values as high as 60% to 80% [175].

3.2 Near-field imaging with photoactive polymers

Nanofabricated photonic materials offer a unique opportunity for controlling the local electromagnetic field. As seen in the last section, even a single subwavelength slit can generate complex and spectrally-rich bound modes along metallic surfaces. While far-field techniques can be used to probe wave propagation and evolution, they cannot yield direct information about the local mode intensity. Ideally, the scattering and localization of surface plasmons could be directly visualized with subwavelength-scale resolution. Of course, since surface plasmons are non-radiative, direct visualization is not straightforward. Several studies have

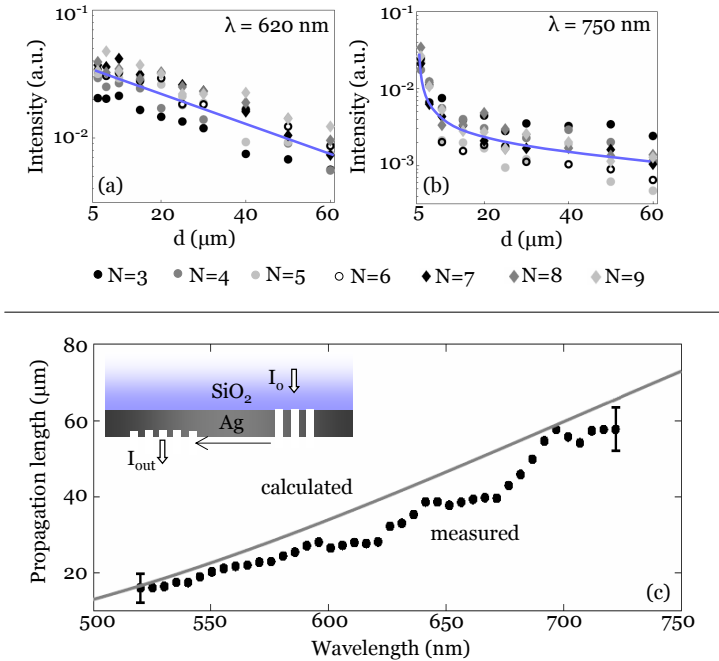


Figure 3.3. Experimental surface wave decay and plasmon propagation lengths along an Ag/air interface. In (a) and (b), surface wave decay is plotted on a logarithmic scale both for wavelengths matched to the surface plasmon wavelength (a) and off the plasmon peak (b). Grating inputs and outputs of various periods are used to selectively filter the plasmon component and extract the mode propagation length, (c) as a function of wavelength.

proposed and implemented techniques involving near-field microscopy [164, 89], photolithography [89], and cathodoluminescence [162, 62] to probe planar plasmonic modes. However, the resolution of such methods is often limited to about 100 nm. In this section, we directly probe the near-field of surface plasmons propagating along a metal-polymer interface.¹ By using the plasmon field to induce polymeric photoactivity [65, 150, 33], we obtain plasmon intensity maps with near-molecular-scale resolution.

Perhaps the most notable photoactive polymer is poly (Disperse Red 1) Methacrylate (pDR1M). pDR1M is a derivative of the photoresist polyMethyl Methacrylate (PMMA), with azobenzene dye sidechains attached to the polymer. As shown in Figure 3.4 in the *trans* conformation, the N=N azobenzene sidechains have a transition dipole moment aligned parallel to the polarized light [31]. Exposure to linearly polarized light induces a *trans* to *cis* photoisomerization of the N=N azobenzene sidechains. Continued light exposure results in a *cis* to *trans* isomerization back to the original state. As these *trans-cis-trans* cycles repeat, the azobenzene side chains function as molecular ‘bulldozers’, physi-

¹Portions of this work have been adopted from the 2007 Caltech SURF report of Phil Munoz, [99].

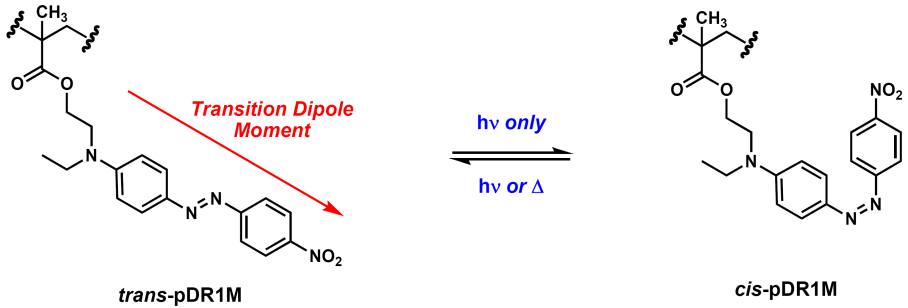


Figure 3.4. Chemical structure of the photoactive polymer, poly Disperse Red 1 Methacrylate, showing both geometric isomers: the *trans* conformation (left) and the *cis* conformation (right).

cally moving the surrounding polymer away from regions of high light intensity. Increased light intensity induces more frequent transitions, so that the resist becomes more concentrated in areas of low electromagnetic intensity. Photoisomerization continues until the illumination ceases. Accordingly, topographical deformations of the resist will reflect the local electromagnetic intensity, with regions of high light intensity corresponding to regions of low resist topography.

In our measurements, we coat a thin layer of pDR1M onto an Au film and excite surface plasmons at the Au/pDR1M interface. The enhanced local fields of the surface plasmons result in pDR1M topographic features that can be mapped using non-contact atomic force microscopy (NC-AFM). Interestingly, the resolution of the resist is limited only by the physical scale of the resist side chains. The technique is therefore capable of printing the electromagnetic intensity maps with deep subwavelength scale resolution. Additionally, unlike conventional photoresist, pDR1M is self-developing, so that samples can be exposed and scanned multiple times. In particular, topographic features can be erased simply by illuminating the resist with circularly-polarized light [31].

Figure 3.5a illustrates a cross section of the geometry used for this ‘plasmonic photolithography.’ A 75-nm-thick layer of Au was evaporated on a polished quartz substrate. Using focussed ion beam milling, shallow grooves were defined to a depth of 25 nm and a width of 100 nm. Figures 3.5b, c, and d show examples of patterned geometries, including linear grooves, circular corrals, and elliptical resonators.

After FIB milling, the samples were coated with a thin layer of pDR1M-based resist. In our measurements, the resist contained the dye, Disperse Red 1 (DR1) [4-(*N*-(2-hydroxyethyl)-*N*-ethyl)-amino-4-nitroazobenzene] grafted as a side chain to PMMA in a 30% molar ratio (DR1M/PMMA). Before coating the Au, the polymer was dissolved in tetrahydrofuran (THF) in a 1.5 wt.% ratio. Empirically, we found a 50-nm-coating of DR1M/PMMA-THF to be sufficiently thick for uniform sample coverage but sufficiently thin for accurate mapping of the local plasmon intensity.

Surface plasmons were excited along the Au/resist interface using normally-incident, linearly polarized light. To overlap the 400 nm - 600 nm absorption

band of the dye, 514 nm illumination was used. Note that at this wavelength, the 75-nm-thick layer of Au is not optically opaque, and transmits about 5% of the normally incident light. The interference between this directly-transmitted light and the propagating plasmons can then be recorded as a topographic modulation in the polymer. To avoid overexposing the polymer, the samples were illuminated for 60 s using an optical power density of 1 mW/mm².

Figure 3.6a shows a NC-AFM scan of a planar plasmonic waveguide excited by a single linear groove. The incident light was polarized perpendicular to the groove to ensure efficient coupling into surface plasmons. In this false color map, brighter hues correspond to peaks (and therefore low plasmon intensity) while darker hues indicate valleys (and therefore high plasmon intensity). For reference, a line scan through the groove is also included. To either side of the patterned groove, two pronounced peaks can be seen, resulting from height-ened transmission through the groove due to the reduced gold thickness. Notice that the resist which originally filled the groove is evacuated, having accumulated to either side of the groove. Further from the groove, the interference of propagating plasmons and the directly transmitted beam is manifest as parallel wavelets. These features exhibit a wavelength of 486 nm and a decay length of 3 μm , in agreement with calculations for plasmons propagating within a SiO₂/Au/pDR1M/air multilayer geometry.

Figure 3.6b shows a NC-AFM image of a circular corral after exposure. The incident light is again horizontally polarized, as indicated by the arrow in the

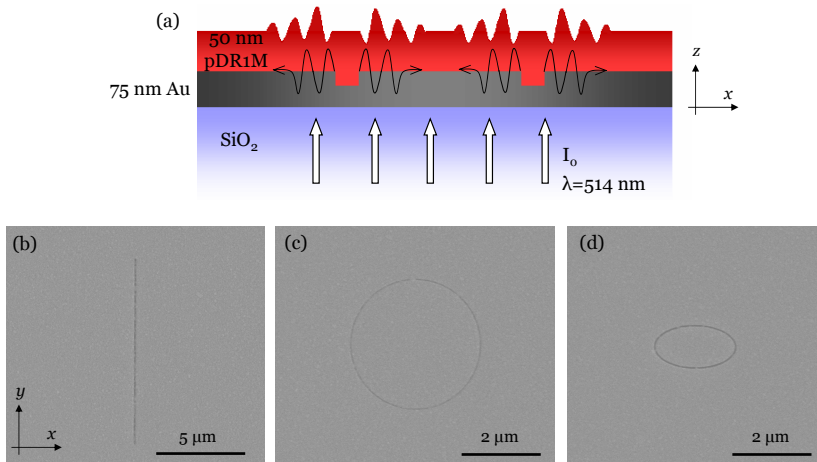


Figure 3.5. Single groove scatterers and corrals for plasmon photolithography. (a) Cross sectional schematic of geometry for plasmon photolithography. A thin layer of Au is coated onto a SiO₂ substrate and coated with a photosensitive polymer, pDR1M. Normally-incident illumination excites surface plasmons at the Au/resist interface. The interference between these plasmons and the directly-transmitted light results in topographical changes in the resist that can be mapped using atomic force microscopy. (b,c,d) Scanning electron micrographs of a single groove, a circular corral, and an elliptical resonator.

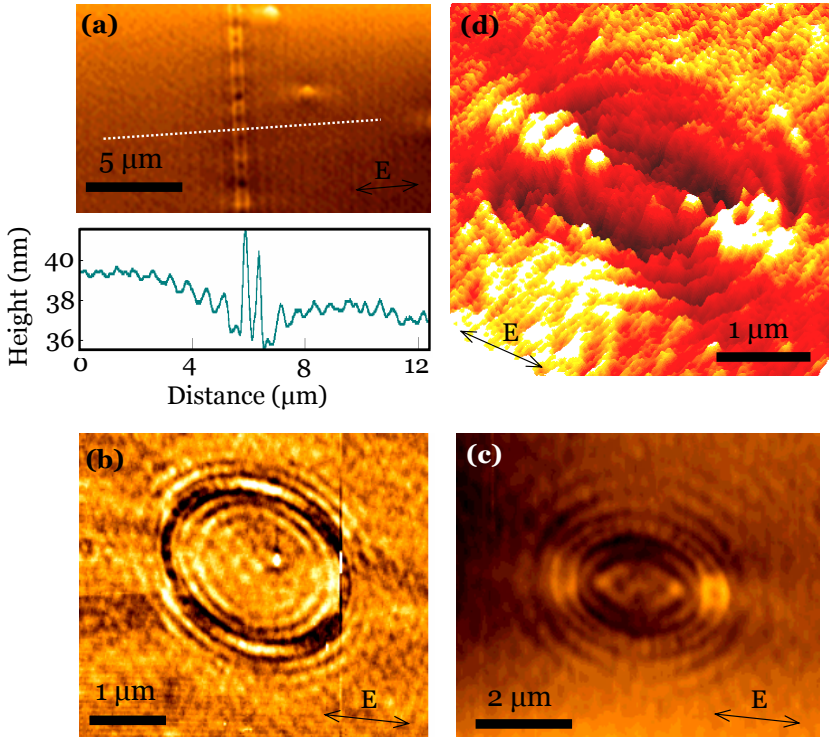


Figure 3.6. Non-contact atomic force microscopy images of **(a)** a single groove, **(b)** a circular corral, and **(c,d)** elliptical corrals after exposure. False color images reveal topography, with light hues indicating high regions and darker shades indicating low regions. The polarization of the incident electric field is indicated by the arrows.

figure. The groove appears as a wide, dark ring, surrounded on either side by several narrower rings that represent the propagating plasmon. Note that the recorded plasmon field exhibits an angular dependence proportional to $\cos(\theta)$, due to the polarization of the incident beam. As with the linear groove, the radial topographic dependence is periodic, suggesting a surface plasmon wavelength of 466 nm.

Figures 3.6c and d show NC-AFM images of elliptical resonators. The polarization of the incident illumination is indicated by the arrows. Similar to the circular corral, these elliptical resonators generate plasmons that propagate away from the groove, with a measured wavelength of 438 nm. In addition, because the dimensions of this geometry are more commensurate with the plasmon decay length, a standing wave can be observed within the resonator. Two foci appear as dark spots in Figure 3.6c and as voids in the three-dimensional view of Figure 3.6d. In both elliptical structures, the maximum observed topographic contrast is 16 nm.

To better understand the mechanism for dye rearrangement under light ex-

posure, we performed finite-difference time-domain simulations of these geometries. The $\text{SiO}_2/\text{Au}/\text{pDR1M}/\text{air}$ multilayer stack was modeled using empirically-determined optical constants. The permittivities of SiO_2 and Au were adopted from Palik's handbook [109], and the index of pDR1M was obtained through spectroscopic ellipsometry. As in the experiments, the structure was illuminated with a linearly polarized plane-wave through the SiO_2 , and the field was monitored at the Au/pDR1M interface.

Prior studies [33, 31] of pDR1M have indicated a conformational change that is sensitive to polarization. For example, it has been shown that this resist swells in regions of high intensity for longitudinal polarizations [55, 56]. However, as previously discussed, the polymer has been observed to shift away from regions of high intensity for transverse polarizations [65]. Accordingly, a linear superposition of field components must be considered to reproduce the observed resist topography.

Figure 3.7 shows the simulated, time-averaged field profile of the circular corral. For reference, the experimental AFM image is also included. Sound agreement between the simulations and the printed resist topography is found for field components summed as $-|E_x|^2 - |E_y|^2 + |E_z|^2$. Consistent with previous research [33], the resist topography is directly proportional to longitudinal field components but is related to the negative value of the transverse components. Notice that regions along the diagonal are characterized by pronounced resist topography, despite lower simulated fields in these regions. We speculate that high transverse fields may result in resist overexposure, effectively enhancing the contrast of adjacent regions. Nevertheless, the qualitative agreement between the simulations and experiments is remarkable. In particular, the simulations reproduce the plasmon wavelength observed in experiments to within 5%.

Figure 3.8 shows the simulated, time-averaged field profile of the elliptical resonator. Again, the experimental AFM scan is shown for reference. Here, the elliptical groove was modeled as 32 discrete point grooves, each with a diameter 100 nm. This simulation geometry allowed for accurate reproduction of the fab-

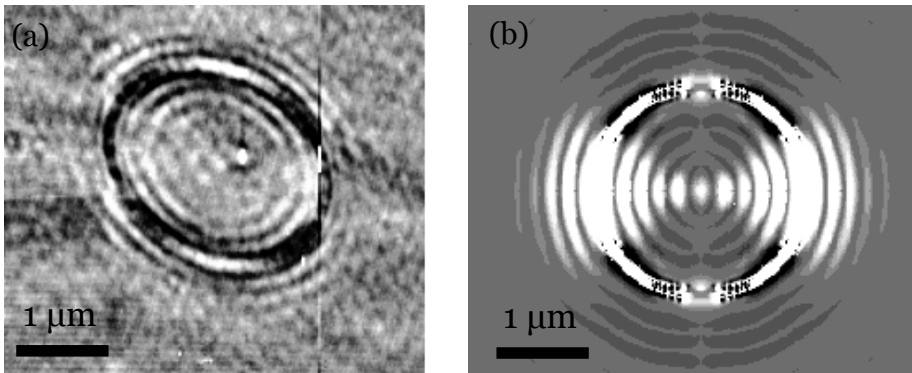


Figure 3.7. AFM scan (a) and FDTD simulation (b) of a circular corral. To reflect the polarization-sensitive conformations of the dye, the simulation plots a linear superposition of longitudinal and transverse field components.

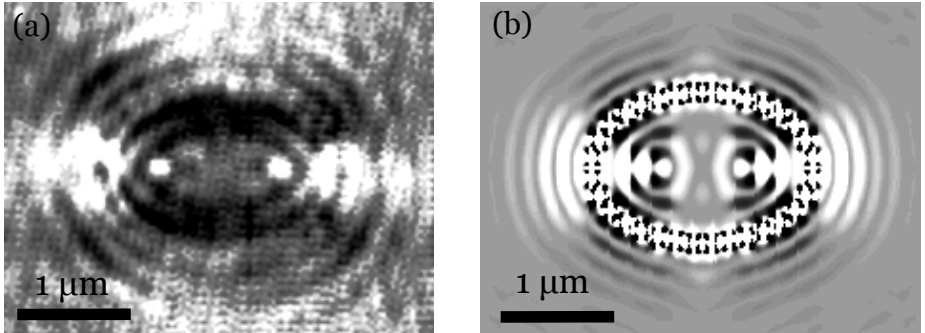


Figure 3.8. AFM scan (a) and FDTD simulation (b) of an elliptical resonator. To reflect the polarization-sensitive conformations of the dye, the simulation plots a linear superposition of longitudinal and transverse field components. To reproduce the fabricated ellipse eccentricity and groove width, the elliptical groove was simulated as 32 discrete point grooves, each with a diameter 100 nm. As seen, the simulations accurately reproduce both the propagating plasmon wavelength outside the ellipse and the standing wave pattern within the ellipse.

ricated ellipse eccentricity and groove width. Though not completely commensurate with the continuous groove, such ‘discrete point’ simulations should provide a first-order approximation to the experimentally-observed fields. As seen in the figure, the simulations exhibit remarkable agreement with the observed resist topography. In particular, the simulations reproduce the propagating plasmon wavelength outside the ellipse and the standing wave pattern within the ellipse. Most notably, both simulations and experiments reveal local plasmon fields confined to spatial regions as small as 50 nm around the foci, corresponding to one-tenth of the free-space wavelength used for excitation. These results represent some of the highest resolution near-field scans of plasmonic geometries to date.

3.3 Chapter Summary

In this chapter, we have demonstrated techniques for exciting and probing plasmons along planar metal-dielectric interfaces. As seen in the first section, far-field spectroscopy can be used to monitor the evolution of grating-coupled plasmons. By varying both the grating vector and the input-output separation, the wavevector and decay of surface waves could be determined. Throughout visible wavelengths, plasmon propagation was observed over tens of microns, consistent with the theory presented in Chapter 2. The second section demonstrated that even a single, shallow groove can serve as an efficient source of surface plasmons in-plane. By launching plasmons along a metal-polymer interface, we could imprint plasmon intensity with near molecular-scale resolution. Combined, near- and far-field microscopy provide the tools for fully characterizing any plasmonic geometry. In the following chapters, we will use these techniques to accurately map dispersion and propagation in rather unusual planar geometries, includ-

ing passive and active plasmonic devices, and also in negative refractive index metamaterials.

4 Experimental Imaging of Surface Plasmons, Part II: The Metal-Insulator-Metal Waveguide

‘Our imagination is stretched to the utmost, not, as in fiction, to imagine things which are not really there, but just to comprehend those things which are there.’

-Richard Feynman

4.1 Plasmonic waveguides for optoelectronic networking

The development of integrated optoelectronics is challenged by the size mismatch between photonic and electronic components. While optical interconnects exhibit a large bandwidth for signal transport, the minimum feature sizes of dielectric components are limited by diffraction. As we have seen in the last two chapters, this diffraction limit can be significantly reduced using surface plasmons. Their wavelength is shorter than that of light, and their modal fields are confined close to the metal surface. Consequently, plasmonic waveguides could be used to interface between wavelength and subwavelength-scale device components in an integrated optoelectronic network [97, 106]. However, such plasmonic interconnects will need to balance long range propagation with high field confinement. Indeed, the modern revolution in computation and information processing was facilitated by ultra-large-scale integration of electronic devices. Very likely, optical components will require the same level of integration to compete with electronic networks.

The metallic core waveguides discussed in Chapter 3 provide for long-range propagation and relatively straightforward coupling between free-space and waveguided modes. However, because of their ‘open’ nature, a considerable fraction of the waveguided mode penetrates into the surrounding dielectric. The large skin depths associated with long-range plasmon propagation are a considerable detriment to dense plasmonic waveguide integration.

As we saw in Chapter 2, inverting this geometry to a ‘closed’ configuration, such as the planar metal-insulator-metal (MIM) waveguide, provides a more favorable balance between propagation and localization. Operating in the optical regime, MIM waveguides can support both transverse electric (TE) and transverse magnetic (TM) photonic polarizations for which the mode momentum is strictly less than the photon momentum (i.e., the propagation constant $\beta = |\text{Real}\{k_x\}|$ obeys $\beta \leq n_d k_0$, where n is the core refractive index and k_0 is the free-space wavevector) [38]. However, MIM, or metallic slot waveguides can also support coupled surface plasmon (SP) modes across each metal-dielectric interface [38, 178]. Like the surface plasmon modes of metallic core waveguides, MIM plasmons are characterized by short wavelengths and high

interface energy densities that ‘squeeze’ photonic modes into subwavelength volumes [121, 153, 167, 13, 37]. Unlike metallic core waveguides, however, the skin depth of surface plasmons in MIM waveguides remains constant in the metallic cladding, even for deeply subwavelength cavities excited far from resonance. Both photonic and plasmonic modes populate the dispersion diagram of MIM geometries, and propagation is calculated to occur over many microns from visible through near-infrared wavelengths [38].

MIM waveguides promise potential for nanophotonic loss-localization balance, but fabricating, coupling to, and characterizing this geometry has proven elusive. Indeed, the very metallic cladding that keeps fields confined within the core challenges the experimentalists’ ability to access and probe these fields. In this chapter, we present the first experimental demonstration of MIM waveguides and wires. Using a combination of far-field detection and near-field interferometry, we directly access the complex propagation constant, determining both the wavelength and propagation length of MIM modes. Attention is given to slab and rectangular waveguides with a Si_3N_4 core and Ag cladding; core thicknesses of 50 - 100 nm and widths of 250 nm - 10 μm are explored. Within these waveguides, we find that mode wavelengths are shortened to values as small as 156 nm for a free-space wavelength of $\lambda=532$ nm. Additionally, propagation lengths of 5λ are achieved with light confined to transverse and lateral dimensions of $\lambda/5$ and $\lambda/2$, respectively.

4.2 Far-field excitation and detection

Chapter 3 introduced far-field techniques for imaging surface plasmon propagation using slit and grating coupling. In this section, we apply similar techniques to map the wavelength and decay of MIM-based modes. Since MIM waveguides are characterized by metallic layers to either side of the dielectric core, in- and out-coupling slits are patterned through each metallic layer. By developing a novel, automated fabrication scheme for dual-sided patterning of waveguides, we can image MIM mode propagation devoid of any parasitic background signal.

Figure 4.1 illustrates the process we developed to fabricate these slot structures. First, a 150-nm- or 300-nm-thick layer of Ag was deposited on one side of a free-standing Si_3N_4 membrane. Using focused ion-beam milling, rectangular wire waveguides were defined by pairs of 1- μm -wide L-grooves etched completely through the membrane to the Ag (see Figure 4.1); the nitride remaining between each groove comprised the wire core. Core widths w were varied between 250 nm and 5 μm and track lengths d were varied from 1 μm to 7 μm in 500 nm increments. The exposed nitride was then coated with Ag to create a rectangular $\text{Si}_3\text{N}_4/\text{Ag}$ slot wire.

Narrow slits (400 nm x 10 μm) milled through each Ag film to the nitride were used to couple light into and out of the waveguide. The slits were placed approximately 1 μm to either end of the nitride track; the vertical arm of the L-groove ensured that light observed from the output was due only to transmission through the finite width track. Input and output slits were also defined over areas with no nitride patterning, in order to investigate waveguide properties

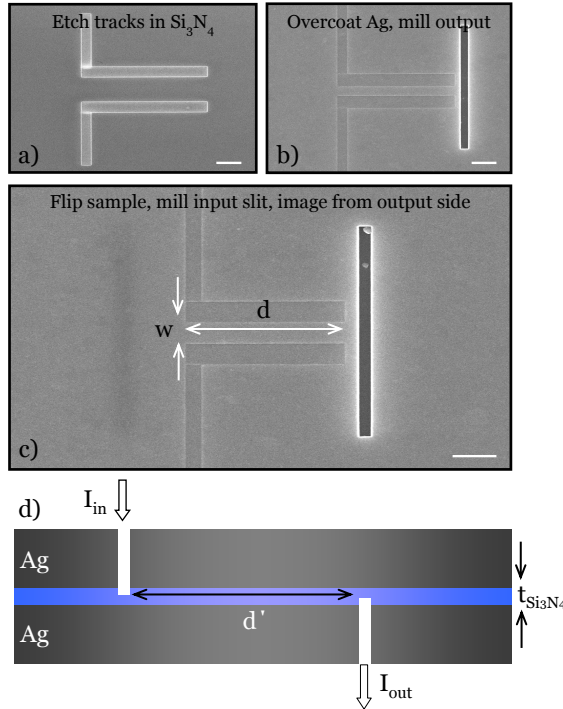


Figure 4.1. MIM waveguide fabrication sequence and experimental schematic. **(a, b, c)** Scanning micrographs at each phase of fabrication. **(a)** Ag is evaporated on one side of a suspended Si_3N_4 membrane before focused ion beam milling is used to define the waveguide core (the nitride remaining between the tracks). **(b)** The exposed nitride is then coated with Ag and the output slit is milled. **(c)** The sample is flipped and the input slit is milled. Waveguides are imaged from the output side using 30 keV electrons that reveal (from left to right) a shadow of the input slit, the contour of the finite-width waveguide, and the output slit. In each panel, the scale bar is $1 \mu\text{m}$. **(d)** Light is coupled into and out of the waveguide via the subwavelength slits, and waveguide transmission is imaged from the output slit using darkfield microscopy.

in slab waveguiding structures. The dual-sided coupling geometry permitted us to image waveguide output in a dark-field transmission configuration with an extremely high signal-to-noise ratio.

Far-field illumination and detection techniques were used to determine waveguide spectral properties and propagation lengths. Input slits were illuminated with either a lamp or laser source, using both polarized and unpolarized excitation. Light emerging from the output slits was collected with a 50x, 0.45 N.A. microscope objective and dispersed with a grating spectrometer onto a cooled CCD camera.

4.2.1 Slab waveguides

Figure 4.2 illustrates the spectra obtained from two-dimensional slab waveguides with Ag / Si₃N₄ / Ag thicknesses of 150 nm / 50 nm / 150 nm (a) and 300 nm / 100 nm / 300 nm (b). Input slits were illuminated with an unpolarized W lamp source, and input-output distances d' were varied from 2-15 μm . To isolate waveguide transmission features, all spectra were normalized with respect to the reference spectrum of the lamp. As seen in Figure 4.2a, the waveguides with 50-nm-thick nitride cores exhibit broadband spectral transmission characteristics. The observed transmission is consistent with the dispersion calculations of Figure 4.2d, which predict the existence of a single propagating mode throughout optical and infrared wavelengths. In particular, 50-nm-core MIM waveguides support a propagating TM mode where the tangential electric field is antisymmetric with respect to the waveguide median ¹. The predicted momentum β of this mode exceeds the free-space momentum of a photon in Figure 4.2, so that light is transported from input to output via interacting surface plasmons.

Figure 4.2a also reveals that the 50-nm-core waveguide spectra display intensity oscillations, the result of wave interference that can be used to confirm the predicted dispersion [52]. While the 150-nm-thick Ag cladding is sufficient to ensure a well-defined mode within the waveguide core, it is thin enough to allow for partial transmission of the source illumination (field intensity E_0). At the output slit, the field transmitted by the waveguide (amplitude $E_t \sim T_w(\lambda)E_0$, where $T_w(\lambda)$ is the transmission coefficient of the waveguide) interferes with the field directly transmitted through the Ag (amplitude $E_p \sim T_p E_0$, where T_p is the transmission coefficient of the Ag film). The observed far-field intensity distribution is then proportional to $E_0^2(T_p + T_w(\lambda) \cdot \cos(n_{\text{eff}}k_0 d'))^2$, where n_{eff} is the effective index of the waveguide. For wavelengths between 600 nm and 900 nm, the fitting parameter n_{eff} is determined to vary between 3.45 and 2.85, slightly higher than the theoretical range $3.35 \geq n_{\text{eff}} \geq 2.25$ derived from Figure 4.2d. Such indices are substantially higher than the refractive index of the nitride ($n \sim 2.04$) and correspond to plasmon wavelengths as small as $\lambda_{SP} = 174$ nm for $\lambda = 600$ nm excitation.

As core thickness is increased, planar slab waveguides are predicted to support both plasmonic and photonic-type modes [38]. Figure 4.2b plots the spectra for slab waveguides with 100-nm-thick nitride cores for variable d' . To prevent interference between the incident beam and the transmitted signal, these waveguides were fabricated with an optically-opaque, 300 nm Ag cladding on each side of the Si₃N₄. In contrast with the 50-nm-thick-core waveguides, increased spectral modulation between visible and near-infrared wavelengths can be discerned. Peak transmission occurs for wavelengths between 650 nm and 750 nm, but comparable transmission efficiencies can also be observed for wavelengths less than 570 nm. The theoretical dispersion curves of Figure 4.2d suggest that these features result from multimode transmission characteristics. For wavelengths exceeding ~ 600 nm, dispersion is comparable to that of the 50-nm-core

¹Note that a field-symmetric TM mode also exists in 50-nm-core waveguides, but this mode is highly damped below the surface plasmon resonance. See Reference [38] and Chapter 2 for details.

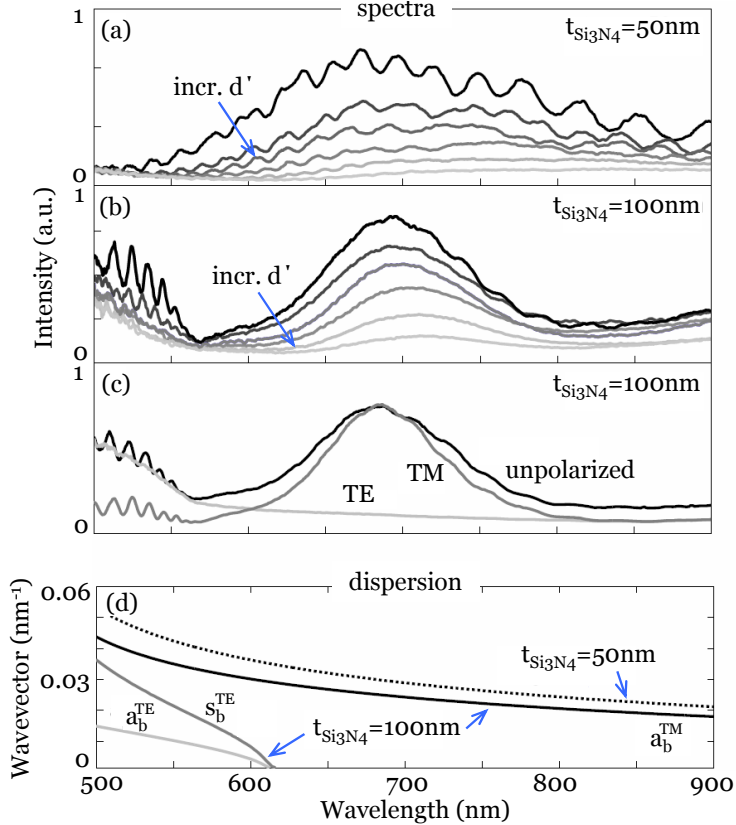


Figure 4.2. Experimental spectra **(a, b, c)** and theoretical dispersion diagrams **(d)** for two-dimensional slab waveguides with nitride core thicknesses of $t = 50$ nm **(a)** and 100 nm **(b, c)**. In **(a)** and **(b)**, spectra from an unpolarized lamp source are plotted for input output slit separations $d' = 2, 3, 4, 5, 7,$ and $8 \mu\text{m}$; the arrow indicates the trend of increasing d' . Polarization-dependent measurements **(c)**, shown here for $d' = 2 \mu\text{m}$, confirm the presence of both TE and TM modes in the 100-nm -thick-core waveguides. Theoretical dispersion curves **(d)** indicate the existence of both photonic and plasmonic waveguiding modes, depending on core thickness (dotted line: $t = 50$ nm; solid lines, $t = 100$ nm). Dispersion is only plotted for propagating modes.

slot waveguides, and only a coupled surface plasmon mode is supported. However, as wavelengths are decreased, the waveguide can also support conventional transverse-electric (TE) photonic modes.

The predicted multimode behavior of 100-nm -core slab waveguides is confirmed by polarization-dependent measurements (see Figure 4.2c). While TE polarized light is responsible for the transmission window at shorter wavelengths, TM polarized light is transmitted for all wavelengths. Interestingly, the oscillations observed in the unpolarized spectra of Figure 4.2b disappear for TE excita-

tion but remain for TM excitation. Such results suggest that the low-wavelength spectral oscillations are not interference between TE and TM-supported modes² but a manifestation of TM Fabry-Perot resonances, perhaps similar to those observed by Miyazaki *et al.* [98].

Mode propagation, defined as a 1/e decay length, can be derived from the dependence of spectral transmission on input-output slit separation. Figure 4.3 plots experimentally-determined propagation lengths as a function of wavelength for waveguides with core thicknesses of both 50 and 100 nm. As seen, propagation length increases with increasing wavelength. At the longest explored wavelength of $\lambda = 840$ nm, propagation reaches 3 and 6 μm for 50- and 100-nm-core slot waveguides, respectively. Figure 4.3 also plots the calculated propagation lengths of the SP mode predicted for these structures (see Figure 4.2d). The magnitude and trend of the predictions are in good agreement with the experimentally-determined values, confirming the SP nature of the mode.

Still, it may be noted that the theoretical calculations of Figure 4.3 lie slightly below the experimentally-determined values. This mismatch likely results from the sensitive dependence of propagation calculations on the complex permittivity of the Ag. While our calculations use an Ag dielectric function derived from ellipsometry measurements on the exterior Ag surface, the optical quality of this interface is inferior to that of the Ag / Si₃N₄ interface experienced by the waveguide mode. As a result, the model will underestimate the actual propagation length. The protection of critical metal/dielectric interfaces from environmental influences is a key attribute of MIM waveguides and ensures consistent and stable device performance with time.

To confirm the wavelength-dependent propagation obtained with the single slit spectra, propagation measurements were repeated on MIM waveguides with grating inputs and outputs. Unlike a single slit - which diffracts all wavevector components equally - a grating input generates a wavepacket with a well defined momentum spread about the grating vector [121, 130, 175, 34]. Gratings were defined with a 50% duty cycle and pitch of 640 nm - 780 nm in 20 nm increments. Figure 4.4 shows the output spectra for input grating periods of 640 nm and 780 nm; for reference, the spectra for the single slit input are also included. For this data, a single slit was used to outcouple light from the waveguide. As expected, the grating input enhances the transmission of certain wavelength while suppressing others; interestingly, the observed minima in transmission is red-shifted by ~ 70 nm with respect to the grating pitch. Computing a 1/e decay length based on this data, propagation trends agree with those observed in Figure 4.3. However, depending on the wavelength, propagation lengths determined from the grating inputs did lie 5%-15% below the theoretical predictions (data not shown).

Replacing the output slit with an output grating did not change the observed spectra. Notably, far-field measurements indicate that emission from the output grating is exclusively confined to the first slit of the 5-slit grating (see upper panels of Figure 4.4). These results suggest that plasmonic-modes within

²Cross-polarization of the input and output indicate that the waveguides are indeed polarization-maintaining.

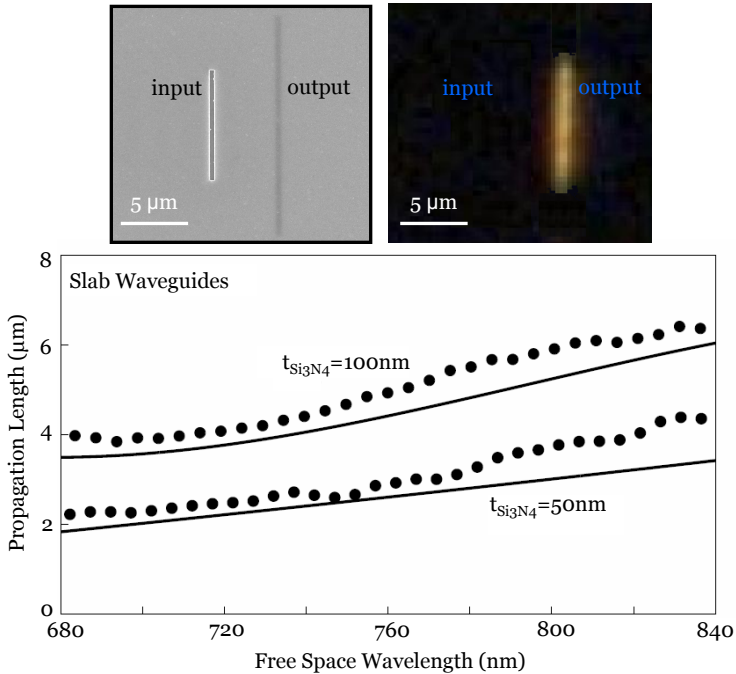


Figure 4.3. Two-dimensional slot waveguide transmission and decay characteristics, using single slit inputs and outputs. Upper panels: Scanning electron micrograph and transmission image of a representative MIM slab waveguide. Transmission and reflected-mode microscopy techniques were used to simultaneously image the waveguide output and the geometry of the slit. Waveguide output remains confined to the length of the input slit. Lower panel: Propagation lengths of two-dimensional slab waveguides with core thicknesses $t = 50$ nm and 100 nm, plotted as a function of wavelength (dots, experiment; solid line, theory; the dot diameter encompasses the error).

nanometer-scale slot waveguides are readily converted to free-space modes. In fact, on a per-slit basis, the grating input is actually 1.5 times less efficient than a single slit, as indicated by the spectral intensities of Figure 4.4. Heuristically, when grating-coupling to a slot-waveguide mode, incident light is more likely to escape from a neighboring slit than remain within the core. MIM waveguides thus provide a foundational design for steering subwavelength-confined light around sharp corners and bends.

4.2.2 Finite width waveguides (i.e., MIM ‘wires’)

The spectra and propagation results of Figures 4.2, 4.3, and 4.4 indicate that slab waveguides do not exhibit cutoff for any core thickness or wavelength. This property is consistent with slab waveguide operation in the limit of a perfectly conducting cladding, with one important distinction: While the photonic TM_0 mode dominates for perfect-conducting slot waveguides, plasmonic modes are

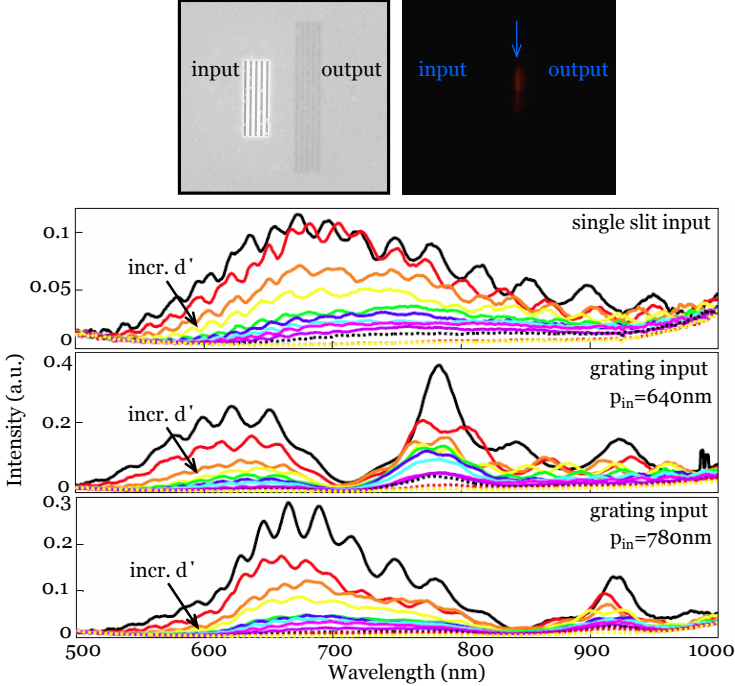


Figure 4.4. MIM slab waveguide transmission and decay characteristics, using grating inputs and outputs. Upper panels: Scanning electron micrograph and transmission image of a representative MIM slab waveguide. Despite the use of a grating output, transmitted light is predominately filtered through the first slit of the output grating. Lower panels: MIM spectra obtained with slit or grating inputs and single slit outputs. The input-output separation is varied from 1 to 8 μm in 500 nm steps.

primarily responsible for wave propagation in ‘real’ subwavelength metallic slot waveguides [38]. Indeed, for visible and near infrared wavelengths, the E_x field antisymmetric (H_y field symmetric) TM SP mode suffers the least dissipation. Among photonic modes, TE modes are only allowed at lower wavelengths (see Figures 4.2); the E_x field symmetric (H_y field antisymmetric) TM mode is also always allowed, but is highly damped below the SP resonance due to absorption [38].

The introduction of side-walls to a slab waveguide is expected to induce cutoff. In the limit of a perfectly-conducting cladding, rectangular waveguides exhibit cutoff for wavelengths $\lambda \geq \lambda_c = \frac{2n}{\sqrt{(m/w)^2 + (p/t)^2}}$, where n is the core refractive index, w and t are the waveguide widths and thicknesses, respectively, and m and p are integers describing the mode order. For a perfect-conducting slot wire, the TE_{10} mode exhibits the lowest attenuation and suffers cutoff for waveguide widths $w < \lambda/2n$; in contrast to slab waveguides, TM_{11} is the lowest possible TM mode. When absorption and field penetration in the metal are included, the presence of plasmonic TM modes may impact the onset of cutoff.

Figure 4.5 illustrates the transmission characteristics of finite width MIM ‘wires’ with a rectangular Si_3N_4 core and an Ag cladding on all sidewalls. The nitride thickness was set to $t = 100$ nm, and waveguide widths of $w = 250$ nm, 500 nm, 750 nm, 1 μm , 2.5 μm , and 5 μm were considered. Propagation was investigated for wavelengths in both the TE and TM regimes of the slab waveguide spectra: at $\lambda = 514$ nm using Ar laser excitation and at $\lambda = 685$ nm using a diode laser. Note that the spectral characteristics of slab waveguides are preserved for finite-width waveguides down to $w = 1$ μm , the smallest waveguide width exhibiting detectable lamp transmission.

Figure 4.5a-c plots intensity as a function of total input-output separation for slab and wire geometries at $\lambda = 514$ nm. Results are qualitatively similar for excitation at 685 nm. Intensities have been linearly normalized to account for the various waveguide widths. Slab waveguide intensities, plotted in Figure 4.5a, exhibit a well-defined exponential decay. As waveguide width is reduced (Figures 4.5b,c), intensity oscillations arise that are equally pronounced for both wide and narrow waveguides. Such oscillations occur for all explored finite-width waveguides, and reflect both the non-adiabatic coupling geometry and wave interference between the various Ag / Si_3N_4 interfaces. Despite signal oscillations, wire waveguide emission is well characterized by an exponentially-decaying envelope that can be used to determine propagation length.

Figure 4.5d illustrates propagation length as a function of waveguide width for excitation wavelengths of $\lambda = 514$ nm and $\lambda = 685$ nm. The measured intensities have been corrected to account for the planar waveguide regions at the entrance and exit of the wire, so that all decay lengths represent propagation within the finite-width track. At $\lambda = 514$ nm, experimentally-determined decay length for the slab waveguides is approximately 1.7 μm . Propagation distance decreases with decreasing width, but waveguides as narrow as $w = 250$ nm (with $t = 100$ nm) still sustain propagation over distance of 1.25 μm . Notably, a 75% decrease in waveguide width only decreases propagation by about 20%. Similar trends are observed at $\lambda = 685$ nm, where reduced material absorption enhances propagation lengths to 3 - 4 μm . The minimal dependence of propagation length on slot waveguide width is in contrast with metallic-core SP waveguides, where propagation is substantially reduced by the introduction of sidewalls [78].

The decay lengths observed in wire waveguides exhibit sound agreement with the propagation lengths predicted for slab waveguides. At 514 nm - a wavelength expected to excite predominantly TE photonic modes - slab decay lengths are predicted to be ~ 2.5 μm for the TE mode and only ~ 0.5 μm for the TM SP mode. Likewise, at 685 nm - a wavelength expected to excite a predominately TM plasmonic mode - surface plasmon decay lengths are predicted to be ~ 4 μm . This agreement suggests that mode distribution may not undergo significant transformation as slot-wire width is reduced.

Interestingly, waveguide transmission at $\lambda = 514$ nm could be observed down to the smallest explored waveguide widths. Such results are consistent with expectations for slot wires with a perfectly-conducting cladding, where the TE_{10} mode does not exhibit cutoff for any wire width. In contrast, at $\lambda = 685$ nm, transmission from the 250-nm-wide wires could not be detected. This result suggests that TM modes are not exempt from cutoff, consistent with TM mode

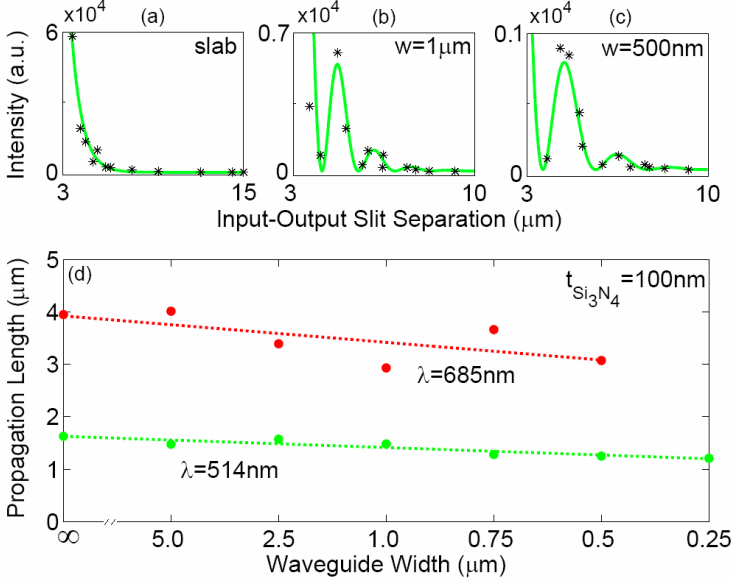


Figure 4.5. Output intensities and propagation lengths of three-dimensional slot wires (finite core thickness $t = 100 \text{ nm}$ and width $w = 5 \mu\text{m}$, $2.5 \mu\text{m}$, $1 \mu\text{m}$, 750 nm , 500 nm , and 250 nm). **(a, b, c)**: Decay at $\lambda = 514 \text{ nm}$ is purely exponential with distance for the slab waveguide **(a)**, but oscillations arise as waveguide width is reduced **(b, $w = 1 \mu\text{m}$ and c, $w = 500 \text{ nm}$)**. Points represent the measured data, while the lines are least-squared fits. Results are qualitatively similar for excitation at $\lambda = 685 \text{ nm}$. **(d)**: Propagation length at $\lambda = 514 \text{ nm}$ and $\lambda = 685 \text{ nm}$ as a function of waveguide width (the dot diameter encompasses the error). Propagation was extracted from the exponential envelope of the intensity distributions. “Infinite” width corresponds to a slab waveguide. No emission could be observed from the 250-nm -wide waveguides under 685 nm excitation, potentially indicating the onset of cutoff.

behavior in the limit of a perfectly conducting cladding. Indeed, for a waveguide of width $w = 500 \text{ nm}$, TM modes within a perfectly-conducting cladding only exist for wavelengths $\lambda < \lambda_c = 400 \text{ nm}$. (In fact, for excitation at 685 nm , waveguides with a perfectly-conducting cladding exhibit TM mode cutoff for all finite width waveguides.) However, our MIM ‘wires’ transport 685 nm light without significant attenuation for structures no wider than $w = 500 \text{ nm}$. By exploiting plasmonic modes in subwavelength slot wires, cutoff wavelengths can be beat by $\sim 300 \text{ nm}$.

Calculations indicate that slot wires support field skin depths no larger than 20 nm [38]. Thus, at $\lambda = 514 \text{ nm}$, slot waveguides propagate optical signals over a distance of $\sim 2.5\lambda$ with fields confined to modal dimensions of approximately $0.3\lambda \times 0.5\lambda$. Longer-wavelength excitation improves this loss-localization ratio: for excitation at $\lambda = 685 \text{ nm}$, optical signals are propagated over distances exceeding 4.5λ with light confined to cross-sectional dimensions of approximately

$0.2\lambda \times 0.5\lambda$.

As illustrated by these far-field measurements, metallic slot waveguides exhibit the fairly low attenuation and extremely high mode confinement essential for optoelectronic integration. Without compromising mode localization, losses may be further reduced by using a lower-index dielectric core. A 100-nm-thick Ag/SiO₂/Ag slab waveguide, for example, is predicted to sustain optical signal propagation as far as 35 μm at $\lambda = 840 \text{ nm}$ [38], and comparable propagation lengths are expected for finite-width wires. When used in conjunction with channel plasmon waveguides [23, 24] and semiconductor slot waveguides [5, 125], these metallic slot waveguides could facilitate development of ultradense intrachip integrated networks - ultimately, enabling realization of a photonic analogue to present silicon-on-insulator electronic networks.

4.3 Near-field imaging with scanning optical microscopy

As demonstrated in the last section, the modes of MIM geometries allow for optical waveguiding in deeply subwavelength structures. Beyond signal transfer, MIM geometries may also impact the transmission, refraction, switching, and storage of light on subwavelength scales. Indeed, MIM-SPPs are responsible for the resonances in slits in metal films that lead to large field enhancements and large resonant transmission [120]. Moreover, MIM-based geometries have been proposed as novel nanoscale cavities and resonators [98, 91, 117], interferometers [24], and metamaterials [134, 139, 83].

In order to study these waves experimentally and develop new nanostructured components to manipulate them, it is crucial to image their fields at the highest possible resolution.³ However, because of the presence of the metal cladding, it is inherently difficult to gain direct access to the near field of these modes. So far, experiments have been limited to spectral analysis of the far field reflection and transmission of finite length waveguides and cavities[36, 98].

In this section, we present the first near-field imaging and analysis of MIM-SPPs. By reducing the thickness of one of the metallic cladding layers of the slot waveguide, tunneling of light from a near-field probe to the highly confined SPP mode is allowed without negatively affecting the interesting properties associated with these waves. Using light scattered from subwavelength slits into the far field, interferometric measurements are performed that provide accurate *in situ* determination of the wave vector of SPP modes guided either in the MIM slot or in the air outside the sample. Excellent correspondence with calculated dispersion is obtained for frequencies from the blue to the near-infrared. The smallest observed MIM-SPP wavelength is 156 nm, measured at a free-space wavelength of 532 nm.

A sketch of the experimental geometry is shown in Figure 4.6a. The sample consists of a 50 nm thick suspended Si₃N₄ membrane, coated on both sides with Ag by thermal evaporation. This design results in small interface roughness determined by the smoothness of the Si₃N₄, which limits scattering losses. The

³This section, including text and figure content, has been adopted from E. Verhagen, J. A. Dionne, *et al.* Reference [163].

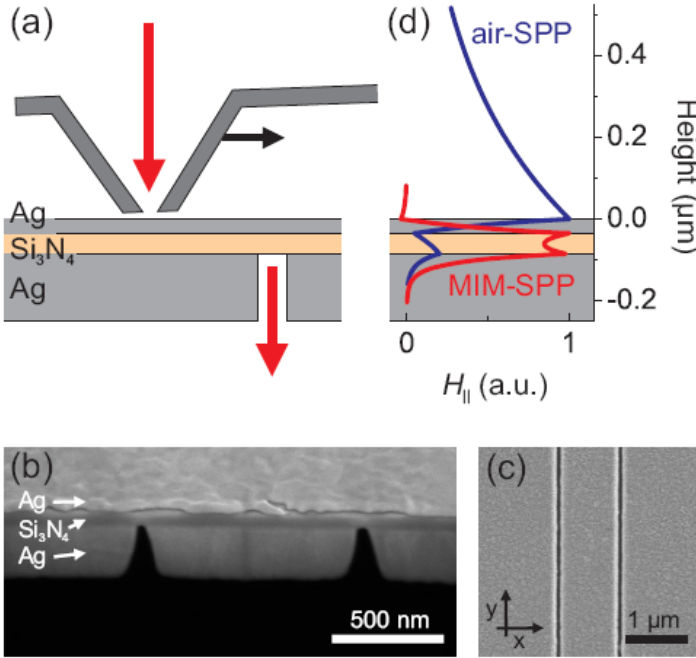


Figure 4.6. **(a)** Schematic depiction of the measurement geometry. Laser light is incident through the aperture of an Al near-field probe, which is scanned with respect to the sample. Light transported through the MIM waveguide is collected after scattering from subwavelength slits in the back Ag film. **(b, c)** SEM micrographs of the fabricated waveguide, shown in cross-section **(b)** and as viewed from the bottom **(c)**. The waveguide consists of 50 nm of Si₃N₄ clad with 35 nm Ag on the top and 310 nm Ag on the bottom. **(d)** H field mode profiles of the two waveguided SPP modes supported by the multilayer stack.

Ag thickness on the front side of the sample is only 35 nm to allow for near-field coupling of a probe outside the sample to the dielectric core of the waveguide. The near-field probe is a hollow Al pyramid on a Si cantilever, with a tip aperture that has a diameter smaller than 100 nm (WITec GmbH). The thickness of the Al sidewalls of the probe is ~ 150 nm. Light from various laser sources is incident through the tip, which is brought into contact with the sample. The Ag film on the back of the membrane is 310 nm thick. Slits with widths smaller than 100 nm and lengths of $5 \mu\text{m}$ were made in the back Ag film by focused ion beam milling. Care was taken to stop the milling once the Si₃N₄ layer was exposed. Both single slits and pairs of slits aligned parallel to each other with various separations were fabricated. Figure 4.6b and c show an SEM micrograph and cross section of a typical structure with two slits spaced $1 \mu\text{m}$ apart. The slits serve to scatter SPPs to the far field at the back side of the sample. The scattered radiation is collected by a 50x microscope objective ($\text{NA} = 0.7$) and focused on a $100 \mu\text{m}$ core diameter multimode optical fiber that is led to an APD detector. Two-

dimensional near-field images are obtained by scanning the piezo-electrically driven sample stage together with the collection objective relative to the near-field tip. In effect, this amounts to scanning the local SPP excitation source (the tip), while monitoring the output from one or two fixed exit slits. From polarization measurements of the tip emission in the far field and from near-field scans across circular slits (see Figure 4.7), we determined that the tip acts as a highly polarized excitation source, and therefore as a highly directional source of SPPs. Throughout the measurements, the sample orientation is kept such that the slits are oriented normal to the dominant direction of SPP excitation.

We first consider the results for a single output slit. Figure 4.8a shows a near-field intensity image taken with 638 nm excitation light. The slit is located in the middle of the scan area and oriented in the vertical direction. Three observations can be readily made. First, the signal is highly modulated, with a period of 300 nm. Such modulations were not observed in near-field experiments on single metal films without the presence of the MIM waveguide [143, 76]. Second, the signal decays as the excitation source is moved away from the output slit. Third, the image is clearly asymmetric with respect to the slit, a fact that appears surprising at first sight considering the symmetry of the measurement geometry.

As we will show, all three observations can be explained by a single model. In the sample geometry that includes the thinned Ag cladding layer, two orthogonal waveguided SPP modes can propagate. These are both hybridized modes arising from the coupling of SPPs on the three metal/dielectric interfaces: the MIM-SPP mode localized predominantly in the Si_3N_4 layer, and a mode that resides mostly in the air outside the sample (termed ‘air-SPP’ from here on). Figure 4.6d shows the magnetic field profiles of both modes at a free-space wavelength of 638 nm, calculated by finding the poles of the transfer matrix for the layered sample. The optical constants of Ag are taken from reference [69]. Arguably, both modes can be excited by the near-field tip, albeit with different excitation probabilities. Both modes also have a fraction of their energy inside the Si_3N_4 layer, where

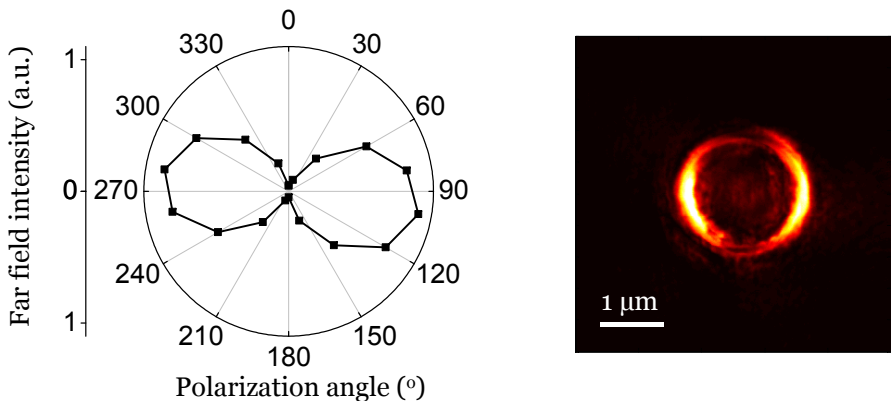


Figure 4.7. Far-field tip emission and near-field scans across a circular slit, illustrating that near-field probes act as highly polarized excitation sources.

they can be scattered by the subwavelength slit to the detector. Because the two modes have a clearly different wave vector, they interfere to produce the oscillating pattern with varying tip-slit distance that is seen in Figure 4.8a. As a first approximation, the field at the slit as a function of tip distance x can be described in a one-dimensional scalar model as $E(x) = c_{air}e^{ik_{air}x} + c_{mim}e^{ik_{mim}x}$ (assuming implicit time-harmonic), where k_{air} and k_{mim} are the complex wave vectors $k=k'+ik''$ of the air-SPP and MIM-SPP modes, respectively. The coefficients c_{air} and c_{mim} include the amplitude and phase with which each mode is excited (normalized at the depth of the output slit). The intensity then becomes

$$I(x) = |c_{air}|^2 e^{-2k''_{air}x} + |c_{mim}|^2 e^{-2k''_{mim}x} + 2|c_{air}||c_{mim}|e^{-(k''_{air}+k''_{mim})x} \cos[(k'_{mim} - k'_{air})x + \Delta\phi], \quad (4.1)$$

where $\Delta\phi$ is the phase difference with which the two modes are excited by the tip.

Figure 4.8b shows the intensity as a function of distance from the slit, obtained by integrating the intensity in Figure 4.8a in the vertical direction. The blue curve is a nonlinear least-squares fit of equation (4.1) to the data, where the coefficients $|c_{air}|$ and $|c_{mim}|$ and the phase difference $\Delta\phi$ were allowed to differ on either side of the slit. The data within a distance of 200 nm from the slit was not fitted, since directly under the tip the field can not be described sufficiently in terms of two waveguided modes only. Figure 4.8b shows that the model fits the data very well. The oscillatory behavior is very well reproduced, and the decay with distance is identical on each side.

The asymmetry is a result of a difference between the amplitude coefficients at either side of the slit. To understand how the excitability of the modes at opposite sides of the slits can be so different, we performed finite-difference time-domain (FDTD) simulations of the geometry [2]. The geometry considered is sketched in the inset of Figure 4.8c. The structure is modeled to be invariant in one dimension. The mesh size is 1 nm in the vicinity of the sample. A p-polarized Gaussian beam with a free-space wavelength of 638 nm is incident through the tip. The output slit is absent in the simulations. The calculated electric field intensity at the bottom side of the Si_3N_4 layer is plotted in Figure 4.8c for two different separation heights between the tip and the sample. Assuming the slit acts as a point scatterer, the intensity in this plane can be directly related to the measured signal collected through the slit.

The calculations show interference patterns with a period and decay very similar to the experiment in Figure 4.8b. For the 10 nm tip-to-sample separation, the overall intensity is larger and the visibility of the fringes is smaller than for the 20 nm tip-to-sample separation. The differing intensities are a result of the fact that the Al sidewalls hinder the excitation of the air-SPP for small separations [60], whereas more power is coupled into the MIM-SPP. Although during the experiment the tip is in contact with the sample surface, small imperfections in the tip can easily result in different local separations between tip and sample at different sides of the tip. As a result, the asymmetries observed in Figure 4.8b for the interference pattern on either side of the slit can be ascribed

to a small asymmetry in the tip shape. Indeed, when performing experiments with different tips on the same sample, different asymmetries are obtained.

By fitting equation 4.1 to the data, the difference of the real part of the wave vectors of the two SPP modes is obtained. From the fit of equation 4.1 to the data, we find $\Delta k' = (k'_{mim} - k'_{air}) = 20.69 \mu\text{m}^{-1}$. This simple one-dimensional model neglects, however, the fact that the SPP waves excited by the near-field tip spread on the two-dimensional sample surface, and that SPPs emitted in different directions travel different distances to the output slit. To account for these effects, we can construct a two-dimensional model that assumes the tip acts as a polarized point source of SPPs as mentioned above, emitting a field

$$E(x) = (c_{air}e^{ik_{air}r} + c_{mim}e^{ik_{mim}r})\frac{\cos(\theta)}{\sqrt{r}}, \quad (4.2)$$

where r is the distance to the tip and θ is the angle with respect to the normal of the output slit. To predict the detected intensity as a function of the distance

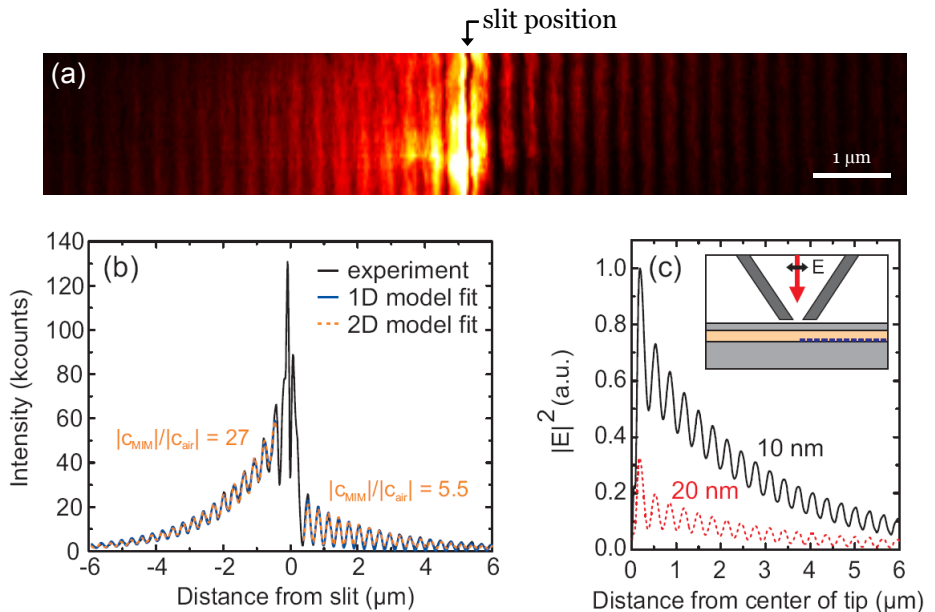


Figure 4.8. **(a)** Near-field image obtained by scanning the excitation tip position over the sample containing a single output slit. The excitation wavelength is 638 nm. **(b)** Collected intensity in **(a)** as a function of tip-slit distance (black curve), and a fit to the data of the one- and two-dimensional models described in the text (blue and orange curves, respectively). The ratio of the amplitudes of both modes in the 2D model is indicated. **(c)** Simulated electric field intensity in the Si_3N_4 film as a function of distance from the center of the tip. The inset shows a schematic of the simulated two-dimensional geometry. The dashed blue line indicates the position at which the calculated intensity is plotted. The tip-sample separation is 10 nm (black) or 20 nm (red).

x between tip and slit, the field distribution along the slit is obtained from equation 4.2. A scalar amplitude point spread function is subsequently used to calculate the field in the image plane of the microscope, and the intensity in this plane is integrated over the area of the fiber core. A resulting fit of this two-dimensional model to the data is shown in Figure 4.8b as an orange dashed curve. This model also fits the data very well, yielding $\Delta k' = 20.43 \mu\text{m}^{-1}$. The fitted propagation length $L=1/(2k')$ of the MIM-SPP mode is $1.4 \mu\text{m}$, which is smaller than the value of $2.6 \mu\text{m}$ obtained from the mode calculation. We ascribe this discrepancy to a deviation of the actual optical constants to those used in the calculation and additional scattering losses. The fact that the obtained value of $\Delta k'$ for the one-dimensional model is so close to that obtained with the two-dimensional model shows that fits of the simple one-dimensional model to the data yield accurate estimations of the real part of the wave vector. In the remaining analysis however, the more accurate two-dimensional model is used.

To determine absolute values of the wavelengths of both SPP modes in addition to the differential wave vector magnitude $\Delta k'$, we performed experiments on pairs of aligned slits separated by μm -scale distances. The collection objective is positioned such that light from both slits is collected. When the tip is scanned outside both slits, a similar interference pattern is expected as for the single slit. However, for a tip position between the two slits, a different interference mechanism comes into play, depicted in the inset of Figure 4.9a. Because the light originating from the two slits is allowed to interfere on the detection fiber, a change of the relative phase of the field at the two slits will alter the detected intensity. MIM-SPP waves excited between the slits in opposite directions will arrive at the two slits with a relative phase difference that depends on the position of the excitation source. Because the difference between the two path lengths scales linearly with twice the distance to one of the slits, an interference pattern with a period of half the MIM-SPP wavelength is expected as the tip scans between the slits. This double-slit geometry also produces an interference pattern with a period of half the air-SPP mode wavelength. However, the single slit experiments showed that the contribution of MIM-SPPs to the output signal is larger than that of air-SPPs. Accordingly, the pattern due to MIM-SPP interference can be discerned with respect to the air-SPP pattern, provided that the slit separation is not much larger than the MIM-SPP propagation length.

Figure 4.9a shows the measured near-field image for 638 nm excitation wavelength and a slit separation of $1 \mu\text{m}$. Between the slits an oscillatory pattern with a period of 102 nm is observed. This interference pattern is superimposed on the pattern that was also observed for the single slit, and that is also present outside the pair of slits.

Experiments for single slits and pairs of slits are repeated for various excitation wavelengths between 458 and 980 nm. Figure 4.9b shows an image taken with a pair of slits with a separation of $2 \mu\text{m}$ taken at 980 nm. Clearly an interference pattern is again observed between the slits, with a larger period than in Figure 4.9a. Because the interference patterns for single slit and double slit experiments provide independent measurements of k'_{mim} and $\Delta k'$ at each frequency, we can construct dispersion curves for both the MIM-SPP and the air-SPP mode. The results are plotted in Figure 4.10. The dispersion of light

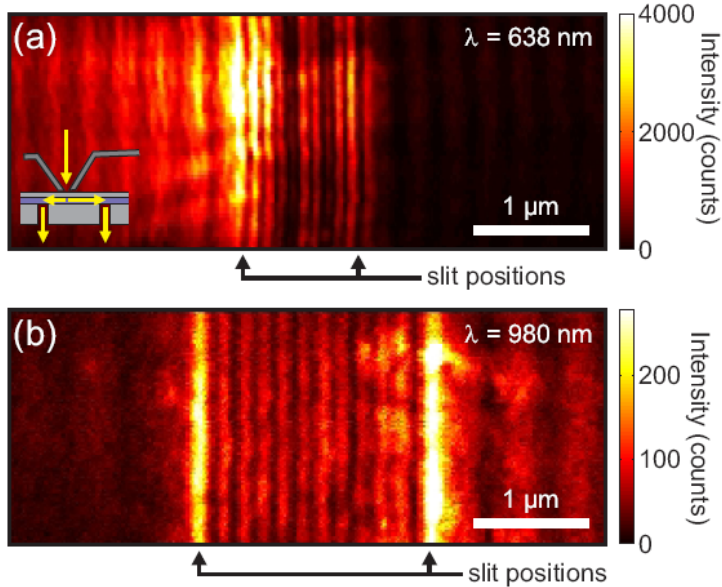


Figure 4.9. **(a)** Near-field image obtained by scanning the excitation tip position over the sample containing a pair of output slits separated by $1 \mu\text{m}$. Excitation wavelength is 638 nm . The inset shows the interference mechanism leading to the fast spatial intensity oscillations between the slit. **(b)** Same as **(a)**, for an excitation wavelength of 980 nm and a slit separation of $2 \mu\text{m}$.

in air and in Si_3N_4 is plotted for reference as dashed lines. For an excitation wavelength of 532 nm the measured MIM-SPP wavelength is 156 nm , corresponding to a wave vector that is 1.7 times larger than that of light in Si_3N_4 . In stark contrast, the dispersion of the air-SPP mode follows the light line in air closely. The solid curves are the calculated dispersion curves for both modes in the multilayer waveguide geometry. The experimentally-determined wave vectors correspond very well with these calculations. For wavelengths shorter than 532 nm it was not possible to accurately determine the value of k'_{mim} independently, because of limited resolution. For these excitation wavelengths, bars are denoted that show the measured magnitude of $\Delta k'$, which corresponds well with calculations up to the shortest used wavelength of 456 nm . This shows that the MIM-SPP mode can be probed with the near-field method throughout the visible and near-infrared frequency regimes. The propagation lengths are of the order of micrometers - long enough to perform interferometric measurements of wave vector differences.

4.4 Chapter Summary

In this chapter, we have demonstrated techniques for probing MIM waveguide modes. Despite the buried nature of these waves, our techniques yield full information about the complex propagation constant without significantly perturbing

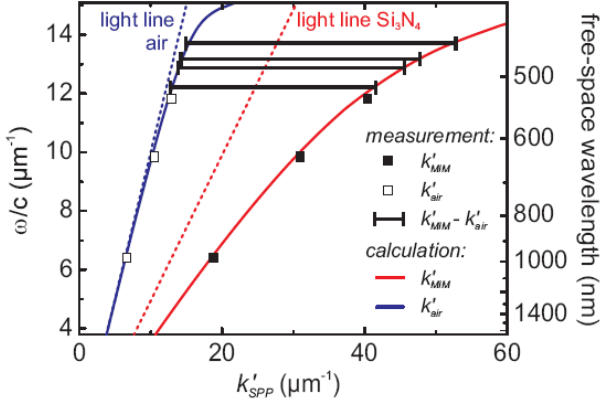


Figure 4.10. Dispersion relations of the two SPP modes that are supported by the system. Closed and open symbols indicate the measured values of k'_{mim} and k'_{air} , respectively. The length of the horizontal bars at high frequencies is equal to the experimentally-determined values of $(k'_{mim} - k'_{air})$. The solid blue and red lines are the calculated dispersion curves for the air and MIM-SPP modes, respectively.

the mode. Far-field measurements allowed for determination of the propagation length of both planar waveguide geometries and rectangular MIM ‘wires.’ Moreover, by thinning the top cladding of MIM waveguides, far-field interferometry allowed determination of the MIM mode wavelength. Direct imaging of MIM-SPPs with subwavelength resolution was achieved using a near-field probe. Interference of MIM-SPPs with air-SPP modes allowed the measurement of the local wave vector and determination of the relative contributions of both modes. Combined, these near- and far-field techniques provide the necessary tools for study of subwavelength components and devices based on MIM geometries. As we will see in the coming chapters, such geometries can serve as the building blocks for future highly integrated photonic circuits, and provide a wealth of opportunities based on their ultrasmall mode size and high local fields.

5 Plasmon-based Negative Index Materials

‘We have no right to assume that any physical laws exist, or if they have existed up to now, that they will continue to exist in a similar manner in the future.’

-Max Planck

5.1 Reversing Newton’s prism: The physics of negative index materials

As we have seen throughout this thesis, the properties of surface plasmons are inextricably tied to the dielectric constants of the host waveguide. For a given waveguide geometry, the number of modes, the propagation constant, and the resonance frequency can all be tuned by varying the core or cladding optical constants. This property is not unique to surface plasmons, but is generally true for electromagnetic waves interacting with any material system. In fact, the interaction of light with matter is almost exclusively determined by two intrinsic material properties - namely, the electric permittivity ϵ and the magnetic permeability μ .

For all known transparent materials, both the permittivity and the permeability are positive, leading to a positive index of refraction. However, if the sign and magnitude of the index could be tuned at will, the flow of light could be controlled in unprecedented ways [114]. Among the many unusual applications of index tunability are negative refraction [136, 134], sub-diffraction-limited microscopy [110, 28, 49, 155], and optical cloaking and invisibility [6, 132, 29]. In this chapter, we explore the opportunities for designing plasmonic materials with a wide range of refractive indices, including negative indices. Our results indicate the accessibility of broadband negative, positive, and near-zero indices in plasmonic waveguides, facilitating design of a new materials class with extraordinary optical properties.

5.1.1 Negative indices and negative refraction

When a beam of light enters a material from vacuum or air at non-normal incidence, it undergoes refraction - a change in its direction of propagation. The angle of refraction depends on the absolute value of the refractive index of the medium, according to Snell’s law. For all naturally-occurring substances, the beam is deflected to the opposite side of the interface normal, and the refractive index is taken to be positive.

In 1968, Veselago studied a theoretical material with simultaneously negative ϵ and μ , predicting it would possess a negative index [166]. Unlike any natural material, the phase velocity of electromagnetic signals in this negative index

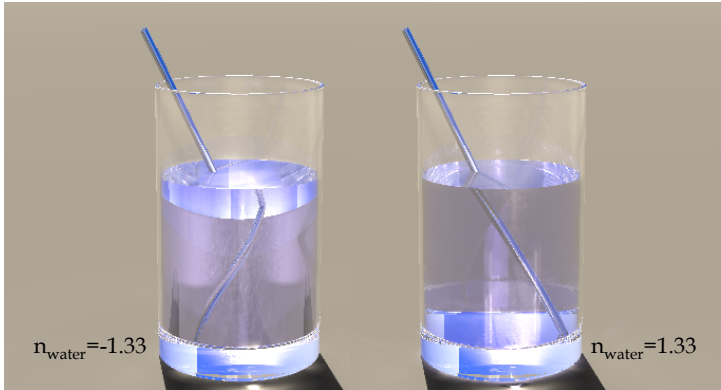


Figure 5.1. Photorealistic image of light refracting from negative and positive index water. Adopted from [43].

material (NIM) would be negative and oriented opposite to the energy velocity. In addition, light crossing the boundary between such a medium and one with a positive index would refract to the same side of the normal. Such a deflection, termed negative refraction, was predicted to lead to a variety of exotic and enabling applications, most notably subwavelength focusing with resolution well below the diffraction limit [122].

The unusual refractive properties of negative index materials are illustrated in Figure 5.1. Here, a ray-tracing algorithm¹ was used to generate photorealistic images of light refraction and reflection from positive and negative index media [43]. On the left, a straw is placed into hypothetical water with a negative index of $n_{\text{water}} = -1.3$. For reference, the figure also includes light refraction into normal water with $n_{\text{water}} = 1.3$. Contrary to our ordinary perception, the glass filled with negative index water exhibits a number of striking features. In particular, the straw is bent to the ‘wrong’ side of the air-water normal and the bottom of glass cannot be seen. Instead, the underside of the air-water interface can be observed, as if the viewer is looking at the glass from below rather than at eye level. Though counterintuitive, these effects can be directly derived from the negative refraction of rays emerging from the air-water interface across the water-glass-air interface.

The simultaneously negative ϵ and μ necessary for achieving negative indices do not violate any physical laws. However, no natural materials exhibit a negative index, since the electric and magnetic resonances necessary to induce a negative ϵ and μ typically occur in completely disparate regions of the electromagnetic spectrum. While metals exhibit a negative real value of the permittivity for optical frequencies, magnetic responses diminish for frequencies exceeding the microwave regime. Achieving a negative index material at optical frequencies thus requires simulating an effective magnetic media in a frequency range where most natural materials are non-magnetic.

¹POV-Ray

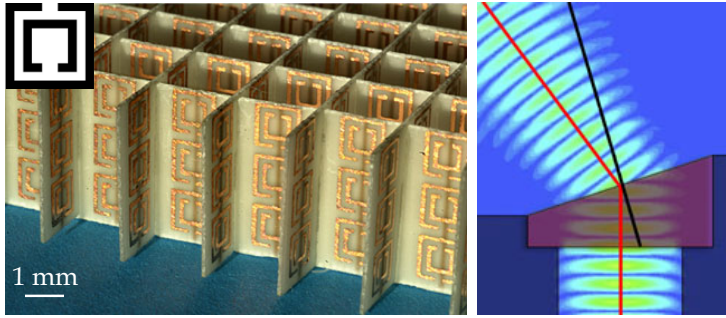


Figure 5.2. Resonator-based metamaterial designed for microwave frequencies. Both simulations (shown) and experiments confirmed the negative response of these split-ring resonator ensembles. Adopted from [136] and [63].

5.1.2 Metamaterials

In recent years, considerable research has been devoted to developing electromagnetic media with negative n resulting from negative ϵ and μ [122, 147]. These engineered materials, called ‘metamaterials,’ are generally composed of subwavelength resonators that serve as artificial atoms of the material. Considered as a bulk material, these metamaterials will exhibit properties altogether distinct from their constituent resonator elements. Through variation of the resonator materials or dimensions, metamaterials allow for refractive index tunability that can span positive, negative, and near-zero indices.

Metamaterials were first implemented at microwave frequencies on the order of 10 GHz, using periodic assemblies of millimeter-scale split-ring resonators and wires [136, 63]. Negative values of ϵ and μ were simultaneously achieved via, respectively, the resonant capacitive-inductive response of the split-rings [111] and the effective plasma response of the wire lattice [112]. All-angle negative refraction in two-dimensions was then demonstrated by direct observation of plane-wave refraction through prism-shaped segments of such assemblies [136, 63], as shown in Figure 5.2.

Efforts are now directed towards scaling down NIMs for operation at visible frequencies [134, 146]. So far, structures have been limited to one [177, 135, 41, 44] or a few [42] layers of discrete resonator elements. Transmission and reflection spectra measured using out-of-plane illumination enable retrieval of ϵ and μ [142]; in this manner, negative indices were inferred at infrared frequencies [177, 135, 42] and recently at the red end of the visible spectrum [44]. However, the thickness of such visible-frequency NIMs is substantially smaller than the free-space wavelength. Accordingly, the interaction volume with the incident radiation remains too small to induce angular deviations of light of sufficient amplitude to provide direct evidence of negative refraction. Achieving negative indices and negative refraction at visible frequencies thus remains a substantial challenge.

5.2 Plasmonic metamaterials: Theory

As we saw in earlier chapters, planar plasmonic materials have the potential to exhibit broad index tunability. Unlike traditional resonator-based metamaterials, these geometries consist of slab waveguides with alternating layers of metals and dielectrics. Light propagates through the structure via one or more surface plasmon waves, which are characterized by group and phase velocities distinct from the incident light. If the waveguide is characterized by only a single propagating mode, light will emerge from the structure as if it had passed through a material with an index equal to the mode index. Such plasmon-based geometries have the potential to exhibit the same response as resonator-based metamaterials, without the necessity of patterning discrete resonator elements. Moreover, while these plasmonic structures are inherently two-dimensional, they can be readily stacked to create a fully three-dimensional NIM.

In this section, we theoretically explore the range of negative and positive indices accessible in surface plasmon waveguides, including calculations of dispersion and absorption. Attention is given to the modes of MIM, IIM, and IMI waveguides. Our analysis will consider both Ag/Si₃N₄- and Ag/GaP-based geometries, varying the core waveguide dimensions from 5 nm to 50 nm in 1 nm increments and the excitation wavelength from the ultraviolet to near-infrared. By carefully exploring the magnitude and sign of complex wavevectors accessible in these structures, we explicitly determine their utility as negative index materials. Our analytic results are confirmed with finite difference time domain simulations that directly demonstrate the refraction of free-space modes into these plasmonic materials. In addition, our analysis provides detailed maps of plasmonic indices and figures of merit as a function of wavelength and geometry. Such maps serve as a ‘guide to the experimentalist’ in designing plasmon-based negative index materials and transformation-based (i.e., index-tuned) optical elements.

5.2.1 Waveguides as Materials: Theoretical foundations

In conventional materials, the complex refractive index can be derived from knowledge of the wavelength and absorption of light in the material. Surface plasmon based geometries are no exception. The plasmon wavevector k_x can be used to uniquely determine the complex refractive index of the structure. Since surface plasmons are plane-waves, the wavelength λ_{SP} and index n of surface plasmons are related to the magnitude of the real component of k_x via

$$\lambda_{SP} = \frac{2\pi}{|Re\{k_x\}|} \quad (5.1a)$$

$$n = \frac{c \cdot Re\{k_x\}}{\omega}. \quad (5.1b)$$

Here, the frequency of light ω is related to its wavelength λ in free space by $\omega=2\pi c/\lambda$. If losses are present in the structure, the absorption can be extracted from the magnitude of the imaginary component of k_x , with mode propagation

lengths L_{SP} given by:

$$L_{SP} = \frac{1}{2 \cdot \text{Im}\{k_x\}}. \quad (5.2)$$

Solving Maxwell's equations subject to continuity of the tangential electric fields and normal displacement fields yields the wavevector. As we saw in Chapter 2, assuming wave propagation along the positive x -direction, surface plasmons take the form of transverse-magnetic plane waves:

$$E(x, z, t) = (E_x \hat{x} + E_z \hat{z}) \cdot e^{i(k_x x - \omega t)} \quad (5.3a)$$

$$B(y, t) = (B_y \hat{y}) \cdot e^{i(k_x x - \omega t)}. \quad (5.3b)$$

For a three-layered geometry with each interface parallel to x and perpendicular to z (see inset of Figure 5.3a), k_x is defined by the dispersion relation:

$$\det \left(\begin{bmatrix} 0 & 1 & 0 & 0 & 0 & 0 \\ 1 & 1 & -1 & -1 & 0 & 0 \\ -\frac{\varepsilon_0}{k_{z0}} & \frac{\varepsilon_0}{k_{z0}} & \frac{\varepsilon_1}{k_{z1}} & -\frac{\varepsilon_1}{k_{z1}} & 0 & 0 \\ 0 & 0 & e^{k_{z1}d_1} & e^{-k_{z1}d_1} & -e^{k_{z2}d_1} & -e^{-k_{z2}d_1} \\ 0 & 0 & -\frac{\varepsilon_1}{k_{z1}}e^{k_{z1}d_1} & \frac{\varepsilon_1}{k_{z1}}e^{-k_{z1}d_1} & \frac{\varepsilon_2}{k_{z2}}e^{k_{z2}d_1} & -\frac{\varepsilon_2}{k_{z2}}e^{-k_{z2}d_1} \\ 0 & 0 & 0 & 0 & 1 & 0 \end{bmatrix} \right) = 0 \quad (5.4)$$

with k_z defined by momentum conservation:

$$k_{z0,1,2}^2 = k_x^2 - \varepsilon_{0,1,2} \left(\frac{\omega}{c} \right)^2. \quad (5.5)$$

Note that the waveguide is assumed to be infinite in y . Each layer $\{0,1,2\}$ is described by either a real or complex electric permittivity $\varepsilon_{0,1,2}$ and a thickness d , with d_0 and d_2 assumed to be semi-infinite. All materials are considered linear and non-magnetic, with the magnetic permeability $\mu=1$.

It is well known that light propagation in negative index materials is characterized by antiparallel phase and energy flow [166]. For all propagating plane waves, the phase velocity is defined by $v_p = \omega / \text{Real}\{k_x\}$. In the absence of losses, the energy velocity v_E is equal to the group velocity $v_g = d\omega / dk_x$. Therefore, for lossless materials, negative indices will manifest themselves by a region of negative slope on a plot of ω versus $|k_x|$.

Figure 5.3 plots the dispersion relationships ω versus $|\text{Real}\{k_x\}|$ for lossless MIM, IIM, and IMI geometries with Ag as the metallic layer and GaP as the dielectric. Here, the Ag is described by a lossless Drude model with a bulk plasma frequency $\hbar\omega = 9.01\text{eV}$. The index of GaP is taken as 3.31. For reference, the surface plasmon resonant frequency is shown as a dotted line. In Figure 5.3a, 50 nm of GaP is surrounded by two semi-infinite layers of Ag. As seen, the dispersion curve of this MIM geometry is characterized by three distinct bands, including a region of negative slope between the bulk and surface plasmon frequencies, and regions of positive slope below the surface plasmon resonance and above the bulk plasma resonance. Note that these three bands correspond to two different modes with varying magnetic field distributions across the waveguide. Below the

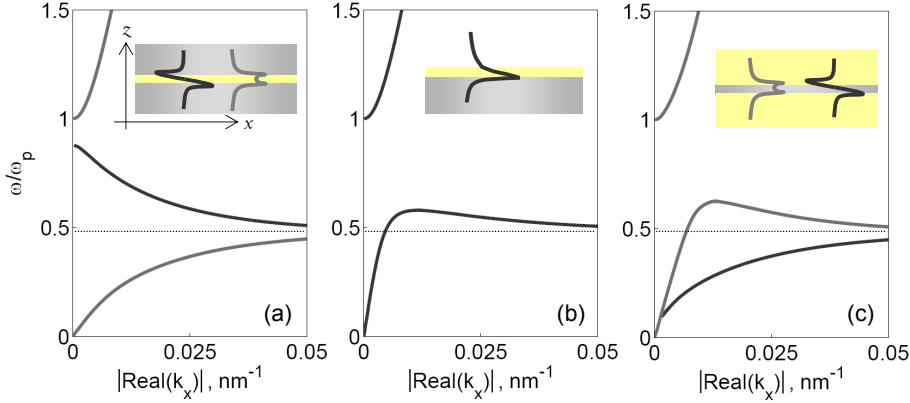


Figure 5.3. Lossless dispersion for three plasmon geometries: **(a)** a MIM waveguide composed of 50 nm GaP clad by Ag; **(b)** an IIM waveguide composed of thick Ag coated with 20 nm GaP; and **(c)** an IMI waveguide composed of 50 nm Ag clad by GaP. Insets show both the waveguide geometry and the associated H_y mode profiles for both the symmetric mode (light gray) and the antisymmetric mode (dark gray). Notice that all three geometries are characterized by regions of negative slope and hence negative indices. However, this negative index regime is single valued in k for the MIM geometry only.

surface plasmon resonance, $H_y = B/\mu$ is symmetric across the waveguide (light gray branch). The wavevectors of this mode are purely real below the surface plasmon resonance, but become purely imaginary for frequencies between the bulk and surface plasmon resonance frequencies. In contrast, H_y is antisymmetric throughout the regime of negative slope (dark gray branch). Interestingly, the wavevectors of this mode become purely imaginary for frequencies below the surface plasmon resonance. Thus, the MIM modes allowed to propagate in the traditional surface plasmon bandgap (between the bulk and surface plasmon resonant frequencies) have a field distribution altogether distinct from the propagating plasmon modes below resonance.

As seen in Figure 5.3a, each input photon frequency is assigned to a unique MIM wavevector throughout the entire k -space domain. Therefore, for a given excitation wavelength, this lossless MIM geometry will be characterized by a single propagating mode. Provided excitation wavelengths are between the bulk and surface plasmon resonance frequencies, the plasmon mode will exhibit a negative index, rendering the entire MIM composite an effective negative index material.

Like the lossless MIM geometry, IIM and IMI waveguides are also characterized by regions of negative slope, and hence negative indices. For example, Figure 5.3b plots the dispersion relationship for the bound modes of a semi-infinite layer of Ag coated with a thin, 20 nm layer of GaP. As seen, this geometry is characterized by a single continuous bound mode for frequencies below and above the surface plasmon resonance. For wavelengths above the surface plasmon resonance, this mode can exhibit negative slope, corresponding to

oppositely-oriented group and phase velocities. Note, however, that this geometry is not characterized by a unique wavevector assignment at each frequency. Above the surface plasmon resonance, for example, this lossless IIM geometry is characterized by two wavevectors, and hence two propagating waves of different wavelength. Since each excitable wavevector resides in regimes of opposite slope, these two waves will be characterized by counter-propagating phase.

Similar features can be observed for the bound modes of the IMI geometry, plotted in Figure 5.3c. Here, 50 nm of Ag is clad by two semi-infinite regions of GaP. Like the MIM geometry, this structure is characterized by both a H_y field anti-symmetric mode (light gray curve, located exclusively below the surface plasmon resonance) and a H_y symmetric mode (dark gray, located both above and below the surface plasmon resonance). The symmetric mode exhibits a regime of negative slope for certain frequencies above the plasmon resonant frequency. However, as with the IIM geometry, this negative index regime is accompanied by wavevectors that exhibit positive slope - and hence a positive index - throughout the same frequency range.

As Figure 5.3 reveals, in the absence of losses all three plasmonic geometries appear to support propagation of negative index modes over a finite frequency range. However, the MIM geometry is the only structure that can be characterized by a single propagating negative index mode - and hence a unique negative index - for these frequencies. Of course, the many enabling and exotic applications of plasmonic systems, including negative indices, do not come without an expense: namely, the cost of losses. Metals are characteristically lossy, particularly near their resonant frequencies, and Ag is no exception. While this section outlined the potential for plasmon waveguides to support propagation of negative index waves, the next section explores the extent to which these results are altered when losses are included.

5.2.2 Lossy dispersion and the necessary condition for negative indices

The equivalence between the energy velocity v_E and the group velocity v_g described above provides a simple way of identifying negative index regimes directly from a dispersion diagram. Unfortunately, this equivalence only holds for non-absorbing media. For absorbing (i.e., lossy) materials, the more general expression of the energy velocity must be used:

$$v_E = \frac{\bar{S}}{\bar{W}}, \quad (5.6)$$

where \bar{S} is the average power flow in the waveguide and \bar{W} is the time-averaged energy density [127]. The average power flow can be derived from the integrated Poynting vector flux, and always points in the direction of wave propagation. Therefore, the direction of power flow will be collinear with the direction of wave decay for lossy materials:

$$\text{sign}(v_E) = \text{sign}(\text{Imag}\{k_x\}). \quad (5.7)$$

In contrast to power flow, phase can flow in either direction, either parallel or opposite to the direction of wave decay. For plane waves, including plasmons, phase flow is described by the ratio of the excitation frequency to the mode wavevector via $v_p = \omega / \text{Real}\{k_x\}$ and so:

$$\text{sign}(v_p) = \text{sign}(\text{Real}\{k_x\}). \quad (5.8)$$

Therefore, to achieve the antiparallel energy and phase velocities associated with negative indices, the plasmon wavevector must satisfy the criteria:

$$\text{sign}(\text{Real}\{k_x\}) \neq \text{sign}(\text{Imag}\{k_x\}). \quad (5.9)$$

Note that this condition on the sign of the real and imaginary components of k is both a necessary and sufficient condition for achieving negative indices in absorbing media, including plasmon-based geometries [151].

Because of point symmetry in the complex k_x plane with respect to the origin, we can impose $\text{sign}(\text{Imag}\{k_x\}) \geq 0$. This choice restricts the direction of net energy flow to the positive x -direction. Then, negative index plasmonic geometries will necessarily be characterized by a negative real component of the plasmon wavevector. Assuring consistency with Figure 5.3, we note that the choice of $\text{sign}(\text{Imag}\{k_x\}) \geq 0$ also affects the sign of $\text{Real}\{k_x\}$ obtained in the lossless dispersion curves. Notably, the branches plotted in Figure 5.3 are accompanied by counterpropagating modes that have $k_x < 0$. Imposing a constraint on the energy flow direction allows only curves with positive slope in the lossless case. The branches with negative slope in Figure 5.3 (which were recognized as exhibiting a negative index) are then omitted. Instead, their counterparts with $k_x < 0$ remain, reflecting the connection between the signs of k_x and n when imposing this restriction on the direction of energy flow. As we will see, these dispersion curves can still be recognized when realistic material parameters, including absorption losses, are used.

The metal-insulator-metal waveguide as a negative index material

Figure 5.4 plots the real and imaginary components of the plasmon wavevector k_x as a function of energy for MIM geometries. Here, the metallic layer is Ag, described by the empirically-determined dielectric constants reported in Johnson and Christy [69]. The insulating layer is again taken to be GaP, with absorption both above and below the bandgap included [109]. GaP core thicknesses of 10 nm, 17 nm, and 25 nm are considered. For reference, the surface plasmon resonance is shown as a dotted line. As noted in Figure 5.3a, MIM geometries are characterized by both a H_y field symmetric mode and a H_y field antisymmetric mode. Both modes are also found in this lossy geometry, with the H_y -symmetric mode shown in blue and the H_y -antisymmetric mode plotted in red.

Recall that in the lossless case, the H_y -symmetric mode exhibited a bandgap between the surface plasmon and bulk plasma frequencies. As seen in Figure 5.4, this H_y -symmetric mode (blue) is actually continuous throughout the entire frequency range, including in the traditional plasmon bandgap. Although this mode exhibits a regime of negative slope, the real wavevector components, and

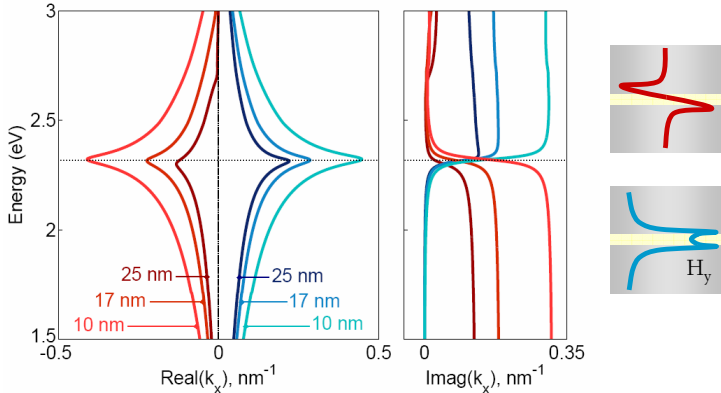


Figure 5.4. Lossy dispersion for MIM waveguides consisting of GaP clad by Ag. Three GaP thicknesses are included ($d = 25$ nm, 17 nm, and 10 nm), and dispersion relations for both H_y -field symmetric (blue hues) and antisymmetric (red hues) modes are shown. Including losses, the necessary condition for negative index modes is: $\text{sign}(\text{Real}\{k_x\}) \neq \text{sign}(\text{Imag}\{k_x\})$. This condition is clearly satisfied for the H_y -field antisymmetric mode, which can exhibit negative indices with very low loss above the plasmon resonance (shown as a dotted line).

hence the phase velocity, remain exclusively positive. As expected, the imaginary components of k_x are positive as well. Note that below the surface plasmon resonance, the losses of this symmetric mode are quite low, with $\text{Imag}\{k_x\} \ll \text{Real}\{k_x\}$. In contrast, this mode become essentially evanescent above the surface plasmon resonance, with $\text{Imag}\{k_x\} \gg \text{Real}\{k_x\}$. Therefore, although the presence of absorption forces $\text{Real}\{k_x\}$ to be non-zero in the traditional plasmon bandgap, such modes are non-propagating. More importantly, even though these bandgap modes exhibit negative slope, both their group velocity and their phase velocity remain positive. Accordingly, these H_y -symmetric modes will be characterized by refractive indices that are exclusively positive throughout all frequencies.

While the H_y -symmetric modes do not exhibit negative indices, MIM waveguides can also support H_y -antisymmetric modes. The real and imaginary wavevector components of these modes are shown in Figure 5.4 in red. As seen, the sign of $\text{Real}\{k_x\}$ is negative throughout the entire frequency domain, corresponding to a negative phase velocity. In contrast, the sign of $\text{Imag}\{k_x\}$ is positive. Therefore, these antisymmetric modes will exhibit oppositely-oriented energy and phase velocities, and hence negative indices. Note that $\text{Imag}\{k_x\} \gg \text{Real}\{k_x\}$ for frequencies below the surface plasmon resonance, indicating that these modes are essentially non-propagating below resonance. However, above resonance, the losses of this H_y -antisymmetric mode become remarkably low - so low, in fact, that losses rival the low $\text{Imag}\{k_x\}$ components seen for the propagating positive index mode. Therefore, between the bulk and surface plasmon resonant frequencies, the H_y -antisymmetric mode will be the only propagating mode. As this mode exhibits opposite phase and energy velocities, MIM geometries will

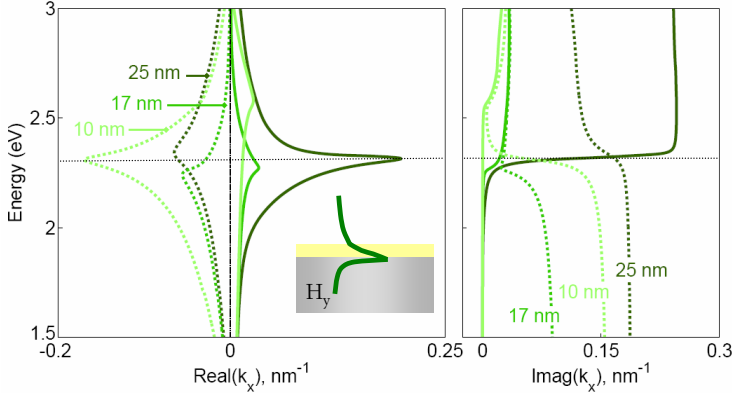


Figure 5.5. Lossy dispersion for insulator-insulator-metal waveguides composed of a thick Ag film coated with a thin layer of GaP and embedded in air. Three GaP thicknesses are included ($d = 25$ nm, 17 nm, and 10 nm), and dispersion relations for both positive index (solid) and negative index (dotted) branches are shown. While solutions satisfying $\text{sign}(\text{Real}\{k_x\}) \neq \text{sign}(\text{Imag}\{k_x\})$ may be found, the losses are quite high, with propagation lengths comparable to or smaller than the mode wavelength.

indeed be characterized by negative indices in this frequency range. The range of achievable refractive indices and figures of merit ($\text{Real}\{k_x\}/\text{Imag}\{k_x\}$) will be discussed in detail in Section 5.2.3.

Insulator-insulator-metal and insulator-metal-insulator waveguides as multimode metamaterials

Figure 5.5 plots the dispersion relationship for the bound modes of an IIM waveguide, considering both the sign and magnitude of $\text{Real}\{k_x\}$ and $\text{Imag}\{k_x\}$. A thick Ag slab is coated with a thin layer of GaP ($d=10$ nm, 17 nm, and 25 nm) and embedded in air. The dielectric functions of Ag and GaP are adopted from empirically determined optical constants, and thus include realistic losses for all plotted frequencies. As with the MIM waveguides, this geometry exhibits real wavevector components that are both positive and negative, corresponding to positive and negative indices, respectively. Below resonance, only the positive index mode exhibits long-range propagation. Above resonance, the losses of this positive index mode increase, while the losses of the negative index modes are reduced. Note however that unlike the MIM geometry, the losses of the IIM negative index mode are generally comparable with the positive index modes. For example, GaP thicknesses of 10 nm and 17 nm exhibit negative-index $\text{Imag}\{k_x\}$ components that are higher than for the positive index mode. As the thickness of GaP is increased to 25 nm, the losses of both modes increase. Although $\text{Imag}\{k_x\}$ for the negative index modes can be lower than $\text{Imag}\{k_x\}$ for the positive index modes, for thicker dielectrics both modes exhibit short propagation lengths that are comparable to the mode wavelength.

Similar features are observed for the H_y symmetric mode of an IMI waveguide.

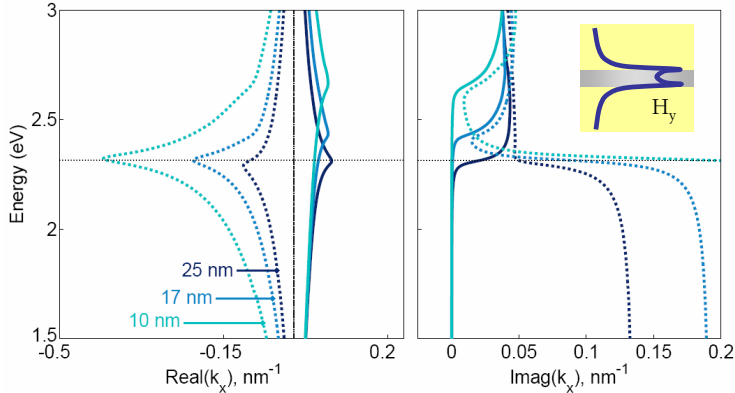


Figure 5.6. Lossy dispersion for insulator-metal-insulator waveguides composed of a thin Ag film clad with GaP. Three Ag thicknesses are included ($d = 25$ nm, 17 nm, and 10 nm), and dispersion relations for the positive and negative index branches of the H_y -field symmetric mode are shown. While solutions satisfying $\text{sign}(\text{Real}\{k_x\}) \neq \text{sign}(\text{Imag}\{k_x\})$ may be again found, the losses of this branch always exceed those of the positive index mode.

uide, shown in Figure 5.6. Recall that this mode exhibited simultaneously positive and negative indices above the surface plasmon resonance for the lossless geometry (Figure 5.3c). Here, a thin Ag slab is embedded in GaP. Ag thickness of $d = 10$ nm, 17 nm, and 25 nm are considered. Note that the wavevectors of the H_y antisymmetric mode are not shown, since this mode is characterized by exclusively positive wavevectors with $\text{Imag}\{k_x\}$ components that generally exceed those of the symmetric mode. As with the MIM and IIM geometries, losses for the positive index IMI modes are low below resonance, and increase only within a regime of negative slope. In contrast, losses for the negative index mode are high below resonance, and can be substantially reduced above resonance. However, the losses for these negative index modes are generally never lower than the losses for the positive index modes.

As Figures 5.5 and 5.6 reveal, both IIM and IMI geometries can support negative index modes. However, these negative index modes are generally found in a frequency regime where additional positive index modes also exist. Such characteristics prohibit assignment of a single, unique index to the IIM and IMI geometries above the plasmon resonance, even including realistic material losses. Therefore, unlike the MIM geometry, planar IIM and IMI waveguides may not be regarded as single-mode, negative index materials. Nevertheless, the existence of multiple modes propagating with opposite phase and comparable absorption may be interesting for a variety of on-chip photonic applications.

5.2.3 Mapping indices and figures of merit: A guide to the experimentalist

Design of practical metamaterials requires precise knowledge of the index and absorption. For plasmonic geometries, such parameters strongly depend on the constituent materials, the structure dimensions, and the excitation wavelength. The preceding sections outlined the potential for vast index tunability in plasmonic waveguides: while MIM geometries can achieve low-loss, single-mode negative indices above the plasmon resonance, IIM and IMI geometries can sustain simultaneous propagation of waves with positive and negative phase. In addition, the magnitude of the wavevectors (and hence the mode indices) can span from near-zero to large positive and negative values. In this section, we explore the range of achievable indices and figures of merit in plasmonic waveguides. The associated plots are intended as a guide to the experimentalist in designing plasmonic materials for a variety of metamaterial and transformation-based applications.

Ag/GaP and Ag/Si₃N₄ MIM metamaterials: Negative indices and Negative refraction

Figure 5.7 plots the achievable refractive indices and figures of merit for MIM geometries, using GaP as the core and Ag as the cladding. Here, the figure of merit (FOM) is defined as the ratio of $\text{Real}\{k_x\}$ to $\text{Imag}\{k_x\}$, or equivalently, $\text{Real}\{n\}$ to $\text{Imag}\{n\}$. GaP core thicknesses are varied from 5 nm to 50 nm in 1 nm increments, and excitation wavelengths are varied from the near-infrared to the ultraviolet (energies of 1.5 - 3.5 eV). Note that each vertical cut through the chart depicts one dispersion diagram, with the index and FOM plotted on the color scale. Index maps are provided for both the negative and positive index modes.

As seen in the figure, both modes achieve refractive index magnitudes spanning from ~ 0 to $|n| > 60$ as the core GaP thickness is reduced. As expected, figures of merit for the negative index mode are near-zero for frequencies below the surface plasmon resonance, but approach 20 for thinner waveguides excited above resonance. Interestingly, these figures of merit can be orders of magnitude higher than the FOM for positive index modes above resonance. Moreover, the FOM for the negative index modes actually increases with decreasing core thickness. For example at a wavelength of ~ 480 nm (2.57 eV), negative indices of $n = -23$ can be achieved with figures of merit equal to 19.7, using a 5 nm thick GaP core. In contrast, the FOM for the positive index mode at the same wavelength is < 0.5 .

To investigate the refraction of light in such a negative index MIM waveguide, we perform a three-dimensional finite-difference time-domain simulation [3] of the structure in Figure 5.8. A 488-nm plane wave of infinite extent is incident from free space on a 30 nm thick GaP slot clad with 400 nm Ag. At this wavelength, this geometry has a negative index of $n = -2.86$ with a figure of merit equal to 10. In order to allow excitation of the H_y -antisymmetric mode in the waveguide, the beam is polarized in the z direction and incident at a slightly oblique angle (10°) to the xy plane. Bloch boundary conditions are used

to simulate an incident plane wave that is infinite in extent. Figure 5.8 shows the simulated H_y field in a plane through the waveguide core at a distance of 5 nm from the top Ag/GaP interface. The incident and reflected beams are visible to the left, making an angle of 30° with respect to the x axis. Inside the MIM waveguide, a wave can be seen to propagate over a micron-sized distance. The wave front angle is consistent with a negative index of $n = -2.9$, as predicted. Additionally, in the first 100 nm from the edge of the waveguide, the quickly decaying contribution of the largely evanescent H_y -symmetric mode can be recognized. By calculating the Poynting vector in the waveguide beyond the first 100 nm, power is seen to flow away from the normal in the direction associated with negative refraction. This result indicates that the negative index mode can indeed enable negative refraction of a light beam.

Replacing the GaP with Si_3N_4 ($n \sim 2.02$) shifts the surface plasmon resonance to higher energies. Figure 5.9 shows index and FOM maps for Ag/ Si_3N_4 MIM geometries, again with core thicknesses spanning 5 nm to 50 nm. As usual, the Ag and Si_3N_4 have been described by frequency-dependent dielectric constants adopted from the literature [69, 109]. As seen, the region of high figure of merit for negative index modes has increased in energy to 3.1 eV. While index magnitudes achievable in this geometry range are comparable with the GaP-based

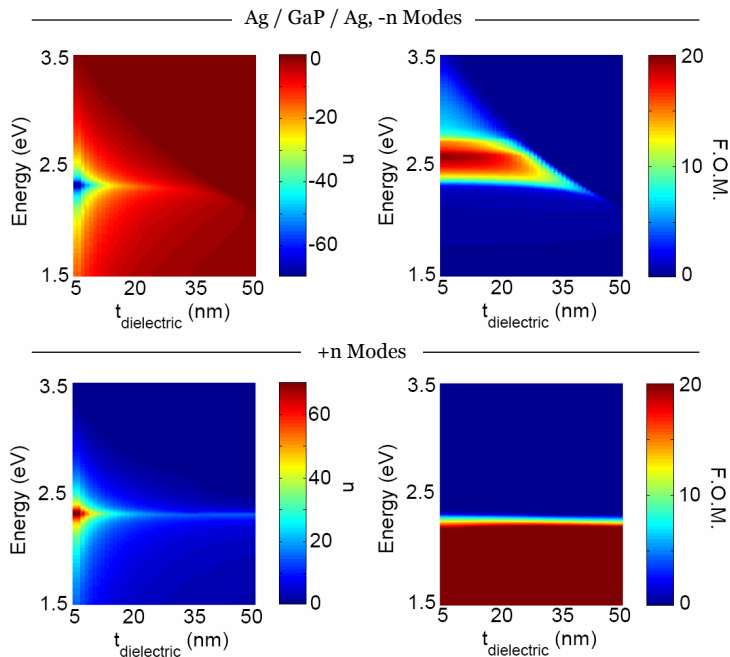


Figure 5.7. Plots of MIM indices and figures of merit (FOM) for Ag/GaP/Ag waveguides as a function of energy and core thickness. Maps for both positive and negative index modes are shown. While the FOM for positive index modes drops to zero above the plasmon resonance frequency, it can be as high as 20 above resonance for negative index modes.

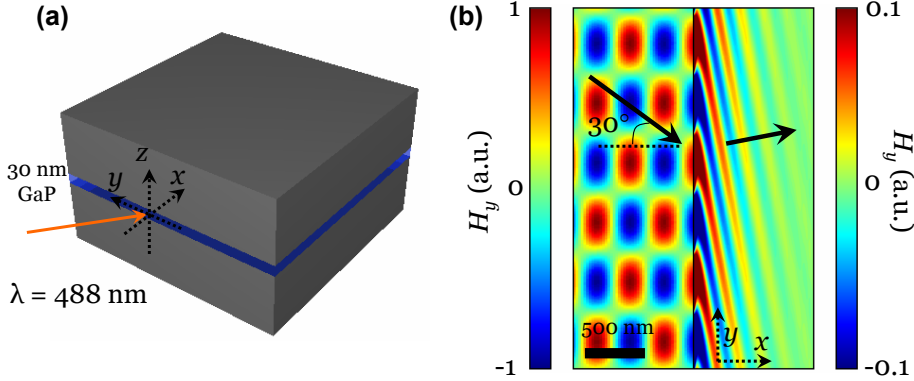


Figure 5.8. FDTD simulation of negative refraction of a 488-nm plane wave into a MIM waveguide. **(a)** Schematic of the simulation geometry. The plane wave is incident at an angle of 30° with respect to the xz plane and 10° with respect to the xy plane. **(b)** H_y field component snapshot in a plane through the waveguide core. Bloch boundary conditions are used to simulate an incident plane wave that is infinite in extent. For clarity, the color scale in the waveguide to the right differs from that in the air region to the left.

geometry, the maximum figure of merit has been reduced to 10. Heuristically, reducing the dielectric index shifts the surface plasmon resonance towards the bulk plasma resonance, where Ag is inherently more absorbing. Nevertheless, the range of index tunability is significant: Not only are high figure-of-merit negative index materials achievable with MIM-based geometries, but these structures can also exhibit broadband operation. High FOM negative indices for this Ag/ Si_3N_4 MIM geometry span wavelengths from 354 nm - 397 nm. Likewise, high figure of merit negative indices for the Ag/GaP MIM geometry span wavelengths of 456 - 524 nm (energies of 2.37 - 2.72 eV) - a wavelength range of nearly 75 nm! Coupled with their ease of fabrication, the broadband, tunable, single mode, and high FOM negative indices of MIM waveguides render them an attractive alternative to resonator-based metamaterials.

Ag/GaP and Ag/ Si_3N_4 IIM and IMI Multimode metamaterials

Figure 5.10 plots the index and FOM maps for the bound modes of an IIM waveguide, considering a thick Ag slab coated with a thin layer of GaP and embedded in air. Figure 5.11 plots equivalent maps, but for a Ag slab coated with a thin layer of Si_3N_4 . As before, the thicknesses of GaP and Si_3N_4 are varied from 5 nm to 50 nm in 1 nm increments. Similar to the results shown in Figure 5.5, Figures 5.10 and 5.11 reveal the existence of high FOM negative index modes. For thin insulating layers ($d < 10$ nm), the figures of merit for these modes can approach 16 and 7 for the GaP and Si_3N_4 geometries, respectively. However, regions of high $-n$ FOM are generally accompanied by large $+n$ mode figures of merit. As seen in the bottom graphs of Figures 5.10 and 5.11, the FOM for the positive index modes does not abruptly decay to zero above the Ag/GaP or

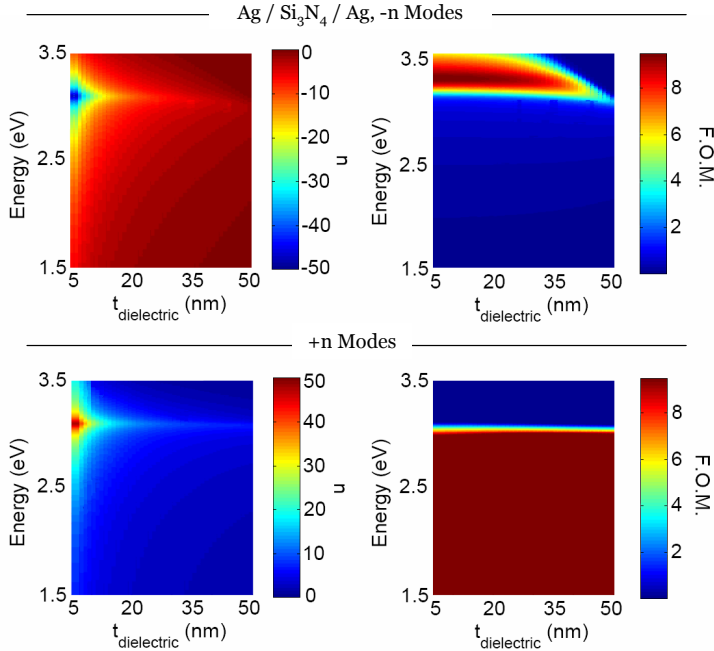


Figure 5.9. Plots of MIM indices and figures of merit for Ag/Si₃N₄/Ag waveguides as a function of wavelength and core thickness. Maps for both positive and negative index modes are shown. The smaller index of Si₃N₄, compared with GaP, shifts the region of high FOM negative indices to shorter wavelengths, where Ag is more absorbing.

Ag/Si₃N₄ plasmon resonance, as it did with the MIM-based geometries. Instead, as the dielectric thickness is decreased, the effective plasmon resonance increases towards the Ag/air plasmon frequency. Note that the transition between a more air-like plasmon and dielectric-like plasmon is evident by the abrupt change in index seen around $d = 20$ nm, and is related to cutoff of the negative index mode. Such results confirm the trends observed of Figure 5.5: namely, that while IIM waveguides can support negative index modes, positive index modes with equally high figures of merit will also be present. Therefore, IIM geometries cannot be characterized as negative index materials identifiable with a unique index at a given wavelength.

Similar results are observed for IMI-based geometries, shown in Figures 5.12 and 5.13 for GaP- and Si₃N₄-clad Ag slabs, respectively. For these waveguides, decreasing the thickness of Ag increases the FOM for both the positive and negative index modes. However, the FOM for the negative index modes never exceeds the FOM for the positive index modes. Indeed, as the Ag thickness is decreased, the electromagnetic field of this H_y symmetric mode penetrates farther into the surrounding dielectric. For metallic slabs thinner than 30 nm, the mode begins to approximate a plane wave traveling in a dielectric with an index equal to the cladding index. Therefore, even though negative index

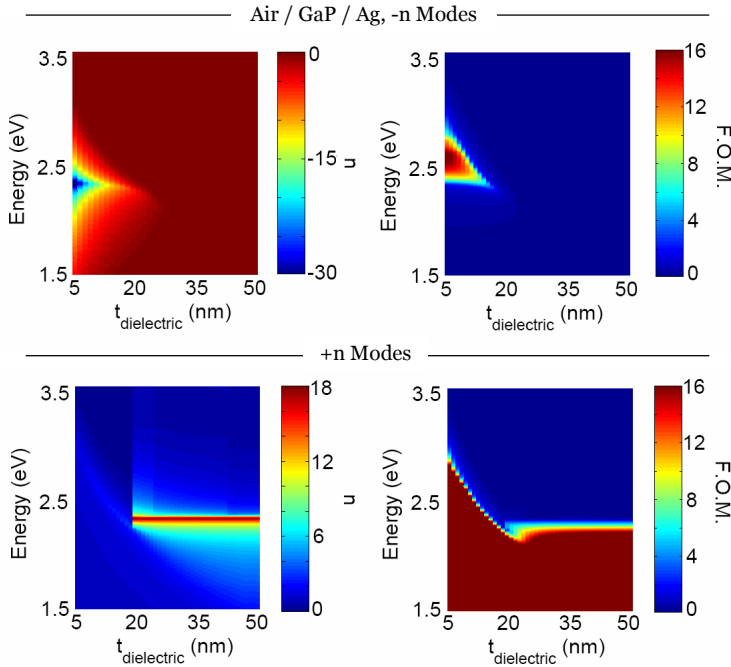


Figure 5.10. Plots of IIM indices and figures of merit for Air/GaP/Ag geometries as a function of wavelength and core thickness. Both negative and positive index branches of the dispersion diagram are shown. While the negative index modes have a high figure of merit for small GaP thicknesses above the Ag/GaP plasmon resonance, the positive index modes also have a very high FOM there, too.

figures of merit can approach 18 and 10 for GaP and Si_3N_4 -clad waveguides, respectively, the propagation of the traditional “long-ranging” positive index plasmon will generally dominate.

5.2.4 Section summary: Theoretical negative index materials

This section has explored the range of positive and negative indices accessible in plasmonic geometries. Among planar plasmonic waveguides, MIM, IIM, and IMI based structures all exhibit modes with negative indices between the bulk and surface plasmon resonances. However, MIM waveguides are the only geometries that support propagation of a single mode with a negative index at a given frequency. In contrast, IIM and IMI waveguide support simultaneous propagation of a positive index mode and a negative index mode above resonance. Heuristically, the ‘open’ nature of these waveguides makes excitation and detection of IIM and IMI negative index modes inherently difficult, particularly since the negative and positive index modes share the same field symmetry. Therefore, IIM and IMI waveguides may not be formally considered metamaterials with a unique index assignment at a given frequency. However, they do provide an interesting platform for index tunability and multimode propagation.

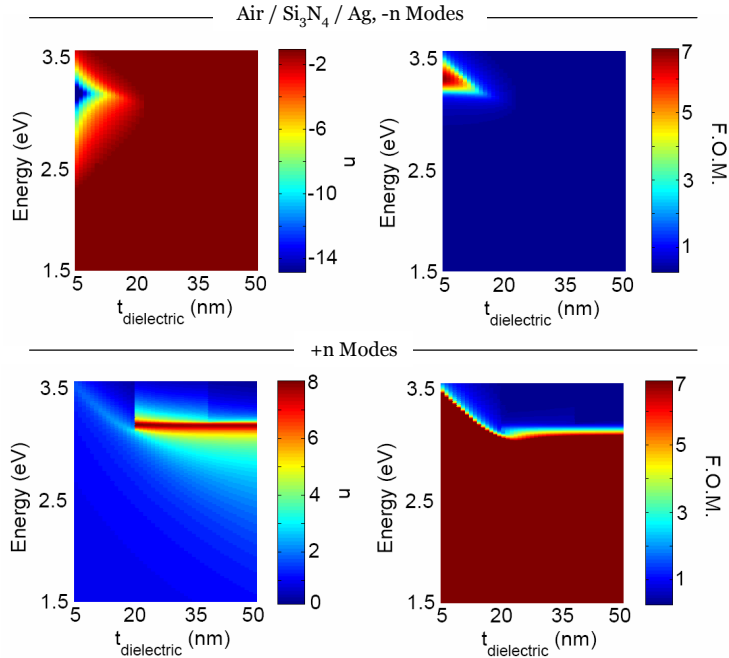


Figure 5.11. Plots of IIM indices and figures of merit for Air/Si₃N₄/Ag geometries as a function of wavelength and core thickness. Both negative and positive index branches of the dispersion diagram are shown. As with the MIM geometries, the reduced index of Si₃N₄ shifts the region of high negative index FOM to shorter wavelengths. However, for this IIM geometry, the FOMs for the negative and positive index modes remain comparable in magnitude above the Ag/Si₃N₄ plasmon resonance.

Unlike these ‘open’ geometries, MIM waveguides are effective metamaterials that can be characterized by a unique index at each wavelength. For wavelengths between the bulk and surface plasmon resonances, MIM geometries support a single propagating surface plasmon mode that exhibits antiparallel energy and phase velocities. Therefore, light will propagate through the MIM waveguide as if through a negative index material, with an index equal to the plasmon mode index. For Ag/GaP geometries, such indices can range from 0 down to $n=-60$, with figures of merit approaching 20. Moreover, negative indices in MIM-based metamaterials can be achieved over a wide range of wavelengths (bandwidths of ~ 75 nm) that are tunable throughout the entire visible spectrum. Their broad index tunability, high figures of merit, and relative ease of fabrication may render MIM-based metamaterials an attractive alternative to resonator-based metamaterials. Moreover, as we will see in the next section, MIM geometries can enable realization of practical negative index and transformation-based optical elements.

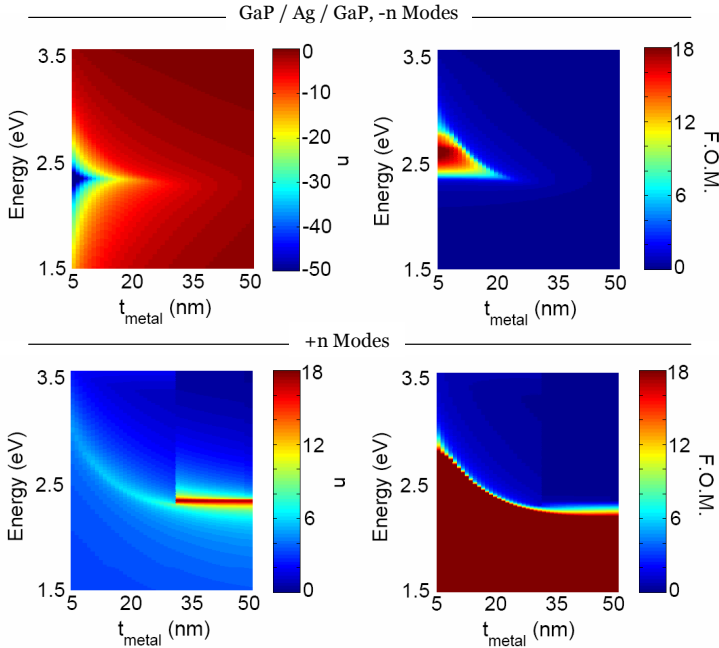


Figure 5.12. Plots of IMI indices and figures of merit for GaP/Ag/GaP geometries as a function of wavelength and core thickness. Both negative and positive index branches of the dispersion diagram are included. Despite the large accessible negative indices, FOMs for this branch never exceeded those of the positive index branch.

5.3 Negative refraction at visible wavelengths

In the mid seventeenth century, Sir Isaac Newton observed the passage of white light through a prism. His famous experiments provided a vivid visual demonstration of material dispersion and refraction, and laid the groundwork for centuries of optical experiments to come. Nearly four hundred years later, microwaves were passed through a metamaterial prism composed of metallic split ring resonators. The observed negative refraction provided unequivocal evidence of the first negative index material (NIM).

Since NIMs were developed in 2001, considerable effort has been devoted to scaling down negative index operation to visible wavelengths.² With discrete resonator-based metamaterials, negative indices have been inferred down to wavelengths as small as 780 nm, using reflection and transmission measurements to extract the index. However, recreating Newton's visible-frequency refraction experiments for NIMs has remained elusive. In this section, we use the MIM waveguides described above to experimentally realize a visible-frequency negative-index material. By shaping the MIM waveguide into a prism, we achieve

²This section, including text and figure content, has been adopted from H. J. Lezec*, J. A. Dionne*, and H. A. Atwater, Reference [83].

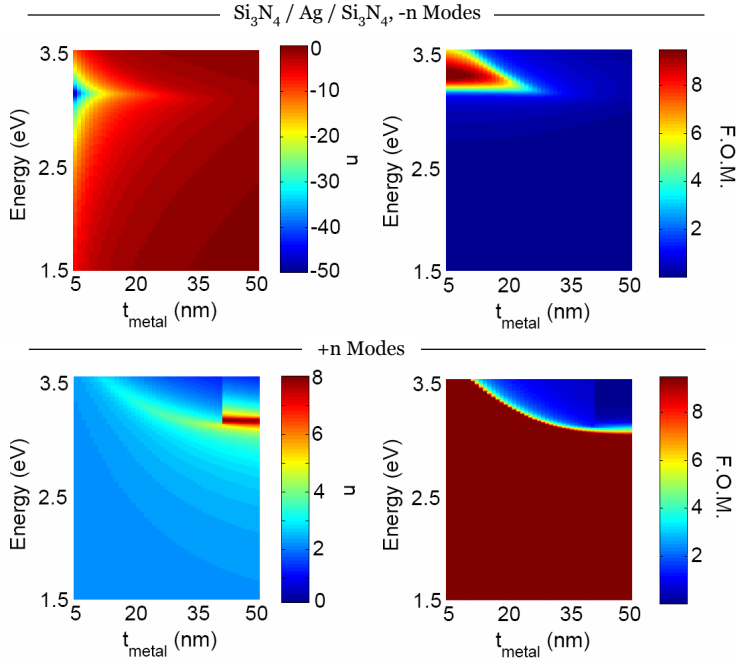


Figure 5.13. Plots of IMI indices and figures of merit for Si₃N₄/Ag/Si₃N₄ as a function of wavelength and core thickness. The lower index of Si₃N₄ shifts the plasmon resonance to shorter wavelengths, reducing the accessible FOM for both negative and positive index modes. However, as with GaP-based IMI waveguides, the FOM for the negative index modes never exceeds that of the positive index mode.

the first direct observation of negative refraction in the blue-green region of the visible.

5.3.1 Snell's law and surface plasmons

Snell's law indicates how the direction of light changes as it crosses the interface between one material and another. In general, when a plane wave traveling in medium 1 is incident at an angle ϕ_1 upon a boundary with medium 2, the resulting refraction angle ϕ_2 is dictated by conservation of the parallel component of k across the boundary as well as conservation of energy [166]:

$$\frac{\sin(\phi_2)}{\sin(\phi_1)} = \frac{\text{sign}(v_p^1 \cdot v_E^1) \cdot c/|v_p^1|}{\text{sign}(v_p^2 \cdot v_E^2) \cdot c/|v_p^2|} \quad (5.10)$$

Here, $v_p^{1,2}$ and $v_E^{1,2}$ are the phase and energy velocities of the electromagnetic waves in medium 1 and 2, respectively. By analogy with the usual form Snell's law:

$$\frac{\sin(\phi_2)}{\sin(\phi_1)} = \frac{n_1}{n_2}, \quad (5.11)$$

an effective refractive index for each medium can be identified:

$$n_{1,2} = \text{sign}(v_p^{1,2} \cdot v_E^{1,2}) \frac{c}{|v_p^{1,2}|}. \quad (5.12)$$

Provided $v_p^1 \cdot v_E^1 \leq 0$, a medium acts as if it had a negative refractive index. When light exits such a medium into positive index media, it will be refracted to the same side of the normal, i.e. to a negative angle according to Eq. 5.11.

To probe the refraction properties of MIM-based metamaterials, two MIM waveguides are cascaded in series. The first waveguide, W1, is designed to sustain propagation of only a single negative-index mode over a broad continuous subset of the visible frequency range. The second waveguide, W2 is tailored to sustain propagation of only positive-index modes. By monitoring the refraction angle of light as it crosses the interface between W1 and W2, we can directly determine the index ratio n_1/n_2 , and hence the sign of n_1 .

Figure 5.14a illustrates the dispersion properties of the geometry chosen for W2: a planar Ag/Si₃N₄/Ag waveguide with a 500-nm-thick Si₃N₄ core. As usual, modal properties were calculated via numerical solution of Maxwell's equations and assume perfect coupling between each metal / dielectric interface [38, 37]. Such a waveguide sustains a number of TM modes³, each identified with the most closely related modes of a parallel-plate microwave waveguide [71]. As seen, most modes lie to the left of the Si₃N₄ light-line, $\omega = ck_0/n_d$, where n_d is the refractive index of the core and $k_0 = 2\pi/\lambda_0$. Unlike conventional plasmonic modes, these photonic modes are characterized by a propagation constant $\beta = |\text{Real}\{k_x\}| \leq n_d k_0$. In addition, a surface plasmon mode is present to the right of the light line. This plasmon mode is characterized by $\beta \geq n_d k_0$ and

³Transverse electric (TE) modes also exist but are not excited given the incident polarization.

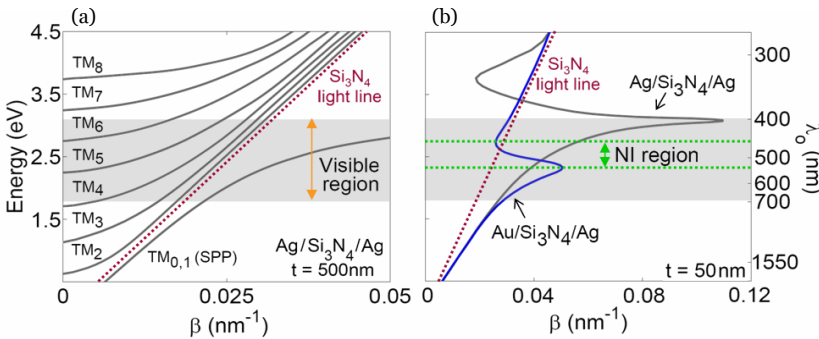


Figure 5.14. Implementation of positive- and negative-index MIM waveguides. **(a)** Calculated dispersion curves for a Ag/Si₃N₄/Ag waveguide with a dielectric core thickness $t = 500$ nm. **(b)** Calculated dispersion curves for Ag/Si₃N₄/Ag and Au/Si₃N₄/Ag waveguides with $t = 50$ nm. The visible frequency range is highlighted in gray, and the calculated negative-index regime for the Ag/Si₃N₄/Au waveguide is indicated in green.

corresponds to the degenerate, cutoff-free TM_0 and TM_1 modes propagating at each metal-dielectric interface. Over the entire visible range ($400 \text{ nm} \leq \lambda_0 \leq 700 \text{ nm}$), all allowed modes are characterized by $\text{Real}\{k_x\} \geq 0$, corresponding to a positive refractive index of light in the waveguide.

As the dielectric core thickness t is reduced, the cut-off energy of each photonic mode increases until only a single propagating plasmon mode remains. Below the surface plasmon resonance, this mode is characterized by a symmetric H_y field distribution and a positive real component of the wavevector. However, between the bulk and surface plasmon resonances, the propagating mode is characterized by an antisymmetric H_y field distribution and a negative real component of the wavevector. Figure 5.14b plots the dispersion diagram $\beta = |\text{Real}\{k_x\}|$ versus energy for this field antisymmetric mode, considering 50 nm of Si_3N_4 surrounded by Ag. As seen in the gray curve, the region of negative slope and hence negative index behavior lies in the ultraviolet. However, by replacing Ag with Au in one of the cladding layers, this region of negative slope can be shifted to the visible (Figure 5.14b, blue curve). In particular, this bimetallic waveguide is characterized by negative indices in the blue-green region of the visible, spanning wavelengths from 470 nm to 530 nm. Note that calculated losses of this structure indicate a figure of merit approximately equal to 4. Although this FOM does not represent the maximum achievable FOM in MIM metamaterials, it is notably higher than the quoted FOMs of resonator-based negative index materials (which range from 3 in the infrared to 0.5 in the visible [134, 146]).

5.3.2 MIM-metamaterial prisms for negative refraction

A schematic of the waveguide geometry used to demonstrate negative refraction is shown in Figure 5.15. As seen, a Au/ Si_3N_4 /Ag waveguide (W1) with a thin dielectric core is positioned between two identical Ag/ Si_3N_4 /Ag waveguides (W2) with thick dielectric cores. While t_1 was allowed to vary around thicknesses of $\sim 30\text{-}75 \text{ nm}$, t_2 was set to 500 nm. Fabrication was accomplished using a sequence of thermal evaporation and focused-ion-beam (FIB) milling steps on a suspended, 500-nm-thick Si_3N_4 membrane. Note that the 100-nm thicknesses of the Ag and Au cladding layers are substantially larger than the mode skin depth⁴. In addition, a 200-nm-thick layer of Al was deposited on each side of the waveguide, to ensure the complete opacity of the top and bottom cladding layers. Rectangular slits ($w=400\text{nm}$) were used to couple light into and out of the waveguide [36]. TM-polarized, coherent light illuminated the input slit at normal incidence, and the waveguide output was imaged using a 50x microscope objective coupled to a liquid-nitrogen-cooled CCD camera.

Direct characterization of positive or negative refraction was achieved by shaping W1 into a prism in the plane of propagation (Figure 5.15 and 5.16). A guided mode is first launched in W2 via the input slit. This mode impinges at normal incidence upon the leading edge of the prism, where it excites a surface plasmon mode that propagates through W1 with effective index n_1 . In turn,

⁴For $470 \text{ nm} \leq \lambda_0 \leq 530 \text{ nm}$, calculated skin depths in the Ag and Au layers do not exceed 21.5 nm and 30.0 nm, respectively.

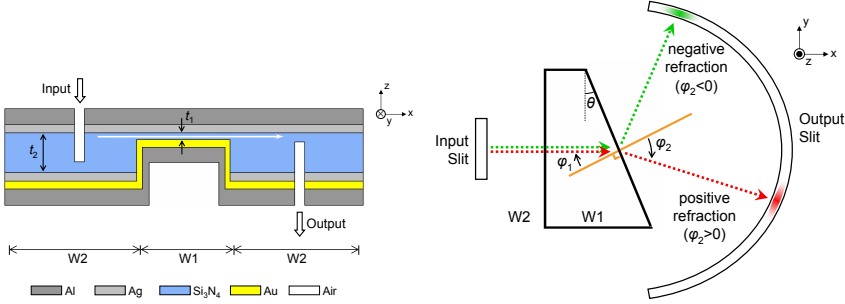


Figure 5.15. Cross-section and plan-view of refraction experiment. A prism-shaped segment of a Au/Si₃N₄/Ag waveguide (‘W1’) with variable dielectric core thickness is imbedded in a Ag/Si₃N₄/Ag waveguide (‘W2’) of fixed core thickness $t = 500$ nm. Two slits extending into the waveguide core are used to excite and intercept a guided electromagnetic mode. *Left*: Cross-section showing path of light through structure. *Right*: Corresponding plan view.

this plasmonic mode impinges upon the slanted interface between W1 and W2, at angle ϕ_1 equal to the prism angle θ . The mode is then refracted into a guided mode of W2 with effective index n_2 . The refraction angle ϕ_2 can be determined from the projected position of the mode on the output slit. Knowing the incident and refracted angles, Snell’s law (Eq. 5.11) can be used to determine the ratio n_1/n_2 .

Refraction results obtained at wavelengths of $\lambda_0 = 685$ nm and 514 nm are illustrated in Figure 5.17. As noted in Figure 5.14, these two wavelengths fall in the calculated positive- and negative-index regions of the MIM prism, respectively. Figure 5.17a evaluates waveguide transmission through W2 in the absence of a prism. The color scale at the output slit indicates normalized transmission intensity. For both $\lambda_0 = 685$ nm and 514 nm, a clear image of the input slit is projected onto the output slit. These results are consistent with previous observations of low lateral mode divergence within MIM waveguides (c.f. Chapter 4).

Figure 5.17b illustrates the effect of introducing two symmetric prisms of W1 into W2, each with Si₃N₄ thicknesses of 30 nm. The diagonal edges of both prisms are parallel and form an angle of 7° with respect to the launched wavefront. Here, refraction through the prisms corresponds to a vertical displacement of the beam at the detection screen. Note that this double-prism configuration corrects for differences in the optical path length, ensuring that the mode experiences uniform absorption during its transit from input slit to output slit. At $\lambda_0 = 685$ nm, the observed output-spot position indicates positive refraction at both slanted interfaces between W1 and W2, with an angle $\phi_2 = +0.1^\circ$. In contrast, at $\lambda_0 = 514$ nm the output-spot position indicates negative refraction between W1 and W2, with an angle $\phi_2 = -51^\circ$. Given the prism angle $\phi_2 = \theta = 7^\circ$, Snell’s law yields an index ratio $n_1/n_2 = +0.01$ and -6.26 at $\lambda_0 = 685$ nm and 514 nm, respectively.

Similar trends are observed for refraction through single MIM prisms, shown

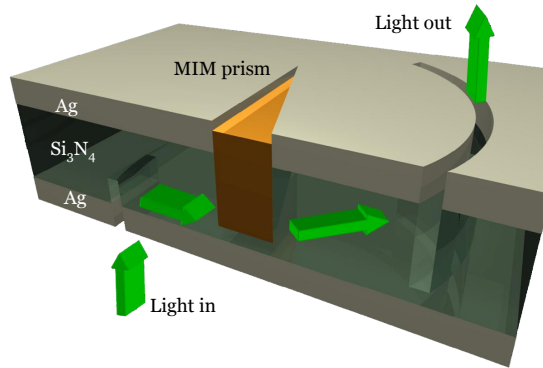


Figure 5.16. Three-dimensional schematic of negative refraction experiment.

in Figure 5.17c. Here, the straight output slit of Figure 5.17b is replaced with a semi-circular slit, to ensure that the refracted mode intersects the slit at normal incidence for any refraction angle. At $\lambda_0 = 685$ nm, the output spot position indicates small positive refraction at the interface between W1 and W2, with an angle $\phi_2 = +0.1^\circ$. When λ_0 is reduced to 514 nm, the output spot position shifts significantly, indicating large negative refraction. For this MIM prism, a refraction angle of $\phi_2 = -43.7^\circ$ can be observed. Given the incident angle $\phi_1 = \theta = 7^\circ$, Snell's law yields an index ratio $n_1/n_2 = -5.57$. For both wavelengths, the refractive index ratios agree well with those measured using the double prism configuration of Figure 5.17b.

The dispersion diagram of Figure 5.14b indicates that MIM metamaterial indices will vary with wavelength. This dispersion can be used to sort wavelengths in a refraction measurement, according to angle. Figure 5.18 illustrates the effect of changing the incident wavelength, spanning four lines available from an Ar laser. For example, at two closely-spaced wavelengths of $\lambda = 501$ nm and $\lambda = 488$ nm, substantially different refraction angles of $\phi_2 = -31.2^\circ$ and -27.1° can be observed. As the wavelength is decreased, negative index magnitudes continue to decrease until the bulk plasma resonance of Au is reached. For shorter wavelengths, the Au becomes effectively transparent, and light propagates along the waveguide as a positive index mode localized along the Ag/Si₃N₄ interface. For the bimetallic waveguides implemented here, calculations indicate a transition to a positive-index SPP mode for wavelengths shorter than $\lambda = 454$ nm. Not surprisingly, the observed refracted angle at $\lambda = 457$ nm is both small and positive.

To derive the refractive index of the Ag/Si₃N₄/Au prism, the index of the surrounding Ag/Si₃N₄/Ag waveguide must be determined. Unfortunately, the predicted multimodal dispersion properties of this 500-nm-thick photonic waveguide make explicit index determination challenging. However, interferometric techniques can be used to approximate an effective waveguide index (c.f. Chapter 4). To this end, Ag/Si₃N₄/Ag waveguides with 500-nm-thick dielectric cores were fabricated with a semi-transparent top Ag cladding layer of 150 nm; no additional Al cladding layer was added. The separation between input and output

slit was varied from $t = 1 \mu\text{m}$ to $3 \mu\text{m}$ in 25 nm increments. Each device was illuminated at normal incidence over its entire area and the intensity emitted from the output slit was monitored. Due to interference between the light transmitted along the waveguide and directly through the top Ag cladding layer, a periodic intensity modulation at the output slit can be observed. (see Figure 5.19). At a given wavelength λ_0 , the effective mode index of the waveguide is approximated as $n_2 = \lambda_0 / 2P$, where P is the period of the modulation.

Effective negative index data for the full set of Ag/Si₃N₄/Au prisms - including various prism thicknesses and angles - is compiled in Figure 5.20. For example, at $\lambda_0 = 514 \text{ nm}$, we obtain $n_2 = 0.82$, which implies refractive indices for the Ag/Si₃N₄/Au prisms which are both large and negative: $n_1 = -4.6$ and -5.1 for the double and single prisms, respectively. Figure 5.20 also displays this data as

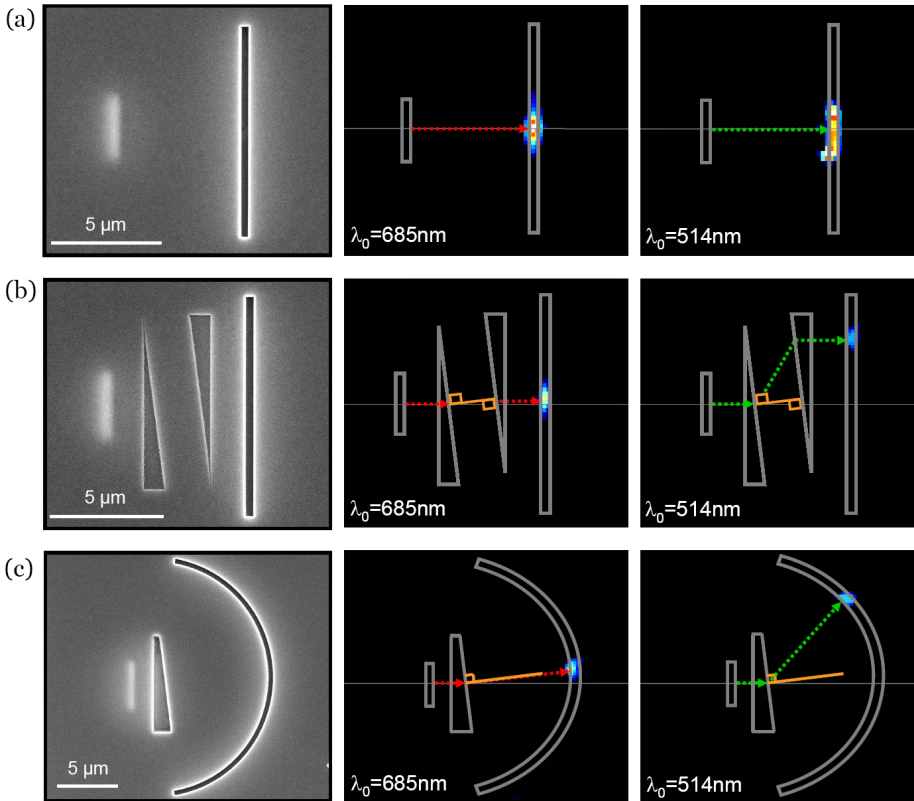


Figure 5.17. Direct visualization of in-plane negative refraction. Three waveguide configurations are explored: **(a)** W2 alone, **(b)** two prisms of W1 ($t_1 = 30 \text{ nm}$, $\theta = 7^\circ$) embedded in W2, and **(c)** one prism of W1 ($t_1 = 30 \text{ nm}$, $\theta = 7^\circ$) embedded in W2. *First column*: SEM image of output side. Input-slit position is revealed by electron-transparency. *Second and third columns*: optical microscope image of output side, given input-side illumination at $\lambda_0 = 685 \text{ nm}$ and 514 nm , respectively.

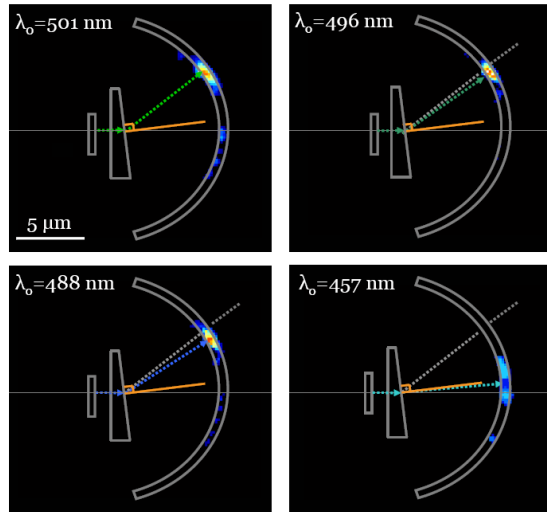


Figure 5.18. Wavelength-dependent refraction through the negative index Au/Si₃N₄/Ag prism. The core thickness and interface angle of the prism are held constant at $t = 45$ nm and $\theta = 7^\circ$, respectively. As the wavelength is scanned from 501 nm through to 488 nm, the refraction angle changes from -31.2° to -27.1° . At $\lambda = 457$ nm, refraction is small and positive as the transition to a positive index mode is reached. Note that in all panels, bands of positive and negative refraction can be observed, corresponding to weak transmission of a highly-damped positive-index mode in addition to the negative-index mode.

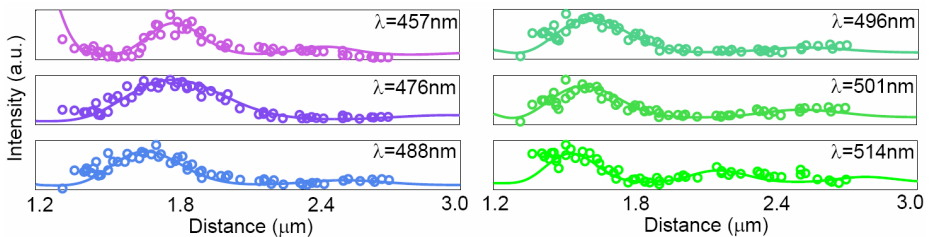


Figure 5.19. Experimental determination of the refractive index n_2 of the thick, Ag/Si₃N₄/Ag input waveguide. Measured output-slit intensity as a function of slit-slit distance t for wavelengths within predicted positive and negative index regions. Distance t is varied from 1 to 3 μm in 25-nm increments. The waveguide index is inversely proportional to the period of modulation. For free-space wavelengths of $\lambda = 457$, 476, 488, 496, 501, 514, and 685 nm, the resulting indices in the Ag/Si₃N₄/Ag waveguide are $n_2 = 0.71$, 0.40, 0.57, 0.50, 0.65, 0.82, and 0.75, respectively.

a dispersion diagram. The experimental data exhibit excellent agreement with the calculated H_y -antisymmetric SPP dispersion curve, shown here for $t=30$ nm. In particular, the experimental data clearly trace a region of negative slope in β versus energy for wavelengths between 476 and 514 nm. This wavelength regime is precisely the interval for which negative refraction is observed, confirming opposite phase and group velocities in this region. Moreover, note that variation of the prism angle yields near-constant indices for each wavelength (see table of Figure 5.20). This constancy of indices verifies the applicability of Snell's Law, and moreover, implies that MIM metamaterials are indeed isotropic in the plane of propagation.

5.3.3 Section summary: Experimental negative index materials

Using specially tailored metal-insulator-metal waveguides, we have demonstrated the first realization of a two-dimensional, isotropic negative-index metamaterial in the blue-green region of the visible. In an experimental application of Snell's Law, negative indices were calculated from direct geometric visualization of negative refraction - a measurement previously achieved only in the microwave regime. This general path to achieving NIMs at optical frequencies circumvents the difficulty of fabricating metamaterial resonator elements with lateral dimensions far smaller than the optical wavelength. Moreover, since light propagates in the plane of the NIM, the interaction lengths necessary to exploit negative refraction in practical applications are readily attained. Since negative indices can be obtained over a relatively large frequency range, MIM waveguides promise potential for broad-band negative refraction. By judicious choice of core and cladding materials and dimension, the operating range for such negative index materials can in principle be tuned throughout the entire electromagnetic spectrum.

5.4 Ongoing research in plasmonic metamaterials

Since Veselago composed his 1968 treatise, *The Electrodynamics of substances with simultaneously negative values of ϵ and μ* , researchers have strived to engineer these unnatural materials. Implementation of negative index materials was not just an exercise in fundamental materials science - indeed, considerable motivation was drawn from the wealth of NIM-based applications. As mentioned in Section 5.1, the ability to tune the index from positive to negative values can lead to such exotic and enabling applications as invisibility cloaks and 'perfect lenses' that can resolve features below the diffraction limit. In addition, negative index materials have been predicted to lead to a reversed Doppler effect, reversed Cerenkov radiation (i.e., radiation that is emitted backwards relative to the particle motion), and even negative radiation pressure [166].

Practical negative index metamaterials have now been implemented from frequencies spanning the microwave to the visible [136, 83, 161]. However, considerable work remains if the applications envisaged by Veselago and Pendry (not to mention Captain Kirk and Harry Potter) are to be fully realized. For

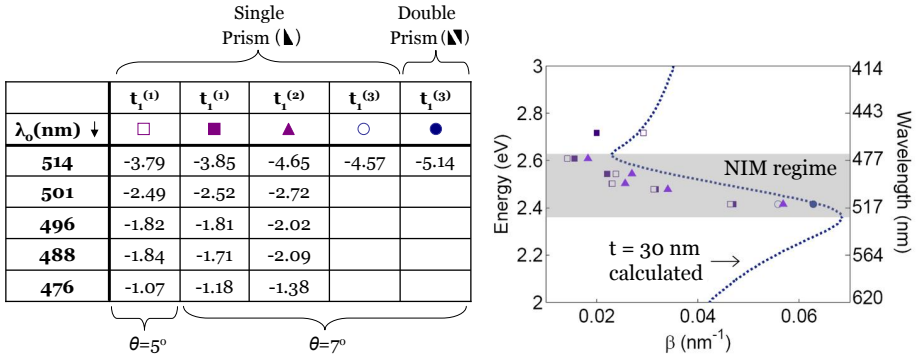


Figure 5.20. Measured mode index and mode dispersion of Au/Si₃N₄/Ag prisms with various values of t and θ , and for frequencies spanning the negative-index region ($t_1^{(1)}, t_1^{(2)}, t_1^{(3)}$) = (75 nm, 45 nm, 30 nm). The calculated H_y -antisymmetric dispersion curve for $t=30$ nm is also included. Note that indices generally increase with decreasing thickness, in agreement with dispersion calculations. Moreover, for $t_1^{(1)} = 75$ nm, mode indices remain constant at each wavelength as the prism angle is varied, confirming the applicability of Snell's law to these metamaterials.

example, the electrodynamics of NIMs remain largely unexplored; to date, research has only probed electrostatics. In addition, extending NIM operation to three-dimensions has not been achieved for any visible-frequency metamaterial. Moving beyond 'flatland photonics' represents a key step to implementing practical NIM designs in the visible.

5.4.1 NIM Electrodynamics: Toward direct observation of negative phase

A powerful technique for probing ultrafast processes on subwavelength scales is the phase-resolved photon scanning tunneling microscope (PSTM). Like a conventional NSOM, a subwavelength fiber aperture is scanned over the sample to obtain intensity distributions with sub-100nm resolution. Phase information is obtained through heterodyne detection: the NSOM output is interfered with a phase-delayed reference signal from the source. Femtosecond time resolution is obtained by pulsing the source and scanning either the probe (a 'fixed time' measurement) or the reference branch (a 'fixed probe' measurement). Ultrafast PSTM can detect signals on the order of fW with a time resolution on the order of 10 fs [128].

In Chapter 4, NSOM was used to probe the near-field of MIM guided modes below the surface plasmon resonance. By thinning the top cladding layer of a MIM waveguide, the interference between the MIM mode and an air-SPP mode could be observed. The MIM wavevector was explicitly determined by scanning double-slit output configurations.

Current experimental efforts are devoted to extending these near-field measurements to MIM-based negative-index materials. By combining NSOM and

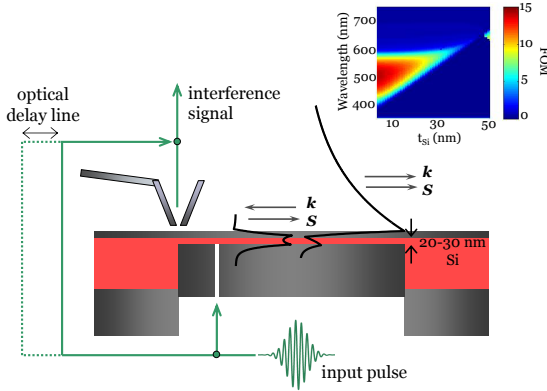


Figure 5.21. Direct probe of electrodynamics in negative index materials, using phase-resolved scanning tunneling microscopy. An input pulse excites the various modes of the Ag/Si-based plasmonic geometry, which can be probed through a semi-transparent top cladding layer. As seen in the inset, Ag/Si-based structures provide high FOM, broadband negative index operation, spanning wavelengths between 400 nm and 600 nm.

PSTM, the electrodynamic properties of negative index MIM geometries can be probed. A schematic of the experimental setup is shown in Figure 5.21. Samples consist of a thin (20-30 nm) Si layer clad with Ag. For this geometry, negative indices can be observed for wavelengths between 400 and 600 nm, with FOMs as high as 15 (see inset). Light is input through a slit in the bottom cladding layer, and the MIM field is probed using a near-field tip in collection mode. Femtosecond pulses coupled with heterodyne detection allow for ultrafast (fs) phase-resolved mapping of the NIM dynamics.

Figure 5.22 illustrates FDTD simulations of the predicted interference between the negative index MIM mode and the positive-index air-SPP mode at a wavelength of $\lambda = 532$ nm. For a tip-to-sample separation of 20 nm, interference fringes between the negative and positive index modes can be observed over distances of 400 nm from the slit. Although this distance is substantially less than the interference extent for positive index MIM modes (shown in the inset for $\lambda=980$ nm), it is sufficient to accurately probe the negative index mode using NSOM. Figure 5.22 also illustrates a FIB image of a single NIM waveguide for this experiment. A 100-nm-thick suspended Si membrane was fabricated using standard chemical etching techniques. Focused ion beam milling was used to locally thin the membranes down to thicknesses of 20-30 nm. Subsequently, thermal evaporation and FIB milling were used to define the cladding layers and input slits. This sample will soon be sent to our collaborators at AMOLF, who will perform preliminary characterization with a standard NSOM. Thereafter, PSTM measurements to map the phase and time evolution of negative index modes will be performed in collaboration with L. Kobus Kuipers at AMOLF, a leader in ultrafast near-field photonics. If successful, these measurements will enable the first direct probe of electrodynamics in negative index materials.

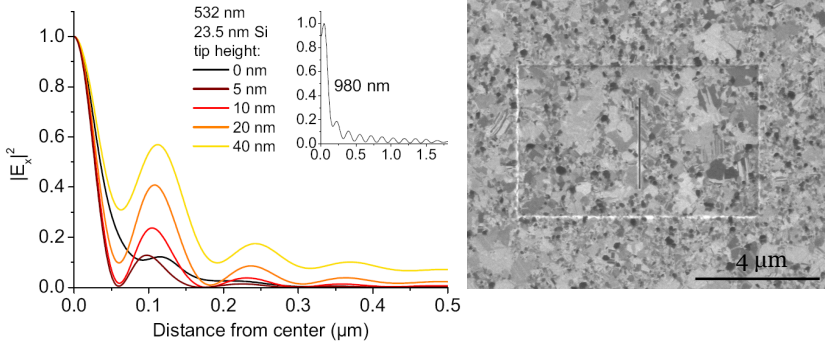


Figure 5.22. Simulation and fabrication of a negative index near-field interferometer. *Left*: Finite-difference time-domain simulations of interference patterns. For various near-field tip-to-sample separations, interference fringes can be observed, resulting from interference between the various modes of the structure. At $\lambda = 532$ nm, interference results from the presence of both positive and negative index modes. The inset plots predicted interference at $\lambda = 980$ nm, where only positive index modes exist in the structure. *Right*: FIB image of fabricated Ag/Si/Ag waveguide, with a single slit input.

5.4.2 Toward a three-dimensional negative index material

MIM waveguides exhibit all the requisite criteria for practical NIM designs: antiparallel group and phase velocities, broadband negative refraction, and ease of fabrication. However, these single-layer MIM waveguides are restricted to two-dimensional operation, since their response is anisotropic out-of-plane. Extension to three dimensions will require stacking these planar slabs, essentially using single MIM waveguides as the building blocks of a three-dimensional metamaterial. To achieve three-dimensionality, two requirements must be satisfied: (i) the metamaterial must be isotropic, i.e., the response of the material to an electromagnetic wave should be independent of angle; and (ii) the metamaterial index must be an intrinsic quantity that does not depend on the surrounding media, i.e., the metamaterial index must not depend on the number of MIM layers in the stacked geometry.

In addressing criteria (i), Gennady Shvets has suggested that photonic waveguides arranged in a triangular lattice can exhibit complete isotropy [140, 141], provided \vec{k} lies within the Brillouin zone. Accordingly, a hexagonal array of MIM waveguides could mimic a three-dimensional metamaterial. However, to address criteria (ii), the metallic cladding layers must be properly designed. For example, if the cladding layers are sufficiently thin, each MIM waveguide will be coupled to its neighboring waveguides and the index will depend on the number of MIM layers. However, if the cladding is too thick, the metamaterial building blocks may lose their subwavelength dimensionality.

Figure 5.23 plots the variation of guided mode indices as a function of the number of insulating layers in a stacked [MIMIM...MIM] waveguide. Here, we consider a simple quasi-three-dimensional structure with each MIM waveguide

stacked directly on top of the previous guide. The metal and dielectric layers are Ag and GaP, respectively, with realistic losses included. Two structures are considered: a metallodielectric stack composed of 30 nm GaP / 100 nm Ag and a metallodielectric stack composed of 30 nm GaP / 70 nm Ag. Analytic waveguide mode indices are calculated at a wavelength of $\lambda = 488$ nm. Note that only one propagating, negative index mode exists for a single slab waveguide at this wavelength, with $n = -2.56$.

As seen in the figure, as the number of GaP layers is increased, the number of modes increases: the guided waves along each insulating layer become coupled. In general, N insulating layers will be characterized by N distinct refractive index modes. For 30 nm GaP surrounded by 100-nm-thick Ag layers, the mode index varies only slightly as the number of layers is increased. The largest calculated index variation spans $-2.57 < n < -2.43$. Moreover, the distribution of indices remains constant for more than 5 GaP layers. In contrast, for 70-nm-thick Ag cladding layers, mode indices vary by over fifty percent, ranging between $n = -2.16$ and $n = -3.26$ as the number of GaP layers is increased. Accordingly, for true three-dimensionality, the metallic cladding layers in a multilayer stack should be at least 100 nm.

To illustrate the negative indices of MIM multilayers, Figure 5.24 plots wave refraction into MIM stacks composed of 100 nm Ag and 30 nm GaP. The source wavelength is again taken to be $\lambda = 488$ nm, and the H_y field is monitored along the xy plane, adjacent to a GaP/Ag interface. The incident angles with respect to the surface normal are 20° and 50° in Figure 5.24a and b, respectively. As expected, horizontal stacking of MIM waveguides produces in-plane negative refraction (c. f. Figure 5.8). Interestingly, vertical stacking of MIM waveguides also produces a refraction pattern analogous to negative refraction. In this case, refraction can be traced across phase fronts, even though the field intensity oscillates between each metal and dielectric layer. Such results may not have been

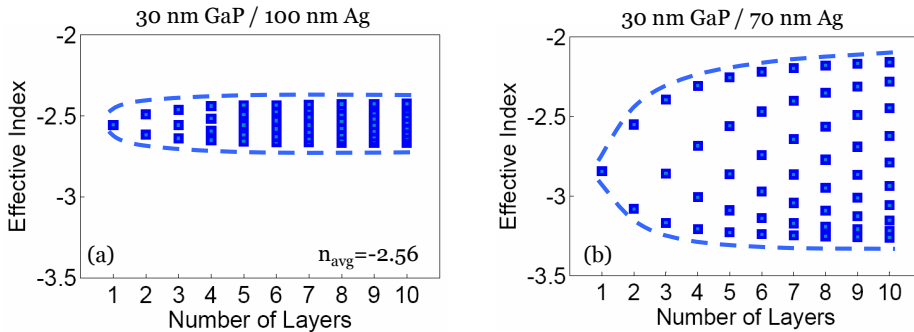


Figure 5.23. Mode indices for three-dimensional negative index geometries, composed of stacks of individual MIM waveguides. For 30 nm GaP clad by 100 nm Ag (a), the effective mode index remains constant with increasing number of “I” layers. However, as the Ag is thinned to 70 nm (b), increasing variability in the calculated mode index is seen. In both geometries, indices are calculated for a free-space wavelength of $\lambda = 488$ nm.

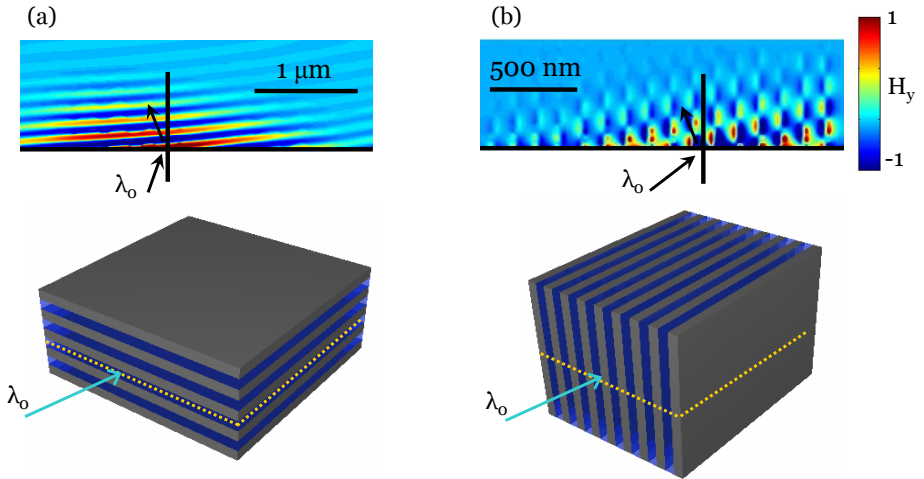


Figure 5.24. Negative refraction into MIM multilayer ‘basis sets’, composed of horizontal or vertical waveguide stacks with 30 nm GaP and 100 nm Ag. Light of wavelength $\lambda_0 = 488$ nm is incident on the structures and refracts toward negative angles in both cases.

expected a-priori, given the fairly weak coupling between each waveguide. Still, both stacking geometries exhibit phase fronts that propagate towards the source. Therefore, these planar multilayer metamaterials could be considered ‘basis sets’ for constructing fully isotropic, three-dimensional negative index materials.

5.5 Chapter Summary

This chapter has explored the use of plasmonic waveguides as metamaterials. In the first section, we saw that IMI, IIM, and MIM waveguides all support negative indices over a finite range of frequencies. However, MIM waveguides proved to be the only structures that could support a single, propagating negative index mode at a given frequency. By designing suitably thin MIM waveguides, we were able to achieve the first negative index material in the blue-green region of the visible. Negative indices were substantiated by direct observation of negative refraction through a prism. Unlike resonator-based metamaterials, MIM geometries depend only on the plasmonic properties of two smooth metal-dielectric interfaces. Therefore, tuning the regime of negative index operation is a straightforward matter of tuning the core and cladding dielectric constants. For example, a Si/Ag-based MIM metamaterial can exhibit negative indices over wavelengths spanning 400 nm - 600 nm, with FOMs as high as 15. The index tunability in MIM waveguides appears promising for implementation of transformation-based optical elements, including magnifying superlenses and invisibility cloaks. In addition, the inherent simplicity of MIM metamaterials allows for direct probing of NIM electrodynamics, and hints at their potential as building blocks for three-dimensional negative index materials.

6 Active Plasmonic Devices Based on Dispersion Engineering

‘I remember the difficulty we had replacing magnetic cores in memories...Eventually we had both cost and performance advantages. But it wasn’t at all clear in the beginning.’

-Gordon Moore

6.1 Plasmonic dispersion has a silver lining

The field of plasmonics has experienced marked growth in the past decade, motivated in part by its potential applicability to on-chip photonics. As seen in the introduction to this thesis, surface plasmons are characterized by both intense local electric fields and extremely small wavelengths relative to free-space. Combined, these two features have allowed for unprecedented manipulation of electromagnetic energy on subwavelength scales. On-chip photonic components including subwavelength waveguides [153, 73, 152], modulators [107, 159], and detectors [39] have become possible because of the unique properties of surface plasmons. In addition, plasmonic components have enabled more efficient light emitting diodes and improved light collection in thin-film photovoltaic cells [20, 118].

While dispersion - the variation of phase velocity with wavelength - is generally frowned upon in photonic applications, it is a critical, albeit inescapable, component of many plasmonic devices. As we saw in the last chapter, light propagation in matter depends only on two intrinsic material properties - the electric permittivity and the magnetic permeability. Since the electric permittivity of metals is a strong function of wavelength, so too is the surface plasmon wavelength. Such dispersion enables ready tuning of the plasmonic index and propagation constant simply by tailoring the waveguide composition and dimensions. Alternatively, small shifts in the waveguide index or dimensions could profoundly impact plasmon propagation.

In this chapter, we explore the dispersive nature of surface plasmons for active photonic applications. Particular attention is given to MIM-based geometries, where optical nonlinearities can be enhanced by high field confinement in the dielectric slot. Section 6.2 discusses development of a Si-compatible field effect MOS plasmonic modulator, called a plasmistor. Electro-optic modulation of up to 11 dB is achieved in device volumes as small as one-fifth of a cubic wavelength with femtoJoule switching energies and the potential for GHz modulation frequencies. Section 6.4 introduces a concept for a full-color, ‘flat-panel’ display based on MIM waveguide-resonators. By appropriate design of the resonator dimensions and end-facets, broadband light is filtered into individual colors that span the visible spectrum; the filtered colors can be switched by replacing the

MIM core with an active transparent dielectric. In both devices, the MIM ‘silver lining’ for dispersion engineering doubles as the waveguide cladding and as the electrical contact.

6.2 The PlasMOStor: A metal-oxide-Si field effect plasmonic modulator

The integrated circuits ubiquitous in modern technology were critically enabled by the invention of the metal-oxide-semiconductor field effect transistor (MOSFET) - a three terminal device that modulates current flow between a source and drain via an applied electric field. Since the first successful demonstration of MOSFETs in the 1960’s, silicon devices and circuits have continuously scaled according to Moore’s law, increasing both the integration density and bandwidth of complementary metal-oxide-semiconductor (CMOS) networks. At present, microprocessors contain over 800 million transistors clocked at 3 GHz, with transistor gate lengths as small as 35 nm [66, 21]. Unfortunately, as gate lengths approach the single-nanometer scale, MOS scaling is accompanied by increased circuit delay and higher electronic power dissipation - a substantial hurdle to Moore’s Law often referred to as the “interconnect bottleneck.”

To circumvent the electrical and thermal parasitics associated with MOS scaling, new switching technologies are being considered. Particular attention has been given to optical technologies, which could achieve high integration densities without significant electrical limitations [97, 169]. Optical components would offer a substantially higher bandwidth, a lower latency, and a reduced power dissipation compared with electronic components [97, 169, 106]. Unfortunately, optical components are generally bulky relative to CMOS electronic devices, comprising dimensions on the order of the signal wavelength.

Use of plasmonic components offers a unique opportunity for addressing the size mismatch between electrical and optical components. Plasmonic devices convert optical signals into surface electromagnetic waves propagating along metal-dielectric interfaces. Because surface plasmons exhibit extremely small wavelengths and high local field intensities, optical confinement can scale to deep subwavelength dimensions in plasmonic structures.

Recent reports have demonstrated passive and active plasmonic components that combine low optical loss with high mode confinement. Metal-dielectric channels [23, 116, 24] and metal-insulator-metal slot structures [178, 38, 36, 138] have formed the basis for subwavelength plasmonic waveguides, interferometers, and resonators [62]. In addition, plasmon modulators based on quantum dots [107], ferroelectric materials [88], or liquid crystals [47] have been proposed and demonstrated. However, in terms of integrating standard Si-based electronics with Si-based photonics, it would be highly desirable to develop a suite of plasmonic devices with Si as the active medium. This approach would allow for compatibility with standard CMOS processing techniques and potential integration into existing ultra-large-scale integration (ULSI) networks. Unfortunately, unstrained Si exhibits an indirect bandgap and no linear electro-optic effect, yielding a continuous-wave optical response that is typically either slow or weak

[145, 144]. To date, neither a Si-based plasmonic waveguide nor plasmonic modulator have been demonstrated.

In this section, we present an experimental demonstration of a field effect Si modulator based on multimode interferometry in a plasmonic waveguide. Like the Si-based modulators implemented by Lipson and colleagues [176], this device utilizes high optical mode confinement to enhance electro-optical nonlinearities in Si. Moreover, like the Si optical modulator of Liu and colleagues [86], this device exploits accumulation conditions in a metal-oxide-semiconductor (MOS) capacitor to achieve GHz modulation frequencies. In contrast with these structures, our plasmonic modulator achieves modulation of over 11 dB in a subwavelength-scale waveguide. In particular, our device illustrates that conventional scaled MOSFETs can operate as optical modulators, by transforming the channel oxide into a plasmon slot waveguide.

Figure 6.1 illustrates the general operation and band diagrams for a *conventional* electronic n-MOSFET. Here, current is modulated between a p-type source and drain via an applied electric field at the gate. For gate voltages

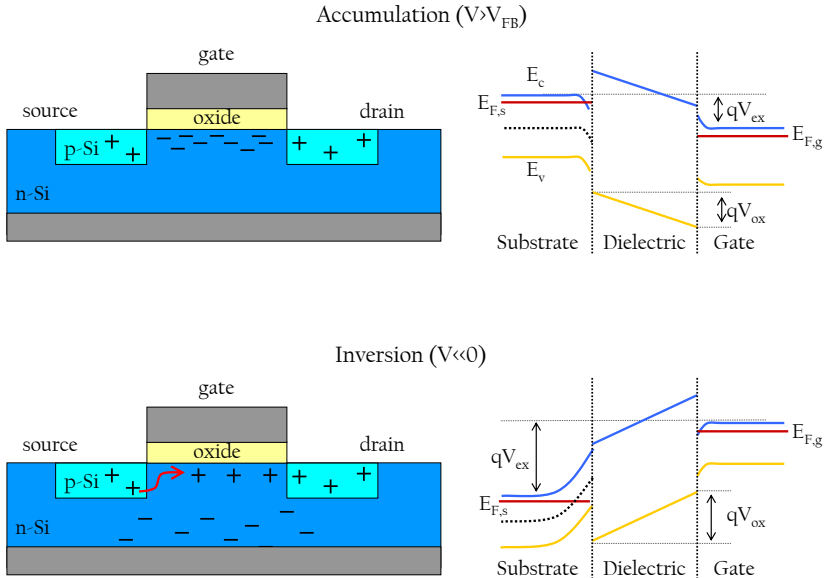


Figure 6.1. Schematic and band diagram of a conventional electronic n-MOSFET. Current is modulated between a p-type source and drain via an applied electric field V_{ex} at the gate. An applied bias induced a voltage drop V_{ox} across the oxide and bends the conduction (E_c), valence (E_v), and fermi (E_F) levels of the gate and Si substrate. *Top*: For gate voltages above the flat-band voltage, the device is in accumulation and electrons in the n-type Si form a two-dimensional electron gas that prohibits the flow of holes from the source to the drain. *Bottom*: For negative applied biases, an inversion layer of minority carriers forms just below the oxide. This layer creates a channel between the source and drain for holes to flow, switching the device to its ‘on’ state.

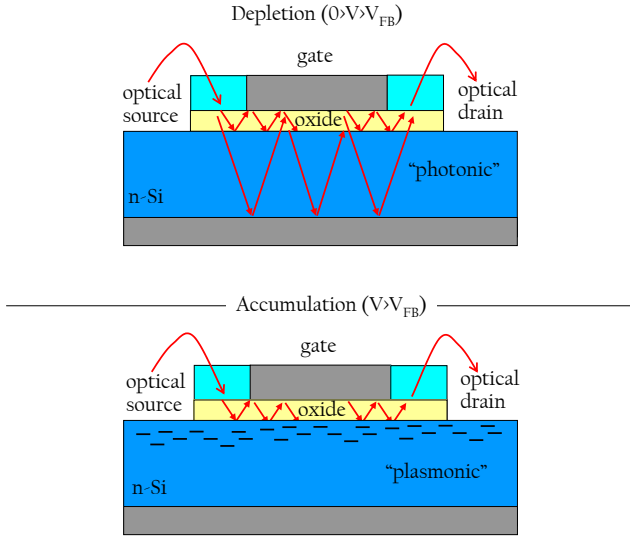


Figure 6.2. Schematic of a plasmonic MOSFET for modulation of optical signals. In the absence of an applied gate voltage, the plasmistor is fully depleted, and light can be guided through both the Si and SiO₂ layers. For applied voltages greater than the flat band voltage, an accumulation layer forms that inhibits wave propagation through the Si. In this accumulated state, light will be almost exclusively guided through the channel oxide and will exit the drain without interference from the Si-guided mode.

above the flat-band voltage, the device is in accumulation and electrons in the n-type Si form a two-dimensional electron gas (2DEG) that prohibits the flow of holes from the source to the drain. In contrast, for negative biases, electrons in the substrate are repelled and an inversion layer of minority carriers forms just below the oxide. This layer creates a channel between the source and drain for holes to flow, switching the device to its ‘on’ state.

Our plasmonic modulator is essentially an n-MOSFET designed to operate in accumulation. A schematic of this ‘plasMOSter’ is shown in Figure 6.2. As seen, the electronic source and drain are replaced with an optical source and drain for light to enter and exit the device. In the absence of an applied field at the gate, the plasmistor is fully depleted and light can be guided through both the Si and SiO₂ layers. Depending on the waveguide length, these two modes will interfere either constructively or destructively at the optical drain. However, for voltages greater than the flat band voltage, an accumulation layer forms that inhibits wave propagation through the Si. In accumulation, light will be almost exclusively guided through the thin channel oxide, and will exit the drain without interference from the Si-guided mode.

Figure 6.3 illustrates the specific geometry of our plasmistor. As seen in Figure 6.3a, the modulator consists of a 4-layer metal-oxide-Si-metal waveguide. The plasmistor was prepared from single-crystalline, n-doped Si-on-insulator wafers. Using standard etching and oxidation techniques (see Appendix C), a

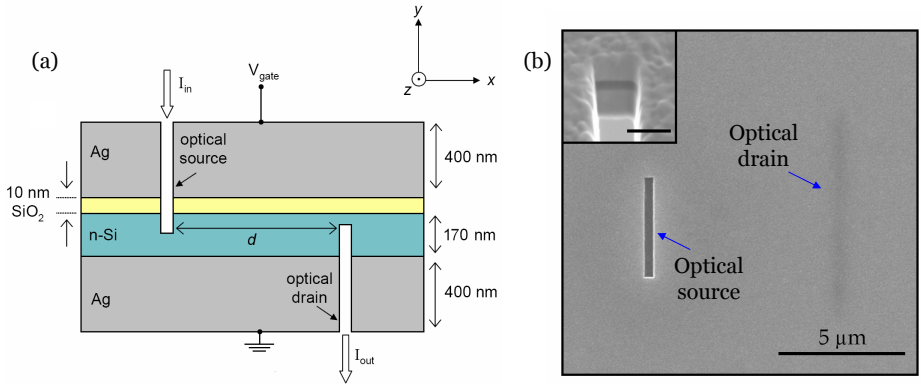


Figure 6.3. Geometry of the fabricated Si field effect plasmonic modulator (plasmistor). **(a)** Cross-sectional schematic of the modulator. Subwavelength slits milled through the Ag cladding form the optical source and drain, through which light is coupled into and out of the modulator. **(b)** Scanning electron micrograph of the plasmistor as viewed from the optical source side. The optical drain is visible due to electron transparency. The inset shows a cross-sectional cut through the 4-layer plasmistor waveguide (scale bar is 500 nm).

large cm-scale suspended Si membrane was fabricated with a uniform thickness of 170 nm, as determined by spectroscopic ellipsometry. Subsequently, a thin 10 nm SiO₂ layer was thermally grown on the top surface of the Si. Thermal evaporation was used to deposit 400-nm-thick Ag layers onto each side of the membrane, forming both the plasmistor cladding and the gate contact. Light was coupled into and out of the plasmistor via subwavelength slits etched into the top and bottom cladding layers (Figure 6.3b), though end-fire excitation could also be used. Use of slits in a double-sided coupling configuration ensures a clean experimental platform devoid of any parasitic background signal. Note that in this geometry, the slits function as the optical source (input) and drain (output) of the plasmistor. To map transmission as a function of device length, the source-drain separation was varied from approximately 1 - 8 μm in 50 nm increments.

Figure 6.4 illustrates the dispersion diagram and mode profiles that characterize the unbiased plasmistor waveguide. Modal properties were calculated via a numerical solution of Maxwell's equations and assume uniform coupling across the waveguide stack. For reference, the dispersion diagram also includes the light lines in Si and SiO₂, corresponding to light propagation through bulk media with refractive index $n = n_{\text{Si}}$ or n_{SiO_2} .

As seen in Figure 6.4, the plasmistor supports a variety of transverse magnetic modes. In particular, at a wavelength of $\lambda = 1.55 \mu\text{m}$, the unbiased plasmistor supports two modes: a photonic mode lying to the left of the Si and SiO₂ light lines (red arrow), and a plasmonic mode lying to the right of the Si light line (blue arrow). Both modes will be generated at the plasmistor source and can interfere either constructively or destructively at the drain, depending on the

source-drain separation. As seen in the table of Figure 6.4, the photonic mode (red) is characterized by an electric field localized predominately in the Si core and a mode index of $n=0.375$. In contrast, the plasmonic mode (blue) exhibits maximal field intensities within the SiO_2 channel and a mode index of $n=3.641$. While the high plasmonic mode index arises from mode overlap with the Ag and Si layers, propagation losses remain relatively low. At $\lambda=1.55 \mu\text{m}$, losses of the plasmonic and photonic modes are $0.207 \text{ dB}/\mu\text{m}$ and $2.37 \text{ dB}/\mu\text{m}$, respectively. For both modes, fields in the metal cladding decay within approximately 20 nm of the Ag-Si and Ag- SiO_2 interfaces.

The nearly flat dispersion of the photonic mode around $\lambda=1.55 \mu\text{m}$ suggests that this mode will be extremely sensitive to changes in the Si complex index. For example, modifying the Si index through free-carrier absorption will push this mode into cutoff, such that the dispersion curve intercepts the energy axis just above $\lambda=1.55 \mu\text{m}$. The remaining plasmonic mode will then propagate through the plasmistor without interference from the photonic mode.

In the plasmistor, such changes in the Si index are induced by applying a positive bias to the gate. For drive voltages above the flat-band voltage, electrons in the n-type Si form an accumulation layer characterized by a peak carrier concentration at the Si/ SiO_2 interface and a spatial extent given by the Debye length. Figure 6.4b tabulates the theoretical change of mode index and propagation length with the onset of accumulation. Here, the accumulation layer is modeled as a multi-layer Drude electron gas with an average carrier concentration of approximately $5 \times 10^{18} \text{ cm}^{-3}$ and a Debye decay length of 14 nm (see Appendix C for details). As expected, the effective index and losses of the plasmonic mode exhibit very little change between the voltage-off (depletion) and voltage-on (accumulation) states. In particular, the plasmonic mode index varies from the off state by $\delta n = 0.008$, and losses are only slightly increased to 0.228

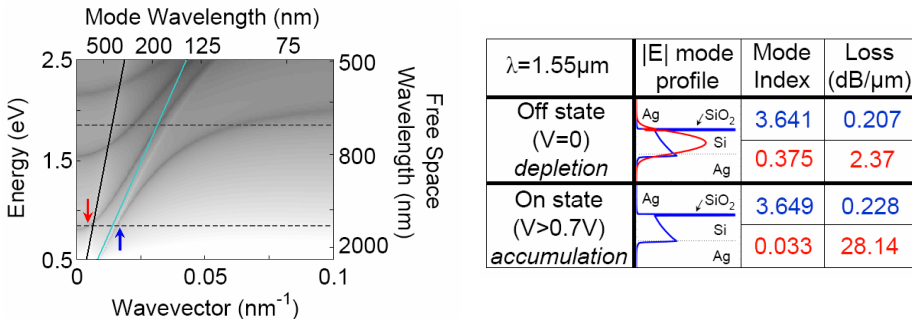


Figure 6.4. Dispersion relations and tabulated mode properties of the plasmistor. **(a)** Calculated transverse-magnetic dispersion relation for the plasmistor in the off (depleted) state; the grey scale indicates the mode line width. Light lines for SiO_2 (black solid line) and Si (cyan solid line) are also included. The horizontal grey dashed lines indicate free-space wavelengths of $\lambda = 1.55 \mu\text{m}$ and $\lambda = 685 \text{ nm}$. **(b)** Tabulated mode profiles, refractive indices and losses for the plasmistor in both depletion (voltage-off) and accumulation (voltage-on) states.

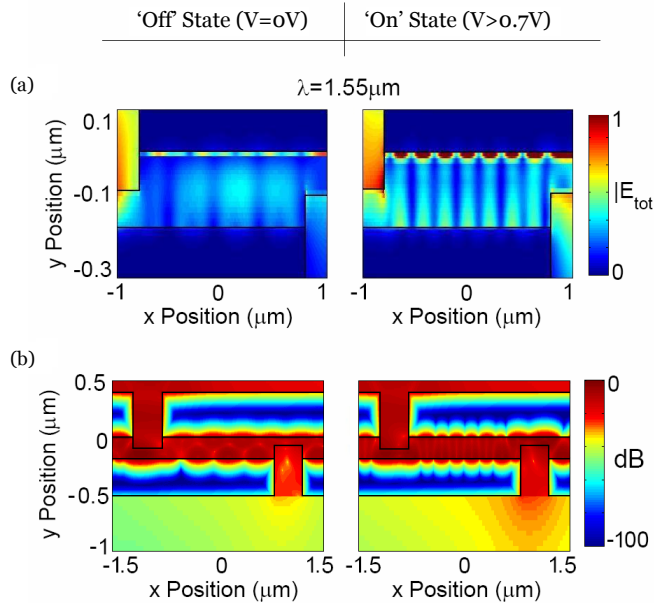


Figure 6.5. Finite difference time domain simulations of the plasmistor, showing the total electric field (a) and the transmitted power (b) for a 2- μm -long optical source-drain separation. Plasmistor mode and power profiles at $\lambda = 1.55 \mu\text{m}$ are shown in both the voltage-off (left column) and voltage-on (right column) states.

$\text{dB}/\mu\text{m}$. However, the photonic mode is pushed into cutoff, as indicated by the near-zero mode index and substantially increased losses (i.e., the photonic mode becomes evanescent and can no longer propagate power through the device). Therefore, in the accumulation state, the plasmistor will guide near-infrared light almost exclusively through the SiO_2 channel[75], solely via the plasmonic mode.

Modulation of the electric field distribution and out-coupled power is illustrated in the finite difference time domain simulations of Figures 6.5 and 6.6.[2] In these simulations, the plasmistor is illuminated through the optical source with a gaussian beam of wavelength $\lambda = 1.55 \mu\text{m}$ or $\lambda = 685 \text{ nm}$, and the source-drain separation is set to $d = 2 \mu\text{m}$. As seen in the left column of Figure 6.5a, in the absence of an applied field, plasmistor transmission at $\lambda = 1.55 \mu\text{m}$ is distributed throughout the Si core with sparse regions of high electric field in the oxide slot. However, with the onset of accumulation, the field transmitted within the Si core is notably decreased. As seen in the right column of Figure 6.5a, plasmistor fields are localized predominately within the 10-nm-thick oxide layer, which acts as a channel between the optical source and optical drain. Within the slot, pronounced maxima and minima within the resonator can be observed with a wavelength of $\sim 225 \text{ nm}$.

By choosing the source-drain separation to correspond to a condition of destructive interference between the photonic and plasmonic mode, plasmistor transmission can be substantially increased by inducing accumulation. Fig-

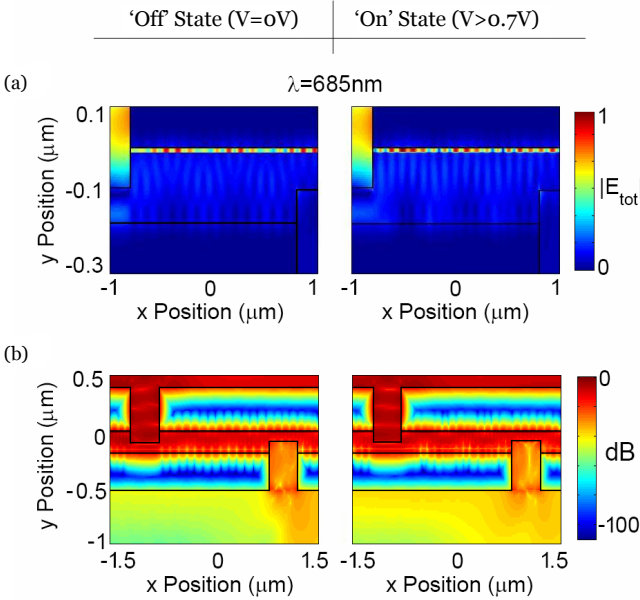


Figure 6.6. Finite difference time domain simulations of the plasmistor, showing the total electric field **(a)** and the transmitted power **(b)** for a $2\text{-}\mu\text{m}$ -long optical source-drain separation. Plasmistor mode and power profiles at $\lambda = 685 \text{ nm}$ are shown in both the voltage-off (left column) and voltage-on (right column) states.

Figure 6.5b plots the total power transmitted through the plasmistor at $\lambda = 1.55 \mu\text{m}$, with $d = 2 \mu\text{m}$. Comparing intensities at the optical drain between the voltage-off and voltage-on states, modulation ratios exceeding $+10 \text{ dB}$ can be observed.

As wavelengths approach the visible range, the plasmistor begins to support a number of photonic and plasmonic modes (see Figure 6.4). At $\lambda = 685 \text{ nm}$, for example, the unbiased plasmistor exhibits three modes with effective indices of $n = 5.36, 3.40,$ and 2.28 . An applied field shifts these indices to $n = 5.35, 3.34,$ and 2.15 . Such multimode behavior is readily visualized in the FDTD simulations of Figure 6.6. However, because Si is more absorbing in the visible, the propagation lengths of these modes do not exceed $3 \mu\text{m}$. The accumulation layer induces higher losses in the structure, and modulation between the voltage-off and voltage-on states results almost exclusively from absorption of all modes. The higher absorption and multi-mode behavior at visible wavelengths suggest that this particular plasmistor design is ideally suited for near-infrared operation.

Experimental capacitance-voltage (CV) curves were used to characterize the electrical response of our fabricated plasmistor. Figure 6.7a shows a high-frequency CV curve obtained with a driving frequency of 100 kHz . As the figure reveals, the plasmistor is in a state of inversion for negative biases, depletion for biases between 0 and 0.7 V , and accumulation for biases greater than 0.7 V . The flat-band voltage, where the Si layer is charge neutral, occurs around

0.5 V. From the total observed accumulation capacitance (35 pF) over the 100 μm by 100 μm measured area A , we infer the capacitance of a typical $2 \times 2 \mu\text{m}^2$ plasmistor as $C_{\text{device}} = C_{\text{total}}(A_{\text{device}}/A_{\text{total}}) = 14 \text{ fF}$.

To characterize the optical response, the out-coupled intensity from the plasmistor was monitored as a function of gate bias. An infrared laser source ($\lambda = 1.55 \mu\text{m}$) was focused onto a single device and transmission through the optical drain was imaged using a 50x microscope objective coupled to a Ge detector. Depending on the source-drain separation - and hence the interference condition of the photonic and plasmonic modes in the depleted state - transmitted intensity could increase or decrease with applied bias. As seen in Figure 6.7b, a modulator of length $d_1 = 2.2 \mu\text{m}$ exhibits a pronounced intensity increase with increasing positive bias for $\lambda = 1.55 \mu\text{m}$. Consistent with the capacitance-voltage curves, modulation saturates around 0.7 V, corresponding to the onset of accumulation. In contrast, a modulator of length $d_2 = 7.0 \mu\text{m}$ exhibits a 30% decrease in transmitted intensity for $\lambda = 1.55 \mu\text{m}$.

Full experimental optical characterization was achieved by varying the source-drain separation and the illumination wavelength, both with and without an applied bias. Figures 6.7c and d show plasmistor transmission as a function of resonator length for source wavelengths of 685 nm and $1.55 \mu\text{m}$, respectively. As seen in Figure 6.7c, at a wavelength of 685 nm, negligible modulation is observed for TM-polarized light between the voltage on and off states of the modulator. For shorter cavity lengths, transmission predominately decreases with applied bias. Cavities longer than $2.5 \mu\text{m}$ are dominated by extinction, consistent with mode propagation lengths derived from calculations.

In contrast, the plasmistor exhibits pronounced modulation for near-infrared sources. As seen in Figure 6.7d, with no applied bias, plasmistor transmission at $\lambda = 1.55 \mu\text{m}$ is characterized by an output signal comprised of both high and low frequency components. As illustrated by the dispersion diagram of Figure 6.4, these components correspond to the plasmonic and photonic waveguide modes, respectively. An applied bias of 0.75 V forces the photonic mode into cut-off, leaving only a single, high-frequency mode in the waveguide. Experimentally, the observed propagation length of this mode is in good agreement with the plasmonic mode losses predicted from calculations. The observed mode index is about half the calculated plasmon index, likely due to aliasing effects arising from the chosen optical source-drain separation step-size. Still, resonator lengths of approximately $2 \mu\text{m}$ exhibit an amplitude modulation ratio of +11.2 dB. Such observations are remarkably consistent with the simulations of Figure 6.5b. To our knowledge, this plasmistor yields the highest reported near-infrared Si modulation depth in the smallest reported volume, with channel areas (length \times thickness) as small as $10 \text{ nm} \times 2 \mu\text{m} = 0.014 \lambda^2$, and device volumes as small as one one-fifth of a cubic wavelength.

Plasmistor modulation depths remain high for wavelengths spanning from $1.48 \mu\text{m}$ to $1.58 \mu\text{m}$ (the range of our infrared source), where changes in the complex refractive index of Si induce cut-off of the photonic mode. For these wavelengths, significant modulation is preferentially observed in shorter resonator lengths ($d \leq 3 \mu\text{m}$), which in the depleted state produce destructive interference between the photonic and plasmonic modes. Previous Si modulators

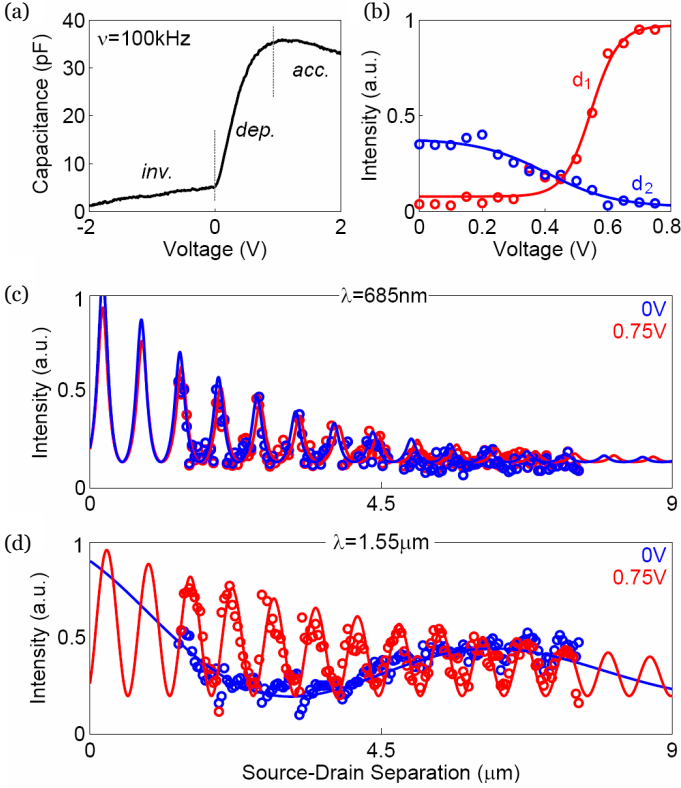


Figure 6.7. Experimental electrical and optical characterization of the plasmotor. **(a)** High-frequency capacitance-voltage curve of the modulator, showing the onset of accumulation at $V = 0.7$ V. **(b)** Optical drain intensity as a function of gate bias for two source-drain separations ($d_1 = 2.2 \mu\text{m}$ and $d_2 = 7.0 \mu\text{m}$) at $\lambda = 1.55 \mu\text{m}$. **(c and d)** Optical drain intensity as a function of source-drain separation for the voltage-off state (blue, $V = 0$) and the voltage-on state (red, $V = 0.75$ V) at $\lambda = 685$ nm **(c)** and $\lambda = 1.55 \mu\text{m}$ **(d)**. Experimental points are shown as open circles, with the radius encompassing the experimental error. Best fits based on resonator theory are shown as solid lines.

based on MOS capacitors, in contrast, require device dimensions on the order of millimeters[86]. Interestingly, the intrinsic losses of the plasmotor are not significantly higher than 1 dB (for a source-drain separation of $d=2.2 \mu\text{m}$, the plasmonic mode has losses as low as 0.5 dB). Thus, despite the higher losses generally associated with plasmonic components, the plasmotor exhibits intrinsic losses that are comparable with and even less than traditional Si- or dielectric-based modulators[86, 176, 87].

High-frequency performance of the plasmotor was characterized by applying a 4 V, 100 kHz pulse train to the modulator with a rise-time of 10 ns. Switching speeds of the plasmotor were determined to be at least as fast as 10 ns, which represents the limit of our experimental detection. Note however that modu-

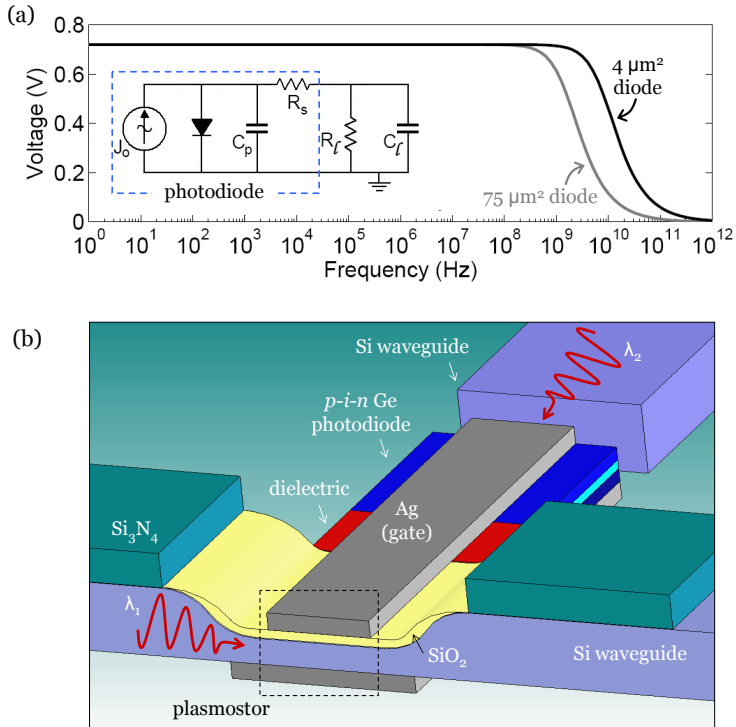


Figure 6.8. An all-optical, SOI-based plasmistor. An ideal photodiode is connected to a load resistor and the plasmistor, forming a three-terminal device capable of GHz operation. **(a)** Circuit analysis of the coupled photodiode-plasmistor system, modelling the photodiode after Reference [70] and the plasmistor as a MOS capacitor. The load resistance was chosen so that the photodiode provides the appropriate gate bias to the plasmistor. Photodiodes with active areas of $75 \mu\text{m}^2$ (grey curve) and $4 \mu\text{m}^2$ (black curve) allow system bandwidths (3 dB roll-off frequencies) of 3 GHz and 15 GHz, respectively. Bandwidths could potentially be improved by further decreasing the photodiode size or the modifying the channel thickness. Circuit parameters for the $75 \mu\text{m}^2$ diode, load resistor (R_ℓ) and plasmistor MOS capacitor (C_ℓ) are: $J_o = 0.6 \text{ mA}$, $C_p = 66 \text{ fF}$, $R_s = 32 \Omega$, $R_\ell = 1200 \Omega$, $C_\ell = 14 \text{ fF}$. Parameters for the $4 \mu\text{m}^2$ diode, resistor, and plasmistor are: $J_o = 0.6 \text{ mA}$, $C_p = 2 \text{ fF}$, $R_s = 50 \Omega$, $R_\ell = 1200 \Omega$, $C_\ell = 14 \text{ fF}$. **(b)** Schematic of an SOI-based all-optical plasmistor. Note that the dimensions of this device could reach deep subwavelength scales.

lation speeds of the plasmistor will be limited only by the speed of formation of the accumulation layer. Therefore, the geometry of this MOS-based device could in principle achieve modulation frequencies in the GHz regime. The circuit simulations below confirm this achievable bandwidth of the plasmistor.

The accumulation-based operation of the plasmistor allows the device to be modelled as a capacitor that can be charged or discharged by either electrical or optical means. For example, a photodiode connected to the plasmistor gate

could provide sufficient power to modulate the channel properties[103]. The plasmistor would be driven into accumulation via all-optical means, provided the photodiode could produce gate voltages exceeding 0.7 V. Figure 6.8 proposes such a scheme for all-optical modulation. As seen, a Ge p-i-n photodiode is connected to the plasmistor in parallel with a dielectric (a resistor). Using a photodiode with an active area of $75 \mu\text{m}^2$ and an ~ 40 GHz bandwidth [70], circuit simulation indicates coupled plasmistor-photodiode bandwidths of 3 GHz (Figure 6.8a). Scaling the photodiode active area to $4 \mu\text{m}^2$ (and thereby increasing the photodiode bandwidth [70]), coupled plasmistor-photodiode bandwidths increase to 15 GHz. Further improvements could be achieved by modifying the oxide thickness or the plasmistor gate length. Moreover, by tuning the magnitude of the optical carrier (λ_1) and signal (λ_2) sources, this coupled photodiode-plasmistor system could exhibit signal gain at the plasmistor drain[103]. This three-terminal, integrated optical device requires no electronic conditioning and can be fabricated from SOI waveguide technology, using, for instance, local oxidation of silicon (LOCOS) processing. Such processing would facilitate CMOS compatibility while minimizing optical insertion losses.¹

The plasmistor offers a unique opportunity for compact, Si-based field effect optical modulation using scaled electronic MOSFET technology. The low switching voltages (0.7 V) and low experimentally-determined capacitance (14 fF) yield a required switching energy $E = CV^2/2$ of approximately 3.5 fJ, commensurate with existing CMOS and optical logic gates[86]. Furthermore, by modulating optical signals with a photodiode coupled to the gate, the plasmistor promises potential for opto-electronic and perhaps even all-optical Si-based modulation.

6.3 Photonic and plasmonic color displays

The near-infrared operation of the plasmistor was chosen to coincide with the C-band for fiber-optic communications ($1530 \text{ nm} \leq \lambda \leq 1565 \text{ nm}$). At such wavelengths, fiber optics exhibit losses of less than 0.2 dB/km and can transmit information at a rate exceeding 15 Tbit/s. Though fiber optic technology has been challenging to implement over the ‘last mile,’ the plasmistor may facilitate implementation throughout the ‘last micron.’

Aside from infrared modulators, many applications require filters and switches for visible wavelengths. Among these applications are color displays. Within the past decade, significant advances have been made in the field of display technologies. Low profile ‘flat-panel’ displays have been realized using plasma, rear projection, organic light-emitting diode, and liquid crystal technologies. To date,

¹For the plasmistor geometry presented in Figure 6.3, insertion losses through the slit source and drain are calculated to be 12.8 dB. However, finite-difference time-domain simulations indicate substantially reduced losses for end-fire excitation. For example, direct end-fire excitation from a 170 nm Si waveguide into the plasmistor can exhibit coupling efficiencies as high as 36%, corresponding to losses of 4.4 dB. Further optimization of the in-coupling structure can lead to insertion efficiencies as high as 93%, corresponding to losses as low as 0.3 dB (see Reference [165]). The LOCOS processing technique proposed in Figure 6.8 inherently takes advantage of such end-fire excitation schemes. Therefore, the total losses of the plasmistor (including insertion losses and propagation losses) could be as low as 0.8 dB by appropriate design of in-coupling structures.

a significant portion of flat-panel computer monitors and virtually all laptop displays are based on liquid crystal display (LCD) technology.²

Liquid crystal displays exploit the properties of birefringent molecules to control the polarization of light. The molecules are placed between two cross-polarized filters and an applied electric field modifies the helicity of the molecule to either allow or inhibit white-light transmission through the two-filter combination. The emission wavelengths are controlled by color filters placed across each pixel. While LCDs have revolutionized visual communications, they suffer from a number of drawbacks associated with resolution, speed, and cost. In particular, LCDs exhibit limited viewing angles, a limited color pallet, a relatively slow response time (generally exceeding 12 ms), and a high cost associated with the multi-layer film deposition required for manufacturing.

Here, we address some of the limitations of liquid crystal displays by exploiting the properties of MIM waveguide dispersion. As we have already seen, MIM geometries provide a particularly appealing platform for dispersion engineering, since the number of supported modes can be readily tuned with the core thickness or index. Moreover, since light can be in and out-coupled on opposite sides of the structure, MIM waveguides naturally provide high-contrast imaging even with low incident or transmitted intensities.

Figure 6.9 illustrates the basic MIM waveguide geometry used for color filtering. As usual, a dielectric layer is sandwiched between two metallic layers. The dielectric is designed to be transparent for visible frequencies with a real or complex refractive index that can be tuned by an applied electric field. Moreover, the dielectric thickness exceeds $\frac{\lambda}{2n}$ so that a number of waveguided modes will be supported. As with the plasmostor, input and output slits (with width ~ 400 nm) are patterned into the top and bottom cladding layers. White light from a lamp or diode illuminates the top cladding layer and is scattered from the slit into the dielectric. The light then propagates through the waveguide and is outcoupled via the slit in the bottom cladding layer. The multiple modes of the waveguide will interfere at the output, producing a specific visible color depending on the input-output (cavity) separation and the slit depth. Because the output is viewed in a dark-field transmission configuration, note that this waveguide design resembles conventional back-lit displays.

Ideally, the MIM display element will be designed to allow a certain number of modes in the off state ($V_{applied}=0$) and either inhibit or introduce additional modes in the on state. For example, Figure 6.9 includes the dispersion curves for 400 nm of LiNbO₃ clad by Ag on each side. LiNbO₃ is a ferroelectric perovskite with one of the largest electro-optic coefficients commercially available [172]; modest applied voltages to *x*-cut LiNbO₃ ($n_e \sim 2.2$) can induce index shifts as large as $\Delta n = +0.11$. In these calculations, both the Ag and LiNbO₃ were modeled using empirically-determined, frequency-dependant dielectric constants, as determined from ellipsometry. The dispersion diagram in the absence of an applied voltage is shown in Figure 6.9a. As seen, four photonic modes and one plasmonic mode are supported for energies between 1.5 and 3.5 eV. By applying

²This section has been adopted from K. Diest, J. A. Dionne, and H. A. Atwater, Reference [35] and CIT Patent [10].

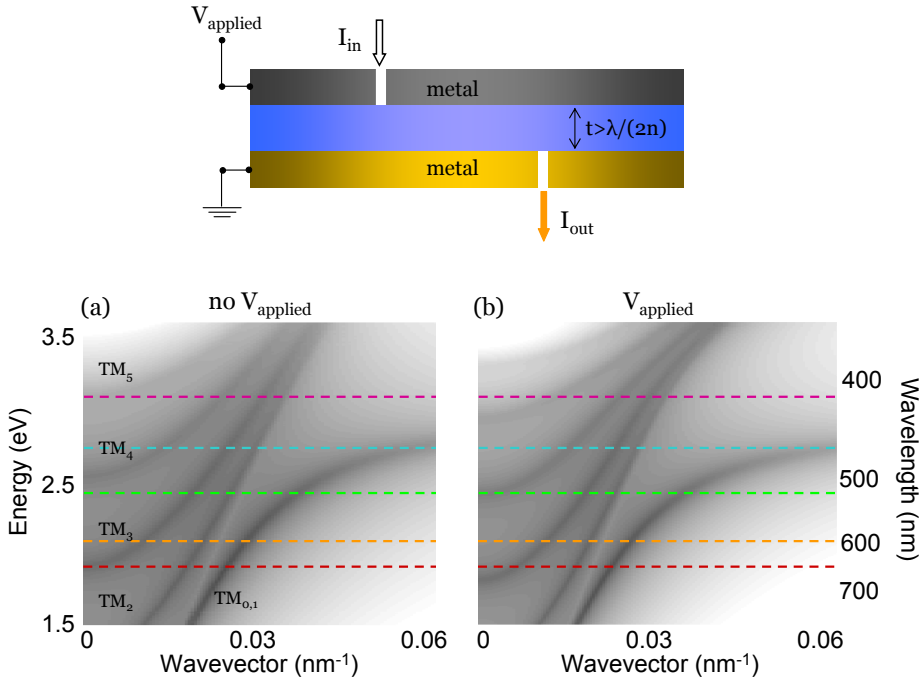


Figure 6.9. Schematic MIM ‘flat-panel’ display and associated dispersion relations. The display is composed of a thick dielectric layer clad with optically-opaque metals on each side. Slits through the metal couple white light into and out of the waveguide; filtered colors are viewed through the output slit in a dark-field, ‘back-lit’ configuration. In **(a)** and **(b)**, dispersion is plotted for an infinitely-long, 400-nm-thick LiNbO_3 slab clad with Ag on each side. A number of photonic modes are supported throughout the visible spectrum in the voltage-off state, **(a)**. These modes are shifted to lower energies in the voltage-on state, **(b)**.

an electric field, and thereby switching the index from n_e to $n_o = n_e + \Delta n$, the distribution of modes can be substantially red-shifted (Figure 6.9b). In particular, an applied field shifts the TM_5 mode to overlap with violet excitation frequencies and the TM_3 mode to overlap with red excitation frequencies.

In general, excitation schemes agnostic to wavevector (i.e., not relying on prism or grating coupling) will most efficiently excite the lowest propagating wavevector available at a given frequency.³ Of course, the spectra of the transmitted signal will be a function of both the complex mode wavevector and the cavity length. Nevertheless, dispersion diagrams alone can provide heuristic guidelines for color filtering. For example, in the absence of an applied voltage, Figure 6.9 suggests that broadband visible-frequency illumination will most ef-

³While this statement has not been strictly proven, it is based on both experimental observations and on analytic calculations. In particular, low wavevector modes are analytically more optimal solutions to the dispersion equations.

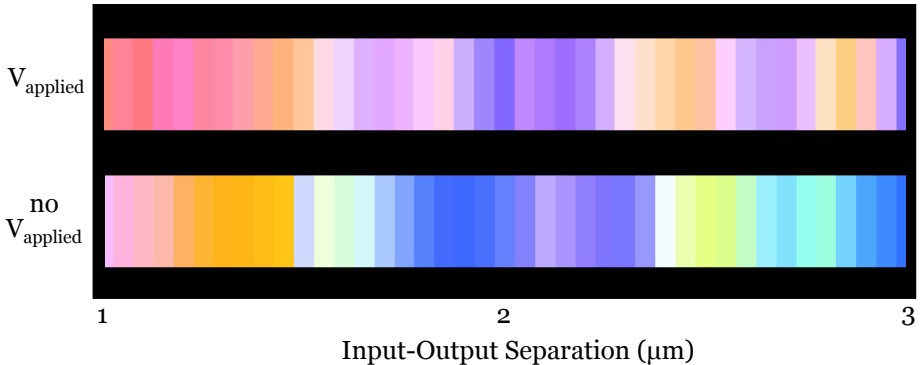


Figure 6.10. Display colors as a function of voltage and input-output separation for a Ag/400nm LiNbO₃/Ag waveguide, simulated using FDTD. Simulations courtesy of K. Diest, adopted from [10] and [35].

ficiently excite the TM₃ and TM₄ modes, spanning wavelengths from the blue through the orange regimes. Therefore, the perceived color at the output slit will depend on interference of these modes. Most significantly, neither red nor violet will be present in the output spectra, since no combination of the excited TM₃ and TM₄ primary colors can produce red or violet. Rather, the colors most strongly transmitted will include hues of orange, yellow, green, and blue.

In contrast, an applied field induces propagation of the TM₃ and TM₅ modes for red and violet frequencies, respectively. In addition, the TM₄ mode becomes predominately excited by blue and violet frequencies, while greener frequencies become cutoff. Therefore, an applied field should shift the color distribution to hues of red, orange, blue, and violet.

Figure 6.10 illustrates the achievable color filtering and switching in a 400-nm-thick LiNbO₃ waveguide clad by Ag. Results were obtained via FDTD simulations [2] of a TM-polarized, broadband pulse ($400\text{nm} \leq \lambda \leq 700\text{nm}$) through the waveguide.⁴ Both the input and output slits penetrated the Ag to a depth halfway through the LiNbO₃; slit widths were defined to be 400 nm. The waveguide length (from slit-edge to slit-edge) was varied from 1 μm to 3 μm in 100 nm increments. The time-dependent signal from the output slit was monitored in the far-field and subsequently fourier transformed to produce a spectrum. The output spectra were correlated to a perceived color by taking the inner product between this signal and the RGB Color Matching Functions [1].

The bottom panel of Figure 6.10 plots perceived color from the Ag/LiNbO₃/Ag waveguide in the absence of an applied field. As seen, the output color varies as a function of waveguide length, but is dominated by hues of orange, blue, yellow, and cyan. In contrast, an applied field shifts these perceived colors to hues of

⁴In the version of Lumerical used for these simulations, the Ag optical constants could only be described at the peak of the input pulse, $\lambda = 550\text{nm}$. Since publication of this section, Lumerical has now released a simulation code that can fit optical constants over a broad range of frequencies with up to six fit parameters.

red, magenta, violet, and orange. For example, color switching from orange to magenta, blue to violet, and blue to orange can be seen for waveguide lengths of $1.3 \mu\text{m}$, $1.9 \mu\text{m}$, and $2.6 \mu\text{m}$, respectively.

While color switching is notable, a full sampling of the primary colors is not present for input-output spacings of less than $3 \mu\text{m}$. Ideally, all primary colors could be generated by a MIM cavity of this size, to allow for the smallest possible ‘pixel’ element. Additional dispersion engineering can be achieved by varying the input-output slit depth, rather than the waveguide length. For example, the dispersion diagrams of Figure 6.9 identified a number of transverse-magnetic modes of this waveguide, each characterized by either a symmetric or antisymmetric field distribution across the waveguide. Naturally, these different modes will project a unique field distribution onto the output slit, depending on the input-output slit separation. Accordingly, distinct colors will be observed depending on the relative amplitudes of the various modes averaged over the output slit. Put otherwise, the output spectrum may be a strong function of slit depth.⁵

⁵For a detailed mathematical discussion of scattering from an abruptly terminated plasmon waveguide, see Appendix D.

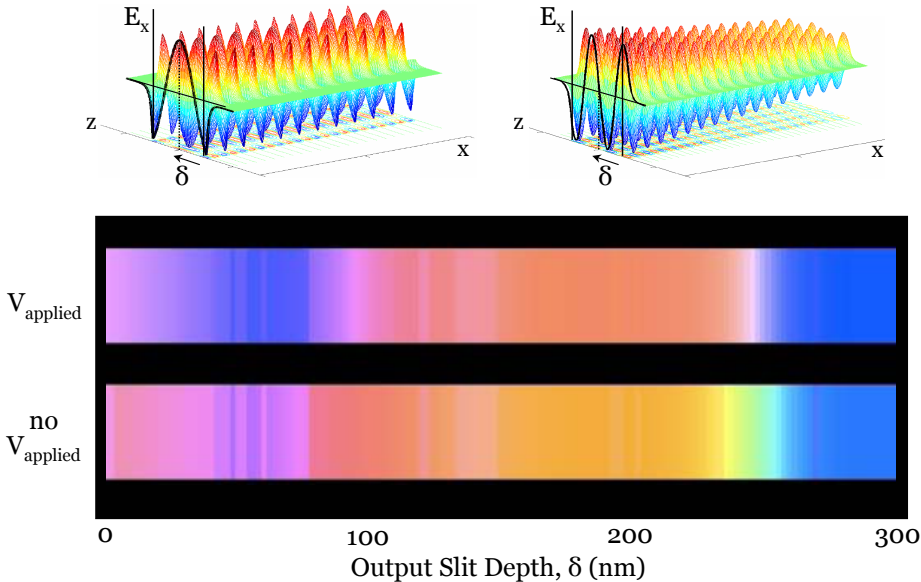


Figure 6.11. Display colors as a function of voltage and output slit depth for a Ag/300nm LiNbO₃/Ag waveguide, simulated using FDTD. The input slit depth is set to extend 150 nm through the 300 nm LiNbO₃. By varying the output-slit depth, excited waveguide modes can be convoluted to produce unique color combinations. For reference, the spatial profile of two tangential electric field modes are included. Note that this waveguide also includes modes with one node and zero nodes. Simulations courtesy of K. Diest, adopted from [10] and [35].

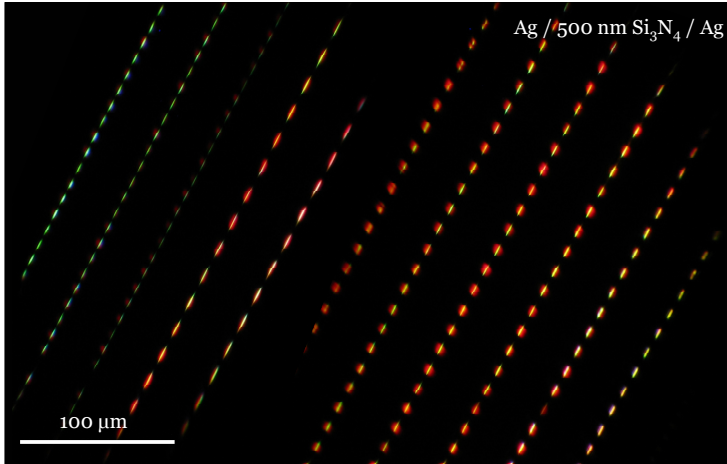


Figure 6.12. Experimental color filtering in passive MIM waveguides composed of 500 nm of Si_3N_4 clad with 400 nm Ag on each side. Input-output spacings are varied along each column from $d = 1 \mu\text{m}$ to $10 \mu\text{m}$ in $\sim 200 \text{ nm}$ increments, and slit depths are varied horizontally across the image in $\sim 20 \text{ nm}$ increments from the top Ag/ Si_3N_4 interface to the bottom. White light illumination through the input slit produces filtered colors from the output slit that span hues of green, cyan, yellow, magenta.

Figure 6.11 illustrates the projected color dependence on slit depth, considering 300 nm of LiNbO_3 clad by Ag. Note that a thinner waveguide was chosen to limit the number of simulations necessary to span the entire core; however, the effect is general to any LiNbO_3 thicknesses that supports multiple modes. In these simulations, the input slit depth was set to extend halfway through the LiNbO_3 , and the input-output separation was fixed at $d = 2.6 \mu\text{m}$. The output slit depth was varied from 0 nm through 300 nm into the LiNbO_3 , in 2 nm increments. For reference, the figure also includes the spatial distribution for the TM_3 and TM_4 modes. As seen, nearly the entire visible spectrum can be generated from the output slit simply by varying the slit depth. Applying a voltage shifts the perceived colors to dominant hues of red and blue.

An experimental demonstration of the achievable color filtering in MIM waveguides is illustrated in Figure 6.12. Here, 500 nm of Si_3N_4 was clad with 400 nm Ag on each side. Slits were defined with lengths of 5 or $10 \mu\text{m}$ and widths of 400 nm, using FIB milling. Input-output spacings were varied along each column from $d = 1 \mu\text{m}$ to $10 \mu\text{m}$ in $\sim 200 \text{ nm}$ increments, and slit depths were varied horizontally across the image in $\sim 20 \text{ nm}$ increments from the top Ag/ Si_3N_4 interface to the bottom. White light illumination from an unpolarized W-lamp source illuminated the structure from the top, and the output color was monitored from the bottom with a 20x microscope objective. As seen, visible colors ranging from cyan to green, yellow, orange, and red are produced. Similar to the LiNbO_3 simulations, many of the generated colors appear to have a pastel tint.

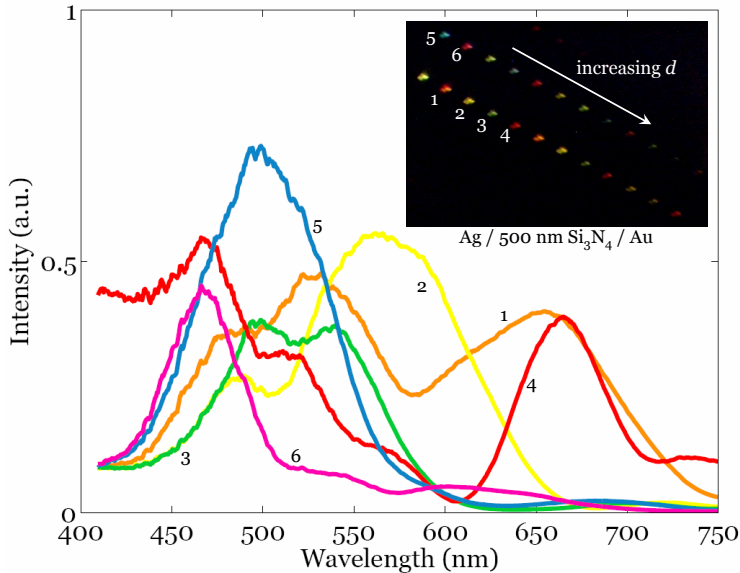


Figure 6.13. Experimental spectra of passive MIM waveguides composed of 500 nm Si₃N₄ clad with 400 nm Ag on one side and 400 nm Au on the other. All spectra have been normalized to the lamp source. As seen in the inset, this bimetallic cladding produces richer hues of the primary colors that span the full visible spectrum. Note that the blur in the inset is an artifact from the image acquisition.

Interestingly, the primary colors can be enhanced by using a bimetallic cladding, as shown in Figure 6.13. Here, 500 nm of Si₃N₄ was clad with 400 nm Ag on the top and 400 nm Au on the bottom. The input and output slit depths were fixed to extend halfway through the Si₃N₄, and the input-output spacing was varied from $d = 1 \mu\text{m}$ to $6 \mu\text{m}$ in 500 nm increments. Note that each column of devices in the inset image represents a distinct slit width - corresponding to 400 nm in the first column and 300 nm in the second. As seen in the spectra, the full range of primary colors can be generated, with notably richer hues than the Ag-based waveguides. While this richness of colors is not well understood, it is likely due to enhanced interference effects arising from plasmons of different phase velocities propagating at each metal-dielectric interface.

Like LiNbO₃, Si₃N₄ has an index close to 2 and low losses that render it transparent to visible frequencies. However, unlike LiNbO₃, Si₃N₄ is not an electro-optic material. Accordingly, the perceived color cannot be switched with an applied voltage. Current efforts are aimed at fabricating active LiNbO₃-based structures for this application, a delicate process that requires a combination of bonding, polishing, and annealing. Such fabrication is beyond the scope of this thesis, but is being actively explored in our lab.

For commercial applications, the active MIM color filters presented here could be easily integrated into a high density color filter or display. By fabricating output slits to each side of the input slit, the transmitted light from an individual

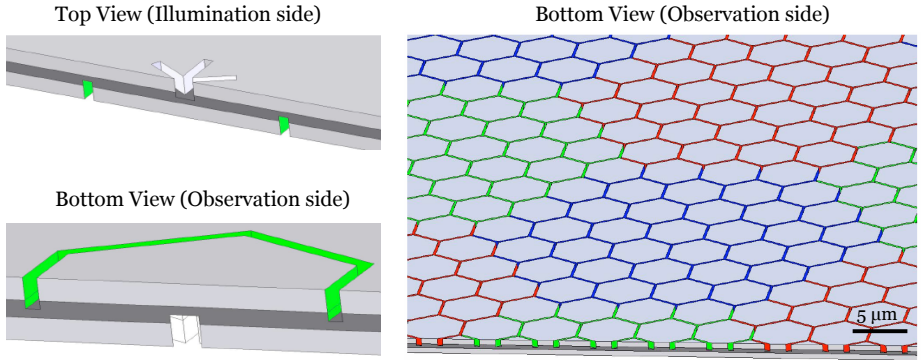


Figure 6.14. Perspective view of a MIM-based pixel element (*left*) and full-color display (*right*). Pixels are patterned as hexagons and tiled together to form the full display screen. Figure courtesy of K. Diest, adopted from [10] and [35].

waveguide could be doubled. Moreover, by interlacing three of these elements together, each rotated 120° from the prior, a hexagonal MIM pixel could be produced. A cross-section of such a waveguide is shown in Figure 6.14. As seen, a central, star-shaped slit serves as the input, launching waveguided modes towards each side of the hexagonal output slits. Overall dimensions of this pixel need not exceed $6\ \mu\text{m}$, orders of magnitude smaller than the optimal high-definition color displays currently available [85]. Additionally, these hexagonal pixels could be tiled together to form ‘superpixels’ that increase the relative transmission of a given color. Indeed, the largest dimension of these superpixels could still be smaller than the $\sim 80\ \mu\text{m}$ resolution of the human eye at a viewing distance of 35 cm [18]. To maintain a uniform density of superpixels, the various colors could be selected by simply varying the depth or width of the output slits, rather than the waveguide length. Moreover, by exploiting the electrooptic effect in LiNbO_3 or another active material, color switching speeds could be as fast as 1 ns, substantially faster than current displays based on liquid crystals or nematic twist filters [174, 8].

6.4 Chapter Summary

By combining active materials with MIM waveguides, modulators for both visible and infrared wavelengths can be designed. In the two applications discussed here - the plasmistor and a color display - MIM geometries reduce the device footprint and increase switching speeds with respect to conventional approaches. Moreover, MIM waveguides have the advantage of integrated cladding layers and electrical contacts, a desirable characteristic for applications requiring compact, high-contrast devices. Whether or not plasmistors and superpixels find a place in commercial technology, they demonstrate an unusual technique for modulation via mode cutoff, based on the unique dispersive properties of plasmonic waveguides.

7 Summary and Outlook

‘Time is the longest distance between two places.’

-Tennessee Williams

In recent years, plasmonic components have rapidly evolved from discrete, passive structures toward integrated active devices that could comprise an all-optical, nanophotonic networking technology. Such progress has been facilitated by opportunities to dispersion engineer metallodielectric systems. Surface plasmons provide access to an enormous phase space of refractive indices and propagation constants that can be readily tuned through variation of material, dimension, or geometry.

Opportunities for dispersion engineering are particularly pronounced in two-dimensional planar metallodielectric geometries, the subject of this thesis. Our journey into ‘flatland photonics’ began with a theoretical discussion of plasmonic modes. Via analytic calculations, we found that planar plasmon waveguides can support extremely small mode wavelengths and large local electric field intensities compared to photons in dielectric media. Within metallic core waveguides, plasmon propagation lengths could approach centimeter scales. However, such long range propagation was achieved at the cost of confinement: the field of metallic core waveguides was found to extend many microns into the surrounding dielectric, hampering applications for on-chip interconnects.

Inverting metallic core waveguides to form a plasmon slot, or metal-insulator-metal (MIM) waveguide, provided a much more favorable localization-loss balance. Within these MIM waveguides, plasmon propagation could extend several tens of microns, with lateral mode dimensions significantly smaller than the wavelength. In addition, MIM waveguides were found to support modes with negative wavevectors, and hence negative indices over a large frequency range.

Experimentally, the modes of metallic core and plasmon slot waveguides were probed using both near and far-field techniques. On open metallic surfaces, the wavelength and decay of surface plasmons was determined via far-field spectroscopy and near-field imaging with a photoactive polymer. Such geometries were characterized by modest plasmon propagation lengths (20 - 60 μm over visible frequencies) and wavelengths as small as one-tenth of the excitation wavelength.

Similar techniques were used for MIM-mode mapping, with one important distinction: all MIM-based measurements were performed using a unique dark-field, transmission configuration. This experimental geometry ensured that all observed transmission emerged from the waveguide and provided an extremely high signal-to-noise ratio. Using this technique, we measured plasmon propagation lengths of five times the excitation wavelength in slot waveguides as small as $\lambda^2/10$. Moreover, we obtained the first direct images of MIM modes in the near-field, revealing plasmon wavelengths as small as $\lambda/5$.

Because of their unique dispersion, MIM waveguides may enable realization of practical negative index and transformation-based optical elements, both in two-dimensional on-chip geometries and as basic elements of three-dimensional metamaterials. As a foundation for such applications, we reported the first experimental realization of a visible-frequency negative-index material, with $n = -5$. By patterning two-dimensional MIM prisms, we observed negative refraction of light in the blue-green region of the visible. Through appropriate choice of core dimensions and material, we determined that negative indices can be sustained over bandwidths exceeding 100 nm in the visible, with figures of merit approaching 20.

While the metallic cladding of MIM waveguides ensures high mode confinement, it can also double as an electrical contact for active opto-electronic devices. Exploiting this opportunity, we demonstrated a subwavelength-scale optical Si modulator, based on field-effect modulation of plasmon modes in a MOS geometry. This “plasMOStor” achieved amplitude modulation ratios of 11.2 dB in device volumes as small as one one-fifth of a cubic wavelength. Because of its low operating energy and high switching speeds, the device could form the basis for a deeply subwavelength optoelectronic transistor technology. Additionally, we demonstrated MIM waveguides as efficient color filters at visible wavelengths. By replacing the insulating core of MIM waveguides with an electrooptic media, color can be dynamically switched, potentially forming the basis for a compact, tunable display technology.

The results of this thesis indicate the accessibility of tunable refractive indices and propagation constants in plasmon waveguides over a wide frequency band. In combination with existing photonic waveguide and metamaterial technologies, these metal-dielectric structures facilitate design of a new materials class with extraordinary optical properties and applications. The following discussion highlights just a few potential avenues for future exploration, including transformation-based optical elements, invisibility cloaks, perfect lensing, and plasmonic manipulation of the local density of states.

1. Transformation optics: Transformation-based optical elements exploit the tunable indices afforded by metamaterials. By creating materials with a continuously graded index and mode profile, electromagnetic waves can be controlled in unprecedented ways. For example, transformation-based elements have been proposed for magnifying superlenses [133], invisibility cloaks [114], optical black holes [80], and an optical Aharonov-Bohm effect [80]. Moreover, transformation media may enable enhanced concentration and absorption of light, which would profoundly impact photovoltaic and photoelectrochemical devices.

In many ways, the field of transformation optics is akin to general relativity, where the path of lightwaves propagating in space-time is warped by the force of gravity. Like the equations of general relativity, Maxwell’s equations are invariant to coordinate transformation; however, the material permittivity ϵ and permeability μ will shift. Transformation optics is grounded on the principle that a coordinate transformation from one electromagnetic space to another requires only a modification of ϵ and μ . Design of any transformation-based element thus requires precise control of ϵ and μ .

In this thesis, the mode indices and propagation constants of plasmonic waveguides were determined from analytical field calculations. Additionally, experimental indices were extracted from near- and far-field interferometry and refraction. However, no calculations or experiments revealed the explicit values of ε and μ . Determination of such parameters would be paramount to any transformation-based applications.

The permittivity and permeability of a material can be derived from knowledge of its impedance, Z_c . For a material with index n , ε and μ are related to Z_c via:

$$\varepsilon = \frac{n}{Z_c}, \quad (7.1a)$$

$$\mu = nZ_c. \quad (7.1b)$$

While Z_c can be determined from reflection and transmission coefficients (see Appendix D), a more elegant approach invokes transmission line analysis. From [32], the characteristic impedance Z_c of a transmission line can be defined as :

$$Z_c = \frac{V}{I} \quad (7.2a)$$

$$P = \frac{1}{2} Z_c |I|^2 \quad (7.2b)$$

$$P = \frac{1}{2} \frac{|V|^2}{Z_c} \quad (7.2c)$$

where P is the power flowing in the transmission line, V is the equivalent transmission-line voltage, and I is the equivalent current. Determination of Z_c thus involves simple arithmetic of P , I , and V in a waveguide.

Unfortunately, the analysis is not quite as straightforward as it seems. Most

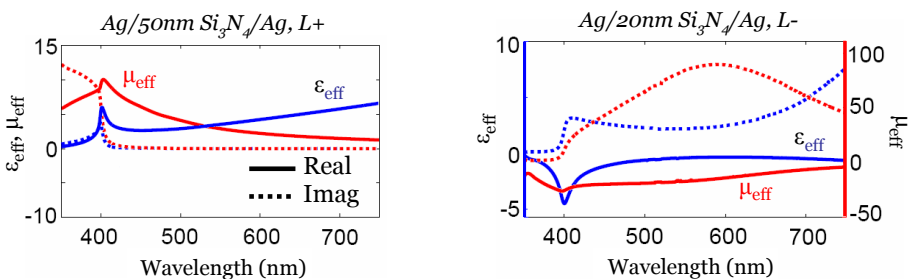


Figure 7.1. Calculations of the effective permittivity and permeability in plasmonic waveguides, for both positive and negative index modes. *Left*: The real and imaginary components of ε and μ for the L+ mode of a MIM waveguide composed of 50 nm Si_3N_4 clad with Ag. *Right*: The real and imaginary components of ε and μ for the L- mode of a MIM waveguide composed of 20 nm Si_3N_4 clad with Ag. In both cases, ε and μ were calculated using Equation (7.2b) and $I = \int_0^\infty -i\omega\varepsilon_\ell E_x dz$

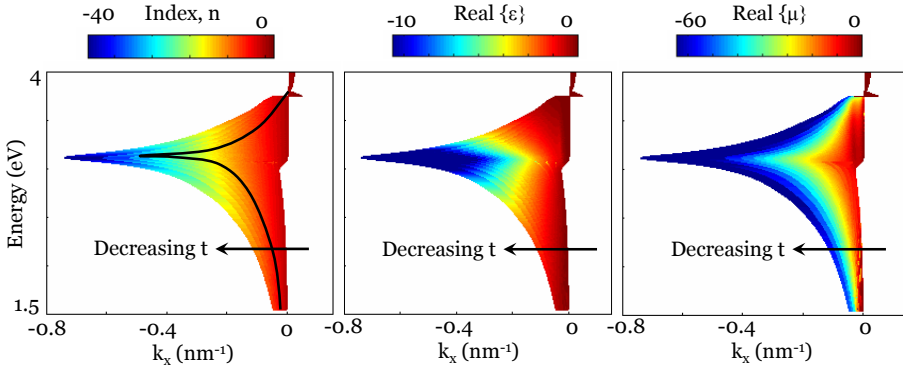


Figure 7.2. Calculations of the mode wavevector, permittivity and permeability in negative-index plasmonic waveguides. Here, the core thickness of a Ag-clad Si_3N_4 waveguide is varied from 5 nm through 50 nm, with individual dispersion traces (black line) corresponding to individual Si_3N_4 thicknesses.

importantly, the above equations only yield equivalent values for Z_c at DC. Moreover, much ambiguity exists in the literature regarding the definition of I and V . For example, many authors define I and V in terms of field integrals across all space. However, for antisymmetric guided modes, such an analysis yields either $Z_c = 0$ or $Z_c = \infty$.

Using the definition of I provided by Alu and Engheta [7] and Equation (7.2b), we have calculated ε and μ for various waveguides and wavelengths, as shown in Figures 7.1 and 7.2. The figures reveal sensible values. Notably, both ε and μ are positive, with μ close to 1, for positive index modes. In addition, both ε and μ are negative for negative index modes. However, the validity of these calculations has not yet been tested. For example, these calculations should be paired with determination of the reflection (R) and transmission (T) coefficients (Appendix D) to check for consistency. Additionally, simulations and experiments of R and T should be performed, to unambiguously define Z_c and hence ε and μ .

Precise knowledge of ε and μ in plasmonic metamaterials could profoundly impact our ability to create transformation-based optical elements, yielding a completely new toolkit for optical manipulation.

2. Invisibility cloaks: Of the many applications for transformation-based optics, invisibility seems to carry the largest appeal (at least with the media). Note that electromagnetic cloaking does not require a negative index, but rather a continuous tuning of the permittivity and permeability from values close to 1 down to zero. For example, to conceal a region of radius R_1 in cylindrical coordinates, a cloak spanning from R_1 to R_2 must be made with permittivities

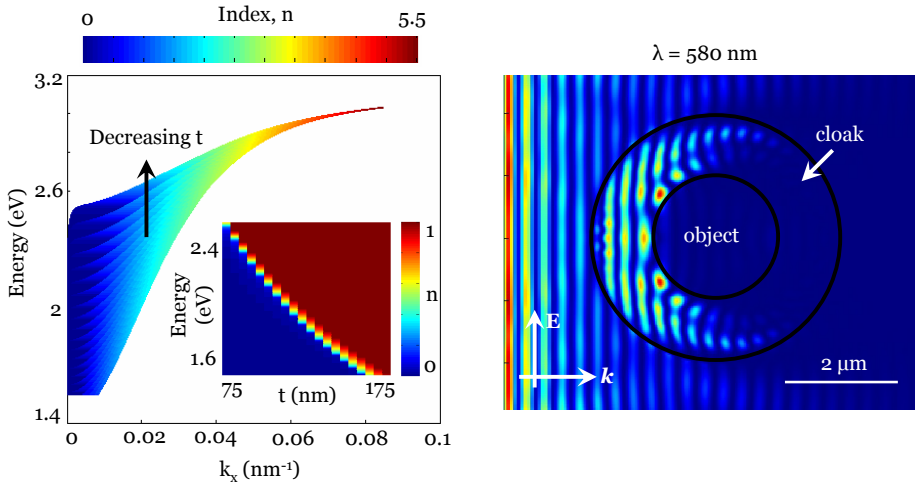


Figure 7.3. Design of a plasmonic cloak. *Left*: Dispersion relationships and calculated mode indices as a function of wavelength and thickness for Ag/Si₃N₄/Ag waveguides. The Si₃N₄ thickness is continuously varied from 75 nm to 175 nm in 1 nm increments, and the index can be seen to vary smoothly from 0 to 1. *Right*: Simulated MIM cloak, using a graded thickness with a \sqrt{r} variation from the outer interface at R_2 to the inner interface at R_1 . Due to poor cloak design, plane waves are not reconstructed at the exit side of the cloak. However, the simulation does indicate very little reflection from the cloak/object combination and only negligible transmission into the object area.

and permeabilities of [114]:

$$\varepsilon_r = \mu_r = \frac{R_2}{R_2 - R_1} \frac{(r - R_1)^2}{r} \quad (7.3a)$$

$$\varepsilon_\theta = \mu_\theta = \frac{R_2}{R_2 - R_1} \quad (7.3b)$$

$$\varepsilon_\phi = \mu_\phi = \frac{R_2}{R_2 - R_1}. \quad (7.3c)$$

While tuning both ε and μ may be possible with plasmonic metamaterials, requirements on μ can be relaxed by considering only TM-polarization. As noted by [29], such reduced coordinate systems only require tuning of $n_r = \sqrt{\varepsilon_r}$, with $\mu_\phi = 1$ and $\varepsilon_\theta = \frac{R_2}{R_2 - R_1}$.

Throughout this thesis, we have seen that plasmonic materials can support mode wavevectors and mode indices that far exceed those of conventional dielectric media. In addition, we have seen that MIM geometries can support hybrid plasmon-photon modes with indices close to zero. By exploiting these hybrid modes, the indices of plasmonic waveguides can be continuously and adiabatically tuned from 1 to 0.

Figure 7.3 shows a dispersion diagram and index map for these hybrid modes,

considering the L -solution of a $\text{Ag}/\text{Si}_3\text{N}_4/\text{Ag}$ waveguide. By varying the Si_3N_4 thickness from 175 nm down to 75 nm, the index can be continuously tuned from 1 to 0 at visible wavelengths. As a proof-of-principle cloak, a cylindrical $\text{Ag}/\text{Si}_3\text{N}_4/\text{Ag}$ waveguide was designed. Using back-of-the-envelope calculations, a thickness grade that varied as \sqrt{r} was chosen to yield an appropriate variation of n_r . Simulations of this cloak operating at $\lambda=580$ nm are shown in Figure 7.3. Light is incident on the cylindrical MIM cloak from the left, and begins to veer around the ‘object’ (here, empty space) as the cloak center is approached. Due to poor cloak design, a plane wave is not reconstructed on the other side of the cloak. Nevertheless, the simulation does indicate very little reflection from the cloak/object combination and only negligible transmission into the object area. While substantial work remains for realizing visible-frequency cloaks, planar MIM waveguides may provide one mechanism for two-dimensional implementation.

3. A ‘perfect’ lens: In a seminal work by Sir John Pendry [110], negative refraction was predicted to create a ‘perfect lens’ - an imaging system that could not only beat diffraction, but perfectly reconstruct an object in an image plane. Perfect lenses focus all Fourier components of an object, including those that do not propagate into the far-field. In addition to image transfer, these lenses can also magnify objects, either in combination with transformation-based optical elements or by appropriate lens curvature.

Despite significant advances in metamaterial and superlens designs, a perfect lens at visible wavelengths has not been demonstrated. Very likely, our MIM waveguides could form the basis for a first negative index perfect lens. However, several challenges to implementation remain. First, gaining access to these guided modes is non-trivial. As seen in Chapter 4, near-field interferometry can be used to directly probe the MIM wavevector. By thinning the top cladding layer of a MIM waveguide, both air and MIM-SP modes are excited. However, care must be taken to ensure that the excitation coefficients of the air and MIM modes are comparable. Second, inserting ‘objects’ will require careful design considerations. Since probes of MIM lensing will likely be external to the MIM guide, the object must be robust enough for high-fidelity transfer across a thinned Ag layer. Third, care must be taken to use an imaging technique that can probe image formation with deep subwavelength-scale resolution. Near-field microscopy, for example, can only resolve features down to about 100 nm. Use of the photoactive polymers introduced in Chapter 3 may be preferred, due to the potential for near-molecular-scale resolution. Additionally, use of resist allows for arbitrarily long exposures, which could be beneficial for this low-signal application. Lastly, the dimensions of the lens must be carefully designed. Given the typical propagation lengths and wavelengths for high FOM negative index materials, negative index lens lengths should not exceed 200-500 nm.

Figure 7.4 depicts the proposed experiment, along with prototype lenses fabricated in Si. Here, the ‘objects’ consist of 50-nm-diameter holes milled into the bottom cladding layer and later infilled with metal (red arrows). These objects are placed within the near-field of the lens, in order to reconstruct all subwavelength details in the image plane. Farther from the lens, a long input slit is

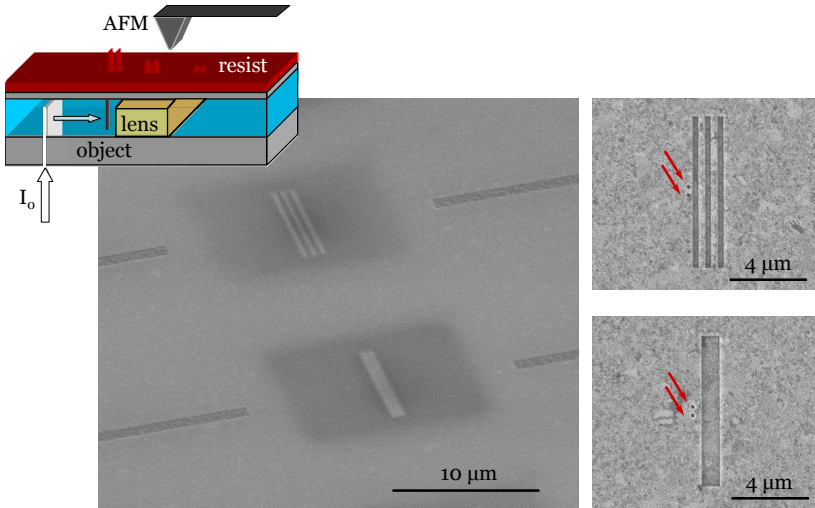


Figure 7.4. Experimental schematic and prototype fabrication of a ‘perfect lens’. A MIM waveguide with a thinned top cladding is used to transfer light across a flat negative index, MIM-based lens. The ‘objects’ consist of 50-nm-diameter holes milled into the bottom cladding layer and later infilled with metal (red arrows). Farther from the lens, a long input slit is patterned to transmit light into the waveguide. Both the air and MIM modes will be recorded in a photoactive polymeric resist, allowing for reconstruction of the object, its image, the propagating mode wavelength, and the mode’s path through the lens. Both continuous and layered lenses may be implemented.

patterned to transmit light into the waveguide. Both the air and MIM modes will be recorded in the resist, allowing for reconstruction of the object, its image, the propagating mode wavelength, and the mode’s path through the lens. Such an experiment would represent the first near-field mapping of negative refraction and subwavelength imaging in visible-frequency negative index materials.

4. Plasmonic manipulation of the local density of states - and a plasmon mirage:

The local density of states (LDOS) describes the total number of eigenmodes - including radiative and nonradiative modes - available to a source at a specific spatial location [64]. In optical systems, the LDOS is strongly correlated with the fluorescence lifetime and spontaneous emission rate of an emitter. Accordingly, control of the LDOS can be used to tailor dipolar emission in applications ranging from biosensing [77] to light-energy harvesting with optical antennas [102].

The LDOS is typically related to the trace of the imaginary component of the Green’s function tensor. Naturally, the LDOS will be high in spatial regions characterized by a large available number of eigenstates. In a fascinating example of LDOS manipulation [92], atomic corrals consisting of Co atoms on a Cu surface were probed using scanning tunneling microscopy. The atoms were

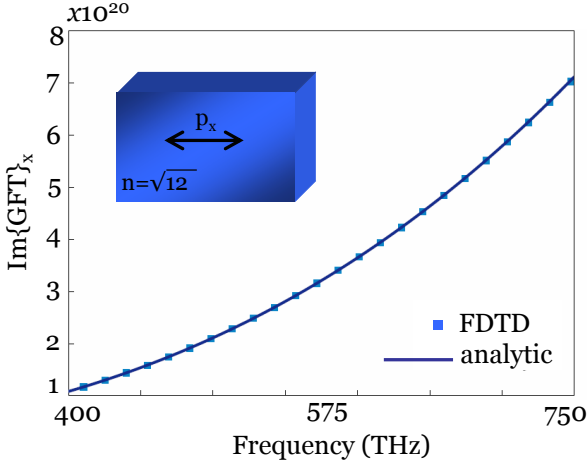


Figure 7.5. Finite difference time domain simulations of the local density of optical states in a homogeneous media. The simulated LDOS exhibits near-perfect agreement with the analytic expression for the LDOS in dielectrics: $\text{Imag}\{\text{GFT}_{hom}\} = \frac{\omega^3 \sqrt{\epsilon}}{6\pi c^3}$.

arranged into an ellipse, with an additional atom placed over one of the foci. By monitoring the differential conductance around the Fermi energy of the metal, LDOS maps of the surface could be formed. As expected, the LDOS was large over each atom of the corral, including the atom at the focus. However, an enhanced LDOS was also found over the other, empty ellipse focus, where no atom was present! In this measurement, the ‘quantum mirage’ was attributed to a Kondo resonance. However, theories based on scattering have also been proposed and validated [170, 4].

Much attention has since been given to both quantum corrals and photonic corrals (composed of metal particles on an transparent surface) [30]. However, little to no attention has been given to plasmonic corrals - enclosed geometries composed of dielectric inclusions on a metallic film. Much like the elliptical structures of Chapter 3, these corrals could combine the high localization of electronic states with the propagation properties of optical states. Additionally, plasmonic systems have already been shown to enhance and inhibit the quantum efficiency, lifetime, and angular emission pattern of fluorophores [77, 20]. Plasmonic corrals should therefore provide interesting and unprecedented opportunities to tailor the LDOS.

As future work, the plasmon LDOS in corrals should be explored, both theoretically and experimentally. Particular attention should be given to investigations of ‘plasmon mirages’ - coherent transfer of the LDOS from one elliptical corral focus to another. Using simulations, we have already mapped the LDOS in homogeneous media (Figure 7.5), obtaining sound agreement with the analytic local density of states. Further, we have begun to map the LDOS in elliptical corrals with with an additional dielectric inclusion at the focus (Fig-

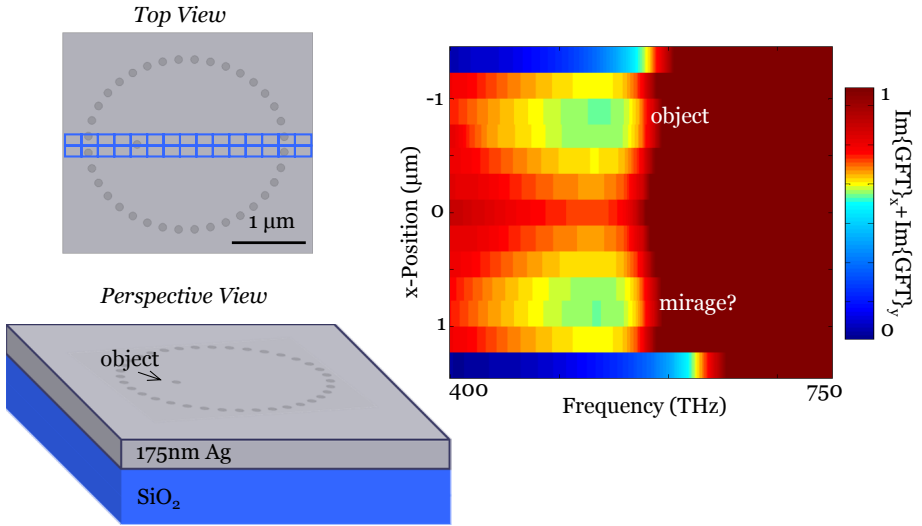


Figure 7.6. Simulations in search of a plasmon mirage. *Left:* The simulated geometry consists of 32 point dielectric inclusions patterned into a 175-nm-thick Ag film. The inclusions are arranged into an ellipse, with an additional inclusion placed at one focus. To generate LDOS maps, simulations were performed for x - and y -dipole polarizations over each position indicated by the blue mesh. *Right:* A frequency-position map of the LDOS obtained via FDTD. Dipole scans 125 nm above the major axis reveal a low partial xy LDOS over the focal inclusion at 580 THz. Interestingly, a low LDOS is also observed over the focus without an inclusion. These results hint at the possibility of engineering a plasmon mirage.

ure 7.6). Using FDTD, preliminary evidence of a mirage appears to be present for frequencies around 580 THz - where the low partial LDOS over the dielectric inclusion at one focus is transferred to the other ellipse focus. However, further work must be performed to confirm the presence of a mirage. Additionally, these simulations should be compared with analytical calculations of the LDOS over the entire corral area and experiments of similar structures.

5. And the list goes on...: A variety of additional explorations in flatland photonics may be identified. Among my personal favorites are: investigations of electrodynamics in negative index materials, all-optical modulation and gain in plasmistor-based structures, repulsive and attractive Casimir forces in MIM waveguides (the original parallel-plate geometry), and optical manipulation of bio-functionalized metallic surfaces. Within planar metallodielectric multilayers, the extent of future work is limited only by our desire and our creativity. While “time is the longest distance between” current technology and future exotic planar plasmonic applications, the famous words of Edwin Abbott resound: “Be patient, for the world is broad and wide.”

A Ag and SiO₂ Optical Constants

Ag dielectric constant ($\varepsilon = \varepsilon'_1 + \varepsilon''_1$) fitting parameters, Johnson and Christy data:

$$\varepsilon'_1 = \begin{cases} \text{cubic spline,} & \lambda < 500 \text{ nm,} \\ 29.34 - 0.11028\lambda + (1.1218 \times 10^{-4})\lambda^2 & \lambda \geq 500 \text{ nm,} \\ \quad - (1.08164 \times 10^{-7})\lambda^3 + (2.44496 \times 10^{-11})\lambda^4, & \end{cases} \quad (\text{A.1})$$

$$\varepsilon''_1 = \begin{cases} \text{cubic spline,} & \lambda < 400 \text{ nm,} \\ -1.753 + 0.009962\lambda - (1.696 \times 10^{-5})\lambda^2 & \lambda \geq 400 \text{ nm,} \\ \quad + (1.178 \times 10^{-8})\lambda^3 - (2.334 \times 10^{-12})\lambda^4, & \end{cases} \quad (\text{A.2})$$

Ag dielectric constant ($\varepsilon = \varepsilon'_1 + \varepsilon''_1$) fitting parameters, Palik data:

$$\varepsilon'_1 = \begin{cases} \text{cubic spline,} & \lambda < 350 \text{ nm,} \\ 10.314 - 0.026295\lambda - (2.51 \times 10^{-5})\lambda^2, & \lambda \geq 350 \text{ nm,} \end{cases} \quad (\text{A.3})$$

$$\varepsilon''_1 = \begin{cases} \text{cubic spline,} & \lambda < 350 \text{ nm,} \\ 1.0481 - 0.003259\lambda + (5.3387 \times 10^{-6})\lambda^2, & \lambda \geq 350 \text{ nm,} \end{cases} \quad (\text{A.4})$$

SiO₂ dielectric constant fitting parameters, Palik data:

$$\varepsilon_2 = \begin{cases} 2.806 - 0.00347\lambda & \\ \quad + (6.10502 \times 10^{-6})\lambda^2 - (3.68627 \times 10^{-9})\lambda^3, & \lambda < 612 \text{ nm,} \\ 2.222 - (2.46178 \times 10^{-4})\lambda & \\ \quad + (1.71928 \times 10^{-7})\lambda^2 - (4.49923 \times 10^{-11})\lambda^3, & \lambda \geq 612 \text{ nm.} \end{cases} \quad (\text{A.5})$$

B Plasmon Dispersion and Minimization Routines

In this appendix, we discuss derivation of the multilayer dispersion relations and field profiles. For concreteness, we consider the specific examples of a 3-layer, symmetric waveguide and a 5-layer waveguide of arbitrary materials and dimensions. Numerical techniques for solving these dispersion relations are also presented.

B.1 Derivation of the thin film dispersion relations for 3-layer, symmetric geometries

This section derives the dispersion relations and electromagnetic fields for the geometry shown in Figure B.1. The structure is assumed to be infinite in y , with wave propagation parallel to x and metallo-dielectric interfaces perpendicular to z . The core and cladding are composed of material 1 and 2, respectively.

Assume the modal electric and magnetic fields take the form:

$$\vec{E} = \vec{E}(z)e^{i(k_x x - \omega t)} \quad (\text{B.1a})$$

$$\vec{B} = \vec{B}(z)e^{i(k_x x - \omega t)} \quad (\text{B.1b})$$

so that the fields have no explicit y -dependence.

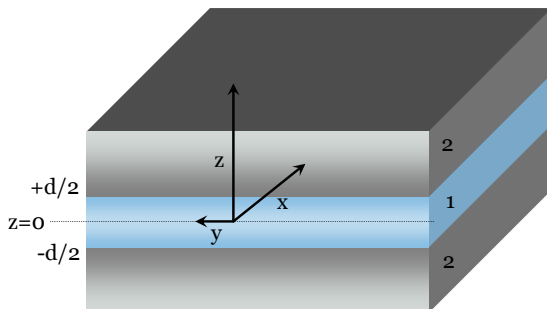


Figure B.1. Geometry of a three-layer, symmetric waveguide. The core (cladding) is composed of material 1 (2), and wave propagation is assumed to be parallel to x .

In the absence of free charges and currents, Maxwell's Equations dictate:

$$\nabla \cdot \vec{E} = 0 \quad (\text{B.2a})$$

$$\nabla \cdot \vec{B} = 0 \quad (\text{B.2b})$$

$$\nabla \times \vec{E} = -\frac{1}{c} \frac{\partial \vec{B}}{\partial t} \quad (\text{B.2c})$$

$$\nabla \times \vec{B} = \frac{1}{c} \varepsilon_\ell(\omega) \frac{\partial \vec{E}}{\partial t}. \quad (\text{B.2d})$$

Explicitly, the curl is written as:

$$\nabla \times \vec{A} = \left[\frac{\partial A_z}{\partial y} - \frac{\partial A_y}{\partial z} \right] \hat{x} + \left[\frac{\partial A_x}{\partial z} - \frac{\partial A_z}{\partial x} \right] \hat{y} + \left[\frac{\partial A_y}{\partial x} - \frac{\partial A_x}{\partial y} \right] \hat{z}. \quad (\text{B.3})$$

Via substitution of our assumed solution into each component of the curl:

$$\nabla \times \vec{E}:$$

$$\hat{x}: -\frac{\partial E_y}{\partial z} = \frac{i\omega}{c} B_x \quad (\text{B.4a})$$

$$\hat{y}: -\frac{\partial E_x}{\partial z} = ik_x E_z = \frac{i\omega}{c} B_y \quad (\text{B.4b})$$

$$\hat{z}: ik_x E_y = \frac{i\omega}{c} B_z \quad (\text{B.4c})$$

$$\nabla \times \vec{B}:$$

$$\hat{x}: -\frac{\partial B_y}{\partial z} = -\frac{i\omega}{c} \varepsilon_\ell E_x \quad (\text{B.4d})$$

$$\hat{y}: \frac{\partial B_x}{\partial z} = -ik_x B_z = -\frac{i\omega}{c} \varepsilon_\ell E_y \quad (\text{B.4e})$$

$$\hat{z}: -ik_x B_y = -\frac{i\omega}{c} \varepsilon_\ell E_z. \quad (\text{B.4f})$$

Now, note that all equations consist either of (E_y, B_x, B_z) or (E_x, E_z, B_y) . Thus, we can assume $E_y = 0 \rightarrow B_x, B_z = 0$ or $B_y = 0 \rightarrow E_x, E_z = 0$. The former corresponds to a transverse magnetic (TM) wave, while the latter corresponds to a transverse electric (TE) wave. However, it is also possible to solve (B.4a) through (B.4f) without assuming zero field components. We will study this case first.

Via substitution:

$$\frac{\partial E_x}{\partial z} - ik_x E_z = \frac{i\omega}{c} \left(-\frac{\omega}{ck_x} \right) \varepsilon_\ell E_z \quad \text{using (B.4b, B.4f)} \quad (\text{B.5a})$$

$$-\frac{\partial \left(\frac{+\omega}{ck_x} \varepsilon_\ell E_z \right)}{\partial z} = \frac{+i\omega}{c} \varepsilon_\ell E_x \quad \text{using (B.4d, B.4f)} \quad (\text{B.5b})$$

$$E_x = \frac{1}{k_x} \frac{\partial E_z}{\partial z} \quad (\text{B.6})$$

$$\frac{\partial^2 E_z}{\partial z^2} - \left(k_x^2 - \left(\frac{\omega}{c} \right)^2 \varepsilon_\ell \right) E_z = 0. \quad (\text{B.7})$$

Define:

$$k_{z\ell}^2 = k_x^2 - \left(\frac{\omega}{c} \right)^2 \varepsilon_\ell. \quad (\text{B.8})$$

Therefore,

$$\frac{\partial^2 E_z}{\partial z^2} - k_{z\ell}^2 E_z = 0 \rightarrow \lambda^2 - k_{z\ell}^2 = 0 \rightarrow \lambda = \pm k_{z\ell}, \quad (\text{B.9})$$

yielding:

$$E_z = \mathcal{A}e^{k_{z\ell}z} \pm \mathcal{B}e^{-k_{z\ell}z}. \quad (\text{B.10})$$

Accordingly, we may solve for E_x via

$$\frac{\partial E_z}{\partial z} = -ik_x E_x = \mathcal{A}k_{z\ell}e^{k_{z\ell}z} \mp \mathcal{B}k_{z\ell}e^{-k_{z\ell}z} \quad (\text{B.11})$$

yielding

$$E_x = -\frac{k_{z\ell}}{ik_x} (\mathcal{A}e^{k_{z\ell}z} \pm \mathcal{B}e^{-k_{z\ell}z}). \quad (\text{B.12})$$

And similarly for E_y

$$B_x = -\frac{c}{i\omega} \frac{\partial E_y}{\partial z} \quad \text{using (B.4a)} \quad (\text{B.13a})$$

$$\frac{\partial B_x}{\partial z} - ik_z B_z = -\frac{i\omega}{c} \varepsilon_\ell E_y \quad \text{using (B.4e)} \quad (\text{B.13b})$$

$$\frac{\partial \left(-\frac{c}{i\omega} \frac{\partial E_y}{\partial z} \right)}{\partial z} - ik_x \left(\frac{ck_x}{\omega} \right) E_y = -\frac{i\omega}{c} \varepsilon_\ell E_y \quad \text{using (B.4c)} \quad (\text{B.13c})$$

$$-\frac{c}{i\omega} \frac{\partial^2 E_y}{\partial z^2} + \frac{c}{i\omega} k_x^2 E_y + \frac{\omega}{c} \varepsilon_\ell E_y = 0, \quad (\text{B.13d})$$

giving:

$$\frac{\partial^2 E_y}{\partial z^2} + \left(-k_x^2 + \left(\frac{i\omega}{c} \right)^2 \varepsilon_\ell \right) E_y = 0. \quad (\text{B.14a})$$

Define

$$\beta_\ell^2 = -k_x^2 + \left(\frac{i\omega}{c} \right)^2 \varepsilon_\ell \rightarrow \beta_\ell = ik_{z\ell}, \quad (\text{B.15})$$

so that:

$$\frac{\partial^2 E_y}{\partial z^2} + \beta_\ell^2 E_y = 0, \quad (\text{B.16})$$

giving

$$E_y = \mathcal{C}e^{i\beta_\ell z} \pm \mathcal{D}e^{-i\beta_\ell z} \quad (\text{B.17a})$$

$$\text{or } E_y = \mathcal{C}e^{-k_z \ell z} \pm \mathcal{D}e^{k_z \ell z}. \quad (\text{B.17b})$$

Then it follows, since $ik_x E_y = \frac{i\omega}{c} B_z$ using (B.4c),

$$B_z = \frac{ck_x}{\omega} (\mathcal{C}e^{i\beta_\ell z} \pm \mathcal{D}e^{-i\beta_\ell z}) \quad (\text{B.18})$$

and correspondingly using (B.4a)

$$-\frac{\partial E_y}{\partial z} = -\mathcal{C}\beta_\ell e^{i\beta_\ell z} \pm \mathcal{D}\beta_\ell e^{-i\beta_\ell z} = \frac{i\omega}{c} B_x, \quad (\text{B.19})$$

yielding

$$B_x = \frac{c}{\omega} \beta_\ell (-\mathcal{C}e^{i\beta_\ell z} \pm \mathcal{D}e^{-i\beta_\ell z}). \quad (\text{B.20})$$

And lastly, using (B.4f): $ik_x B_y = -\frac{i\omega}{c} \varepsilon_\ell E_z$ yielding

$$B_y = -\frac{\omega}{c} \left(\frac{1}{k_x} \right) \varepsilon_\ell (\mathcal{A}e^{k_z \ell z} \mp \mathcal{B}e^{-k_z \ell z}). \quad (\text{B.21})$$

Now, outside the waveguide, we want all field components to decay to zero as $z \rightarrow \infty$. Inside, there are no restrictions (save for finiteness at the origin). Without loss of generality, we assume waves inside are composed of left and right ‘‘propagating’’ waves in equal proportion (i.e., set the normalization coefficients equal to one). Therefore, the field components outside and inside the waveguide are given by:

$$\text{OUTSIDE: } \begin{cases} E_x = -\frac{k_{z2}}{ik_x} (\mp \mathcal{B}e^{-k_{z2}z}) \\ E_y = \mathcal{C}e^{-k_{z2}z} \\ E_z = \pm \mathcal{B}e^{-k_{z2}z} \end{cases} \quad \begin{cases} B_x = -\frac{ic}{\omega} k_{z2} \mathcal{C}e^{-k_{z2}z} \\ B_y = -\frac{\omega}{c} \left(\frac{1}{k_x} \right) \varepsilon_\ell (\mp \mathcal{B}e^{-k_{z2}z}) \\ B_z = \frac{ck_x}{\omega} \mathcal{C}e^{-k_{z2}z} \end{cases} \quad (\text{B.22a})$$

$$\text{INSIDE: } \begin{cases} E_x = -\frac{k_{z1}}{ik_x} (e^{k_{z1}z} \mp e^{-k_{z1}z}) \\ E_y = e^{-k_{z1}z} \pm e^{k_{z1}z} \\ E_z = e^{k_{z1}z} \pm e^{-k_{z1}z} \end{cases} \quad \begin{cases} B_x = \frac{ic}{\omega} k_{z1} (-e^{-k_{z1}z} \pm e^{k_{z1}z}) \\ B_y = -\frac{\omega}{c} \left(\frac{1}{k_x} \right) \varepsilon_\ell (e^{k_{z1}z} \mp e^{-k_{z1}z}) \\ B_z = \frac{ck_x}{\omega} (e^{-k_{z1}z} \pm e^{k_{z1}z}) \end{cases} \quad (\text{B.22b})$$

To solve for the coefficients, we must implement the boundary conditions:

- E_x, D_z continuous at $z = \pm d/2$
- E_y continuous at $z = \pm d/2$
- B_x continuous at $z = \pm d/2$, $\frac{1}{\mu} B_{x,y}$ continuous at $z = \pm d/2$

Condition 1: E_x , D_z continuous:

$$E_x \longrightarrow \frac{ik_{z1}}{k_x} (e^{k_{z1}z} \mp e^{-k_{z1}z}) = \pm \frac{k_{z2}}{ik_x} \mathcal{B} e^{-k_{z2}z} \quad (\text{B.23a})$$

$$D_z \longrightarrow \varepsilon_1 (e^{k_{z1}z} \pm e^{-k_{z1}z}) = \pm \varepsilon_2 \mathcal{B} e^{-k_{z2}z} \quad (\text{B.23b})$$

leads to

$$ik_{z1} (e^{k_{z1}z} \mp e^{-k_{z1}z}) = \frac{k_{z2}}{i} \frac{\varepsilon_1}{\varepsilon_2} (e^{k_{z1}z} \pm e^{-k_{z1}z}) \quad (\text{B.24})$$

$$- \varepsilon_2 k_{z1} (e^{k_{z1}z} \mp e^{-k_{z1}z}) = \varepsilon_1 k_{z2} (e^{k_{z1}z} \pm e^{-k_{z1}z}) \quad (\text{B.25})$$

$$- \varepsilon_2 k_{z1} = \varepsilon_1 k_{z2} \left\{ \begin{array}{l} \coth(k_{z1}d/2) \\ \tanh(k_{z1}d/2) \end{array} \right\} \quad (\text{B.26})$$

yielding

$$\varepsilon_1 k_{z2} + \varepsilon_2 k_{z1} \left\{ \begin{array}{l} \tanh(k_{z1}d/2) \\ \coth(k_{z1}d/2) \end{array} \right\} = 0. \quad (\text{B.27})$$

Condition 2: E_y continuous:

$$e^{-k_{z1}z} \pm e^{k_{z1}z} = \mathcal{C} e^{-k_{z1}z} \quad (\text{B.28})$$

yielding

$$\mathcal{C} = e^{k_{z2}d/2} (e^{-k_{z1}d/2} \pm e^{k_{z1}d/2}). \quad (\text{B.29})$$

Condition 3: H_x , H_y , B_z continuous:

$$H_y \longrightarrow -\frac{\omega}{c} \left(\frac{1}{k_x} \frac{\varepsilon_1}{\mu_1} \right) (e^{k_{z1}d/2} \mp e^{-k_{z1}d/2}) = -\frac{\omega}{c} \left(\frac{1}{k_x} \frac{\varepsilon_1}{\mu_1} \right) (\mp \mathcal{B} e^{-k_{z2}d/2}) \quad (\text{B.30})$$

$$\varepsilon_1 \mu_2 (e^{k_{z1}d/2} \mp e^{-k_{z1}d/2}) = \varepsilon_2 \mu_1 (\mp \mathcal{B} e^{-k_{z2}d/2}) \quad (\text{B.31})$$

yielding

$$\mathcal{B} = \frac{\varepsilon_1 \mu_2}{\varepsilon_2 \mu_1} e^{k_{z2}d/2} (e^{k_{z1}d/2} \mp e^{-k_{z1}d/2}) \quad (\text{B.32})$$

$$B_z \longrightarrow \frac{ck_x}{\omega} (e^{-k_{z1}d/2} \pm e^{k_{z1}d/2}) = \frac{ck_x}{\omega} \mathcal{C} e^{-k_{z2}d/2} \quad (\text{B.33})$$

verifying

$$\mathcal{C} = e^{k_{z2}d/2} (e^{-k_{z1}d/2} \pm e^{k_{z1}d/2}) \quad (\text{B.34})$$

$$H_x \longrightarrow \frac{ick_{z1}}{\omega \mu_1} (-e^{-k_{z1}d/2} \pm e^{k_{z1}d/2}) = -\frac{ick_{z2}}{\omega \mu_2} \mathcal{C} e^{-k_{z2}z} \quad (\text{B.35})$$

$$\mathcal{C} = -\frac{k_{z1} \mu_2}{k_{z2} \mu_1} e^{k_{z2}d/2} (-e^{k_{z1}d/2} \pm e^{-k_{z1}d/2}), \quad (\text{B.36})$$

and implying that

$$-\frac{k_{z1}}{k_{z2}} \left(-e^{-k_{z1}d/2} \pm e^{k_{z1}d/2} \right) = e^{-k_{z1}d/2} \pm e^{k_{z1}d/2} \quad (\text{B.37})$$

$$\frac{k_{z1}\mu_2}{k_{z2}\mu_1} \left(e^{-k_{z1}d/2} \mp e^{k_{z1}d/2} \right) = \left(e^{-k_{z1}d/2} \pm e^{k_{z1}d/2} \right) \quad (\text{B.38})$$

$$\mp k_{z1}\mu_2 \left(e^{k_{z1}d/2} \mp e^{-k_{z1}d/2} \right) = \pm k_{z2}\mu_1 \left(e^{k_{z1}d/2} \pm e^{-k_{z1}d/2} \right) \quad (\text{B.39})$$

$$\mp k_{z1}\mu_2 = \pm k_{z2}\mu_1 \left\{ \begin{array}{l} \coth(k_{z1}d/2) \\ \tanh(k_{z1}d/2) \end{array} \right\} \quad (\text{B.40})$$

yielding

$$\pm \mu_1 k_{z2} \pm \mu_2 k_{z1} \left\{ \begin{array}{l} \tanh(k_{z1}d/2) \\ \coth(k_{z1}d/2) \end{array} \right\} = 0. \quad (\text{B.41})$$

However, note that this dispersion relation is not equivalent to the dispersion relation derived via continuity of E_x , D_z , (B.26).

Thus, we can either satisfy continuity of E_x , D_z , H_y OR continuity of E_y , H_x , H_z , corresponding to the existence of TM waves or TE waves in the waveguide.

B.2 Derivation of the thin film dispersion relations for 5-layer, arbitrary materials geometries

In this section, we derive the dispersion relation for a 5-layer metallodielectric structure composed of arbitrary materials. The dispersion relation derived in this section is general, and can easily be extended to N -multilayers or non-planar geometries (i.e., cylindrical or spherical geometries). The geometry is shown in Figure B.2. As before, wave propagation is assumed to be parallel to x .

From the previous section, we know the electric field components can be written as:

$$\begin{aligned} E_{x\ell} &= e^{ik_x x} (a_\ell e^{k_{z\ell} z} + b_\ell e^{-k_{z\ell} z}) \\ E_{z\ell} &= \left(\frac{ik_x}{k_{z\ell}} \right) e^{ik_x x} (-a_\ell e^{k_{z\ell} z} + b_\ell e^{-k_{z\ell} z}) \\ E_{y\ell} &= 0 \end{aligned} \quad (\text{B.42})$$

Implementing the boundary conditions (E_x , D_z continuous) at each interface, we find:

At the 1-2 interface:

$$a_1 + b_1 = a_2 + b_2 \quad (\text{B.43a})$$

$$\frac{\varepsilon_1}{k_{z1}} (-a_1 + b_1) = \frac{\varepsilon_2}{k_{z2}} (-a_2 + b_2) \quad (\text{B.43b})$$

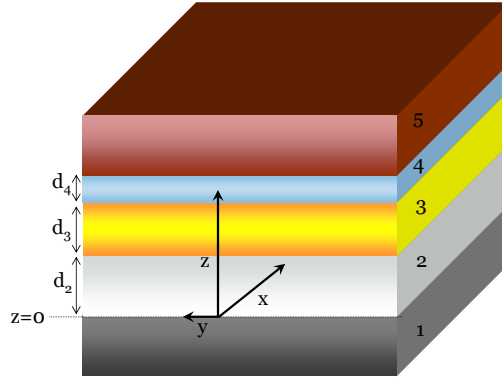


Figure B.2. Geometry of a five-layer waveguide composed of arbitrary materials 1, 2, 3, 4, and 5. Wave propagation is assumed to be parallel to x .

At the 2-3 interface:

$$a_2 e^{k_{z2} d_2} + b_2 e^{-k_{z2} d_2} = a_3 e^{k_{z3} d_2} + b_2 e^{-k_{z3} d_2} \quad (\text{B.44a})$$

$$\frac{\varepsilon_2}{k_{z2}} (-a_2 e^{k_{z2} d_2} + b_2 e^{-k_{z2} d_2}) = \frac{\varepsilon_3}{k_{z3}} (-a_3 e^{k_{z3} d_2} + b_3 e^{-k_{z3} d_2}) \quad (\text{B.44b})$$

At the 3-4 interface:

$$a_3 e^{k_{z3}(d_2+d_3)} + b_3 e^{-k_{z3}(d_2+d_3)} = a_4 e^{k_{z4}(d_2+d_3)} + b_4 e^{-k_{z4}(d_2+d_3)} \quad (\text{B.45a})$$

$$\frac{\varepsilon_3}{k_{z3}} (-a_3 e^{k_{z3}(d_2+d_3)} + b_3 e^{-k_{z3}(d_2+d_3)}) = \frac{\varepsilon_4}{k_{z4}} (-a_4 e^{k_{z4}(d_2+d_3)} + b_4 e^{-k_{z4}(d_2+d_3)}) \quad (\text{B.45b})$$

At the 4-5 interface:

$$a_4 e^{k_{z4}(d_2+d_3+d_4)} + b_4 e^{-k_{z4}(d_2+d_3+d_4)} = a_5 e^{k_{z5}(d_2+d_3+d_4)} + b_5 e^{-k_{z5}(d_2+d_3+d_4)} \quad (\text{B.46a})$$

$$\frac{\varepsilon_4}{k_{z4}} (-a_4 e^{k_{z4}(d_2+d_3+d_4)} + b_4 e^{-k_{z4}(d_2+d_3+d_4)}) = \frac{\varepsilon_5}{k_{z5}} (-a_5 e^{k_{z5}(d_2+d_3+d_4)} + b_5 e^{-k_{z5}(d_2+d_3+d_4)}) \quad (\text{B.46b})$$

and

$$E_z \rightarrow 0 \text{ as } z \rightarrow \pm\infty : b_1 = 0, a_5 = 0 \quad (\text{B.47})$$

Therefore, we have generated ten equations in ten unknowns: $a_1, b_1, a_2, b_2, a_3, b_3, a_4, b_4, a_5, b_5$. A nontrivial solution exists if and only if the determinant of the matrix of coefficients, $\det(L) = 0$. This condition will determine the dispersion relation connecting k_x and ω .

Note that embedded in this matrix is the dispersion relationship for 2, 3, and 4-layer geometries. For example, the dispersion for a 2-layer structure is given by the determinant of the matrix:

$$L = \begin{bmatrix} 0 & 1 & 0 & 0 \\ 1 & 1 & -1 & -1 \\ -\frac{\varepsilon_1}{k_{z1}} & \frac{\varepsilon_1}{k_{z1}} & \frac{\varepsilon_2}{k_{z2}} & -\frac{\varepsilon_2}{k_{z2}} \\ 0 & 0 & 1 & 0 \end{bmatrix}. \quad (\text{B.50})$$

Equivalently, the dispersion for a 3-layer structure is given by the determinant of the matrix:

$$L = \begin{bmatrix} 0 & 1 & 0 & 0 & 0 & 0 \\ 1 & 1 & -1 & -1 & 0 & 0 \\ -\frac{\varepsilon_1}{k_{z1}} & \frac{\varepsilon_1}{k_{z1}} & \frac{\varepsilon_2}{k_{z2}} & -\frac{\varepsilon_2}{k_{z2}} & 0 & 0 \\ 0 & 0 & e^{k_{z2}d_2} & e^{-k_{z2}d_2} & -e^{k_{z3}d_2} & -e^{-k_{z3}d_2} \\ 0 & 0 & -\frac{\varepsilon_2}{k_{z2}}e^{k_{z2}d_2} & \frac{\varepsilon_2}{k_{z2}}e^{-k_{z2}d_2} & \frac{\varepsilon_3}{k_{z3}}e^{k_{z3}d_2} & -\frac{\varepsilon_3}{k_{z3}}e^{-k_{z3}d_2} \\ 0 & 0 & 0 & 0 & 1 & 0 \end{bmatrix}. \quad (\text{B.51})$$

Of course, for structures with cylindrical symmetry, this matrix may be modified by a change of basis (i.e., the basis modes are composed of Bessel and Hankel functions, modified by a complex exponential, e^{ikx}).

B.3 Numerical Methods

In this section, we outline the numerical methods used for solving the dispersion relations. In general, the dispersion relations will consist of transcendental equations where both k and ω are complex [12]. In the context of monochromatic excitation of a waveguided mode, it is sensible to impose the frequency to be real. Unfortunately, $\det(\mathbf{L})=0$ has no exact solution in the real frequency domain, so minimization routines must be used.

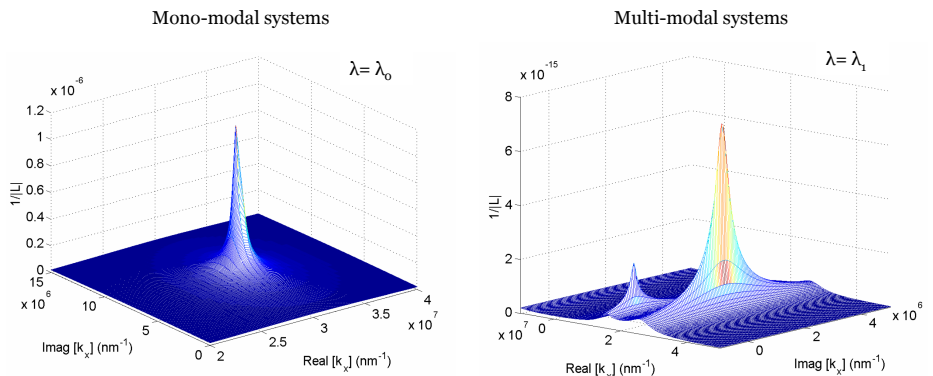


Figure B.3. Complex landscape of mono-modal and multi-modal systems, plotting $1/|L|$ as a function of $\text{Real}(k_x)$ and $\text{Imag}(k_x)$ at a single wavelength λ .

Depending on the waveguide geometry, one or more solutions will exist for each wavelength in the complex domain. Figure B.3 shows examples of waveguided systems consisting of one and two solutions. For clarity, the plots depict $1/|\det(\mathbf{L})|$, which will be a maximum when $\det(\mathbf{L})$ is a minimum. For mono-mode systems, only a single solution to the dispersion relations exists at each wavelength, and can be found through global minimization routines. For multi-mode systems, multiple solutions exist, and can be found either through local minimization routines or through an eigenvalue decomposition followed by a global minimization.

In this thesis, numerical methods are designed to search for complex wavevectors at a given frequency, iterating in the frequency-domain to form a continuous dispersion curve. Minimization is achieved using a Nelder-Mead algorithm [100], which implements multidimensional minimization based on a simplex method. Nelder-Mead minimizations are direct search algorithms which do not use numerical or analytic gradients. Rather, given an initial guess \mathbf{k}_0 , the routine defines a simplex with n vertices centered about \mathbf{k}_0 . The vertex with the largest function value is replaced with a new vertex obtained by reflection about the simplex centroid. The algorithm ends when the simplex size is below a threshold value.

For multimodal systems, multiple initial guesses may be used to initialize the simplex method. Alternatively, a singular value decomposition (SVD) can be used to decompose the dispersion relation matrix into its constituent singular values. For any complex $m \times n$ matrix \mathbf{L} , the SVD of \mathbf{L} will be given by $\mathbf{L}=\mathbf{P}\mathbf{D}\mathbf{Q}$, where \mathbf{P} and \mathbf{Q} are unitary matrices and \mathbf{D} is a diagonal matrix composed of the singular values of \mathbf{L} . The singular values are sorted in decreasing order and are equal to the square root of the eigenvalues. Note that the dispersion relations are defined by $\det(\mathbf{L})=\det(\mathbf{P}\mathbf{D}\mathbf{Q})=\det(\mathbf{P})\det(\mathbf{D})\det(\mathbf{Q})=0$. Since \mathbf{P} and \mathbf{Q} are

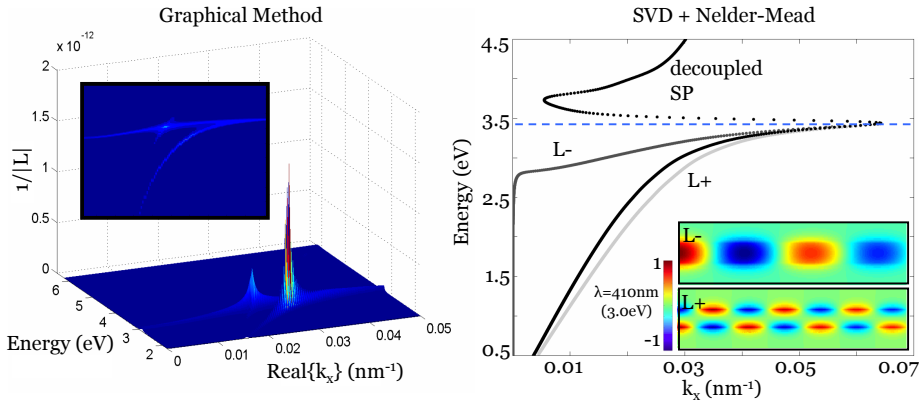


Figure B.4. Graphical versus analytic minimization routines. On the left, a graphical representation of the complex plane through $\text{Imag}(k_x)=0$ is shown for an example layered waveguide. On the right, the dispersion relations obtained via a single value decomposition and Nelder-Mead minimization routine are shown. The results of the minimization are in excellent agreement with the predictions from the graphical representation.

unitary, $\det(\mathbf{P})=\det(\mathbf{Q})=1$. Therefore, determination of the dispersion relations requires solution of $\det(\mathbf{D})=0$, or equivalently, $D_{ii}=0$.

Figure B.4 illustrates the result of an algorithm using a SVD followed by a Nelder-Mead minimization. For reference, a graphical cut of the complex plane through $\text{Imag}(k)=0$ is also shown. As seen, the results of the minimization routine are in excellent agreement with the wavevectors generated by graphical techniques.

C Plasmator Sample Preparation and Experimental Techniques

Samples were prepared by masking a window in the handle substrate of an SOI wafer. The silicon, oxide, and handle layers were $1.4\ \mu\text{m}$, $3.5\ \mu\text{m}$, and $525\ \mu\text{m}$, respectively, and the Si was n-doped with carrier concentrations of $9 \times 10^{16}/\text{cm}^3$. The handle substrate and oxide layer were etched using a mixture of between 3:1 and 10:1 nitric to hydrofluoric acid, creating a suspended Si membrane. The Si layer was thinned to the final desired thickness ($173\ \text{nm}$) using wet oxidation and a buffered oxide etch; the channel oxide was also grown via wet oxidation of Si. Typical membrane sizes ranged from $1\ \text{mm}^2$ to $1\ \text{cm}^2$ (see Figure C.1). Membranes exhibited tensile strain corresponding to a uniform stress of $500\ \text{MPa}$, as determined by Raman spectroscopy and x-ray diffraction (see Figure C.2).

Optical sources and drains were defined via focused ion beam milling with Ga^+ ions at $30\ \text{keV}$. Slit widths were defined to be $400\ \text{nm}$, and slit depths extended approximately halfway through the Si. A given membrane contained a square grid of devices of varying optical source-drain separation, with each device separated by $100\ \mu\text{m}$ from its neighbouring device. Electrical contact was made across the entire membrane, so that the gate bias was applied simultaneously to each individual modulator.

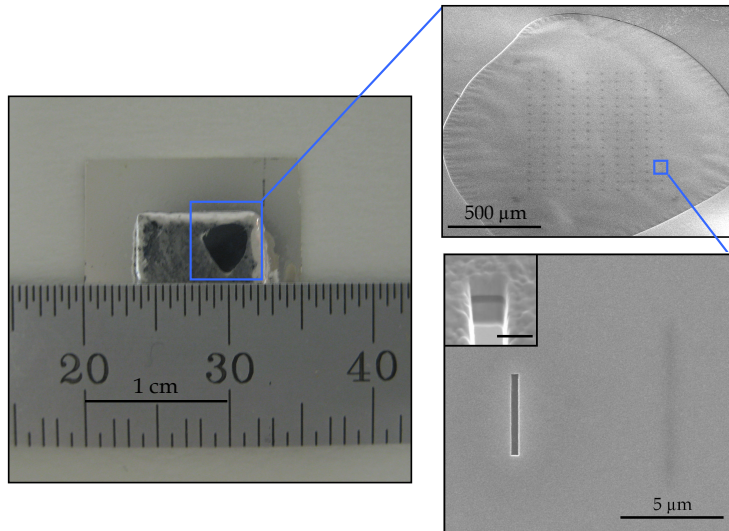


Figure C.1. Scanning electron micrographs of the fabricated plasmator membrane, from the cm-scale to the nm-scale. The scale bar on the device inset is $500\ \text{nm}$.

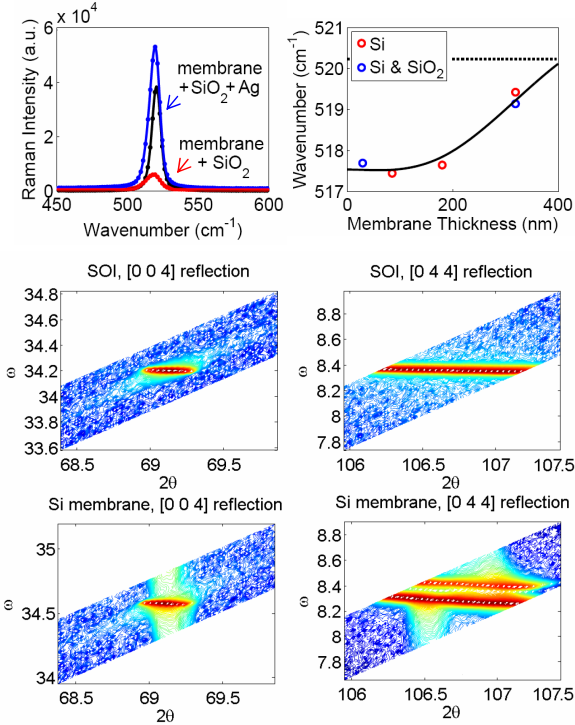


Figure C.2. Raman spectra and x-ray diffraction reciprocal space maps of the plasmistor membrane. Both Raman and XRD indicate that the plasmistor membranes are in tensile strain with a stress of approximately 500 MPa. As seen in the plot of Raman wavenumber versus membrane thickness, the strain is inherent to thinning, and does not arise because of the oxide layer.

Optical measurements were performed by focusing a tunable infrared laser onto a single device. Light was incoupled to the plasmistor through the slit in the top Ag cladding (the optical source) and outcoupled through the slit in the bottom Ag cladding (the optical drain). Transmission through the drain was monitored with a microscope objective coupled to a cooled Ge detector. Ag cladding layers were defined to be optically opaque, so that plasmistor transmission was imaged in a dark-field configuration. The laser was pulsed at 250 Hz and the time-averaged optical drain signal was monitored using a SR830 lock-in amplifier. Note that transmitted plasmistor intensities approached the saturation limit of the Ge detector, so that lock-in techniques were used only for ease of data collection and were not essential to achieve a high signal-to-noise ratio. Time-resolved measurements were conducted using a 4 V pulse train from a function generator with a 10 ns rise time; here, the laser was operated at CW, and the drain signal was detected with an LN₂-cooled PMT.

Dispersion calculations and simulations were based on the experimentally-determined complex optical constants of Si, Ag, and SiO₂, as obtained from spectroscopic ellipsometry. Accumulation conditions were modelled by solving the

one-dimensional Poisson equation subject to metallic boundary conditions at the back Si/Ag contact. A numerical solution was obtained for the spatially-varying charge distribution in the Si core, neglecting quantum mechanical effects. The resultant exponential charge decay was modelled as five discrete Drude layers of varying conductivity, assuming scattering times and effective masses characteristic of accumulation layers [48]. Thickness t , carrier concentration N , and conductivity s for each layer were taken as: $(t_1, N_1, s_1)=(5 \text{ nm}, 7 \times 10^{19}/\text{cm}^3, 2.17 \times 10^6 \text{ S/cm})$; $(t_2, N_2, s_2)=(12 \text{ nm}, 3 \times 10^{19}/\text{cm}^3, 9.30 \times 10^5 \text{ S/cm})$; $(t_3, N_3, s_3)=(33 \text{ nm}, 8 \times 10^{18}/\text{cm}^3, 2.48 \times 10^5 \text{ S/cm})$; $(t_4, N_4, s_4)=(50 \text{ nm}, 5 \times 10^{17}/\text{cm}^3, 1.55 \times 10^4 \text{ S/cm})$; $(t_5, N_5, s_5)=(73 \text{ nm}, 1 \times 10^{16}/\text{cm}^3, 309.8 \text{ S/cm})$, with the first layer adjacent to the SiO_2 -Si interface and the fifth layer adjacent to the bottom Ag interface. Weighted over the entire Si core, such Drude conductivities correspond to an average accumulation-layer carrier concentration of $5.78 \times 10^{18}/\text{cm}^3$ and a characteristic plasma frequency of $7.94 \times 10^{14} \text{ Hz}$. This discretized accumulation layer model was used both in the mode calculations of Figure 6.4 and in the finite-difference time-domain simulations of Figures 6.5 and 6.6. Note that the effects of strain on the Si refractive index were not explicitly included in calculations or simulations, but were considered in setting the effective Drude electron mass. However, such strain may directly contribute to plasmon modulation [67], from, e.g., a strain-induced electro-optic coefficient $\chi(2)$.

D Scattering from an Abruptly Terminated Plasmon Waveguide

In this appendix, we prescribe a recipe for calculating the reflection and transmission coefficients, field distribution, and far-field radiation pattern from an abruptly terminated plasmonic waveguide. The derivation could be used to explicitly determine the permittivity ε and permeability μ of surface plasmon waveguides. Alternatively, the derivation could be used to determine the field profile along the output slit of a plasmonic waveguide cavity. The former application would address whether stacked plasmonic waveguides can be formally considered as effective media or "metamaterials": if the interaction of electromagnetic radiation with the waveguide stack cannot be distinguished from the interaction of light with bulk media with index n and impedance Z , then the waveguide stack is indeed a metamaterial. From [142], note that ε , μ , n , and Z are related to the reflection R and transmission T coefficients via:

$$\varepsilon = \frac{n}{Z} \quad (\text{D.1a})$$

$$\mu = nZ \quad (\text{D.1b})$$

where

$$z = \pm \sqrt{\frac{(1+R)^2 - T'^2}{(1-R)^2 - T'^2}} \quad (\text{D.2})$$

and the index n is given by:

$$\cos(nkd) = \frac{1}{2T'}[1 - (R^2 - T'^2)]. \quad (\text{D.3})$$

Here, $T' = Te^{ik_o d}$, where d is the length of the material slab and k_o is the wavevector of the normally-incident radiation. Note that the index n determined from R and T should be consistent with the mode index determined from dispersion calculations.

In this appendix, we consider the three-layer symmetric plasmonic waveguide shown in Figure D.1. For simplicity, we only consider light scattering from one end of the waveguide, rather than light scattering from two ends of a finite-length waveguide. Moreover, we only consider transverse-magnetic guided modes. For this geometry, then, only a single component of the magnetic field, parallel to the y -axis, exists and is given by:

$$B_0(z) = \begin{cases} \frac{-\omega\varepsilon_2}{ck_x} (e^{-ik_{z1}z} \mp e^{ik_{z1}z}) & |x| \leq d/2 \\ \frac{-\omega\varepsilon_1}{ck_x} (e^{-ik_{z1}z} \mp e^{ik_{z1}z}) e^{ik_{z2}(z-d/2)} & |x| \geq d/2 \end{cases} \quad (\text{D.4})$$

Here, as usual, $k_x^2 = k_o^2 n_i^2 - k_{zi}^2$ with $i = 1, 2, 3$.

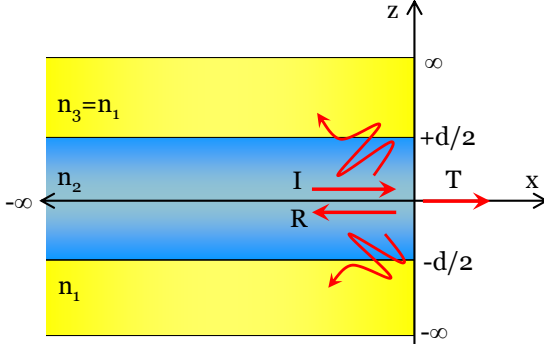


Figure D.1. Scattering from a three-layer symmetric plasmonic waveguide. A waveguided mode is incident from the left and encounters the discontinuity at $z = 0$. This discontinuity excites both waveguided modes and radiation waves for $z > 0$ and $z < 0$.

The existence of the discontinuity excites radiation waves and a guided mode propagating along the $-x$ axis [157]. The radiation waves are defined by a continuous spectrum of eigenwaves, satisfying the wave equation, that are oscillatory as $z \rightarrow \infty$:

$$B_y(z, \rho) = \Psi(z, \rho) e^{-i\beta x} \frac{d^2 \Psi(z, \rho)}{dz^2} + [k_o^2 n_i - \beta^2] \Psi(z, \rho) = 0 \quad (\text{D.5a})$$

with solutions:

$$\Psi(z, \rho) = Q \times \begin{cases} \cos(\rho(z - d/2) + a) & x > d/2 \\ A(k_{z1}) \cos(pz) + B(\rho) \sin(pz) & -d/2 < x < d/2 \\ \cos(\rho(z + d/2) - a) & x < -d/2. \end{cases} \quad (\text{D.6})$$

Here, the wavevectors ρ and p are defined by: $\rho^2 = k_o^2 n_1^2 - \beta^2 = k_o^2 n_3^2 - \beta^2$ and $p^2 = k_o^2 n_2^2 - \beta^2$. Q is a normalization factor that can be determined using Dirac delta functions according to [93].

It can be proven [156] that the spectrum $B_0(z), \Psi(z, \rho), 0 \leq \rho \leq \infty$ constitutes a complete set of orthogonal functions satisfying:

$$\int_{-\infty}^{\infty} \Psi(z, \rho) \Psi(z, \rho') dz = \delta(\rho - \rho') \quad (\text{D.7})$$

$$B_0(z) B_0(z') + \int_{-\infty}^{\infty} \Psi(z, \rho) \Psi(z', \rho) d\rho = \delta(z - z'). \quad (\text{D.8})$$

Therefore, in the waveguide region ($z < 0$), the solutions represent a superposition of the incident bound mode, the reflected guided mode (with reflection coefficient R_o) and the reflected radiation modes (with reflection coefficients R_ρ) [156, 157]:

$$\Phi_1(x, z) = B_0(z) [e^{-ik_x x} + R_0 e^{ik_x x}] + \int_0^\infty R_p \Psi(z, \rho) e^{i\gamma(\rho)x} d\rho. \quad (\text{D.9})$$

For $z > 0$, the incident wave scatters into plane waves of the form:

$$\phi_0(z, \lambda) = \frac{1}{\sqrt{\pi}} [\cos(\lambda z) + \sin(\lambda z)]. \quad (\text{D.10})$$

Satisfying the orthogonality relations:

$$\int_{-\infty}^\infty \phi_0(z, \lambda) \phi_0(z, \lambda') dz = \delta(\lambda - \lambda') \quad (\text{D.11a})$$

$$\int_{-\infty}^\infty \phi_0(z, \lambda) \phi_0(z', \lambda) dz = \delta(z - z'). \quad (\text{D.11b})$$

Therefore, in free-space ($z > 0$), we have:

$$\Phi_2(x, z) = \int_0^\infty T(\lambda) \phi_0(z, \lambda) e^{-i\delta(\lambda)x} d\lambda \quad (\text{D.12})$$

where $T(\lambda)$ is the transmission coefficient of the forward-scattered waves.

To determine R_0 , $R(\rho)$, and $T(\lambda)$, we must satisfy the boundary conditions at $x=0$, including continuity of the field components B_y and E_z .

Via continuity of B_y at $x = 0$:

$$B_0 [1 + R_0] + \int_0^\infty R_p \Psi(z, \rho) e^{i\gamma(\rho)x} d\rho = \int_0^\infty T(\lambda) \phi_0(z, \lambda) d\lambda. \quad (\text{D.13})$$

Additionally, using the orthogonality relations defined for Ψ and ϕ , we find:

$$T(\lambda) = \int_{-\infty}^\infty B_y(z) \phi_0(z, \lambda) dz \quad (\text{D.14a})$$

$$R_0 = 1 + \int_{-\infty}^\infty B_y(z) B_0 dz \quad (\text{D.14b})$$

$$R_p = \int_{-\infty}^\infty B_y(z) \Psi(z, \rho) dz. \quad (\text{D.14c})$$

Now, we seek to find $B_y(x=0) = B_y(z)$. To do so, we will use continuity of the tangential electric field, E_z , defined by:

$$\frac{\partial B_y}{\partial x} = \frac{-i\omega}{c} \varepsilon E_z. \quad (\text{D.15})$$

After some math, we find:

$$2k_x B_0 = \int_{-\infty}^\infty B_y(z) \zeta(z, z') dz \quad (\text{D.16})$$

where:

$$\zeta(z, z') = k_z B_0(z) B_0(z') + \int_0^\infty \gamma(\rho) \Psi(z, \rho) \Psi(z', \rho) d\rho + \int_0^\infty \delta(\lambda) \phi_0(z, \lambda) \phi_0(z', \lambda) d\lambda. \quad (\text{D.17})$$

Note that this integral is a Fredholm equation of the first kind. Unfortunately, this type of problem has no closed-form solution unless the kernel is a function of $(z' - z)$. However, we can transform (D.17) into a Fredholm equation of the second kind [157, 158], which is amenable to an iterative solution. By adding into $\zeta(z, z')$ the identities (D.8) and (D.11b) multiplied by $k_0 n_1$ and $k_0 n_0$, respectively, we find [156, 157]:

$$B_y(x=0, z) = \tilde{B}_0(z) + \int_{-\infty}^\infty B(z') K(z, z') dz \quad (\text{D.18})$$

where

$$\tilde{B}_0(z) = \frac{2k_z}{k_0(n_0 + n_1)} B_0(z) \quad (\text{D.19})$$

and

$$K(z, z') = \frac{-1}{k_0(n_0 + n_1)} \left[(k_x - k_0 n_1) B_0(z) B_0(z') + \int_0^\infty \{\gamma(\rho) - k_0 n_1\} \Psi(z, \rho) \Psi(z', \rho) d\rho + \int_0^\infty \{\delta(\lambda) - k_0 n_0\} \phi_0(z, \lambda) \phi_0(z', \lambda) d\lambda \right]. \quad (\text{D.20})$$

The solution is a Liouville-Newmann series, where B_y can be solved for using successive terms in the series:

$$B_N(z) = B_0(z) + \sum_{n=1}^N C_n(z) \quad (\text{D.21a})$$

$$C_n(z) = \int_{-\infty}^\infty dz_1 \int_{-\infty}^\infty dz_2 \dots \int_{-\infty}^\infty dz_n K(z, z_1) K(z_1, z_2) \dots K(z_{n-1}, z_n) B(z_n). \quad (\text{D.21b})$$

Bibliography

- [1] “Color and vision research laboraotries color & vision database,” <http://www.cvrl.org/>. 117
- [2] “Lumerical fdtd solutions 5.0.” 66, 109, 117
- [3] “Lumerical fdtd solutions 6.0.” 82
- [4] O. Agam and A. Schiller, “Projecting the kondo effect: Theory of the quantum mirage,” *Physical Review Letters*, vol. 86, pp. 484–487, 2001. 130
- [5] V. R. Almeida, Q. F. Xu, C. A. Barrios, and M. Lipson, “Guiding and confining light in void nanostructure,” *Optics Letters*, vol. 29, no. 11, pp. 1209–1211, 2004. 28, 63
- [6] A. Alu and N. Engheta, “Achieving transparency with plasmonic and metamaterial coatings,” *Physical Review E*, vol. 72, no. 1, Jul. 2005. 71
- [7] ———, “Optical nanotransmission lines: synthesis of planar left-handed metamaterials in the infrared and visible regimes,” *Journal of the Optical Society of America B-optical Physics*, vol. 23, no. 3, pp. 571–583, Mar. 2006. 126
- [8] L. Arizmendi, “Photonic applications of lithium niobate crystals,” *Phys. Stat. Sol.*, vol. 201, pp. 253–283, 2004. 121
- [9] H. A. Atwater, “The promise of plasmonics,” *Scientific American*, vol. April, pp. 58–63, 2007. 4
- [10] H. A. Atwater, K. A. Diest, and J. A. Dionne, “Slot waveguides for color displays,” U.S. Provisional Application No. 61/070,524, Tech. Rep., 2008. 115, 117, 118, 121
- [11] S. Baher and M. G. Cottam, “Theory of nonlinear guided and surface plasmon-polaritons in dielectric films,” *Surface Review and Letters*, vol. 10, no. 1, pp. 13–22, 2003. 9
- [12] A. S. Barker and R. Loudon, “Response functions in the theory of Raman scattering by vibrational and polariton modes in dielectric crystals,” *Rev. Mod. Phys.*, vol. 44, pp. 18–47, 1972. 143
- [13] W. L. Barnes, A. Dereux, and T. W. Ebbesen, “Surface plasmon subwavelength optics,” *Nature*, vol. 424, no. 6950, pp. 824–830, 2003. 54

- [14] P. Berini, “Plasmon-polariton modes guided by a metal film of finite width,” *Optics Letters*, vol. 24, no. 15, pp. 1011–1013, 1999. 10
- [15] —, “Plasmon-polariton modes guided by a metal film of finite width bounded by different dielectrics,” *Optics Express*, vol. 7, no. 10, pp. 329–335, 2000. 10
- [16] —, “Plasmon-polariton waves guided by thin lossy metal films of finite width: Bound modes of symmetric structures,” *Physical Review B*, vol. 61, no. 15, pp. 10 484–10 503, 2000. 10
- [17] —, “Plasmon-polariton waves guided by thin lossy metal films of finite width: Bound modes of asymmetric structures,” *Physical Review B*, vol. 63, no. 12, p. 125417, 2001. 10
- [18] D. Betancourt and C. del Rio, “Study of the human eye working principle: An impressive high angular resolution system with simple array detectors,” *Fourth IEEE Workshop on Sensor Array and Multichannel Processing*, pp. 93–97, 2006. 121
- [19] H. A. Bethe, “Theory of diffraction by small holes,” *The Physical Review*, vol. 66, pp. 163–182, 1944. 1
- [20] J. S. Biteen, D. Pacifici, N. S. Lewis, and H. A. Atwater, “Enhanced radiative emission rate and quantum efficiency in coupled silicon nanocrystal-nanostructured gold emitters,” *Nano Letters*, vol. 5, no. 9, pp. 1768–1773, 2005. 103, 130
- [21] M. Bohr, “Intels silicon research and development pipeline,” Intel, Tech. Rep., 2006. 104
- [22] S. I. Bozhevolnyi and V. Z. Lozovski, “Second-harmonic scanning optical microscopy of individual nanostructures,” *Physical Review B*, vol. 65, no. 23, 2002. 9
- [23] S. I. Bozhevolnyi, V. S. Volkov, E. Devaux, and T. W. Ebbesen, “Channel plasmon-polariton guiding by subwavelength metal grooves,” *Physical Review Letters*, vol. 95, no. 4, 2005. 63, 104
- [24] S. I. Bozhevolnyi, V. S. Volkov, E. Devaux, J. Y. Laluet, and T. W. Ebbesen, “Channel plasmon subwavelength waveguide components including interferometers and ring resonators,” *Nature*, vol. 440, no. 7083, pp. 508–511, 2006. 63, 104
- [25] M. L. Brongersma and P. G. Kik, Eds., *Surface Plasmon Nanophotonics*. Dordrecht, NL: Springer, 2007. 5
- [26] L. Brzozowski, E. H. Sargent, A. S. Thorpe, and M. Extavour, “Direct measurements of large near-band edge nonlinear index change from 1.48 to 1.55 μm in InGaAs/InAlGaAs multiquantum wells,” *Applied Physics Letters*, vol. 82, no. 25, pp. 4429–4431, 2003. 16

- [27] J. J. Burke, G. I. Stegeman, and T. Tamir, "Surface-polariton-like waves guided by thin, lossy metal-films," *Physical Review B*, vol. 33, no. 8, pp. 5186–5201, 1986. 9, 10, 28
- [28] W. S. Cai, D. A. Genov, and V. M. ShalaeV, "Superlens based on metal-dielectric composites," *Physical Review B*, vol. 72, no. 19, 2005. 71
- [29] W. Cai, U. K. Chettiar, A. V. Kildishev, and V. M. ShalaeV, "Optical cloaking with metamaterials," *Nature Photonics*, vol. 1, no. 4, pp. 224–227, APR 2007. 71, 127
- [30] C. Chicanne, T. David, R. Quidant, J. Weeber, Y. Lacroute, E. Bourillot, A. Dereux, G. Colas des Francs, and C. Girard, "Imaging the local density of states of optical corrals," *Physical Review Letters*, vol. 88, p. 097402, 2002. 130
- [31] C. Cojocariu and P. Rochon, "Light-induced motions in azobenzene-containing polymers," *Pure and Applied Chemistry*, vol. 76, pp. 1479–1497, 2004. 46, 47, 50
- [32] R. E. Collin, *Field Theory of Guided Waves*. IEEE Press, 1991. 125
- [33] M. Derouard, J. Hazart, G. Lrondel, R. Bachelot, P.-M. Adam, and P. Royer, "Polarization-sensitive printing of surface plasmon interferences," *Optics Express*, vol. 15, pp. 4238–4246, 2007. 46, 50
- [34] E. Devaux, T. W. Ebbesen, J.-C. Weeber, and A. Dereux, "Launching and decoupling surface plasmons via micro-gratings," *Applied Physica Letters*, vol. 83, p. 49364938, 2003. 58
- [35] K. A. Diest, J. A. Dionne, and H. A. Atwater, "Tunable photonic and plasmonic filters for spectral imaging and color displays," in preparation. 115, 117, 118, 121
- [36] J. A. Dionne, H. J. Lezec, and H. A. Atwater, "Highly confined photon transport in subwavelength metallic slot waveguides," *Nano Letters*, vol. 6, no. 9, pp. 1928–1932, 2006. 63, 91, 104
- [37] J. A. Dionne, L. A. Sweatlock, H. A. Atwater, and A. Polman, "Planar metal plasmon waveguides: frequency-dependent dispersion, propagation, localization, and loss beyond the free electron model," *Physical Review B*, vol. 72, no. 7, Aug. 2005. 9, 28, 35, 54, 90
- [38] —, "Plasmon slot waveguides: Towards chip-scale propagation with subwavelength-scale localization," *Physical Review B*, vol. 73, no. 3, Jan. 2006. 53, 54, 56, 60, 62, 63, 90, 104
- [39] H. Ditlbacher, F. R. Aussenegg, J. R. Krenn, B. Lamprecht, G. Jakopic, and G. Leising, "Organic diodes as monolithically integrated surface plasmon polariton detectors," *Applied Physics Letters*, vol. 89, no. 16, OCT 16 2006. 103

- [40] B. Dold and R. Mecke, "Optische eigenschaften von edelmetallen ubergangsmetallen und deren legierungen im infrarot .1," *Optik*, vol. 22, no. 6, p. 435, 1965. 11
- [41] G. Dolling, C. Enkrich, M. Wegener, C. M. Soukoulis, and S. Linden, "Simultaneous negative phase and group velocity of light in a metamaterial," *Science*, vol. 312, no. 5775, pp. 892–894, 2006. 73
- [42] G. Dolling, M. Wegener, and S. Linden, "Realization of a three-functional-layer negative-index photonic metamaterial," *Optics Letters*, vol. 32, no. 5, pp. 551–553, 2007. 73
- [43] G. Dolling, M. Wegener, S. Linden, and C. Hormann, "Photorealistic images of objects in effective negative-index materials," *Optics Express*, vol. 14, no. 5, pp. 1842–1849, MAR 6 2006. 72
- [44] G. Dolling, M. Wegener, C. M. Soukoulis, and S. Linden, "Negative-index metamaterial at 780 nm wavelength," *Optics Letters*, vol. 32, no. 1, pp. 53–55, 2007. 73
- [45] T. Ebbesen, H. Lezec, H. F. Ghaemi, T. Thio, and P. A. Wolff, "Extraordinary optical transmission through sub-wavelength hole arrays," *Nature*, vol. 391, pp. 667–669, 1998. 2
- [46] E. N. Economou, "Surface plasmons in thin films," *Physical Review*, vol. 182, no. 2, p. 539, 1969. 9, 11, 29
- [47] P. R. Evans, G. A. Wurtz, W. R. Hendren, R. Atkinson, W. Dickson, A. V. Zayats, and R. J. Pollard, "Electrically switchable nonreciprocal transmission of plasmonic nanorods with liquid crystal," *Applied Physics Letters*, vol. 91, no. 4, 2007. 104
- [48] F. F. Fang, A. B. Fowler, and A. Hartstein, "Effective mass and collision time of (100) Si surface electrons," *Physical Review B*, vol. 16, no. 10, pp. 4446–4454, 1977. 149
- [49] N. Fang, H. Lee, C. Sun, and X. Zhang, "Sub-diffraction-limited optical imaging with a silver superlens," *Science*, vol. 308, no. 5721, pp. 534–537, 2005. 71
- [50] M. Fleischmann, P. Hendra, and A. McQuillan, "Raman spectra of pyridine adsorbed at a silver electrode," *Chemical Physics Letters*, vol. 26, 1974. 5
- [51] F. J. Garcia-Vidal and J. B. Pendry, "Collective theory for surface enhanced Raman scattering," *Physical Review Letters*, vol. 77, no. 6, pp. 1163–1166, 1996. 4, 9
- [52] G. Gay, O. Alloschery, B. V. D. Lesegno, C. O'Dwyer, J. Weiner, and H. J. Lezec, "The optical response of nanostructured surfaces and the composite diffracted evanescent wave model," *Nature Physics*, vol. 2, no. 4, pp. 262–267, Apr. 2006. 45, 56

- [53] C. Genet and T. W. Ebbesen, "Light in tiny holes," *Nature*, vol. 445, pp. 39–46, 2007. 3
- [54] J. Gersten and A. Nitzan, "Electromagnetic theory of enhanced raman-scattering by molecules adsorbed on rough surfaces," *Journal of Chemical Physics*, vol. 73, no. 7, pp. 3023–3037, 1980. 4, 9
- [55] Y. Gilbert, R. Bachelot, P. Royer, A. Bouhelier, W. G.P., and L. Novotny, "Longitudinal anisotropy of the photoinduced molecular migration in azobenzene polymer films," *Optics Letters*, vol. 31, pp. 613–615, 2006. 50
- [56] T. Grosjean and D. Courjon, "Photopolymers as vectorial sensors of the electric field," *Optics Express*, vol. 14, pp. 2203–2210, 2006. 50
- [57] A. J. Haes and R. P. Van Duyne, "A unified view of propagating and localized surface plasmon resonance biosensors," *Analytical and Bioanalytical Chemistry*, vol. 379, no. 7–8, pp. 920–930, 2004. 9
- [58] ———, "Nanoscale optical biosensors based on localized surface plasmon resonance spectroscopy," vol. 5221, pp. 47–58, Aug. 2003. 9
- [59] N. Halas, "Plasmonic nanostructures and their applications in biosensing," *Abstracts of Papers of the American Chemical Society*, vol. 225, pp. U988–U988, 2003, part 1. 4
- [60] B. Hecht, H. Bielefeldt, L. Novotny, Y. Inouye, and D. W. Pohl, "Local excitation, scattering, and interference of surface plasmons," *Physical Review Letters*, vol. 77, no. 9, pp. 1889–1892, 1996. 66
- [61] L. R. Hirsch, J. B. Jackson, A. Lee, N. J. Halas, and J. West, "A whole blood immunoassay using gold nanoshells," *Analytical Chemistry*, vol. 75, no. 10, pp. 2377–2381, 2003. 9
- [62] C. E. Hofmann, E. J. R. Vesseur, L. A. Sweatlock, H. J. Lezec, F. J. Garcia de Abajo, A. Polman, and H. A. Atwater, "Plasmonic modes of annular nanoresonators imaged by spectrally resolved cathodoluminescence," *Nano Letters*, vol. 7, no. 12, pp. 3612–3617, 2007. 46, 104
- [63] A. A. Houck, J. B. Brock, and I. L. Chuang, "Experimental observations of a left-handed material that obeys snell's law," *Physical Review Letters*, vol. 90, no. 13, pp. 1–137 401, Apr. 2003. 73
- [64] C. Huang, A. Bouhelier, G. Colas des Francs, G. Legay, J. Weeber, and A. Dereux, "Far-field imaging of the electromagnetic local density of states," *Optics Letters*, vol. 33, p. 300, 2008. 129
- [65] C. Hubert, A. Rumyantseva, G. Lerondel, J. Grand, S. Kostcheev, L. Billoit, A. Vial, R. Bachelot, R. P., S. Chang, S. Gray, G. Wiederrecht, and G. C. Schatz, "Near-field photochemical imaging of noble metal nanostructures," *Nano Letters*, vol. 5, pp. 615–619, 2005. 46, 50

- [66] H. Iwai, "Cmos downsizing toward sub-10 nm," *Solid-State Electronics*, vol. 48, no. 4, pp. 497–503, 2004. 104
- [67] R. S. Jacobsen, K. N. Andersen, P. I. Borel, J. Fage-Pedersen, L. H. Frandsen, O. Hansen, M. Kristensen, A. V. Lavrinenko, G. Moulin, H. Ou, C. Peucheret, B. Zsigri, and A. Bjarklev, "Strained silicon as a new electro-optic material," *Nature*, vol. 441, no. 7090, pp. 199–202, 2006. 149
- [68] D. L. Jeanmaire and R. P. Van Duyne, "Surface raman spectroelectrochemistry: Part i. heterocyclic, aromatic, and aliphatic amines adsorbed on the anodized silver electrode," *Journal of Electroanalytical Chemistry*, vol. 84, pp. 1–20, 1977. 5
- [69] P. B. Johnson and R. W. Christy, "Optical constants of the noble metals," *Physical Review B*, vol. 6, no. 12, pp. 4370–4379, 1972. 11, 29, 65, 78, 83
- [70] M. Jutzi, M. Berroth, G. Wohl, M. Oehme, and E. Kasper, "Ge-on-si vertical incidence photodiodes with 39-ghz bandwidth," *IEEE Photonics Technology Letters*, vol. 17, no. 7, pp. 1510–1512, 2005. 113, 114
- [71] K. Y. Kim, Y. K. Cho, H. S. Tae, and J. H. Lee, "Light transmission along dispersive plasmonic gap and its subwavelength guidance characteristics," *Optics Express*, vol. 14, no. 1, pp. 320–330, 2006. 90
- [72] K. L. Kliewer and R. Fuchs, "Collective electronic motion in a metallic slab," *Physical Review*, vol. 153, no. 2, p. 498, 1967. 9, 11, 22
- [73] J. R. Krenn, B. Lamprecht, H. Ditlbacher, G. Schider, M. Salerno, A. Leitner, and F. R. Aussenegg, "Non diffraction-limited light transport by gold nanowires," *Europhysics Letters*, vol. 60, no. 5, pp. 663–669, 2002. 103
- [74] E. Kroger, "Calculations of energy losses of fast electrons in thin foils with retardation," *Zeitschrift Fur Physik*, vol. 216, no. 2, p. 115, 1968. 21
- [75] M. Kuijk and R. Vounckx, "Optical plasma resonance in semiconductors: Novel concepts for modulating far-infrared light," *Journal of Applied Physics*, vol. 66, no. 4, pp. 1544–1548, 1989. 109
- [76] E. S. Kwak, J. Henzie, S. H. Chang, S. K. Gray, G. C. Schatz, and T. W. Odom, "Surface plasmon standing waves in large-area subwavelength hole arrays," *Nano Letters*, vol. 5, no. 10, pp. 1963–1967, Oct. 2005. 65
- [77] J. R. Lakowicz, J. Malicka, I. Gryczynski, Z. Gryczynski, and C. D. Geddes, "Radiative decay engineering: the role of photonic mode density in biotechnology," *J. Phys. D: Appl. Phys.*, vol. 36, pp. R240–R249, 2003. 129, 130
- [78] B. Lamprecht, J. R. Krenn, G. Schider, H. Ditlbacher, M. Salerno, N. Felidj, A. Leitner, F. R. Aussenegg, and J. C. Weeber, "Surface plasmon propagation in microscale metal stripes," *Applied Physics Letters*, vol. 79, no. 1, pp. 51–53, 2001. 61

- [79] L. D. Landau, P. L. P. Lifshitz, and L. P. Pitaevskii, Eds., *Electrodynamics of Continuous Media*, 2nd ed. Reed Educational and Professional Publishing Ltd, 1984. 18, 37
- [80] U. Leonhardt and T. Philbin, “General relativity in electrical engineering,” *New Journal of Physics*, vol. 8, p. 247, 2006. 124
- [81] G. Leveque, C. G. Olson, and D. W. Lynch, “Reflectance spectra and dielectric functions for Ag in the region of interband-transitions,” *Physical Review B*, vol. 27, no. 8, pp. 4654–4660, 1983. 11
- [82] H. J. Lezec, A. Degiron, E. Devaux, R. A. Linke, L. Martin-Moreno, F. J. Garcia-Vidal, and T. W. Ebbesen, “Beaming light from a subwavelength aperture,” *Science*, vol. 297, pp. 820–822, 2002. 2
- [83] H. J. Lezec, J. A. Dionne, and H. A. Atwater, “Negative refraction at visible frequencies,” *Science*, vol. 316, no. 5823, pp. 430–432, 2007. 63, 88, 96
- [84] H. Lezec and T. Thio, “Diffracted evanescent wave model for enhanced and suppressed optical transmission through subwavelength hole arrays,” *Optics Express*, vol. 12, pp. 3629–3651, 2004. 45
- [85] A. Lien, C. Cai, R. John, J. Galligan, and J. Wilson, “16.3” qsxga high resolution wide viewing angle tft-lcds based on ridge and fringe-field structures,” *Displays*, vol. 22, pp. 9–14, 2001. 121
- [86] A. S. Liu, R. Jones, L. Liao, D. Samara-Rubio, D. Rubin, O. Cohen, R. Nicolaescu, and M. Paniccia, “A high-speed silicon optical modulator based on a metal-oxide-semiconductor capacitor,” *Nature*, vol. 427, no. 6975, pp. 615–618, 2004. 105, 112, 114
- [87] J. Liu, M. Beals, A. Pomerene, S. Bernardis, R. Sun, J. Cheng, L. Kimerling, and J. Michel, “Waveguide-integrated, ultra-low-energy geSi electro-absorption modulators,” *Nature Photonics*, vol. 2, pp. 433–437, 2008. 112
- [88] S. W. Liu and M. Xiao, “Electro-optic switch in ferroelectric thin films mediated by surface plasmons,” *Applied Physics Letters*, vol. 88, no. 14, 2006. 104
- [89] Z. Liu, J. M. Steele, W. Srituravanich, Y. Pikus, C. Sun, and X. Zhang, “Focusing surface plasmons with a plasmonic lens,” *Nano Letters*, vol. 5, pp. 1726–1729, 2005. 46
- [90] S. A. Maier, P. G. Kik, H. A. Atwater, S. Meltzer, E. Harel, B. E. Koel, and A. A. G. Requicha, “Local detection of electromagnetic energy transport below the diffraction limit in metal nanoparticle plasmon waveguides,” *Nature Materials*, vol. 2, no. 4, pp. 229–232, 2003. 9
- [91] S. A. Maier, “Effective mode volume of nanoscale plasmon cavities,” *Optical and Quantum Electronics*, vol. 38, no. 1, pp. 257–267, Jan. 2006. 63

- [92] H. C. Manoharan, C. P. Lutz, and D. M. Eigler, “Quantum mirages formed by coherent projection of electron structure,” *Nature*, vol. 43, p. 512, 2000. 129
- [93] D. Marcuse, *Theory of Dielectric Optical Waveguides*, P. Liao and P. Kelley, Eds. Academic Press, 1991. 152
- [94] J. C. Maxwell Garnett, “Colours in metal glasses and in metallic films,” *Philosophical Transactions of the Royal Society of London*, vol. 203, 1904. 4
- [95] A. D. McFarland and R. P. Van Duyne, “Single silver nanoparticles as real-time optical sensors with zeptomole sensitivity,” *Nano Letters*, vol. 3, no. 8, pp. 1057–1062, 2003. 9
- [96] G. Mie, “Beiträge zur optik trüber medien, speziell kolloidaler metallösungen,” *Annalen Der Physik*, vol. 25, no. 3, pp. 377–445, 1908. 5
- [97] D. A. B. Miller, “Rationale and challenges for optical interconnects to electronic chips,” *Proc. of the IEEE*, vol. 88, no. 6, pp. 728–749, 2000. 53, 104
- [98] H. T. Miyazaki and Y. Kurokawa, “Squeezing visible light waves into a 3-nm-thick and 55-nm-long plasmon cavity,” *Physical Review Letters*, vol. 96, no. 9, 2006. 58, 63
- [99] P. Munoz, J. A. Dionne, J. L. Stockdill, and H. A. Atwater, “Photochemical near-field imaging of plasmon corrals with nanometer-scale resolution (surf report, 2007).” 46
- [100] J. A. Nelder and R. Mead, “A simplex-method for function minimization,” *Computer Journal*, vol. 7, no. 4, pp. 308–313, 1965. 21, 144
- [101] T. Nikolajsen, K. Leosson, I. Salakhutdinov, and S. I. Bozhevolnyi, “Polymer-based surface-plasmon-polariton stripe waveguides at telecommunication wavelengths,” *Applied Physics Letters*, vol. 82, no. 5, pp. 668–670, 2003. 9
- [102] L. Novotny, “Effective wavelength scaling for optical antennas,” *Physical Review Letters*, vol. 98, p. 266802, 2007. 129
- [103] A. K. Okyay, A. J. Pethe, D. Kuzum, S. Latif, D. A. B. Miller, and K. C. Saraswat, “Sige optoelectronic metal-oxide semiconductor field-effect transistor,” *Optics Letters*, vol. 32, no. 14, pp. 2022–2024, 2007. 114
- [104] D. P. O’Neal, L. R. Hirsch, N. J. Halas, J. D. Payne, and J. L. West, “Photo-thermal tumor ablation in mice using near infrared-absorbing nanoparticles,” *Cancer Letters*, vol. 209, no. 2, pp. 171–176, 2004. 4
- [105] A. Otto, “Excitation of nonradiative surface plasma waves in silver by the method of frustrated total reflection,” *Zeitschrift fur Physik*, 1968. 5

- [106] E. Ozbay, “Plasmonics: Merging photonics and electronics at nanoscale dimensions,” *Science*, vol. 311, no. 5758, pp. 189–193, 2006. 53, 104
- [107] D. Pacifici, H. J. Lezec, and H. A. Atwater, “All-optical modulation by plasmonic excitation of cdse quantum dots,” *Nature Photonics*, vol. 1, no. 7, pp. 402–406, 2007. 103, 104
- [108] E. Palik, Ed., *Handbook of Optical Constants of Solids*. Academic Press, New York, 1985. 29
- [109] E. Palik and G. Ghosh, Eds., *Handbook of Optical Constants of Solids II*. Academic Press, New York, 1991. 11, 50, 78, 83
- [110] J. B. Pendry, “Negative refraction makes a perfect lens,” *Physical Review Letters*, vol. 85, no. 18, pp. 3966–3969, Oct. 2000. 71, 128
- [111] J. B. Pendry, A. J. Holden, D. J. Robbins, and W. J. Stewart, “Magnetism from conductors and enhanced nonlinear phenomena,” vol. 47, no. 11, pp. 2075–2084, Nov. 1999. 73
- [112] J. B. Pendry, A. J. Holden, W. J. Stewart, and I. Youngs, “Extremely low frequency plasmons in metallic mesostructures,” *Physical Review Letters*, vol. 76, no. 25, Jun. 1996. 73
- [113] J. B. Pendry, L. Martin-Moreno, and F. J. Garcia-Vidal, “Mimicking surface plasmons with structured surfaces,” *Science*, vol. 305, no. 5685, pp. 847–848, 2004. 11
- [114] J. B. Pendry, D. Schurig, and D. R. Smith, “Controlling electromagnetic fields,” *Science*, vol. 312, no. 5781, pp. 1780–1782, 2006. 9, 71, 124, 127
- [115] R. B. Pettit, J. Silcox, and R. Vincent, “Measurement of surface-plasmon dispersion in oxidized aluminum films,” *Physical Review B*, vol. 11, no. 8, pp. 3116–3123, 1975. 21
- [116] D. F. P. Pile and D. K. Gramotnev, “Channel plasmon-polariton in a triangular groove on a metal surface,” *Optics Letters*, vol. 29, no. 10, pp. 1069–1071, 2004. 104
- [117] D. F. P. Pile, T. Ogawa, D. K. Gramotnev, Y. Matsuzaki, K. C. Vernon, K. Yamaguchi, T. Okamoto, M. Haraguchi, and M. Fukui, “Two-dimensionally localized modes of a nanoscale gap plasmon waveguide,” *Applied Physics Letters*, vol. 87, no. 26, 2005. 63
- [118] S. Pillai, K. R. Catchpole, T. Trupke, G. Zhang, J. Zhao, and M. A. Green, “Enhanced emission from si-based light-emitting diodes using surface plasmons,” *Applied Physics Letters*, vol. 88, p. 161102, 2006. 103
- [119] D. Pines, “Collective energy losses in solids,” *Reviews of Modern Physics*, vol. 28, pp. 184–198, 1956. 5

- [120] J. A. Porto, F. J. Garcia-Vidal, and J. B. Pendry, “Transmission resonances on metallic gratings with very narrow slits,” *Physical Review Letters*, vol. 83, no. 14, pp. 2845–2848, 1999. 63
- [121] H. Raether, *Surface Plasmons on Smooth and Rough Surfaces and on Gratings*. Berlin: Springer-Verlag, 1988. 3, 13, 28, 54, 58
- [122] S. A. Ramakrishna, “Physics of negative refractive index materials,” *Rep. Prog. Phys.*, vol. 68, pp. 449–521, 2005. 72, 73
- [123] R. H. Ritchie, “Plasma losses by fast electrons in thin films,” *Physical Review*, vol. 106, 1957. 5, 9
- [124] A. Roberts, “Electromagnetic theory of diffraction by a circular aperture in a thick, perfectly conducting screen,” *J. Opt. Soc. Am. A*, vol. 4, pp. 1970–1983, 1987. 1
- [125] J. T. Robinson, C. Manolatou, L. Chen, and M. Lipson, “Ultrasmall mode volumes in dielectric optical microcavities,” *Physical Review Letters*, vol. 95, no. 14, 2005. 63
- [126] R. Ruppin, “Decay of an excited molecule near a small metal sphere,” *Journal of Chemical Physics*, vol. 76, no. 4, pp. 1681–1684, 1982. 15
- [127] —, “Electromagnetic energy density in a dispersive and absorptive material,” *Physics Letters a*, vol. 299, no. 2–3, pp. 309–312, 2002. 77
- [128] M. Sandtke, “Surface plasmon polariton propagation in straight and tailored waveguides,” Ph.D. dissertation, University of Twente, 2007. 97
- [129] D. Sarid, “Long-rand surface-plasma waves on very thin metal-films,” *Physical Review Letters*, vol. 47, no. 26, pp. 1927–1930, 1981. 9
- [130] U. Schröter and D. Heitmann, “Grating couplers for surface plasmons excited on thin metal films in the kretschmann-raether configuration,” *Phys. Rev. B*, vol. 60, no. 7, pp. 4992–4999, Aug 1999. 58
- [131] S. Schultz, D. R. Smith, J. J. Mock, and D. A. Schultz, “Single-target molecule detection with nonbleaching multicolor optical immunolabels,” *Proceedings of the National Academy of Sciences of the United States of America*, vol. 97, no. 3, pp. 996–1001, 2000. 9
- [132] D. Schurig, J. J. Mock, B. J. Justice, S. A. Cummer, J. B. Pendry, A. F. Starr, and D. R. Smith, “Metamaterial electromagnetic cloak at microwave frequencies,” *Science*, vol. 314, no. 5801, pp. 977–980, 2006. 71
- [133] D. Schurig, J. B. Pendry, and D. R. Smith, “Transformation-designed optical elements,” *Optics Express*, vol. 15, no. 22, pp. 14 772–14 782, 2007. 9, 124
- [134] V. M. Shalaev, “Optical negative-index metamaterials,” *Nature Photonics*, vol. 1, no. 1, pp. 41–48, Jan. 2007. 63, 71, 73, 91

- [135] V. M. Shalaev, W. S. Cai, U. K. Chettiar, H. K. Yuan, A. K. Sarychev, V. P. Drachev, and A. V. Kildishev, "Negative index of refraction in optical metamaterials," *Optics Letters*, vol. 30, no. 24, pp. 3356–3358, 2005. 73
- [136] R. A. Shelby, D. R. Smith, and S. Schultz, "Experimental verification of a negative index of refraction," *Science*, vol. 292, no. 5514, pp. 77–79, Apr. 2001. 71, 73, 96
- [137] Y. Shen and P. N. Prasad, "Nanophotonics: a new multidisciplinary frontier," *Applied Physics B — Lasers and Optics*, vol. 74, no. 7–8, pp. 641–645, 2002. 9
- [138] K. T. Shimizu, R. A. Pala, J. D. Fabbri, M. L. Brongersma, and N. A. Melosh, "Probing molecular junctions using surface plasmon resonance spectroscopy," *Nano Letters*, vol. 6, no. 12, pp. 2797–2803, 2006. 104
- [139] H. Shin and S. H. Fan, "All-angle negative refraction for surface plasmon waves using a metal-dielectric-metal structure," *Physical Review Letters*, vol. 96, no. 7, 2006. 63
- [140] G. Shvets, "Photonic approach to making a material with a negative index of refraction," *Physical review. B, Condensed matter and materials physics*, vol. 67, no. 3, p. 035109, 2003, 1098-0121. 99
- [141] —, "Photonic approach to making a material with a negative index of refraction," *Physical Review B*, vol. 67, no. 3, 2003. 99
- [142] D. R. Smith, S. Schultz, P. Markos, and C. M. Soukoulis, "Determination of effective permittivity and permeability of metamaterials from reflection and transmission coefficients," *Physical Review B*, vol. 65, no. 19, 2002. 73, 151
- [143] C. Sonnichsen, A. C. Duch, G. Steininger, M. Koch, G. von Plessen, and J. Feldmann, "Launching surface plasmons into nanoholes in metal films," *Applied Physics Letters*, vol. 76, no. 2, pp. 140–142, 2000. 65
- [144] R. A. Soref, "Silicon-based optoelectronics," *Proc. of the IEEE*, vol. 81, no. 12, pp. 1687–1706, 1993. 105
- [145] R. A. Soref and B. R. Bennett, "Electrooptical effects in silicon," *IEEE Journal of Quantum Electronics*, vol. 23, no. 1, pp. 123–129, 1987. 105
- [146] C. M. Soukoulis, S. Linden, and M. Wegener, "Negative refractive index at optical wavelengths," *Science*, vol. 315, no. 5808, pp. 47–49, 2007. 73, 91
- [147] C. M. Soukoulis, M. Kafesaki, and E. N. Economou, "Negative-index materials: New frontiers in optics," *Advanced Materials*, vol. 18, no. 15, pp. 1941–1952, Aug. 2006. 73

- [148] G. I. Stegeman, J. J. Burke, and D. G. Hall, “Non-linear optics of long-range surface-plasmons,” *Applied Physics Letters*, vol. 41, no. 10, pp. 906–908, 1982. 9
- [149] E. A. Stern and R. A. Ferrell, “Surface plasma oscillations of a degenerate electron gas,” *Physical Review*, vol. 120, no. 1, pp. 130–136, 1960. 11
- [150] B. Stiller, T. Geue, K. Morawetz, and M. Saphiannikova, “Optical patterning in azobenzene polymer films,” *Journal of Microscopy*, vol. 219, pp. 109–114, 2005. 46
- [151] M. I. Stockman, “Slow propagation, anomalous absorption, and total external reflection of surface plasmon polaritons in nanolayer systems,” *Nano Letters*, vol. 6, no. 11, pp. 2604–2608, 2006. 78
- [152] L. A. Sweatlock, S. A. Maier, H. A. Atwater, J. J. Penninkhof, and A. Polman, “Highly confined electromagnetic fields in arrays of strongly coupled ag nanoparticles,” *Physical Review B*, vol. 71, no. 23, 2005. 40, 103
- [153] J. Takahara, S. Yamagishi, H. Taki, A. Morimoto, and T. Kobayashi, “Guiding of a one-dimensional optical beam with nanometer diameter,” *Optics Letters*, vol. 22, no. 7, pp. 475–477, 1997. 54, 103
- [154] M. Tanaka, “Description of a wave packet propagating in anomalous dispersion media — a new expression of propagation velocity,” *Plasma Phys. Controlled Fusion*, vol. 31, no. 7, p. 1049, 1989. 15
- [155] T. Taubner, D. Korobkin, Y. Urzhumov, G. Shvets, and R. Hillenbrand, “Near-field microscopy through a sic superlens,” *Science*, vol. 313, p. 1595, 2006. 71
- [156] T. G. Theodoropoulos and I. G. Tigelis, “Radiation modes of a five-layer symmetric slab waveguide,” *International Journal of Infrared and Millimeter Waves*, vol. 16, pp. 1811–1824, 1995. 152, 154
- [157] I. G. Tigelis and A. B. Manenkov, “Scattering from an abruptly terminated asymmetrical slab waveguide,” *J. Opt. Soc. Am. A*, vol. 16, pp. 523–532, 1999. 152, 154
- [158] I. G. Tigelis, T. G. Theodoropoulos, and I. A. Papakonstantinou, “Radiation properties of an abruptly terminated five-layer symmetric slab waveguide,” *J. Opt. Soc. Am. A*, vol. 6, pp. 1260–1267, 1997. 154
- [159] J. Tominaga, C. Mihalcea, D. Buchel, H. Fukuda, T. Nakano, N. Atoda, H. Fuji, and T. Kikukawa, “Local plasmon photonic transistor,” *Applied Physics Letters*, vol. 78, no. 17, pp. 2417–2419, 2001. 103
- [160] H. Tuovinen, M. Kauranen, K. Jefimovs, P. Vahimaa, T. Vallius, J. Turunen, N. V. Tkachenko, and H. Lemmetyinen, “Linear and second-order nonlinear optical properties of arrays of noncentrosymmetric gold nanoparticles,” *Journal of Nonlinear Optical Physics & Materials*, vol. 11, no. 4, pp. 421–432, 2002. 9

- [161] J. Valentine, S. Zhang, T. Zentgraf, E. Ulin-Avila, D. A. Genov, G. Bartal, and X. Zhang, “Three-dimensional optical metamaterial with a negative refractive index,” *Nature*, 2008. 96
- [162] J. van Wijngaarden, E. Verhagen, A. Polman, C. Ross, H. Lezec, and H. Atwater, “Direct imaging of propagation and damping of near-resonance surface plasmon polaritons using cathodoluminescence spectroscopy,” *Appl. Phys. Lett.*, vol. 88, p. 221111, 2006. 46
- [163] E. Verhagen, J. A. Dionne, L. K. Kuipers, H. A. Atwater, and A. Polman, “Near-field visualization of strongly confined surface plasmon polaritons in metal-insulator-metal waveguides,” *Nano Letters*, vol. 8, pp. 2925 – 2929, 2008. 63
- [164] E. Verhagen, A. Polman, and L. Kuipers, “Nanofocusing in laterally tapered plasmonic waveguides,” *Optics Express*, vol. 16, p. 45, 2008. 46
- [165] G. Veronis and S. H. Fan, “Theoretical investigation of compact couplers between dielectric slab waveguides and two-dimensional metal-dielectric-metal plasmonic waveguides,” *Optics Express*, vol. 15, no. 3, pp. 1211–1221, 2007. 114
- [166] V. G. Veselago, “Electrodynamics of substances with simultaneously negative values of sigma and mu,” *Soviet Physics Uspekhi-ussr*, vol. 10, no. 4, p. 509, 1968. 71, 75, 89, 96
- [167] F. Villa, T. Lopez-Rios, and L. E. Regalado, “Electromagnetic modes in metal-insulator-metal structures,” *Physical Review B*, vol. 63, no. 16, 2001. 54
- [168] R. Vincent and J. Silcox, “Dispersion of radiative surface plasmons in aluminum films by electron-scattering,” *Physical Review Letters*, vol. 31, no. 25, pp. 1487–1490, 1973. 23
- [169] Y. A. Vlasov, M. O’Boyle, H. F. Hamann, and S. J. McNab, “Active control of slow light on a chip with photonic crystal waveguides,” *Nature*, vol. 438, no. 7064, pp. 65–69, 2005. 104
- [170] M. Weissmann and H. Bonadeo, “A simple interpretation of quantum mirages,” *Physica E*, vol. 10, pp. 544–548, 2001. 130
- [171] P. Winsemius, F. F. Vankampen, H. P. Lengkeek, and C. G. Vanwent, “Temperature-dependence of optical-properties of au, ag and cu,” *Journal of Physics F-Metal Physics*, vol. 6, no. 8, pp. 1583–1606, 1976. 11
- [172] K. K. Wong, *Properties of Lithium Niobate*. INSPEC, Inc., 2002. 115
- [173] R. W. Wood, “On a remarkable case of uneven distribution of light in a diffraction grating spectrum,” *Phil. Mag.*, vol. 4, p. 396, 1902. 4

- [174] E. L. Wooten, K. M. Kissa, A. Yi-Yan, E. J. Murphy, D. A. Lafaw, P. F. Hallemeier, D. Maack, D. V. Attanasio, D. J. Fritz, G. J. McBrien, and D. E. Bossi, "A review of lithium niobate modulators for fiber-optic communications systems," *IEEE J. Quantum Elec.*, vol. 6, pp. 69–82, 2000. 121
- [175] P. T. Worthing and W. L. Barnes, "Efficient coupling of surface plasmon polaritons to radiation using a bi-grating," *Applied Physics Letters*, vol. 79, p. 3035, 2001. 45, 58
- [176] Q. F. Xu, B. Schmidt, S. Pradhan, and M. Lipson, "Micrometre-scale silicon electro-optic modulator," *Nature*, vol. 435, no. 7040, pp. 325–327, 2005. 105, 112
- [177] S. Zhang, W. J. Fan, N. C. Panoiu, K. J. Malloy, R. M. Osgood, and S. R. J. Brueck, "Experimental demonstration of near-infrared negative-index metamaterials," *Physical Review Letters*, vol. 95, no. 13, 2005. 73
- [178] R. Zia, M. D. Selker, P. B. Catrysse, and M. L. Brongersma, "Geometries and materials for subwavelength surface plasmon modes," *Journal of the Optical Society of America A*, vol. 21, no. 12, pp. 2442–2446, 2004. 29, 53, 104
- [179] S. L. Zou and G. C. Schatz, "Silver nanoparticle array structures that produce giant enhancements in electromagnetic fields," *Chemical Physics Letters*, vol. 403, no. 1–3, pp. 62–67, 2005. 4, 9